1991

High-resolution Core-level Spectroscopies Of Molecular Silicon Compounds Using Monochromatized Synchrotron Radiation

John D. Bozek

High Resolution Core-Level Spectroscopies of Molecular Silicon Compounds Using Monochromatized Synchrotron Radiation

by
John D. Bozek

Department of Chemistry

Submitted in partial fulfilment
of the requirements for the degree of
Doctor of Philosophy

Faculty of Graduate Studies
The University of Western Ontario
London, Ontario
June 1991

ISBN 0-315-66332-4

ABSTRACT

High-resolution core-level photoabsorption, photoelectron and photoionization mass spectra of numerous substituted silane molecules have been measured in the gas phase around the Si $2p$ ionization edges using monochromatized synchrotron radiation. Photoabsorption spectra were also measured around the Si $2s$ ionization edges and the Cl $2p$ ionization edges of the chlorine-containing molecules. Multiple-scattering Xα calculations were performed to aid in the assignment of the peaks observed in the photoabsorption spectra. The chemical series approach, where the effects of small systematic chemical changes in the composition of the molecule under study on the observed spectra provide useful aids for assignments, has been used throughout this work.

Photoabsorption spectra of the core electronic levels are reported for three series of silicon molecules, the fluoromethylsilane compounds: $Si(CH_3)_xF_{4-x}$, the chloromethylsilane compounds; $Si(CH_3)_xCl_{4-x}$, and the chlorosilane compounds; SiH_xCl_{4-x}, x = 0–4. Theoretical results from MS-Xα calculations along with trends observed in the experimental spectra facilitate the identification and assignment of numerous features in the spectra. Below the ionization edges, the observed peaks are assigned to result from electronic transitions of the core electrons into virtual molecular orbitals and Rydberg orbitals. Above the ionization edges, peaks in the photoabsorption cross sections are assigned to transitions into a variety of quasibound states in the continuum: virtual molecular orbitals supported by the shape of the molecular potential, shape resonances, and delayed-onsets resulting from centrifugal barriers to the exiting electron.

Using a newly constructed photoelectron spectrometer, Si $2p$ photoelectron spectra of eleven substituted silane molecules were measured with unprecedented experimental resolution. The spectra exhibit vibrational broadening, and for silane, tetrafluorosilane and ethylsilane, individual vibrational bands are resolved on the Si $2p$ photoelectron lines. Very high experimental resolution is required to

resolve individual vibrational bands. Extensive use is made of the equivalent-cores approximation to aid in the interpretation of the observed vibrational structure. Chemical effects on the lifetimes of the Si $2p$ core holes are also investigated.

Total ion yield spectra, total electron yield spectra, photoionized mass spectra and mass-resolved photoion yield spectra of the fluoromethylsilane compounds, $Si(CH_3)_xF_{4-x}$; x = 0–4, measured using photon energies around the Si $2p$ core ionization edges are also reported. In the fragmentation patterns observed following irradiation of the sample with monochromatized synchrotron radiation, the methyl groups are found to be more labile than the fluorine atoms at photon energies below and above the Si $2p$ ionization edges. Partial ion yields of the SiF^+ and $SiMe^+$ fragment ions are seen to exhibit specific enhancement at the Si $2p \rightarrow \sigma^*$ resonances below the ionization edge.

ACKNOWLEDGEMENTS

I would like to express my sincere thanks to the supervisor of my Ph.D. research, Dr. G.M. Bancroft, who provided guidance, encouragement and endless enthusiasm over the course of my studies.

Much of the work presented here is a direct result of the technical assistance provided by K.H. Tan, L.L. Coatsworth, J.S. Tse and R. Jones, for which I am grateful.

I also wish to acknowledge the support of other members of the department who were friends and co-workers: Joanne Bice, Jeff Cutler, Margaret Hyland, Rosemary Hynes, Masoud Kasrai, Mike Jennings, Zhi Feng Lui, Ron Martin, Ian Muir, Richard Mycroft, Jamie Price, Doug Sutherland, Dong Sheng Yang, and Brian Yates.

I am grateful for the financial support provided by the Natural Sciences and Engineering Research Council and The University of Western Ontario over the term of my studies.

Finally, I would like to thank my parents and family for their support and understanding with a special thank you to Liz Moxon and Sam who helped to make it fun. I dedicate this work to them.

TABLE OF CONTENTS

LIST OF TABLES

LIST OF FIGURES

CHAPTER 1.
General Introduction

1.1. Synchrotron Radiation

The availability of tunable high-resolution monochromatized synchrotron radiation has revolutionized the spectroscopy of core-level electrons in atoms, molecules, and solids. Unprecedented photon fluxes and bandwidths, both of which are essential for obtaining high-resolution core-level spectra, are now being achieved in the soft x-ray region of the electromagnetic continuum ($10 \lesssim h\nu \lesssim 1000$ eV) using new monochromator designs[1] and "high-brightness" synchrotron radiation sources. Around the world, over 35 dedicated synchrotron radiation sources are available or will become available in the near future for spectroscopic studies.[2] The "third-generation" sources are also presently being constructed[3–5] and with suitable advanced monochromator designs, should greatly improve the photon flux, bandwidth and spatial resolution of the monochromatized synchrotron light available for spectroscopic studies once they are fully commissioned.

Synchrotron radiation was first observed in 1947 and characterized shortly after[6–8] using a 70 MeV electron accelerator at General Electric. The University of Wisconsin 240 MeV electron storage ring, *Tantalus*, became the first synchrotron light source dedicated to the production of photons for use in spectroscopy.[9] Synchrotron light source electron storage rings with higher electron energies have since been constructed, including the 1 GeV *Aladdin* storage ring which recently replaced *Tantalus* as the "workhorse" ring at University of Wisconsin. The energy of the electrons circulating in the storage ring is one of the parameters which

determines the characteristics of the light emitted from the ring. Other important parameters include the radius of curvature of the electron orbit, the magnetic field in the bending magnets, the electron current, etc. Several excellent treatises describing the operating characteristics of numerous synchrotrons are available[10] and will not be discussed in detail here. Equations describing the output from a synchrotron source have been developed[11,12] and characteristic photon flux and brightness values have been calculated as a function of the photon energy for numerous cases. Typically, the spectral distribution curve rises sharply from a short wavelength ($\lambda < 0.1$ Å), peaks near the critical wavelength, λ_c, which is related to the bending radius of the electron path, and falls off slowly to longer wavelength. The radiation emitted from an electron storage ring or synchrotron therefore forms a broad continuum extending over the infrared, visible, ultraviolet, soft X-ray and X-ray regions of the electromagnetic continuum.

To be useful for most high resolution spectroscopic studies, a tunable monochromator is required to select a narrow bandwidth of photons with the desired energy. A variety of optical designs have been employed to achieve maximum throughput and resolution for different photon energy ranges. In the low energy domain ($h\nu < 30$ eV), normal incidence or near-normal incidence optics can be used. Above that energy however,($30 \lesssim h\nu \lesssim 1000$ eV), glancing incidence angle optics must be used to prevent undesirable absorption of the incident radiation.[13] In the high energy domain ($h\nu \gtrsim 1000$ eV), glancing incidence optics with crystal monochromators operating on the principles of Bragg diffraction are usually employed to disperse the polychromatic radiation from the synchrotron radiation source.[14] The energy range of interest dictates what type of monochromator design is suitable. For a given energy range, numerous types of monochromators are used, each with strengths and weaknesses with respect to the other designs.

1.2. CSRF Beamline and Grasshopper Monochromator

The spectra reported in this thesis were all measured at the Canadian Synchrotron Radiation Facility (CSRF) which was located on beam port 093 of the 1 GeV *Aladdin* electron storage ring in Wisconsin, U.S.A. A 2.0 m grazing incidence monochromator, nicknamed a "Grasshopper" monochromator because of its appearance, is the central element of the CSRF beamline. The design and operation of the CSRF beamline and "Grasshopper" monochromator have been described in detail elsewhere[15,16] and will only be outlined briefly here. The first optical element of the beamline is an M_0 mirror which collects 14 mrad of horizontal radiation from the electron storage ring and focuses it horizontally to the exit slit of the monochromator. The M_0 mirror is a one metre long piece of gold-coated float glass bent to the appropriate curvature for the desired focussing effects.

Following the M_0 mirror, the synchrotron radiation enters the "Grasshopper" monochromator and is first incident upon the M_1 vertically focussing mirror at a glancing angle of 1°. The M_1 mirror focuses the radiation in the vertical direction onto the adjustable entrance slit which is of the Codling type, with one physical slit jaw and a mirror corresponding to a virtual slit. The photon beam is reflected from the slit mirror onto the grating, which disperses the polychromatic radiation. The wavelength of the light transmitted through the exit slit is selected by the relative positions and angles of the M_1 mirror, the entrance slit mirror, and the grating, which can be mechanically varied by changing the linear position of the monochromator carriage. The entrance slit, grating and exit slit all lie on a Rowland circle geometry by design, ensuring a constant angle of exit for the monochromatized radiation. The relative position of the focus is therefore constant for all photon energies and the experimental station does not have to be repositioned for each photon energy. The photon resolution (bandwidth) of the monochromatized photon beam is controlled by the adjustable slit widths and

the spacing of the rulings on the grating. Both 1200 line/mm and 900 line/mm gratings were used for the studies reported here, and with the physical minimum slit widths of 20 μm, minimum practical photon resolutions $\Delta\lambda$ = 0.08 Å and $\Delta\lambda$ = 0.12 Å (corresponding to 0.065 eV and 0.097 eV at $h\nu$ = 100 eV) respectively can be calculated from

$$\Delta\lambda\,(\text{Å}) = x \times \text{slitwidth}\,(\mu\text{m}) \qquad (1.2.1)$$

where x=0.004 for the 1200 line/mm grating and 0.006 for the 900 line/mm grating. The adjustable slit widths allow selection of the desired photon resolution with the trade-off that the photon flux decreases sharply with decreasing slit widths. The photon energy or wavelength transmitted by the monochromator was determined by the linear position of the grating carriage. A high-resolution stepper motor was used to translate the position of the monochromator and the position determined to ±0.001 mm using a digital encoder over the ~40 cm travel of the carriage.

The vertically and horizontally diverging monochromatized photon beam from the exit slit of the "Grasshopper" monochromator is refocused by a toroidal mirror to a minimum spot size at the interaction region. Mostly owing to imperfections in the optics of the beamline, the spot size was typically 1-2 mm in the vertical direction and ~10 mm in the horizontal direction. A two stage differential pumping station comprised of two chambers separated by a glass light pipe and pumped by an ion pump and cryopump was used to isolate the beamline from the experimental station. After the final differential pumping chamber, an additional light pipe in the experimental chamber separated it from the rest of the beamline. The differential pumping system worked very well, allowing pressures of ~2-4$\times 10^{-5}$ in the experimental chamber while maintaining the high vacuum regions of the monochromator at a good vacuum of ~10^{-9} - 10^{-10} torr. Various components of the beamline could be isolated with pneumatic gate valves, and a photon shutter.

radiation shutter and pneumatic gate valve isolated the entire beamline from the vacuum tank of the synchrotron when it was not in use.

1.2.1. Monochromator scanning

To be useful for measuring spectra as a function of photon energy (or wavelength), the monochromator had to be scanned in synchronicity with the measurement of the spectroscopic signal. A computer controlled two-channel TTL pulse output module was used to drive the monochromator with a 24 bit BCD input for feedback of the monochromator position from the linear encoder. A relationship between the displacement of the monochromator, D, from the zero order position, L_0, and the wavelength of the transmitted light can be derived,[17]

$$\lambda = d\left[\sin\alpha + \sin\left[\sin^{-1}\left(\frac{D-L_0}{R}\right) - (180^\circ - \alpha)\right]\right] \qquad (1.2.2)$$

where d is the spacing of the rulings on the grating in Å, α the angle of incidence and R the radius of the grating (mm). Using the positions of known absorption lines[18] and a non-linear least squares fitting routine, the parameters α, L_0 and R can be determined and used in the scanning equation Eq. (1.2.2) to calculate the monochromator position for a given photon energy.

A spectrum of the photon flux from the "Grasshopper" monochromator measured with a gold diode and normalized using the standard gold yield values[19] is presented in Fig. 1.2.1. In the region of interest for this thesis, between ~100 eV and 250 eV, the flux spectrum is relatively smooth, dropping sharply from a maximum at ~110 eV to a minimum at~250 eV, and should not therefore introduce any spurious sharp structure into the spectra reported here. At higher photon energies, minima are observed in the gold yield spectrum in Fig. 1.2.1. Carbon contamination of the optical surfaces of the beamline results in the strong absorption at ~290 eV, just above a sharp increase in the photon flux at ~280 eV and oxygen contamination in the weaker absorption at ~540 eV.

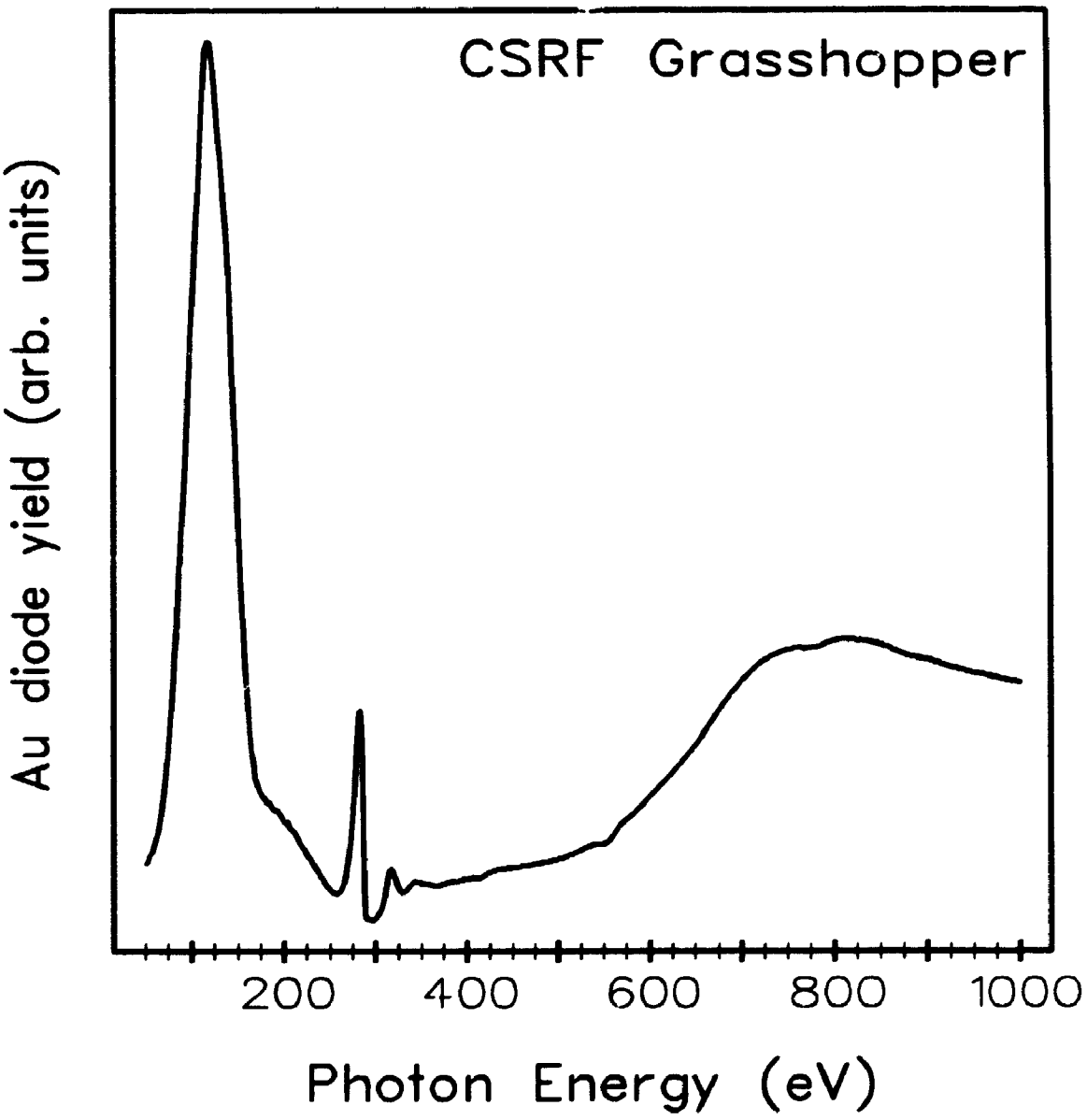

Figure 1.2.1: Photon flux spectrum from the CSRF beamline with a 1200 line/mm grating in the "Grasshopper" monochromator measured with a gold diode and normalized to the standard gold yields.

Data acquisition software for obtaining up to 4 simultaneous voltage signals as a function of photon energy was written in the FORTRAN programming language for a PDP-11/23 MINC computer. Variations of this software were used to measure the photoabsorption spectra presented in Chapter 2 and the mass resolved ion yield spectra presented in Chapter 4. Up to 5000 data points could be accumulated for each spectrum, but typically ~2000 data points were used. More recently, the required hardware for interfacing a PC computer to the monochromator was acquired (8 channel, 12-bit A/D, stepper motor controller, and 24-bit digital I/O computer boards), new interface cables constructed, and the data acquisition software re-coded in the "C" programming language. This system has been used extensively to measure total electron yields from solid samples.[20,21]

1.3. Electronic Transitions Involving Core-Level Electrons

This thesis is concerned with photoabsorption, photoelectron and photofragmentation spectra of core electronic levels of silane and substituted silane compounds in the gas phase. The very high resolution and high throughput of the "Grasshopper" monochromator at $h\nu \approx 100$ eV make it ideally suited for studying the Si $2p$ core electronic levels of these compounds. Accordingly, high resolution photoabsorption, photoelectron, and photofragmentation spectra of several silane compounds have been measured using monochromatized synchrotron radiation with energies around the Si $2p$ ionization edge. Photoabsorption spectra have also been measured around the Si $2s$ edges and the Cl $2p$ edges of the chlorine containing molecules. All of these spectra involve excitation and/or ionization of the core electrons from the molecules. It is therefore instructive to consider the electronic processes involving core electrons which are important for these spectra.

Core electron orbitals are strongly localized around their associated nuclei and core-level electronic spectra therefore probe the local environment around the atomic site of the excitation. When the energy, $h\nu$, of the incident photon is less

than the binding energy, $E_b(i)$, of the core electron, i, the core electron can be *excited* into a bound virtual state, k^*, if the relationship:

$$h\nu = E_b(i) - E_b(k^*) \tag{1.3.1}$$

is satisfied (ignoring multielectron effects). The virtual orbital, k^*, may be an unoccupied molecular orbital (antibonding), a Rydberg-type orbital or a mixed orbital with contributions from both antibonding and Rydberg orbitals. Antibonding orbitals generally lie lower in energy than Rydberg orbitals which usually merge into the continuum. This type of transition is represented schematically in Fig. (a) where the core electron is photoexcited into a generic virtual orbital.

If the photon energy exceeds the energy required to ionize the core electron, the core electron can be ionized into the continuum with the excess energy of the photon over the binding energy of the core electron conserved in the kinetic energy, $E_k(i)$ of the excited electron (again ignoring multielectron effects):

$$h\nu = E_b(i) + E_k(i) \tag{1.3.2}$$

This is represented schematically in Fig. 1.3.1 (b). The ejected electron is sometimes temporarily trapped in the vicinity of the molecule by the effects of the molecular potential but will usually tunnel out into the continuum after a short period of time.[22]

In both of the above cases, excitation and ionization of a core electron leaves the molecule in an excited state with a large excess of energy. Two competing processes can occur to fill the core-electron hole and dissipate the excess energy. An electron from an orbital closer to the vacuum level, j, can fill the core hole and emit a second photon, $h\nu'$, with photon energy roughly equal to the difference between the binding energies of the core electron-hole orbital and the orbital of the electron filling the core hole:

$$h\nu' = E_b(i) - E_b(j) \tag{1.3.3}$$

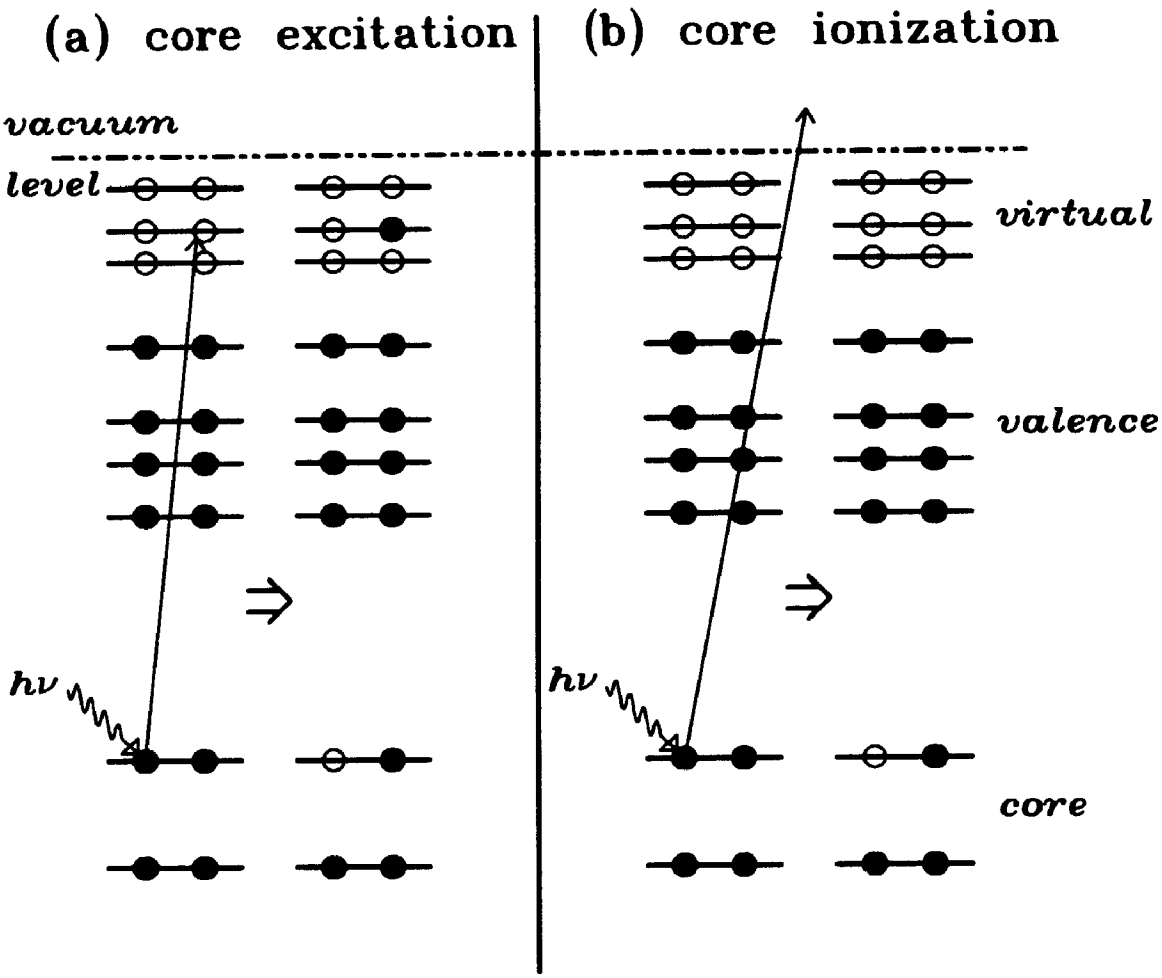

Figure 1.3.1: Schematic of the (a) excitation and (b) ionization of a core electron by a high energy photon, $h\nu$.

Numerous electrons in a molecule or atom are usually available to fill the core hole, even the electron in the virtual orbital in the core-excited case. This is the fluorescence process, which is represented schematically in Fig. 1.3.2 for (a) a core-excited molecule and (b) a core-ionized molecule.

Numerous fluorescence lines, corresponding to the different electrons involved in filling the core hole are observed. Note that following the fluorescence process,

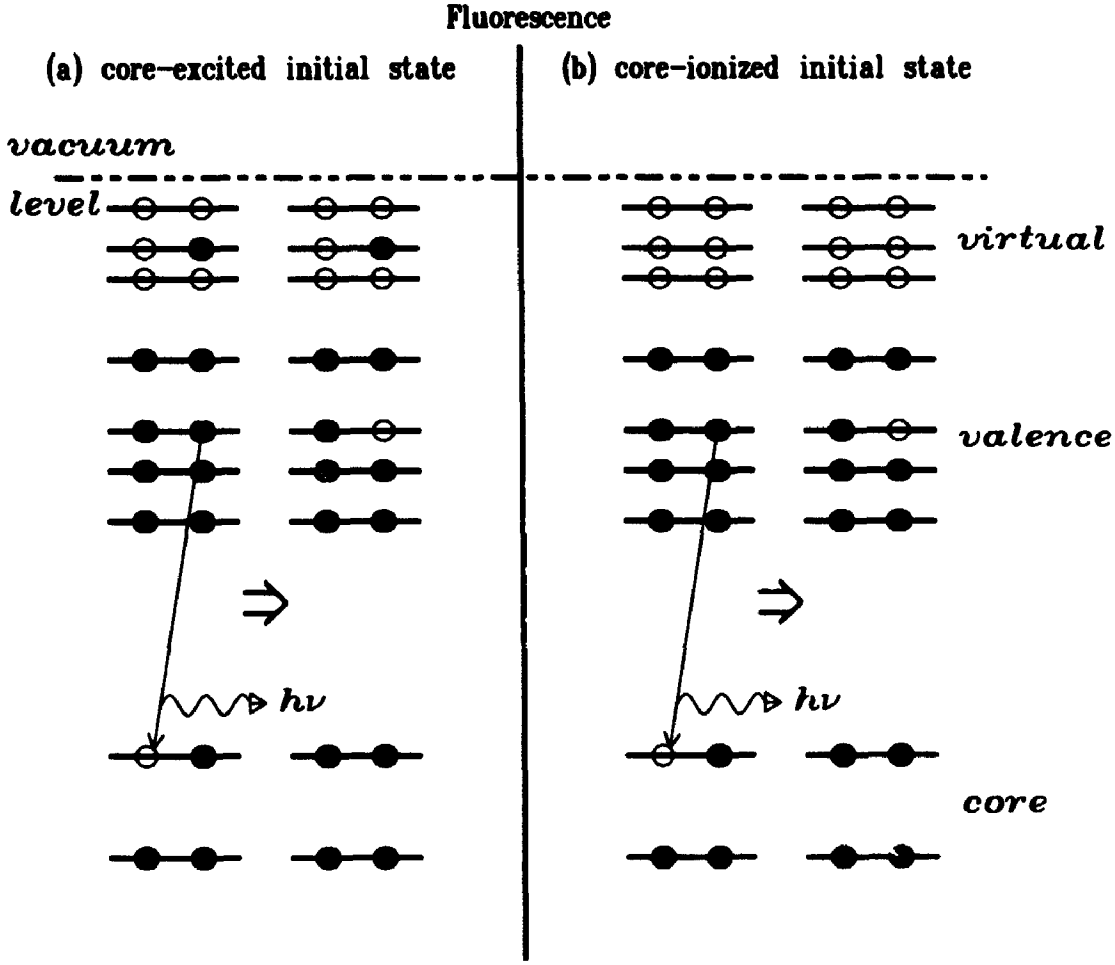

Figure 1.3.2: Schematic of the electronic processes involved in the fluorescence filling of a core-hole in an (a) excited core-hole state and (b) an ionized core hole state.

the molecule or atom may still be in an excited electronic state with a hole in a higher core or valence level.

Fluorescence is not the dominant relaxation process for core electron holes in lighter elements, $Z < 30$. Instead, the Auger electronic process fills the core hole[27–29] relaxing some of the energy in the core hole state. In a fashion similar to that in the fluorescence process, a higher energy electron fills the core hole in the

Auger process, but rather than emitting the excess energy as a photon, it is used to eject a second electron from the atom or molecule as represented schematically in Fig. 1.3.3.

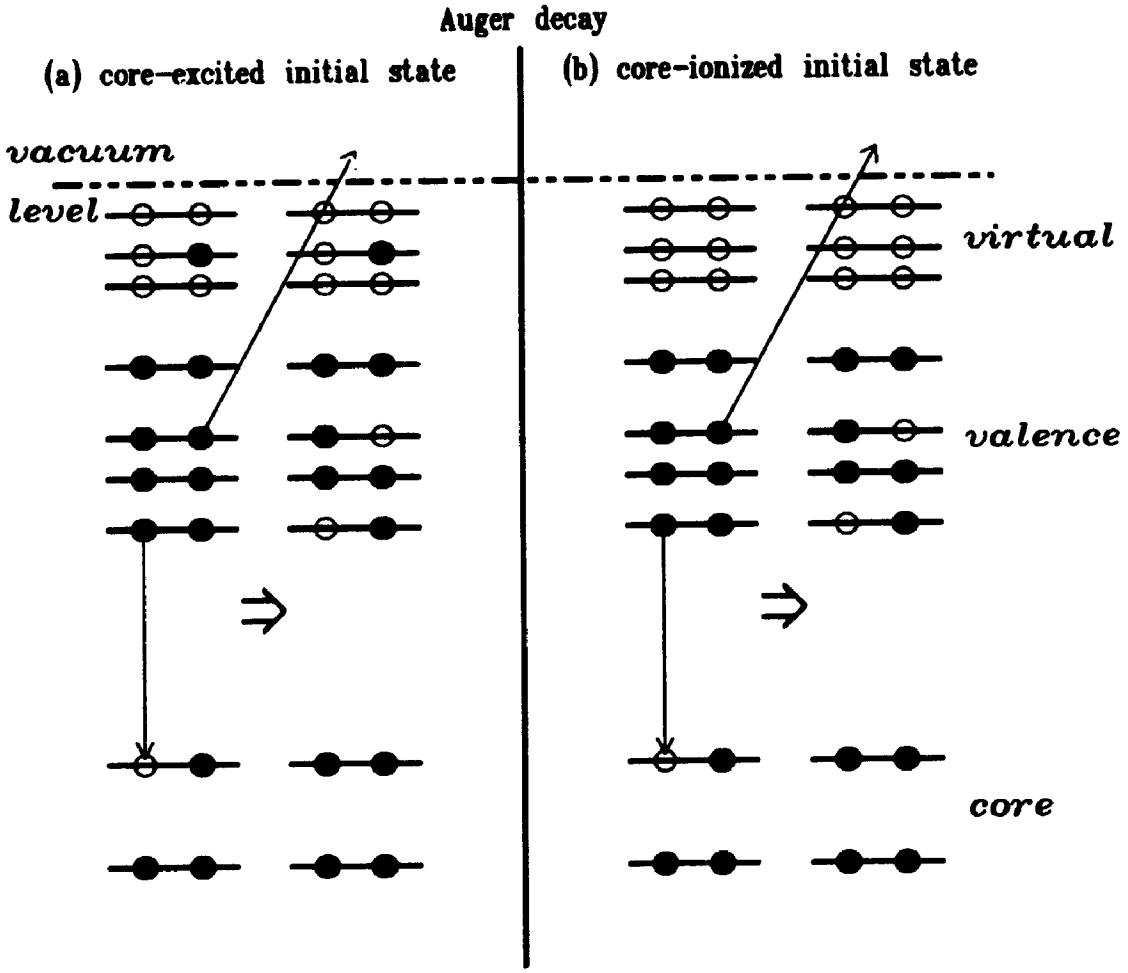

Figure 1.3.3: Schematic representation of the Auger electronic process filling a core hole in (a) an excited core-hole state and (b) an ionized core-hole state.

Energetically, any two electrons, m, n, in the molecule which obey the approximate relationship:

$$E_b(i) - E_b(m) > E_b(n) \tag{1.3.4}$$

can be involved in the Auger process. In the core-excited atom or molecule, the electron in the virtual orbital may either participate in the Auger decay process (autoionization, participator Auger decay), or remain in the virtual orbital during the decay (spectator Auger decay). Observations for several polyatomic molecules[23–26] suggest that spectator Auger decay is the predominant decay channel for core-excited molecules. After the Auger process the molecule is in a 2 hole excited state or a 2 hole – 1 electron excited state, and if the original core hole was deeper than the outermost core shell, multiple Auger processes can occur in a so-called Auger cascade,[30] leaving the atom or molecule in a highly ionized state.

When a deep core hole in a molecule relaxes via an Auger cascade[31,32], which is depicted in Fig. 1.3.4, most of the valence electrons can be stripped from the molecule. The multiply positively charged nuclei in the stripped molecule repel each other in a "Coulombic explosion".[33] Preferential depopulation of specific molecular orbitals by a single or multiple Auger processes can also result in a more specific cleavage of the molecule around certain bonds.[34] The presence of an excited electron in an antibonding orbital, combined with the Auger decay process can also result in the enhancement of specific fragmentation pathways.[35]

The spectra presented in this thesis probe the core electron excitation by photoabsorption spectroscopy (PAS), and ionization processes by PAS and photoelectron spectroscopy (PES), the nature of the core-ionized states by PES and the relaxation or de-excitation processes by mass resolved ion spectroscopy. In particular, the photoabsorption spectra of the fluoromethylsilane, chloromethylsilane and chlorosilane compounds were measured to study the effects of the changing molecular potential across the molecular series on the nature of the empty bound molecular orbitals and the cross sections in the ionization continua. These spectra are reported in chapter 2. Electronic transitions of the core electrons into virtual molecular orbitals which obey Eq. (1.3.1) are observed as peaks in the

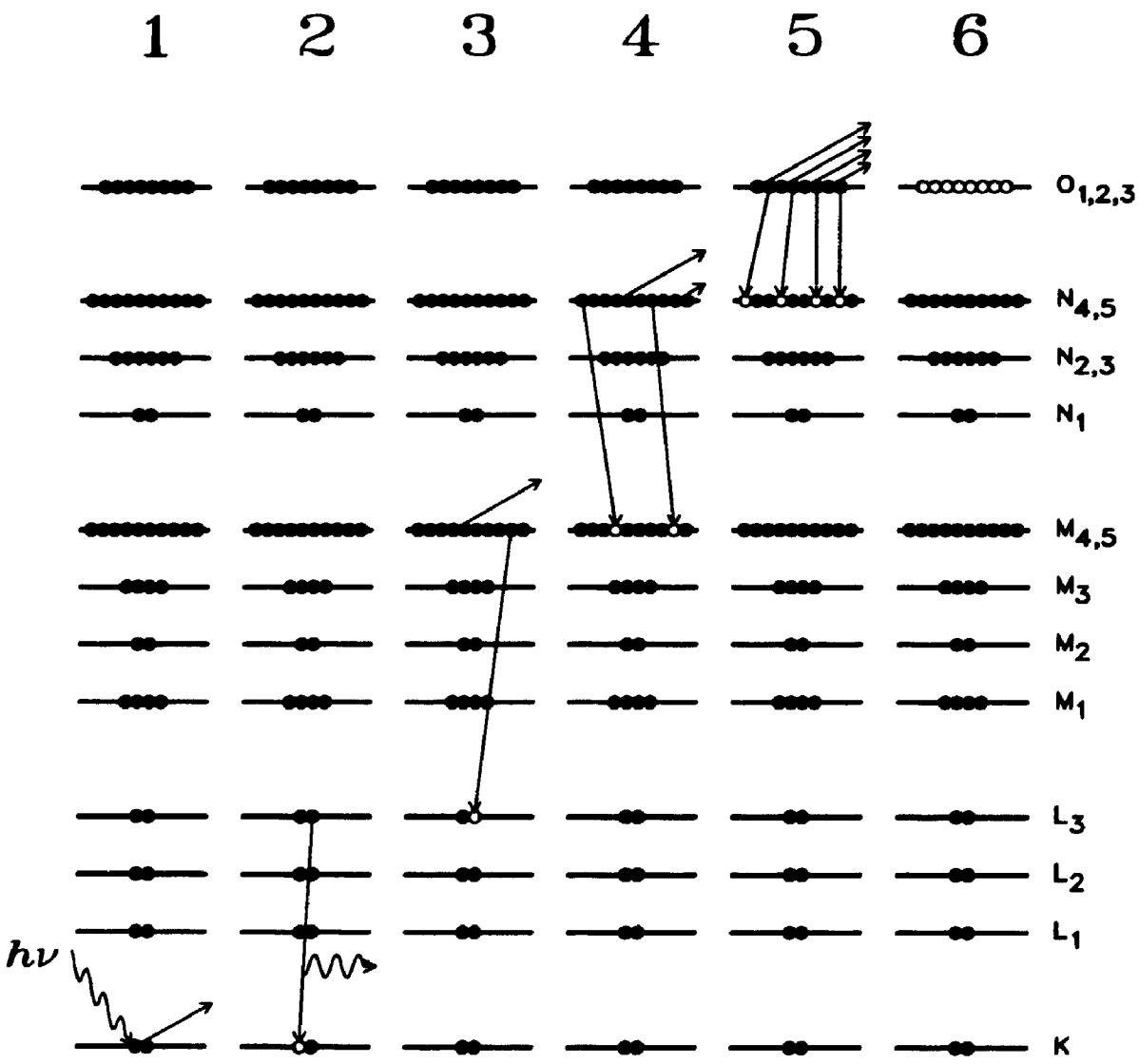

Figure 1.3.4: Schematic representation of the processes involved in an Auger cascade in Xe:

1. core-ionization creating a core hole in the Xe K-shell
2. $L \rightarrow K$ fluorescence
3. LMM Auger transition
4. MNN Auger transitions ($\times 2$)
5. NOO Auger transitions ($\times 4$)
6. leaving Xe^{8+}

pre-edge photoabsorption spectra. These peaks are significantly broadened by the lifetime of the core hole which is affected by Coster-Kronig intershell Auger transitions for the Si 2*s* spectra and molecular effects such as vibrational splitting in the Si 2*p* hole state. Above the ionization edge, structure in the photoabsorption cross sections is observed and attributed to diffuse molecular orbitals in the continuum or trapping of the outgoing photoelectron by the molecular potential and/or centrifugal barriers. The molecular series approach highlights the effects of the various ligands around the central Si atom on the absorption spectra and by inference, the manifold of virtual orbitals and the nature of the molecular potential.

Photoelectron spectra of the Si 2*p* core-level electrons of several silicon containing compounds including SiH_4 and SiF_4 were measured with unprecedented experimental resolution and are presented in Chapter 3. The very high-resolution obtained for this work allows individual vibrational bands to be resolved in the core level photoelectron spectra for only the second time. Vibrational bands have previously been observed in the C 1*s* photoelectron spectrum of CH_4,[36–38] but the much higher experimental resolution obtained here individually resolves component vibrational bands. The vibrational structure results from differences in the equilibrium nuclear geometries of the ground and Si 2*p* core-ionized electronic states. Manifolds of vibrational bands are assigned to all of the Si 2*p* photoelectron spectra reported in Chapter 3, even when individual vibrational peaks could not be resolved, based on observations for SiH_4 and SiF_4. The results suggest that vibrational broadening will be an important limiting factor in the achievable resolution for core level spectra of some compounds.

Mass-resolved ion spectra of the fluoromethylsilane compounds around the Si 2*p* ionization edges, presented in Chapter 4, detect the final products of the core electron excitation, ionization and Auger de-excitation processes. Numerous ionic fragments are detected for each compound at all photon energies: in the valence

ionization region, at the core-to-bound excitations, and in the core-ionization region. Relative yields of fragment ions with respect to the other fragment ions and as a function of photon energy are used to characterize the de-excitation pathways for the initial core electron excitation/ionization. The greater lability of the methyl ligands with respect to the fluorine ligands in the mixed fluoromethylsilane compounds suggests that valence electrons associated with the Si–CH_3 bonding orbitals are more likely to be involved in the relaxation of the core hole than those associated with the Si–F bonding orbitals. The results are consistent with predictions of relative Auger rates and their effects on core-electron hole lifetimes.[39]

1.4. References

1. C.T. Chen and F. Sette, Rev. Sci. Instrum. 60, 1616 (1989).
2. H. Kobayakawa and K. Huke, Rev. Sci. Instrum. 60, 2548 (1989).
3. M. Cornacchia, Rev. Sci. Instrum. 60, 1388 (1989).
4. D.E. Moncton, E. Crosbie and G.K. Sheng, Rev. Sci. Instrum. 60, 1403 (1989).
5. J.-L. Laclare, Rev. Sci. Instrum. 60, 1403 (1989).
6. F.R. Elder, A.M. Gurewitsch, R.V. Langmuir and H.D. Pollack, Phys. Rev. 71, 829 (1947).
7. F.R. Elder, A.M. Gurewitsch, R.V. Langmuir and H.D. Pollack, J. Appl. Phys. 18, 810 (1947).
8. F.R. Elder, R.V. Langmuir and H.D. Pollack, Phys. Rev. 74, 52 (1948).
9. E.M. Rowe and F.E. Mills, Part. Accel. 4, 211 (1973).
10. G. Margaritondo, *Introduction to Synchrotron Radiation*, (Oxford University Press, New York, 1988), *and references therein.*
11. H. Winick, "Properties of Synchrotron Radiation", in: *Synchtrotron Radiation Research*, eds. H. Winick and S. Doniach, (Plenum Press, New York, 1980), p. 11.
12. S. Krinsky, M.L. Perlman and R.E. Watson, "Characteristics of Synchrotron radiation and its sources", in: *Handbook on Synchrotron Radiation*, ed. E.E. Koch, vol. 1a, (North-Holland Publishing, New York, 1983), p. 65.
13. R.L. Johnson, "Grating monochromators and optics for the VUV and soft X-ray region", in: *Handbook on Synchrotron Radiation*, ed. E.E. Koch, vol. 1a, (North-Holland Publishing, New York, 1983), p. 173.

14. T. Mashushita and H. Hashizume, "X-ray monochromators", in: *Handbook on Synchrotron Radiation*, ed. E.E. Koch, vol. 1a, (North-Holland Publishing, New York, 1983), p. 261.

15. B.W. Yates, Ph.D Thesis, University of Western Ontario, (1986).

16. K.H. Tan, G.M. Bancroft, L.L. Coatsworth and B.W. Yates, Can. J. Phys. 60, 131 (1982).

17. J.A.R. Samson, *Techniques of Vacuum Ultraviolet Spectroscopy*, (Pied Publications, Lincoln, Nebraska, 1967), p. 10.

18. F.C. Brown, "Inner-Shell Threshold Spectra", in: *Synchtrotron Radiation Research*, eds. H. Winick and S. Doniach, (Plenum Press, New York, 1980), p. 61.

19. C. Kunz and K. Codling, eds., *Synchrotron Radiation: techniques and application*, (Springer-Verlag, New York, 1979).

20. M. Kasrai, M.E. Fleet, T.K. Sham, G.M. Bancroft, K.H. Tan and J.R. Brown, Sol. State. Comm. 68, 507 (1988).

21. M. Kasrai, J.D. Bozek, L.L. Coatsworth, M.E. Fleet, T.K. Sham, K.H. Tan, J.R. Brown and G.M. Bancroft, Physica B 158, 515 (1989).

22. J.L. Dehmer, A.C. Parr and S.H. Southworth, "Resonances in molecular photoionization", in: *Handbook on Synchrotron Radiation*, vol. 2, ed. G.V. Marr (North-Holland, New York, 1987), p.241.

23. S. Aksela, K.H. Tan, and G.M. Bancroft, Phys. Rev. A 33, 258 (1986).

24. T.A. Ferrett, M.N. Piancastelli, D.W. Lindle, P.A. Heimann and D.A. Shirley, Phys. Rev. A 38, 701 (1988).

25. S. Aksela, O.-P. Sairanen, H. Aksela, G.M. Bancroft and K.H. Tan, Phys. Rev. A 37, 2934 (1988).

26. G.M. Bancroft, K.H. Tan, O.-P. Sairanen, S. Aksela and H. Aksela, Phys. Rev. A 41, 2716 (1990).

27. M.P. Auger, Compt. Rend. 180, 65 (1925).

28. M.P. Auger, J. de Phys. Radium 6, 205 (1925).

29. M.P. Auger, Compt. Rend. 182, 773 (1926).

30. T.A. Carlson, W.E. Hunt and M.O. Krause, Phys. Rev. 151, 41 (1966).

31. T.A. Carlson and R.M. White, J. Chem. Phys. 44, 4519 (1966).

32. T.A. Carlson and R.M. White, J. Chem. Phys. 48, 5191 (1968).

33. T.A. Carlson, *Photoelectron and Auger Spectroscopy*, (Plenum Press, New York, 1975).

34. D.A. Lapiano-Smith, C.I. Ma, K.T. Wu and D.M. Hanson, J. Chem. Phys. 90, 2162 (1989).

35. W. Eberhardt, T.K. Sham, R. Carr, S. Krummacher, M. Strongin, S.L. Weng and D. Wesner, Phys. Rev. Lett. 50, 1083 (1983).

36. U. Gelius, S. Svensson, H. Siegbahn, E. Basilier, Å. Faxälv and K. Siegbahn, Chem. Phys. Lett, 28, 1 (1974).

37. U. Gelius, L. Asplund, E. Basilier, S. Hedman, K. Helenelund and K. Siegbahn, Nucl. Inst. Methods B 229, 85 (1984).

38. L. Asplund, U. Gelius, S. Hedman, K. Helenelund, K. Siegbahn and P.E.M. Siegbahn, J. Phys. B 18, 1569 (1985).

39. M.A. Coville and T.D. Thomas, Phys. Rev. Lett., *unpublished results.*

CHAPTER 2.
Core Level Photoabsorption Spectroscopy of the Fluoromethylsilane, Chloromethylsilane and Chlorosilane Compounds

2.1. INTRODUCTION

Photoabsorption spectroscopy of the core electronic levels of atoms and molecules in the gas phase is an active area of research as evidenced by the large number of publications in the recent literature.[1] Electronic transitions of core-level electrons into bound and unbound states and scattering of the outgoing photoelectron by neighbouring atoms give rise to maxima and minima (features) in the absorption spectrum. Core-level absorption spectra therefore contain information about the electronic and geometric structure of the sample. However, the correlation between the spectral features and phenomena associated with them is not always apparent. Core-level electrons are strongly localized around the atomic nuclei and are usually well separated in energy from other core levels in the molecule associated with either the same or different atoms, allowing spectral features from different core-levels to be easily identified. This ability to probe the local electronic and geometric structure around a *specific* atom in a molecule, by examining core-level photoabsorption spectra of that atom, results in considerable interest in core level photoabsorption spectroscopy as an analytical tool.[2] Ongoing developments in synchrotron radiation sources, high energy monochromators and electron energy-loss spectrometers resulting in ever improving experimental intensity, resolution and spectral range facilitate the characterization of these spectral features.[3]

Photoabsorption spectroscopy (PAS) measures the attenuation of an incident beam of electromagnetic radiation (light) by a sample of interest as a function of the energy (or wavelength or frequency) of the incident radiation. ***Core-level photoabsorption spectroscopy*** in particular, refers to the case where core-level electrons in the sample are excited or ionized by the incident radiation. The spectral region of interest for core-level PAS extends from from ~12 eV (>1000 Å) (Cs 5*p*) to >100 000 eV (<0.1 Å) (U 1*s* at 115 606 eV). This spectral region spans the vacuum UV and X-ray regions of the electromagnetic continuum, and photoabsorption spectroscopy of core-levels is therefore often referred to as X-ray absorption spectroscopy (XAS). Photoabsorption spectra of core-levels of atoms, molecules and solids can be roughly divided into two regions, the near-edge region extending from several eV below to ~50 eV above the ionization edge, and the extended region beyond ~50 eV above the ionization edge. Structure in the extended region of an X-ray absorption spectrum is often referred to as EXAFS (Extended X-ray Absorption Fine Structure) and results from backscattering of the outgoing photoelectron by the atoms surrounding the atomic site of the X-ray absorption.[4] Analytical methods have been developed for extracting structural information from the EXAFS structure in the X-ray absorption spectra of molecules and solids[5] and EXAFS spectroscopy is now widely used as a tool for structural determination.[4] In the near-edge region of X-ray absorption spectra the peaks observed in the absorption spectra result from electronic transitions of core-electrons into a variety of bound and unbound electronic states.[6] These peaks are commonly referred to as NEXAFS (Near-Edge X-ray Absorption Fine Structure) and/or XANES (X-ray Absorption Near-Edge Structure). Below the ionization limit of the core-level electron excited in the photoabsorption process, in what is called the ***discrete region*** of the spectrum, the final state for the core electron can be a bound molecular orbital, Rydberg orbitals or an orbital with mixed character. Above the ionization threshold, in what is

called the *continuum region*, the electron can be ejected directly into the vacuum or it may be temporarily trapped in the vicinity of the molecule before escaping into the vacuum, resulting in an enhancement (i.e. a peak) in the photoabsorption cross section. Peaks in the photoabsorption spectra of molecules in the XANES region therefore result from electronic transitions involving the core electrons. These peaks are sometimes referred to as "resonances", reflecting the dynamics of the interaction between the oscillating electromagnetic field and the sample which results in the electronic transitions which are observed as peaks in the absorption profile. The nature of these electronic transitions, and in particular of the final states for the excited electron, is the subject of this chapter, and photoabsorption spectra of the Si $2p$, Si $2s$ and Cl $2p$ core-levels of several silane molecules are presented and analyzed here.

In order to better understand the core-level photoabsorption spectra of polyatomic molecules, it is instructive to examine some of the equations describing the first-order interaction of electromagnetic radiation with atoms, i.e. photoabsorption by atoms. The absorption coefficient, $\mu(\omega)$, can be used to describe the degree of absorption by the sample and it is simply the amount of energy removed per second per unit volume from a beam of unit intensity

$$\mu = -\frac{1}{I}\frac{dI}{dx} \tag{2.1.1}$$

For a sample of finite thickness, x, the intensity decreases exponentially

$$I = I_0 e^{-\mu x} \tag{2.1.2}$$

The absorption cross section, σ, which is the amount of radiation absorbed per atom or molecule is used more frequently to describe the absorption of light by gaseous samples. It is related to the absorption coefficient, μ by

$$\mu = N_A \sigma \tag{2.1.3}$$

where N_A is the number of molecules per cm^3. Alternatively, the cross section can be given in units of megabarns (1 Mb = 10^{-18} cm^2) at STP, in which case,

$$\mu\,(\mathrm{cm}^{-1}) = \frac{N_A \sigma\,(\mathrm{Mb})}{26.9} \tag{2.1.4}$$

when μ is at STP.[7]

The absorption coefficient, $\mu(\omega)$, at frequency ω can be shown to be related to the electronic structure of the atom.[7] Assuming the dipole approximation to be valid, the absorption coefficient is given by

$$\mu(\omega) = \frac{4\pi^2}{\eta}\frac{e^2}{\hbar c}\hbar\omega \sum_{ij} |M'_{ij}|^2 \delta(E_j - E_i - \hbar\omega) \tag{2.1.5}$$

where η is the index of refraction, M'_{ij} is the dipole matrix element, and the delta function, $\delta(E_j - E_i - \hbar\omega)$ ensures that only transitions between the quantized energy levels of the system are allowed.

The oscillator strength, f_{ij}, first introduced in the classical theory of radiation, is a unitless quantity including the important factors from Eq. (2.1.5)

$$f_{ij} = \frac{2m\hbar\omega}{\hbar^2}|M'_{ij}|^2 \tag{2.1.6}$$

In the classical definition of oscillator strength, an N electron atom in a given initial state i obeys the sum rule:

$$\sum_j f_{ij} = N \tag{2.1.7}$$

The same result can be derived quantum mechanically and is know as the Thomas-Kuhn-Reiche sum rule.[8] Most of the oscillator strength for core electronic transitions is in the continuum above the ionization threshold. In the continuum, the oscillator strength, f_{ij}, is replaced by the spectral density df/dE and Eq. (2.1.7) becomes:

$$\sum_j f_{ij} + \int_{E_I}^{\infty} \frac{df}{dE} dE = N \tag{2.1.8}$$

where E_I is the ionization energy. Oscillator strengths and absorption coefficients are related by:

$$\mu(\omega) = \frac{\pi e^2 h}{mc} N_A f_{ij} \tag{2.1.9}$$

in the discrete part of the spectrum and by:

$$\mu(\omega) = \frac{\pi e^2 h}{mc} N_A \frac{df}{dE} \tag{2.1.10}$$

in the continuum.

The dipole matrix element, M'_{ij}, is evaluated by integrating over the entire electronic configuration and summing over the n electrons in the atom

$$\begin{aligned} M'_{ij} &= \int \Psi_j^* \sum_n \mathbf{r}_n \Psi_i d\tau_n \\ &= \langle \Psi_j^* | \sum_n \mathbf{r}_n | \Psi_i \rangle \end{aligned} \tag{2.1.11}$$

where Ψ_i and Ψ_j^* are the initial and excited wavefunctions for the atom involving the coordinates of all n electrons, and $\mathbf{r}_n$ is the instantaneous dipole moment of the system. When the many electron wave functions, Ψ, are replaced by n one electron wavefunctions, ψ, $n-1$ of which are assumed to be unchanged by the electronic transition in the one-electron approximation, the dipole matrix becomes

$$\begin{aligned} M'_{ij} &= \int \psi_j^* \mathbf{r} \psi_i d\tau_r \\ &= \langle \psi_j^* | \mathbf{r} | \psi_i \rangle \end{aligned} \tag{2.1.12}$$

A large absorption coefficient therefore implies a high degree of spatial overlap for the initial and final state wavefunctions. Conversely, when the overlap between the initial and final state wavefunctions is small, the absorption coefficient is necessarily also small. Since core electronic wavefunctions have significant amplitude only in the immediate vicinity of the associated nucleus, final state wavefunctions must also have significant amplitude in the vicinity of the nucleus for appreciable intensity to be seen in the photoabsorption spectrum of transitions to these states.

The dipole matrix, M_{ij}^{l}, can be further simplified by separating the wavefunctions, ψ, into angular, $\mathcal{Y}(\theta,\phi)$, and radial, $\mathcal{R}(r)$, components

$$\psi = \psi_{n\ell m} = \mathcal{R}_{n\ell}(r)\,\mathcal{Y}_{m}(\theta,\phi) \tag{2.1.13}$$

The dipole matrix element becomes

$$M_{ij}^{l} = \int_{0}^{\infty} \mathcal{R}_{n\ell}(r)\, r \mathcal{R}_{n,\ell\pm1}(r)\, dr \tag{2.1.14}$$

The radial components of the wavefunction must satisfy the radial Schrödinger equation

$$\frac{d^2\mathcal{R}_{n\ell}}{dr^2} + \frac{2m}{\hbar^2}\left[E_{n\ell} - V(r) - \frac{\ell(\ell+1)\hbar^2}{2mr^2}\right]\mathcal{R}_{n\ell} = 0 \tag{2.1.15}$$

which can be obtained by separation of the radial and angular components and rearrangement of the general Schrödinger equation

$$\left[-\frac{\hbar^2}{2m}\nabla^2 + V(r)\right]\psi_{nlm} = E_{n\ell m}\psi_{n\ell m} \tag{2.1.16}$$

where $V(r)$ is the effective central potential of the atom. The centrifugal term, $\ell(\ell+1)\hbar/2mr^2$ in Eq. (2.1.15), has important consequences in the absorption spectra of some atoms and molecules. The shape of the potential, $V(r)$, also results in dramatic enhancements in the core-level photoabsorption spectra of some molecules.

The *shape* of the molecular potential was originally proposed to account for the very strong absorption features observed both below and above the core ionization edges of the central atom in the photoabsorption spectra of fluorine containing compounds such as SF_6 [9], SiF_4, BF_3 and NF_3 [10] by Nefedov in 1970.[11] The core-level photoabsorption spectra of these compounds are characterized by several strong absorption bands below and above the ionization edge and by a lack of detectable Rydberg peaks below threshold. Nefedov proposed that the features in the S 2*p* photoabsorption spectrum of SF_6 resulted from a "potential barrier" created by the strongly electronegative fluorine ligands surrounding the central

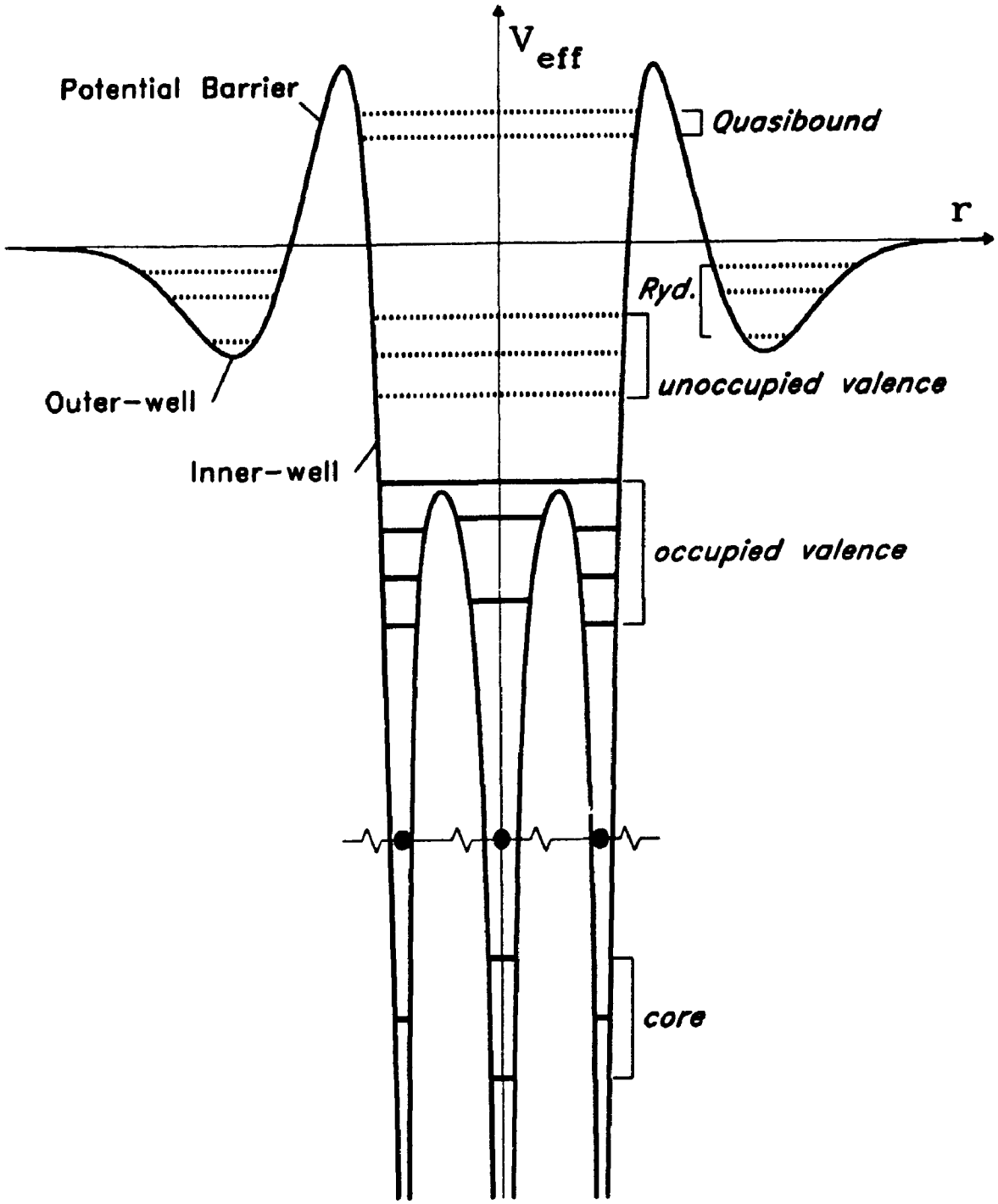

Figure 2.1.1: Schematic representation of the effective potential, V_{eff}, of a hypothetical triatomic molecule with a potential barrier. Normally occupied orbitals are represented by the solid thick horizontal lines and unoccupied ones by the dotted lines.

sulfur atom.[11] In the proposed model, the electron density on the electronegative fluorine atoms acts as a Coulombic barrier at the periphery of the molecule, preventing the excited electron from leaving the region of the molecule. This type of potential barrier is represented schematically in Fig. 2.1.1 which shows the effective potential, V_{eff}, of a hypothetical linear triatomic molecule as a function of distance, R, from the central atom along the bond axis. The potential barrier separates the potential experienced by an electron around the molecule into inner-well and outer-well regions. Core and valence orbitals, as well as unoccupied valence (antibonding) orbitals are all localized within the inner-well region of the molecular potential. Rydberg orbitals, however, which are know to be diffuse and extend well beyond the region of the molecule,[12] are prevented from penetrating into the inner-well region by the barrier in the potential at the periphery of the molecule. Additional "quasibound" orbitals can also be supported above the vacuum level because of the barrier. The overlap between the initial, ψ_i, and final, ψ_j, electronic states in Eq. (2.1.12) will therefore be much larger for transitions from the core orbitals, which are strongly localized around the atomic cores, to the unoccupied valence orbitals than for transitions to the Rydberg orbitals. The quasibound states, also localized in the inner-well region, will also have significant overlap with the core orbitals resulting in strong peaks in the continuum region of the photoabsorption spectrum. Resonances which are enhanced by the shape of the effective potential barrier are aptly called "shape resonances".

Dehmer generalized the potential barrier model, noting that effects other than Coulombic repulsion could also create a "psuedo-potential barrier" resulting in the enhancement of inner-well states in photoabsorption spectra.[13] He proposed four types of interaction which create barriers to the escape of an electron from the molecular potential :

1. Coulombic repulsion by the electron density concentrated on electronegative ligands at the periphery of the molecule.

2. Local exchange interaction with the electrons on the electronegative ligands – forces related to the Pauli exclusion principle.
3. Centrifugal effects in final states with $\ell > 2$, from the $\ell(\ell+1)\,\hbar/2mr^2$ term Eq. (2.1.15)).
4. The requirement that the wavefunction representing the photoelectron to be orthogonal to all of the occupied orbitals in the molecule.

The interactions are not mutually exclusive, and several contributions may lead to a potential barrier in some systems. In SF_6 for instance, Coulombic and exclusion forces probably contribute to form the barrier in the potential which is manifested by the strong resonances in the core-level absorption spectra.[7] Shape resonances are not limited to core electronic levels. Any process which involves the interaction of an electron with a molecular potential exhibiting a barrier will exhibit shape resonances. The cross sections of different valence orbitals in the same molecule often exhibit very different shape resonance behavior.[14–18] This can be caused by the anisotropic nature of the barrier in non-symmetric molecules and/or different symmetries of the outgoing channels for the various molecular orbitals. Since the potential barrier need not be spherically symmetric around the site of a core excitation or ionization, the escaping electron may experience a repulsion or barrier in certain directions and not in others.[13] This was recently demonstrated in the core-level electron energy loss spectra of ClF_3 [19] which exhibit both intense shape resonances and strong Rydberg peaks.

Centrifugal barriers have also been identified in atomic potentials giving rise to a "delayed onset" [20] where the absorption cross section is suppressed near threshold and rises to a maximum somewhere above the ionization edge. For example, the photoabsorption spectrum of xenon above the 4*d* levels exhibits this behaviour with the cross section reaching a maximum ~30 eV above threshold.[21] Centrifugal effects are also responsible for the shape resonances observed in covalent molecules such as N_2 [22–24] and CO [22–24] where strong absorption

peaks are observed above threshold. Using multiple scattering Xα (MS-Xα) calculations, Dehmer and Dill showed that the shape resonances in the N 1*s* cross section of N_2 were caused by a centrifugal barrier acting on the $\ell = 3$ angular momentum component of the σ_u continuum wavefunction.[25] The calculations were extended to the partial photoionization cross sections for the valence levels of N_2 and CO by Davenport,[26] who found that similar resonance features were observed in the valence photoionization cross sections. A molecular orbital based theoretical calculation of the N 1*s* photoabsorption cross section of N_2 based on conventional Roothan–Hartree–Fock calculations was subsequently performed and similar results, in slightly better quantitative agreement with the experimental results, were obtained.[27] Applications of both the MS-Xα [28] and the MO based theory[29] to evaluating photoionization cross section have been reviewed recently and both provide useful and often complementary information for assigning features in photoabsorption spectra.

An empirical correlation of the carbon–carbon bond length with the position of the σ^* shape resonances assigned above the core levels of numerous gas phase organic molecules has been noted recently,[30] and shown to be applicable for a variety of other molecules.[31–35] The length of the bond, R, between adjacent atoms was found to correlate linearly with the energy, δ of the σ shape resonance associated with the bond according to the simple formula

$$\delta = m - nR \tag{2.1.17}$$

for bond between atoms having the same sum of the atomic masses, Z_T.[31] For instance, the relationship holds for N_2, CO, and BF_3 where $Z_T = 14$ for all three molecules. For a fixed value of R, the energy of the σ shape resonance was also found to vary almost linearly with Z_T. Similar relationships between bond length and position of the σ shape resonance in chemisorbed molecules were observed.[36,37] In a very critical evaluation of the correlation, however, Piancastelli *et al*[38] noted that the features being assigned as σ shape resonances in the molecules were

usually weak and not well characterized as one-electron shape resonances. An excellent description of shape resonances and the criteria for assigning a spectral feature as a shape resonance is developed. Using their more stringent criteria, Piancastelli *et al* found no correlation between the shape resonance positions and bond length and found no theoretical basis for the correlation.[38] Both groups conceded that partial photoionization cross section measurements and theoretical calculations are both required to unequivocally assign a feature observed in a photoabsorption cross section as a shape resonance.[39,40] A subsequent theoretical study of the relationship between interatomic distance and σ shape resonance position concluded the molecular orbital model provides a basis for the correlation, but that an inverse squared relationship

$$\delta = m + nR^2 \tag{2.1.18}$$

is more appropriate.[41] The debate over the correlation of shape resonance position with bond length highlights some of the difficulties encountered when trying to assign features observed in core level photoabsorption spectra.

Scattering of the ejected core electrons from surrounding atoms in the molecule has also been proposed to account for continuum resonances observed >15−20 eV above threshold. The assignment was based on MS-Xα calculations of cross sections from "F_2"[42] and "F_6"[43]"cage" molecules where the central Xe and S atoms respectively have been removed from the molecular spectra.

Core-level photoabsorption spectra of a relatively large number of different types of molecules have been studied in an attempt to identify the effects of different molecular environments on the spectra. Initial work concentrated primarily on diatomic and triatomic compounds of second row (Li – Ne) compounds such as N_2,[22−24,26,27,44−47] CO,[22−24,26,45,48,49] CO_2,[50,51] N_2O,[50,51] N_2O,[52−54] and others. Because of the relatively small number of electrons in these compounds the spectra are more readily calculated in high level ab initio calculations then for compounds of heavier elements. Recent developments in high

resolution monochromators have resulted in renewed interest in these compounds and a variety of new features have been recently resolved.[55–60] The C 1s photoabsorption spectra of larger organic molecules have also been reported.[61–63] Smaller organic molecules such as ethylene and benzene have also been studied in great detail recently with a focus on vibrational fine structure observed in the C $1s \rightarrow \sigma^*$ bands.[64–67] Core-level photoabsorption spectra of the hydrides of various elements such as, CH_4,[48,68–70] PH_3,[71,72] SiH_4,[71–75] PH_3,[71,72,74,76] and H_2S,[72,77] have also been studied in detail. These molecules are of interest because the H atoms do not greatly perturb the atomic potential of the central atom . The hydride compounds therefore exhibit spectral properties intermediate between those of atoms and of molecules containing larger ligands. Molecules with a central atom surrounded by electronegative groups such as the freon molecules CF_4,[78–80] CF_3Cl,[81] and CF_2Cl_2,[82] and others such as NF_3,[52] SiF_4,[78,83–86] $SiCl_4$,[87–90], SF_6,[43,91–93], SeF_6,[91,93] and TeF_6 [93,94] have also been studied in detail following the introduction of the potential barrier model by Nefedov[11] and Dehmer.[13] More recently, core-level spectra of a number of transition metal compounds in the gas phase have been reported.[95–99] Similarly, a concerted effort has been underway to study the photoabsorption spectra of sulfur containing compounds[92,100–107] in part to attempt to establish a bond-length shape resonance position correlation for third row elements.

While most efforts have been aimed at establishing the nature of continuum resonances in core-level photoabsorption spectra, the assignment of many pre-edge features remains uncertain. In particular, the assignments of peaks in the discrete portion of core-level photoabsorption spectra as transitions to unoccupied molecular orbitals or Rydberg orbitals remains difficult.[90,108,109] The exclusion of Rydberg orbitals from the inner-well region (Fig. 2.1.1) by electronegative ligands led some workers to suggest that transitions to Rydberg orbitals would only be observed in core level absorption spectra of atoms and hydride molecules.[108]

However, recent MS-Xα calculations of the discrete portions of the Si and Cl core-level photoabsorption spectra of $SiCl_4$ predicted numerous transitions to Rydberg orbitals with significant contributions to the overall intensity of the spectrum.[90] Contour diagrams of low angular momentum Rydberg wavefunctions indicated that they are able to penetrate into the inner-well region, resulting in significant oscillator strengths for transitions to those orbitals. Experimental evidence for the assignment of a peak in the discrete portion of a core-level photoabsorption spectrum can be obtained by comparing the spectra of gaseous and condensed samples.[12] Rydberg orbitals, which extend far beyond the periphery of the atoms in the molecule, are perturbed in the condensed phase and peaks observed in the gas phase spectra which are due to transitions into these orbitals are washed out in the condensed spectra. A classic example is the Si 2*p* photoabsorption spectrum of SiH_4 which exhibits a series of sharp lines below threshold in the gas phase that are absent in spectra of the condensed sample.[74]

The chemical series method can also yield valuable information about the nature of both the discrete and continuum resonances in core-level photoabsorption spectra. Small changes in the chemical environment of the absorbing species can be correlated with the changes observed in the photoabsorption spectra. The method has been applied to the core-level photoabsorption spectra of a number of species including the chloromethanes,[110] fluoromethanes,[111] PX_3 compounds,[112–114] SiX_4 compounds,[108,115–117] ($X = H, CH_3, F, Cl, \ldots$) and the $SiMe_xCl_{4-x}$ compounds[118–120] as well as others. This method is used throughout this thesis and its value for identifying and assigning trends observed in the spectra is demonstrated in detail.

Core-level photoabsorption spectra of three chemical series of silane molecules, $Si(CH_3)_xF_{4-x}$, $Si(CH_3)_xCl_{4-x}$, and SiH_xCl_{4-x}; $x = 0 - 4$, are presented in this chapter and compared with theoretical results obtained from MS-Xα calculations. The discrete and continuum regions of the Si 2*p*, Si 2*s* and Cl 2*p* levels are

studied in detail and compared with previous results where they are available. The chemical series approach highlights trends resulting from changes in the molecular potential around the central silicon atom and aid in the assignment of the discrete and continuum regions of the photoabsorption spectra. The calculations, which are in good agreement with the experimental results, also play an important role in the assignment of the spectra. Following brief descriptions of the experimental and theoretical methods employed in this work, the results are divided into three sections, one for each of the three molecular series. Conclusions are made based on common features observed in the three series.

2.2. EXPERIMENTAL

Photoabsorption spectra were obtained at the Canadian Synchrotron Radiation Facility (CSRF) located on the Aladdin electron storage ring at the Synchrotron Radiation Center (SRC) in Wisconsin, U.S.A. A Mark IV Grasshopper monochromator equipped with a 1200 groove/mm grating was used to monochromatize the photon beam with a band pass of 0.125 Å(0.1 eV at 100 eV → 0.4 eV at 200 eV). The beamline and monochromator were described in detail in Chapter 1. Monochromatized radiation was passed through ar 11.3 cm cell limited by two polypropylene windows of approximately 1000 Å thickness. The output current from a photomultiplier tube was converted to a voltage signal by a picoammeter and digitized as a function of photon energy to yield spectra of the transmitted light intensity using a computer controlled data acquisition system. The control system was written in FORTRAN and utilized a DEC–PDP 11 MINC computer with

- a fast 12 bit A/D converter used to measure a voltage proportional to the current on the photomultiplier, and
- a 24 bit digital input used to read the absolute position of the monochromator carriage which is related to the photon energy, and
- a TTL pulse output controller which was used to drive the monochromator stepper motor thereby scanning the photon energy.

Spectra of the transmitted light intensity were measured for the cell charged with the gas of interest (I) and for the empty cell (I_0), and the data was normalized using the expression:

$$\sigma(\lambda) \; \alpha \; ln\left(\frac{I_0(\lambda)}{I(\lambda)}\right) \tag{2.2.1}$$

which arises from Eq. (2.1.2). No attempt was made to quantify the absorption cross sections for these compounds.

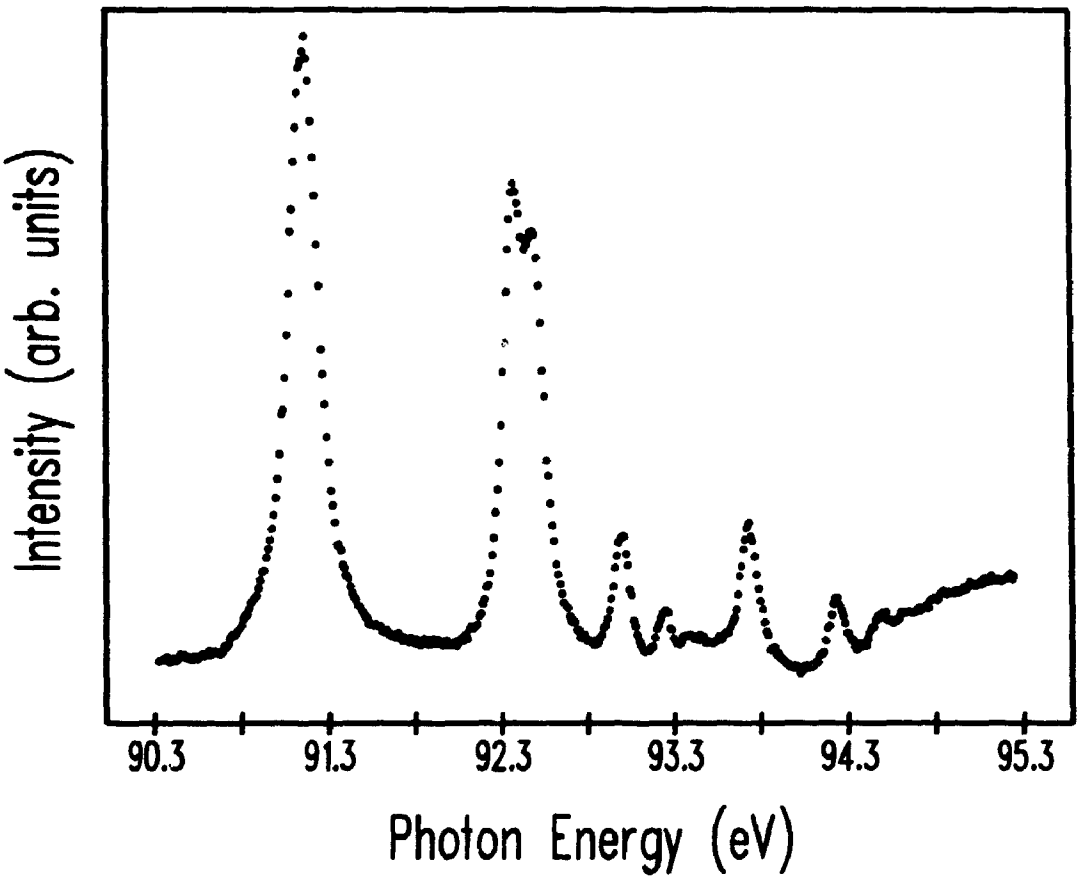

Figure 2.2.1: Photoabsorption spectrum of the Kr $3d \rightarrow nd$ Rydberg structure used to calibrate the monochromator

The relationship between the photon energy and the carriage position of the monochromator was calibrated by measuring the absorption spectra of the Kr 3*d* Rydberg levels (Fig. 2.2.1) which are seen as a series of sharp lines below 95 eV.[121] This provides an accurate calibration of the photon energy for the Si 2*p* pre-edge region and the calibration is estimated to yield errors of ~0.1 eV around 100 eV with less accuracy at the higher photon energies. For the pre-edge absorption features, the monochromator resolution is the limiting factor in determining the positions of the discrete resonances in most cases. In the continuum regions, resonances are much broader, making it more difficult to identify the peak of the intensity and the estimated error in their positions are ~0.5eV.

Samples of the compounds studied were purchased in high purity from commercial sources (Aldrich, Matheson and Petrarch Systems). Samples which were liquids at room temperature were degassed with repeated freeze-pump-thaw cycles and introduced into the evacuated photoabsorption cell without further purification. Gaseous samples were introduced directly into the cell. Pressures of between 0.5 and 1.5 torr were used in the cell for the absorption scans in order to highlight certain absorption features in the discrete and continuum regions. Usually 10–20 spectra were measured for each compound at different pressures and photon resolutions and spectra exhibiting the best resolution of the features were selected for presentation in this chapter.

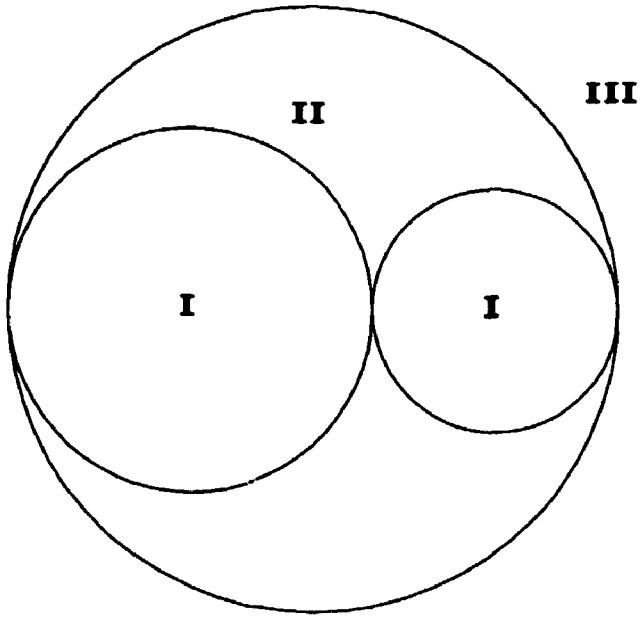

Figure 2.3.1: Schematic of the muffin-tin potential used in the Xα method.

2.3. THEORY: Xα Calculations

Multiple scattering Xα calculations were performed to generate theoretical cross sections for the discrete and continuum regions of the Si 2*p* and Si 2*s* core-levels of all 13 of the silane molecules reported in this chapter. The calculations were carried out on DEC-VAX and CDC-Cyber mainframe computers using the standard MS-Xα method[122] and the continuum cross section program of Davenport.[123] Use of the Xα method for calculating electronic properties of polyatomic molecules has been reviewed in detail previously,[124–126] and only a brief outline will be presented here. The method is a self-consistent-field (SCF) method which approximates the one-electron potential with a "muffin-tin" potential. The muffin-tin potential, which is represented schematically in Fig. 2.3.1, uses three regions to describe the potential of the molecule.

Inside the atomic spheres, region I, spherical averages of the atomic potentials are used. In region II, between the atomic spheres, a constant potential equal to the average over the interatomic region is used. In the extra-molecular region, region III, a spherically averaged potential is used. The three component potentials together approximate the molecular potential.

The many-electron Schrödinger equation is reduced to a series of one-electron equations by approximating the exchange energy with a scaled electron density as proposed by Slater.[127] The muffin-tin potential is used in the solution of the one-electron Schrödinger equations in each of the three regions

$$\left[-\nabla^2 + V_c(\mathbf{R}) + V_{X\alpha}(\mathbf{r})\right]\psi_i(\mathbf{r}) = \epsilon_i\psi_i(\mathbf{r}) \tag{2.3.1}$$

where ∇^2 is the kinetic energy, $V_c(\mathbf{r})$ is the electrostatic potential energy (nuclear and electronic) at position $\mathbf{r}$ (computed classically) and

$$V_{X\alpha}(\mathbf{r}) = -6\alpha\left[\frac{3}{8}\pi\rho(\mathbf{r})\right]^{1/3} \tag{2.3.2}$$

is the $X\alpha$ statistical approximation to the exchange correlation which is further a function of the electronic charge density, $\rho(\mathbf{r})$ and the scaling parameter, α. In the SCF calculation, the potential begins as a superposition of the atomic potentials averaged to fit the muffin-tin model. This starting potential is used to solve the one electron equations resulting in the one electron eigenvalues ϵ_i from which the one-electron wavefunctions ψ_i can be calculated in their proper forms with the boundary condition that the wavefunctions and their first derivatives be continuous at the sphere boundaries. The orbitals are populated by the criteria specified in the calculation and used to calculate a new potential which is averaged to fit the muffin-tin model, resulting in a new starting potential and completing one iteration. The procedure is repeated to a specified tolerance yielding the SCF molecular potential. Equations of the form of Eq. (2.1.5) are used to calculate the absorption coefficients in the discrete and continuum regions by incorporating the

proper scattering boundary conditions. The form of the continuum wavefunction and the details of how the dipole matrix elements are evaluated in the multiple scattering method has been treated in detail elsewhere.[123,128,129]

molecule	bond lengths (Å)	bond angles	reference
SiF_4	d_{SiF} 1.552	∠FSiF 109.5°	Ref. 130
$SiCH_3F_3$	d_{SiC} 1.828, d_{SiF} 1.570	∠FSiF 106.8°	Ref. 130
$Si(CH_3)_2F_2$	d_{SiC} 1.836, d_{SiF} 1.586	∠FSiF 104.6°, ∠CSiC 116.7°	Ref. 130
$Si(CH_3)_3F$	d_{SiC} 1.848, d_{SiF} 1.600	∠CSiC 111.5°	Ref. 130
$Si(CH_3)_4$	d_{SiC} 1.880	∠CSiC 109.5°	Ref. 130
$Si(CH_3)_3Cl$	d_{SiC} 1.890, d_{SiCl} 2.090	∠CSiC 113.0°	Ref. 131
$Si(CH_3)_2Cl_2$	d_{SiC} 1.830, d_{SiCl} 1.990	∠CSiC 112.0°, ∠ClSiCl 108.6°	Ref. 131
$SiCH_3Cl_3$	d_{SiC} 1.848, d_{SiCl} 2.026	∠CSiCl 110.3°	Ref. 131
$SiCl_4$	d_{SiCl} 2.016	∠ClSiCl 109.5°	Ref. 132
$SiHCl_3$	d_{SiH} 1.466, d_{SiCl} 2.012	∠HSiCl 108.3°	Ref. 133
SiH_2Cl_2	d_{SiH} 1.480, d_{SiCl} 2.033	∠HSiH 111.3°, ∠ClSiCl 109.7°	Ref. 134
SiH_3Cl	d_{SiH} 1.482, d_{SiCl} 2.048	∠HSiCl 107.9°	Ref. 135
SiH_4	d_{SiH} 1.487	∠HSiH 109.5°	Ref. 136

Table 2.3.1: Structural parameters used to calculate the atomic position matricies of the silane molecules in this study for the MS-Xα calculations. Positions of the H's in the methyl groups were calculated from the parameters d_{CH} 1.09 Å and ∠HCH 110.0°.

The MS-Xα method was used to calculate the eigenvalues and charge distributions of the unoccupied levels of the silane molecules along with the corresponding oscillator strengths for transitions to the identified virtual orbitals from the Si 2*p* and Si 2*s* core-levels. All calculations were carried out in the appropriate idealized symmetry for the molecule under consideration (T_d, C_{3v} and C_{2v}). Transition state potentials, SCF potentials calculated by removing $\frac{1}{2}$ electron from the core-level orbital of interest (Si 2*p* or Si 2*s*), were used for all of the oscillator strength and cross section calculations. Continuum photoionization cross sections above the Si 2*p* and Si 2*s* ionization edges have also been evaluated, and contributions from the symmetry allowed eigenchannels determined using Davenport's program.[123] The positions of the atoms in the molecules were determined from experimental measurements of the ground state

molecule	Region	Radius (au)	α_{HF}	l_{max}	
				initial state	final state
SiF_4	outersphere	4.35	0.7361	4	6
	Si	1.52	0.7275	3	5
	F	1.41	0.7373	2	4
$SiCH_3F_3$	outersphere	4.71	0.7426	4	6
	Si	2.35	0.7275	3	5
	F	1.22	0.7373	2	4
	C	1.81	0.7593	2	4
	H	1.00	0.7772	1	3
$Si(CH_3)_2F_2$	outersphere	4.90	0.7491	4	6
	Si	2.35	0.7275	3	5
	F	1.22	0.7373	2	4
	C	1.77	0.7593	2	4
	H	1.00	0.7772	1	2
$Si(CH_3)_3F$	outersphere	5.30	0.7555	4	6
	Si	2.42	0.7275	3	5
	F	1.21	0.7373	2	4
	C	1.77	0.7593	2	4
	H	1.00	0.7772	0	1
$Si(CH_3)_4$	outersphere	5.70	0.7620	4	6
	Si	2.06	0.7275	3	5
	C	1.48	0.7593	2	4
	H	1.00	0.7772	0	2

Table 2.3.2: Parameters used in the MS-Xα calculations of the fluoromethylsilane molecules, $(CH_3)_xSiF_{4-x}$; x=0-4.

molecule	Region	Radius (au)	α_{HF}	l_{max}	
				initial state	final state
$SiCl_4$	outersphere	6.21	0.7238	4	7
	Si	2.20	0.7275	2	3
	Cl	2.40	0.7233	2	3
$SiCH_3Cl_3$	outersphere	5.95	0.7334	4	7
	Si	2.16	0.7275	2	3
	Cl	2.45	0.7233	2	3
	C	1.90	0.7593	1	2
	H	1.00	0.7772	0	1
$Si(CH_3)_2Cl_2$	outersphere	6.20	0.7429	4	7
	Si	2.16	0.7275	2	3
	Cl	2.40	0.7233	2	3
	C	1.92	0.7593	1	2
	H	1.00	0.7772	0	1
$Si(CH_3)_3Cl$	outersphere	6.47	0.7524	4	7
	Si	2.30	0.7275	2	3
	Cl	2.52	0.7233	2	3
	C	1.90	0.7593	1	2
	H	1.00	0.7772	0	1
$Si(CH_3)_4$	outersphere	5.70	0.7620	4	7
	Si	2.40	0.7275	2	3
	C	1.90	0.7593	1	2
	H	1.00	0.7772	0	1

Table 2.3.3: Parameters used in the MS-Xα calculations for the chloromethylsilane molecules, $(CH_3)_xSiCl_{4-x}$; x=0-4.

molecule	Region	Radius (au)	α_{HF}	l_{max}	
				initial state	final state
$SiCl_4$	outersphere	6.21	0.7238	4	7
	Si	2.20	0.7275	2	3
	Cl	2.40	0.7233	2	3
$SiHCl_3$	outersphere	6.21	0.7260	4	7
	Si	2.16	0.7275	2	3
	Cl	2.40	0.7233	2	3
	H	1.20	0.7772	1	2
SiH_2Cl_2	outersphere	6.25	0.7295	4	7
	Si	2.20	0.7275	2	3
	Cl	2.40	0.7233	2	3
	H	1.20	0.7772	1	2
SiH_3Cl	outersphere	6.30	0.7360	4	7
	Si	2.20	0.7275	2	3
	Cl	2.40	0.7233	2	3
	H	1.20	0.7772	1	2
SiH_4	outersphere	4.10	0.7524	4	7
	Si	2.04	0.7275	2	3
	H	1.20	0.7772	1	2

Table 2.3.4: Parameters used in the MS-Xα calculations for the chlorosilane molecules, H_xSiCl_{4-x}; x=0-4.

geometry and the bond lengths and angles used are summarized in Table 2.3.1. Summaries of the sphere sizes, exchange parameters and maximum azimuthal quantum numbers used in the calculations are given in Table 2.3.2 for the $Si(CH_3)_xF_{4-x}$ molecules, in Table 2.3.3 for the $Si(CH_3)_xCl_{4-x}$ molecules, and in Table 2.3.4 for the SiH_xCl_{4-x} molecules. The atomic exchange parameters, α_{HF}, are from Schwarz's tabulations [137] and for the intersphere and outersphere regions, α_{HF} values were obtained by averaging the atomic values weighted by the number of valence electrons for each atom. Atomic sphere radii were determined using the Norman procedure [138] and enlarged by 10–20%. Overlapping spheres have been found to result in improved descriptions of the ionization potentials and total energies of molecules[139,140] and result in well behaved cross sections.[14] For the continuum cross section calculations, a Latter tail[141] was added to the outersphere potential after the final iteration to account for the asymptotic behaviour of the potential at large r.

2.4. RESULTS: Fluoromethylsilane Compounds, $Si(CH_3)_xF_{4-x}$

2.4.1. Core Ionization Potentials

The positions of resonances above different core levels of a given molecule can be compared directly with the use of *term values*. The term value of a spectral feature, $\mathcal{T}_j$, is defined as the difference between the ionization potential of the appropriate core level, IP_i, and the energy of the cross section maximum, $\mathcal{E}_j$.

$$\mathcal{T}_j = IP_i - \mathcal{E}_j \tag{2.4.1}$$

The term value, $\mathcal{T}_j$, of a discrete resonance in a core level photoabsorption spectrum is directly related to the energy, ε_{k^*} of the final state virtual orbital, k^* and given by,

$$\mathcal{T}_j = \varepsilon_{k^*} + J(ik^*) - K(ik^*) + \mathcal{C} \tag{2.4.2}$$

where $\mathcal{C}$ is the difference between core relaxation and correlation effects in the ion and the core-excited neutral molecule, and $J(ik^*)$ and $K(ik^*)$ are the Coulomb and exchange integrals respectively.[108] Term values of resonances above different ionization edges in a molecule are comparable if the terms $J(ik^*) - K(ik^*) + \mathcal{C}$ in Eq. (2.4.2) are assumed to be independent of the core hole. This results in a transferability of term values between different core holes which can be very useful for assigning the symmetry of virtual molecular orbitals.[108,142]

Accurate core level ionization potentials, IP_i, are important for the determination of accurate term values of discrete and continuum resonances in the photoabsorption spectra of the fluoromethylsilane compounds. It is impossible to determine the Si $2p$ ionization potentials of the fluoromethylsilanes directly from the absorption spectra owing to the complexity of the Si $2p$ pre-edge spectra further compounded by the absence of distinguishable edge jumps at threshold. Ionization potentials from XPS experiments must be used instead.

Values for the Si $2p_{3/2}$ ionization potentials of SiF_4 and $Si(CH_3)_4$ of 111.70 eV and 105.94 eV respectively, were assigned using XPS data from Kelfve *et al.*[143] Perry and Jolly[144] and Drake *et al*[145] have reported similar values. The ionization potential of the Si $2p_{3/2}$ level of $Si(CH_3)_3F$ was reported by Drake *et al* to be 107.15 eV.[145] Experimental values for the silicon core ionization potentials of $Si(CH_3)_2F_2$ and $SiCH_3F_3$ have not been reported.

Estimates of ionization potentials for the Si $2p_{3/2}$ edges of $Si(CH_3)_2F_2$ and $SiCH_3F_3$ were calculated using known Si $2p_{3/2}$ ionization potentials of the chloromethylsilane molecules, $Si(CH_3)_xCl_{4-x}$; $x = 0 - 4$.[145] In order to calculate ionization potentials for the fluoromethylsilane molecules, differences in ionization potential between consecutive members of the chloromethylsilane series were divided by the difference between $SiCl_4$ and $Si(CH_3)_4$. The resulting values express the difference in ionization potential between consecutive members of the molecular series as a fraction of the total difference. Assuming that the relative differences are similar for the fluoromethylsilane series, the calculated values were multiplied by the difference between the ionization potentials of SiF_4 and $Si(CH_3)_4$ yielding estimates for the Si $2p_{3/2}$ ionization potentials of the mixed fluoromethylsilanes. The resulting values for the ionization potentials of $SiCH_3F_3$, $Si(CH_3)_2F_2$ and $Si(CH_3)_3F$ are 110.30 eV, 108.81 eV and 107.23 eV respectively. The latter value compares favourably with 107.15 eV, the experimentally determined Si $2p_{3/2}$ ionization potential of $Si(CH_3)_3F$ [145] suggesting that the two other estimated values are accurate to within 0.10 eV. The Si $2p_{3/2}$ - Si $2p_{1/2}$ spin-orbit splitting, estimated previously to be ~0.61 eV [71,143] and recently accurately measured to be 0.612 eV in SiH_4 [146] was used to calculate the Si $2p_{1/2}$ ionization potentials of the fluoromethylsilanes.

Experimental values for the Si $2s$ ionization potentials for the compounds of interest were not available. Values were estimated using a Si $2p - 2s$ splitting of 51.2 eV as reported by Sodhi *et al*,[142] which is in good agreement with a splitting

of 51.4 eV suggested by Fomichev *et al.*[118] Values of the Si $2p_{3/2}$, Si $2p_{1/2}$ and Si $2s$ ionization potentials for the fluoromethylsilane molecules are included in Tables 2.4.1 – 2.4.5.

2.4.2. Experimental Photoabsorption Spectra

Photoabsorption spectra of the five fluoromethylsilane molecules are presented in Fig. 2.4.1 for the photon energy range 100 - 200 eV which encompasses the discrete and continuum regions of the Si $2p$ and Si $2s$ edges for all five molecules. Ionization edges for each molecule are indicated on the experimental curves, with the flag at lower energy corresponding to the averaged Si $2p$ ionization potential and the higher energy mark indicating the Si $2s$ ionization edge.

The spectra in Fig. 2.4.1 illustrate several features of the fluoromethylsilane photoabsorption spectra. First, spectra of the fluorine containing molecules have large contributions to the cross section at 100 eV from valence fluorine $3p$ and $3s$ orbitals. The effect is most noticeable in the spectrum for SiF_4, where the Si $2p$ and $2s$ core level absorption features are superimposed on a strongly decreasing valence cross section. The effect is lessened as the number of fluorine atoms in the molecule is decreased. Second, there is a sharp "step" in all of the photoabsorption spectra at ~140 eV. This feature is due to second order light from the monochromator being absorbed by carbon in the molecule and the windows of the cell. In the case of SiF_4, no carbon is present in the sample, but owing to slight flaws in the normalization procedure, absorption of second order light by the polypropylene windows is evident. Also of interest is the structure in the absorption spectrum of $Si(CH_3)_3F$ above the Si $2s$ ionization edge. This structure is probably due to a sulfur contaminant in the sample. The pattern and position of the peaks is similar to the SF_6 photoabsorption spectrum.[91] Absorption of the contaminant interferes only with the Si $2s$ continuum region of $Si(CH_3)_3F$.

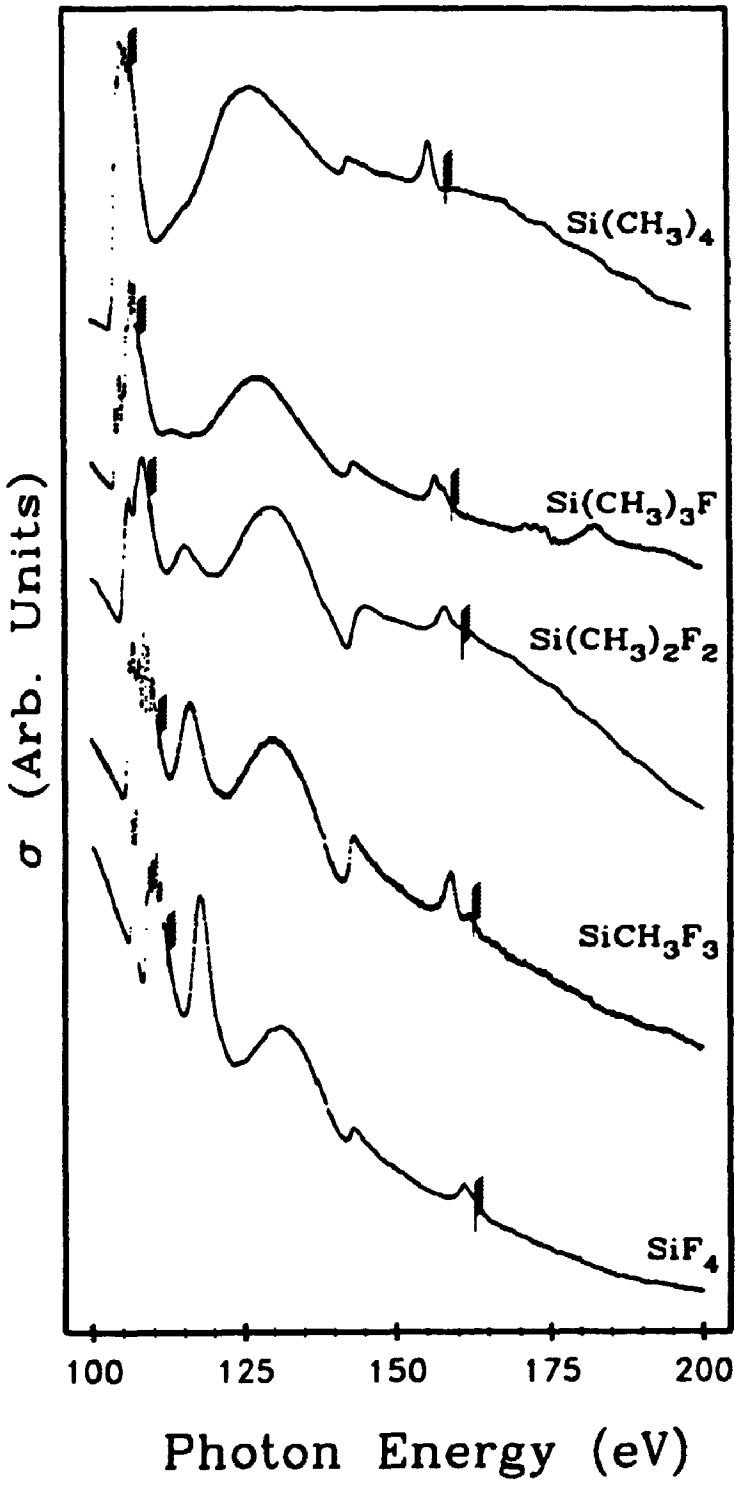

Figure 2.4.1: Photoabsorption spectra of the fluoromethylsilane compounds around the Si 2*p* and Si 2*s* ionization edges.

Resonances in the discrete and continuum regions of the Si 2*p* and 2*s* ionization edges are of primary interest in this study. It is evident from Fig. 2.4.1 that the Si 2*p* pre-edge regions in the spectra of all five fluoromethylsilane compounds are rich in structure, with many well resolved peaks. Continuum resonances above the Si 2*p* edges are also well resolved in the 110 - 140 eV photon energy range. The relative intensities of the Si 2*s* pre-edge and continuum features with respect to the Si 2*p* features appear to be much weaker than the corresponding intensities in the spectrum of silicon tetrachloride (see next section).

2.4.2.1. Si 2p pre-edge spectra

High resolution spectra of the Si 2*p* pre-edge regions of the five fluoromethylsilane molecules are presented in Fig. 2.4.2, and the energies and term values of the indicated features are given in tables 2.4.1 – 2.4.5. In this section a general description of the Si 2*p* pre-edge photoabsorption spectra is presented along with a discussion of the changes upon substitution of a $-CH_3$ for a -F ligand on the central Si atom. Several trends are apparent when similarities and differences between the five spectra are considered. Firstly, the term values of the peaks at the lowest photon energies in the spectra decrease from SiF_4 with each substitution of a methyl for a fluorine ligand. The empty orbitals into which the Si $2p_{3/2}$ electron is excited are therefore closer to threshold in $Si(CH_3)_4$ than they are in SiF_4. This is manifested in the apparent convergence of peaks 1 and 2 in Fig. 2.4.2 with peaks closer to threshold as the number of methyl groups around the central silicon atom is increased. Second, the intensity of the lowest energy resonance (peaks 1 and 2) is roughly proportional to the number of fluorine ligands in the molecule. For SiF_4, the spin-orbit split band 1,2 is the most intense peak in the pre-edge absorption spectrum. As fluorine ligands are replaced with methyl ligands, the intensity of the 1,2 band, which becomes convoluted with overlapping bands, decreases relative to the intensity of other peaks in the spectra. The intensity of peak 1, and by

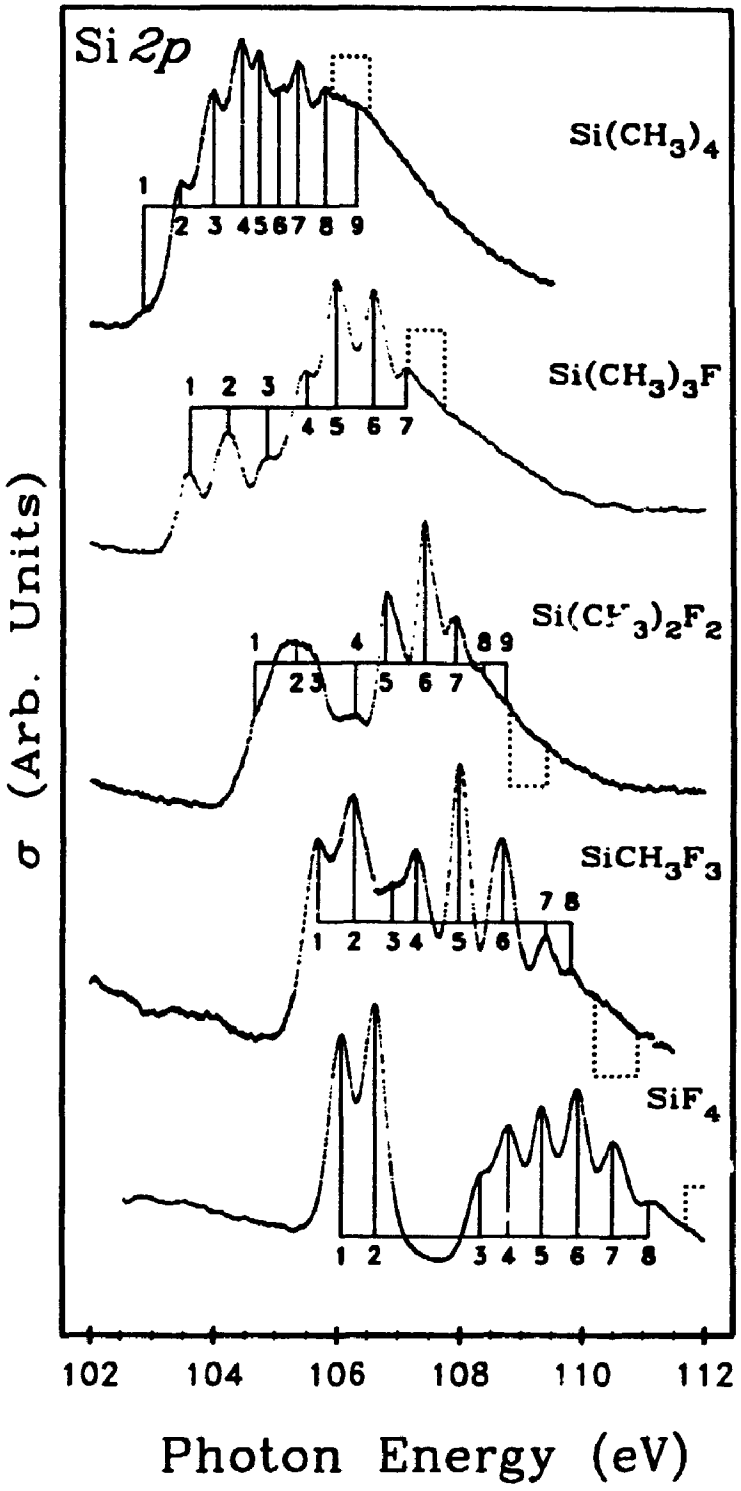

Figure 2.4.2: Photoabsorption spectra of the fluoromethylsilane compounds below the Si 2*p* ionization edges.

inference its spin orbit partner peak in the absorption spectrum of $Si(CH_3)_4$, is greatly reduced relative to the other peaks in the spectrum. Finally, the Si 2*p* pre-edge spectra of the fluoromethylsilanes are also similar to each other, with approximately the same number of peaks in each spectrum. This is not surprising, since all of the molecules have relatively similar valence electronic and geometric structure around the central silicon atom. The major chemical difference between members of the fluoromethylsilane molecules is the electronegativity of the ligands. As a consequence, the energies and perhaps ordering of the virtual orbitals change from one fluoromethylsilane molecule to the others.

The Si 2*p* pre-edge photoabsorption spectrum of gaseous SiF_4 has been studied in detail in several previous reports.[13,20,83,71,84,85,108,109] Spectra of condensed SiF_4 have also been reported.[147,148] The absorption spectrum of the gaseous sample consists of a lower energy doublet of peaks, 1 and 2, and a group of six discernable peaks, 3-8, closer to the Si 2*p* ionization thresholds. Positions of the eight peaks indicated on the SiF_4 spectrum in Fig. 2.4.2, their term values with respect to both the Si $2p_{3/2}$ and $2p_{1/2}$ ionization edges, and a comparison with the positions from a previous report are given in Table 2.4.1. The positions of the resonances compare favourably with previous observations. Term values of the discrete resonances in the SiF_4 absorption spectrum can easily be grouped into four spin orbit split pairs; 1-2, 3-4, 5-6 and 7-8. Differences in term value between these pairs of peaks are all equal to the Si 2*p* spin orbit splitting to within 0.10 eV in all cases except for pair 3-4 where the difference is 0.15 eV. The position of peak 3 is uncertain since it lacks a distinct maximum. Using the 0.61 eV spin-orbit splitting criterion, it is also possible to assign a total of six overlapping spin-orbit split pairs for the spectrum; 1-2, 3-4, 4-5, 5-6, 6-7, and 7-8.

The intensity ratio of the spin orbit split peaks 1-2 is not consistent with the statistically expected ratio of 2:1. A disagreement between the observed and statistical spin-orbit pair intensity ratio has been observed for numerous

(a) Si 2p pre-edge

peak label	energy (eV)	energy (eV)†	term value (eV)		assignments		
			$Si2p_{3/2}$	$Si2p_{1/2}$	resonance		$Si2p_{3/2} \rightarrow$
1	106.09	106.13	5.61	6.22	a		$1a_1^*$
2	106.63	106.68	5.07	5.68		a	-
3	108.31	108.4	3.39	4.00	b		$1t_2^*$
4	108.77	108.9	2.93	3.54	c	b	$2a_1^*$
5	109.31	109.4	2.39	3.00	d	c	$2t_2^*$, $1e^*$
6	109.89	110.0	1.81	2.42	e	d	$3a_1^*$, Ryd.
7	110.45	110.7	1.25	1.86	f	e	Ryd.
8	111.05	111.4	0.65	1.26		f	-
$Si2p_{3/2}$	111.70	111.6	-	-	-	-	-
$Si2p_{1/2}$	112.31	112.21	-	-	-	-	-

† Ref. 84

(b) Si 2p continuum

peak label	energy (eV)	term value (eV)	calc. term value (eV)	phase shift (π)	symmetry channel
1	112.0	−0.9	−0.5	1.0	ka_1
2	117.3	−6.2	−8.3	0.3	ke
3	131.6	−20.5	−16.5	1.0	kt_2

(c) Si 2s

peak label	energy (eV)	term value (eV)	Si 1s term value (eV)‡	calc. term values (eV)	assignment
1	159.3	4.0	6.0,3.5,2.3		anti.
Si2s	163.6	-	-	-	-
2	173.1	−9.5	−5.5		kt_2
3	180.3	−16.7	−12.5	−13.6	kt_2

‡ Ref. 117

Table 2.4.1: Energies, term values and assignments of the discrete and continuum resonances in the Si 2p and 2s photoabsorption spectra of SiF_4.

other molecular spectra, including SF_6.[91] $SiCl_4$ (see next section) and second row hydrides[72] and has been discussed by Schwarz.[72] Schwarz noted that the intensities of the spin-orbit split lines in the second row hydrides are sensitively dependent on the exchange interaction between the excited-electron and the core hole. Two electron interaction raises the intensity of the $2p_{1/2}$ excitation and weakens the Si $2p_{3/2}$ transition.[72] Intensity ratios in the multiplet structure (peaks

3 - 8) are also inconsistent with the presence of three spin orbit split resonances, but better agreement is obtained by the assignment of five overlapping spin orbit pairs. Assuming contributions from five spin orbit split pairs produce the multiplet structure in the Si $2p$ pre-edge absorption spectrum of SiF_4 an estimate of the shape of the resulting spectrum can be constructed. If the intensities of the resonances are all equal and the spin orbit pairs obey the statistical intensity ratio of 2:1 for the Si $2p_{3/2}$ and $2p_{1/2}$ components, then the estimated intensity ratios of peaks 3-8 would be 1:1.5:1.5:1.5:1.5:0.5. These ratios, obtained with a very simplified and idealized calculation are similar to the intensity ratios which are actually observed in the multiplet band in the experimental Si $2p$ pre-edge photoabsorption spectrum of SiF_4. The agreement of the experimental intensities with those calculated above, and the MS-Xα calculations below, suggest that the assignment of six spin orbit split peaks to the Si $2p$ pre-edge absorption spectrum is the correct one. Assignment of the spin orbit split resonances is indicated in Table 2.4.1. The assignment of six pre-edge resonances in the Si $2p$ pre-edge region of SiF_4 is consistent with assignments for the other fluoromethylsilane molecules.

The Si $2p$ pre-edge absorption spectrum of $SiCH_3F_3$ over a photon energy range 102 to 112 eV is presented in Fig. 2.4.2. The spectrum of condensed $SiCH_3F_3$ has also been reported,[148] but no other gas phase results have been published. The spectrum is similar to that of SiF_4 but differs in that there is no well separated pair of peaks at low photon energy. In addition, as evidenced by the poor resolution of peaks 1 and 2, most peaks in the $SiCH_3F_3$ spectrum are broader than the corresponding peaks in the SiF_4 spectrum. Energies and term values of the eight pre-edge peaks in the Si $2p$ spectrum of $SiCH_3F_3$ indicated on Fig. 2.4.2 are given in Table 2.4.2. Six spin orbit split pairs can be readily assigned to the spectrum using the term values: 1-2, 2-3, 4-5, 5-6, 6-7, and 7-8. With the exception of the 7-8 pair, the term value differences between the assigned pair peaks are all within

(a) Si 2p pre-edge

peak label	energy (eV)	term value (eV)		assignments		
		$Si2p_{3/2}$	$Si2p_{1/2}$	resonance		$Si2p_{3/2} \rightarrow$
1	105.73	4.57	5.18	a		$1a_1^*$
2	106.30	4.00	4.61	b	a	$1e^*$
3	106.94	3.36	3.97		b	-
4	107.29	3.01	3.62	c		$2a_1^*$
5	107.99	2.31	2.92	d	c	$2e^*$, $3a_1^*$
6	108.70	1.60	2.21	e	d	Ryd.
7	109.39	0.91	1.52	f	e	Ryd.
8	109.81	0.49	1.10		f	-
$Si2p_{3/2}$	110.20	-	-	-	-	-
$Si2p_{1/2}$	110.91	-	-	-	-	-

(b) Si 2p continuum

peak label	energy (eV)	term value (eV)	calc. term value (eV)	phase shift (π)	symmetry channel
1	110.7	0.0	−0.1	0.3	ka_1
2	115.8	−5.1	−8.2	0.6	ke
3	130.6	−19.8	−16.4,−19.2	0.3, 0.3	ka_1, ke

(c) Si 2s

peak label	energy (eV)	term value (eV)	calc. term value (eV)	assignment
1	157.2	4.7	-	$1a_1^*$
2	160.2	1.7	-	mixed+Ryd.
Si2s	161.9	-	-	-
3	172.6	−10.7	−14.0	$ka_1 + ke$

Table 2.4.2: Energies, term values and assignments of the discrete and continuum resonances in the Si 2*p* and 2*s* photoabsorption spectra of $SiCH_3F_3$

0.10 eV of the 0.61 eV Si 2*p* spin orbit splitting value. Owing to the weak intensity of the peak at position 8, there is greater inherent error in determining its position.

Slightly offset overlapping peaks could partly explain the odd distribution of peak widths in the $SiCH_3F_3$ spectrum in Fig. 2.4.2. In the Si 2*p* pre-edge photoabsorption spectrum of $SiCH_3F_3$, peaks 2, 4 and 6 are noticeably broader than peaks 1, 5 and 7. The intensities of the peaks relative to their assigned spin orbit partner do not follow the pattern expected from statistical arguments. As

(a) Si 2p pre-edge

peak label	energy (eV)	term value (eV)		assignments		
		$Si2p_{3/2}$	$Si2p_{1/2}$	resonance		$Si2p_{3/2}$ —
1	104.69	4.12	4.73	a		$1a_1^*$
	105.06	3.75	4.36	b		$2b_2^*$
2	105.34	3.47	4.08		a	-
3	105.67	3.14	3.75	c	b	$3a_1^*$
4	106.31	2.50	3.11		c	-
5	106.80	2.01	2.62	d		$6a_1^*$, $2b_2^*$
6	107.42	1.39	2.00	e	d	$3b_2^*$, Ryd.
7	107.92	0.89	1.50		e	-
8	108.36	0.45	1.06	f		Ryd.
9	108.74	0.07	0.68		f	-
$Si2p_{3/2}$	108.81	-	-	-	-	-
$Si2p_{1/2}$	109.42	-	-	-	-	-

(b) Si 2p continuum

peak label	energy (eV)	term value (eV)	calc. term value (eV)	phase shift (π)	symmetry channel
1	109.2	0.0	−0.1, −0.1	0.3, 0.3	ka_1, kb_1
2	114.4	−5.2	−4.2, −5.6	0.4, 0.2	ka_2, ka_1
3	128.5	−19.3	−16.5, −17.8, −20.5	0.1, 0.1, 0.1	kb_1, ka_1, kb_2

(c) Si 2s

peak label	energy (eV)	term value (eV)	calc. term value (eV)	assignment
1	155.9	4.5	-	$1b_2^*$
2	158.7	1.7	-	mixed+Ryd.
Si2s	160.4	-	-	-
3	173.1	−12.7	−16	$ka_1 + kb_1 + kb_2$

Table 2.4.3: Energies, term values and assignments of the discrete and continuum resonances in the Si 2p and 2s photoabsorption spectra of $Si(CH_3)_2F_2$

illustrated previously for SiF_4, it is conceivable that the overlapping assignment of the peaks given in Table 2.4.2 (*a*) could result in the complicated intensity pattern observed.

A high resolution Si 2p pre-edge absorption spectrum of $Si(CH_3)_2F_2$ is presented in Fig. 2.4.2. No other gas phase spectra of $Si(CH_3)_2F_2$ have been

reported although the spectrum of the condensed sample was recently reported.[148] Several peaks were identified and are indicated on the figure. Energies and term values of the indicated features are given in Table 2.4.3. The spectrum is different from the previous two spectra in that the lower energy peaks, 1-3, are not resolved. Positions for peaks 1-3 were inferred from the shape of the absorption curve, but no deconvolution techniques were applied to the spectrum. Using term values as a guide, the assignment of three spin orbit split resonances is immediately apparent; 1-2, 3-4 and 5-6. This assignment leaves out several peaks and does not account for the poor resolution of peaks 1, 2 and 3. Peaks 8 and 9 probably form a spin-orbit split pair corresponding to a very weak resonance near threshold. The weak intensity of these peaks and their position on a strongly sloping baseline produces greater uncertainty in their positions and hence term values. The spin orbit partner of peak 7 likely underlies the strong peak 6. This assignment is consistent with the broad and slightly asymmetric shape of peak 6. In order to account for the unresolved low energy absorption feature in the $Si(CH_3)_2F_2$ spectrum, an unresolved resonance is assigned between positions 1 and 2, corresponding to a Si $2p_{3/2}$ spin orbit partner of peak 3 which is therefore its Si $2p_{1/2}$ component. A peak midway between 1 and 2 at ~105.06 eV could result in the absorption pattern observed.

The intensity of feature 3 also supports the assignment of a peak at 105.06 eV. If peak 3 corresponds to the spin-orbit partner to peak 4 it would be expected to have much less intensity than it exhibits in the experimental spectrum. The strong intensity of peak 6 relative to its assigned spin orbit partner, peak 5, supports the assignment of 6-7 as a spin-orbit split pair. While spin orbit split peaks in the Si $2p$ pre-edge absorption spectra of the fluoromethylsilanes are not expected to exhibit statistical intensity ratios, they do seem to exhibit similar intensities as illustrated by the well resolved spin orbit pair 1-2 in SiF_4. The intensity of peak 6 in the Si $2p$ absorption spectrum of $Si(CH_3)_2F_2$ is therefore not expected to differ

(a) Si 2p pre-edge

peak label	energy (eV)	term value (eV)		assignments		
		$Si2p_{3/2}$	$Si2p_{1/2}$	resonance		$Si2p_{3/2} \rightarrow$
1	103.65	3.50	4.11	a		$1a_1^*$
2	104.26	2.89	3.50	b	a	$1e^*$
3	104.89	2.26	2.87	c	b	$2e^*$
4	105.51	1.64	2.25	d	c	$4a_1^*$
5	105.99	1.16	1.77	e	d	$3e^*$
6	106.60	0.55	1.16	f	e	Ryd.
7	107.10	0.05	0.66		f	-
$Si2p_{3/2}$	107.15	-	-	-	-	-
$Si2p_{1/2}$	107.76	-	-	-	-	-

(b) Si 2p continuum

peak label	energy (eV)	term value (eV)	calc. term value (eV)	phase shift (π)	symmetry channel
1	108.3	−0.7	−0.1	0.3	ka_1
2	113.1	−5.5	−9.7, −9.7	0.1, 0.8	ka_1, ke
3	126.3	−18.7	−15.1	0.25	ke

(c) Si 2s

peak label	energy (eV)	term value (eV)	assignment
1	155.0	3.8	mixed
2	156.3	2.5	mixed+Ryd.
Si2s	158.8	-	-

Table 2.4.4: Energies, term values and assignments of the discrete and continuum resonances in the Si 2p and 2s photoabsorption spectra of $Si(CH_3)_3F$.

substantially from that of peak 5 unless there is a second resonance contributing intensity to peak 6. Using the above energy and intensity patterns, the Si 2p pre-edge absorption spectrum of $Si(CH_3)_2F_2$ is assigned with six spin orbit split resonances. The obvious spin orbit pairs are 1-2, 3-4 and 5-6, the less apparent pairs are 6-7, 8-9 and an unresolved resonance is assigned at 105.06 eV paired with peak 3.

A high resolution Si 2p pre-edge absorption spectrum of $Si(CH_3)_3F$ is also presented in Fig. 2.4.2. The Si-2p pre-edge spectrum of condensed $Si(CH_3)_3F$ has

also been reported recently.[148] The spectrum consists of seven peaks as indicated on the figure. Energies and corresponding Si $2p_{3/2}$ and Si $2p_{1/2}$ term values of the seven labelled peaks are reported in Table 2.4.4. Consistent spacing of ~0.6 eV between the seven peaks in the spectrum simplifies the assignment of spin orbit split pairs to the pre-edge region. Six pairs are assigned to the Si $2p$ pre-edge spectrum of $Si(CH_3)_3F$ for consistency with the other fluoromethylsilanes; 1-2, 2-3, 3-4, 4-5, 5-6, and 6-7.

The intensity pattern of the seven peaks of the Si $2p$ pre-edge absorption spectrum of $Si(CH_3)_3F$ also supports the assignment of six spin-orbit split pairs. Assuming that the spin-orbit pairs of peaks exhibit statistical or near statistical intensity ratios, it is relatively easy to construct an intensity pattern for six spin orbit split pairs which approximates the experimentally observed spectrum.

The Si $2p$ pre-edge photoabsorption spectrum of $Si(CH_3)_4$ (Fig. 2.4.2) has been the subject of numerous previous studies[108,109,118,142,149] and is included here to complete the series. There are nine resolved features indicated on the photoabsorption spectrum and the respective energies and term values are listed in Table 2.4.5. A comparison of these results with peak positions from previous studies of the Si $2p$ pre-edge region of $Si(CH_3)_4$ is also in Table 2.4.5.[142] Surveying the term values in Table 2.4.5, there are four obvious spin-orbit pairs; 1-2, 2-3, 4-6 and 5-7 based on the 0.61 eV spin orbit splitting for the Si $2p$ levels. This leaves peaks 8 and 9 unassigned. It is possible that 8 and 9 form a spin orbit pair corresponding to a very weak resonance near threshold. Considering the intensities of peak 7 and its spin orbit partner 5, it is also conceivable that 7-8 form a spin orbit pair. It is possible that peak 9 is not a discrete resonance but rather an above-edge feature in the Si $2p_{3/2}$ continuum.

The intensity pattern of the first three peaks in the spectrum is not consistent with the above assignment. Since the intensity of peak 1 is very weak, the other spin orbit component of peak 1 would be expected to contribute very little intensity

(a) Si 2p pre-edge

peak label	energy (eV)	energy (eV)†	energy (eV)‡	term value (eV)		assignments		
				$Si2p_{3/2}$	$Si2p_{1/2}$	resonance		$Si2p_{3/2} \rightarrow$
1	102.87	103.5	-	3.15	3.76	a		$1t_2^*$
2	103.47	103.65	103.6	2.55	3.16	b	a	$2t_2^*$
3	104.02	104.15	-	2.00	2.61	c	b	$3b_2^*$
4	104.47	-	104.19	1.55	2.16	d	c	Ryd.
5	104.76	104.8	104.73	1.26	1.87	e		Ryd.
6	105.07	-	105.45	0.95	1.56	f	d	Ryd.
7	105.37	-	-	0.62	1.26		e	-
8	105.83	105.7	105.97	0.19	0.80	g	f	Ryd.
9	106.33	-	-	−0.31	0.30		g	-
$Si2p_{3/2}$	106.02			-	-	-	-	-
$Si2p_{1/2}$	106.63			-	-	-	-	-

† Ref. 118.
‡ Ref. 142.

(b) Si 2p continuum

peak label	energy (eV)	term value (eV)	calc. term value (eV)	phase shift (π)	symmetry channel
1	107.7	−1.3	−1.2	0.8	ka_1
2	113.7	−7.3	−4.2	0.3	ke
3	125.7	−18.0	−17.5	0.5	kt_2

(c) Si 2s

peak label	energy (eV)	term value (eV)	Si 1s term value (eV)§	calc. term value (eV)	phase shift (π)
1	154.8	2.8	2.5	1.1, 0.9, 0.7, 0.5	-
Si2s	157.6	-	-	-	-
2	158.4	−0.8	−2.1	−0.1	0.1
3	163.1	−5.5	−7.8	−4.2	0.8
4	169.7	−12.1		−14.4	0.9
5	177.5	−19.9			
6	184.8	−27.2		−40.0	0.2

§ Ref. 108.

Table 2.4.5: Energies, term values and assignments of the discrete and continuum resonances in the Si 2p and 2s photoabsorption spectra of $Si(CH_3)_4$

to peak 2. The Si $2p_{1/2}$ component of the resonance corresponding to the pair 2-3 would have to be twice as intense as the $2p_{3/2}$ component in order to yield the observed intensity pattern. This is not likely and leads us to suggest the existence

of another resonance contributing to peaks 3 and 4. Using the Si 2*p* spin orbit splitting and intensity considerations, the Si 2*p* pre edge region of the $Si(CH_3)_4$ absorption spectrum is assigned with seven spin-orbit split resonances; 1-2, 2-3, 3-4, 4-6, 5-7, 7-8 and 8-9.

2.4.2.2. Si 2p continuum spectra

Photoabsorption spectra of the Si 2*p* discrete and continuum regions of the fluoromethylsilane molecules over the photon energy range 100 to 140 eV are presented in Fig. 2.4.3. The pre-edge region is included to provide a relative measure of the intensity of the continuum resonances. The intensities of the spectra have been normalized to make the best use of space on the figure. Photoabsorption spectra of the continuum regions of SiF_4 [13,20,83,85,86,108,109] and $Si(CH_3)_4$ [108,109,142,149,150] have been presented and interpreted in previous studies. They are included here to complete the series and to highlight trends observed in the molecular series of the fluoromethylsilane molecules.

The continuum regions of the Si 2*p* photoabsorption spectra are considerably less complicated than the discrete regions. The five continuum spectra of the fluoromethylsilane molecules are also very similar, each exhibiting two distinct continuum resonances and a shoulder near threshold. Energies and term values of the resonances identified on the figure are presented in Table 2.4.1 (*b*) Table 2.4.5 (*b*) for SiF_4 - $Si(CH_3)_4$ respectively. Spectra for all the molecules have a cross section maximum very close to the Si 2*p* threshold. This intensity could be due to either the discrete features tailing into the continuum or a resonance in the continuum at or near threshold. Continuum Si 2*p* cross sections minimize ~3-4 eV above the ionization potential for the fluoromethylsilanes, and it is unlikely that the discrete features could contribute intensity that deeply into the continuum. It is therefore concluded that the Si 2*p* absorption spectra of the fluoromethylsilane molecules all have a continuum resonance near the Si 2*p* ionization threshold.

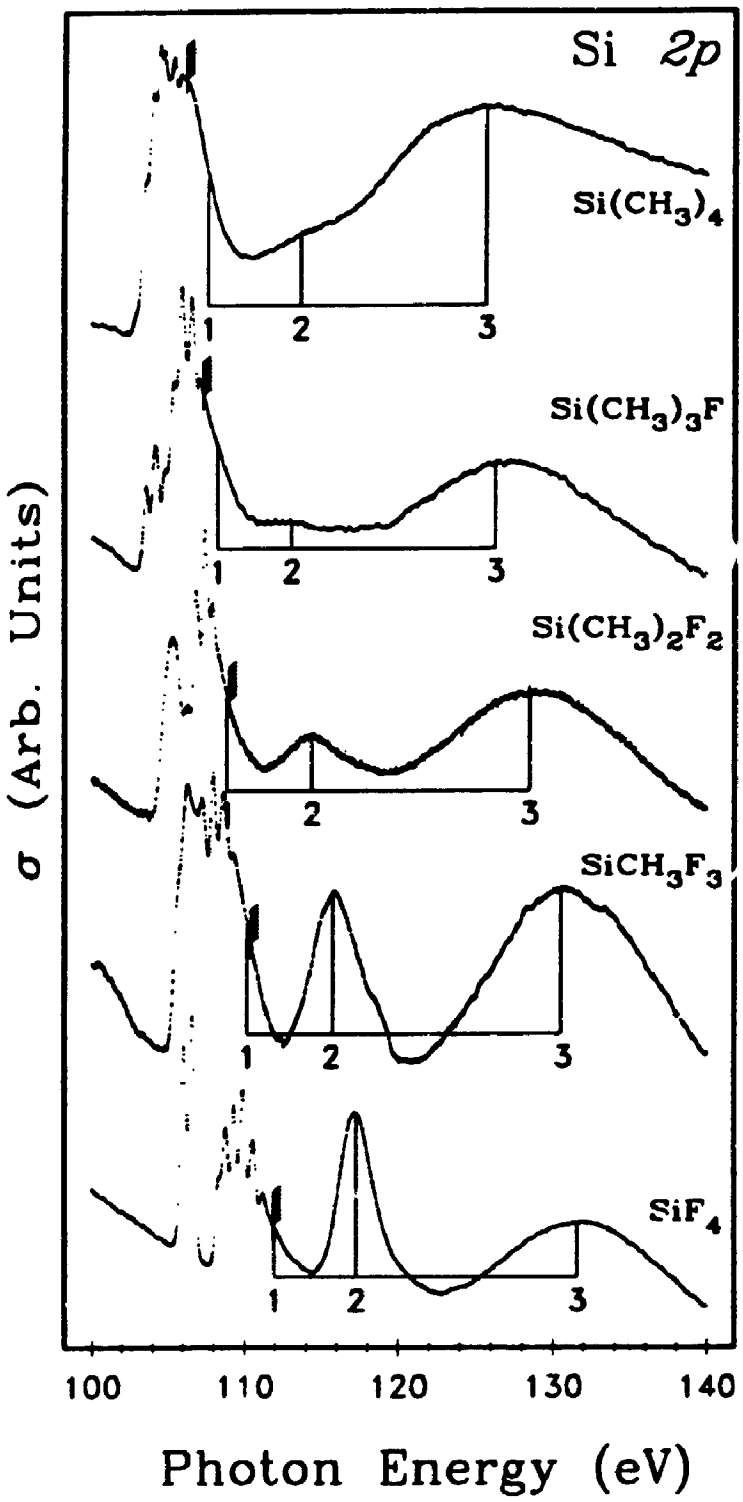

Figure 2.4.3: Photoabsorption spectra of the fluoromethylsilane compounds around the Si 2*p* ionization edges.

The Si 2*p* continuum absorption spectra of the fluoromethylsilane molecules containing one or more fluorine ligands also exhibit a continuum resonance ~5 eV above the ionization potential. There is also a resonance at ~7 eV in the spectrum of $Si(CH_3)_4$ (feature 2) which is indicated on Fig. 2.4.3, but owing to the intensity pattern observed in the spectra of the fluorine containing molecules it is thought to be the result of a different phenomenon. In the SiF_4 Si 2*p* continuum spectrum, feature 2 has twice the intensity of the broader resonance 3 at higher energy. The intensity of peak 2 is also comparable to the intensity of the Si 2*p* pre-edge resonances of SiF_4. The intensity of peak 2 in the spectrum of $SiCH_3F_3$ is comparable to the intensity of the higher energy resonance. Relative to the pre-edge intensities, the intensity of feature 2 is decreased in $SiCH_3F_3$ compared to SiF_4. The intensity of peak 2 is further reduced in $Si(CH_3)_2F_2$ and $Si(CH_3)_3F$ relative to both the intensity of the higher energy resonance and the pre-edge intensities. The resonance observed ~5 eV above the Si 2*p* ionization threshold in fluorine containing fluoromethylsilane molecules is therefore certainly dependent upon the presence of the fluorine ligands surrounding the central Si atom.

The Si 2*p* continuum absorption spectra of all five fluoromethylsilane compounds exhibit a broad resonance ~20 eV above threshold. The intensity of the higher energy resonance relative to the pre-edge intensity is fairly constant for the fluorine containing molecules but increases for $Si(CH_3)_4$. The consistent positions, intensities and shapes of the high energy resonances for all five different molecules suggests that they are probably not the result of scattering of the photoelectron by the ligands.[42]

2.4.2.3. Si 2*s* pre-edge and continuum spectra

Photoabsorption spectra of the Si 2*s* pre-edge and continuum regions of the fluoromethylsilane molecules are presented in Fig. 2.4.4. Linear baselines, determined using background intensities at 150 and 190 eV, were subtracted

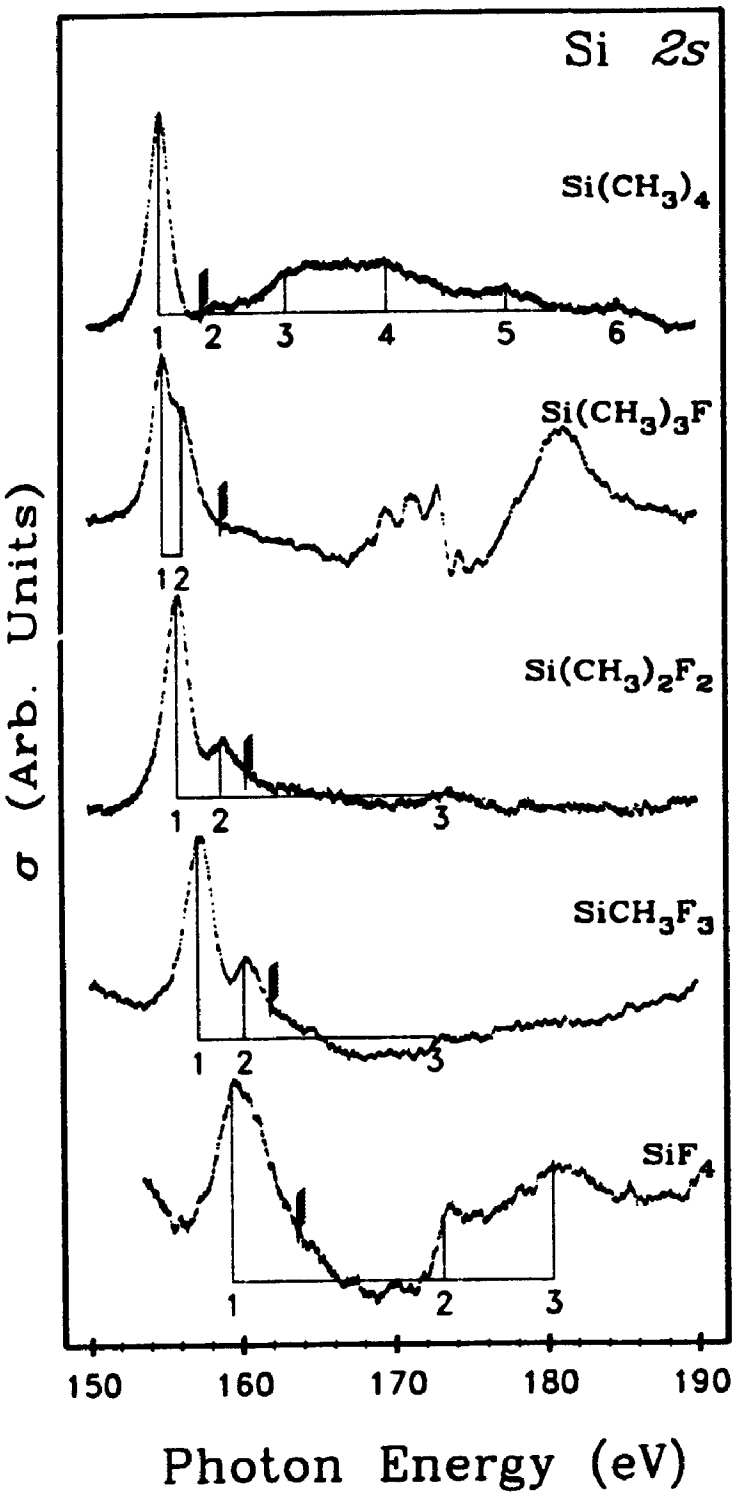

Figure 2.4.4: Photoabsorption spectra of the fluoromethylsilane compounds around the Si 2*s* ionization edges.

from the data for presentation purposes. Since the Si 2*s* spectral features of the fluoromethylsilane molecules are very weak, scatter in the data appears to be greatly amplified in Fig. 2.4.4. The spectra of SiF_4 and $SiCH_3F_3$ also appear to have curved backgrounds resulting from the curvature in the original backgrounds for these molecules (see Fig. 2.4.1). The Si 2*s* continuum features will not be discussed here since they could not be identified with any level of confidence.

The Si 2s pre-edge region of the SiF_4 absorption spectrum consists of a very broad asymmetric peak centered at ~159.3 eV as indicated in Table 2.4.1 (*c*). The feature has a term value of ~3 eV. This is consistent with a previously reported term value of 3.6 eV for the same feature.[84] The Si 1*s* absorption spectrum has three pre-edge features with term values of 6.0, 3.5 and 2.3 eV.[108,117] This is also consistent with the 2*s* results since the first peak at 6.0 eV is very weak and the Si 2*s* half-widths are greater than the Si 1*s* half-widths due to line broadening effects such as Coster-Kronig Auger transitions.[8] As a result of the increased line widths for the Si 2*s* spectrum, the two features observed in the Si 1*s* spectrum overlap into one peak. Electric dipole selection rules allow only for transitions to t_2^* final states from the a_1 Si 2*s* level in T_d symmetry.[151] The broad peak in the Si 2*s* pre-edge absorption spectrum is therefore assigned as unresolved transitions from the Si 2*s* level into one or more virtual orbitals of t_2^* symmetry.

The Si 2*s* pre-edge region of the absorption spectrum of $SiCH_3F_3$ has better resolution than the SiF_4 spectrum. Two features are observed with term values of 4.7 and 1.7 eV as indicated in Table 2.4.2 (*c*). The Si 2*s* level of the C_{3v} molecule $SiCH_3F_3$ has a_1 symmetry and hence the observed peaks could be due to transitions into a_1^* or e^* virtual orbitals. The improved resolution of the Si 2*s* pre-edge spectrum relative to the SiF_4 spectrum suggests that the poor resolution of the pre-edge in SiF_4 is due in part to overlapping bands and not entirely lifetime broadening effects such as Coster-Kronig transitions.

The Si 2*s* pre-edge spectrum of $Si(CH_3)_2F_2$ is very similar to tLat of $SiCH_3F_3$. There are two pre-edge peaks in the spectrum, 4.7 and 1.7 eV above the Si 2*s* ionization threshold (Table 2.4.3 (*c*)). In the C_{2v} molecule $Si(CH_3)_2F_2$, the Si 2*s* core has a_1 symmetry and hence transitions to a_1^*, b_1^*, and b_2^* virtual orbitals are all dipole allowed.

The Si 2*s* absorption spectrum of $Si(CH_3)_3F$ is dominated by the absorption spectrum of a contaminant in the continuum region. In the pre-edge region two peaks with term values of 3.8 and 2.5 eV (Table 2.4.4 (*c*)) are evident. Resolution of the pre-edge peaks appears to be equivalent to that observed in $SiCH_3F_3$ and $Si(CH_3)_2F_2$. The Si 2*s* core orbital has a_1 symmetry in the C_{3v} molecule $Si(CH_3)_3F$ and hence the pre-edge peaks could be due to transitions to a_1^* and e^* virtual orbitals.

Finally, the Si 2*s* absorption spectrum of $Si(CH_3)_4$ is also presented in Fig. 2.4.4. The pre-edge has one peak with a term value of 2.8 eV (Table 2.4.5 (*c*)) and a half-height width of ~2 eV. The shape and position of the pre-edge feature compares favourably with previous Si 2*s* [142] and Si 1*s* [108,117] results in which the pre-edge peak was assigned term values of 2.8 and 2.2 eV with respect to the Si 2*s* and Si 1*s* ionization edges respectively.

2.4.3. DISCUSSION: Assignment Using MS-Xα Results

Theoretical MS-Xα cross sections of the Si 2*p* and 2*s* pre-edge and continuum regions for the five fluoromethylsilane molecules are presented in simulated photoabsorption spectra and the results are summarized in Table 2.4.1 Table 2.4.5. As mentioned previously, the Si core level photoabsorption spectra of SiF_4 and $Si(CH_3)_4$ have been the subject of numerous previous experimental and theoretical studies, but controversy persists over the assignments of the peaks in the spectra. In this section, theoretical results are used in conjunction with the trends described in the previous section to assign all peaks in the spectra.

Trends observed in the spectra of the molecular series are important for making the assignments.

orbital assignment	term value	Q_{out} (%)	Q_{int} (%)	Q_{Si} (%)	Q_F (%)	oscillator strength	orbital type
$1a_1^*$	6.70	28.9	46.9	5.7	18.5	9.83×10^{-3}	anti.
$1t_2^*$	4.86	31.9	49.7	4.5	13.9	1.71×10^{-2}	anti.
$2a_1^*$	2.88	42.0	17.5	20.8	19.6	3.57×10^{-2}	mixed
$2t_2^*$	1.98	86.0	10.9	1.6	1.4	7.19×10^{-3}	mixed
$1e^*$	1.85	81.6	14.2	0.1	4.0	1.16×10^{-3}	mixed
$3a_1^*$	1.69	86.0	7.2	4.5	2.4	7.65×10^{-3}	mixed
$3t_2^*$	1.51	93.1	5.1	0.9	0.9	1.35×10^{-3}	Ryd. (d)
$4t_2^*$	1.09	92.7	6.0	0.9	0.4	3.14×10^{-3}	Ryd. (p)
$4a_1^*$	0.95	97.1	1.9	0.8.	0.2	1.30×10^{-3}	Ryd. (s)
$7t_2^*$	0.64	96.5	2.8	0.5	0.2	1.59×10^{-3}	Ryd. (p)

Table 2.4.6: Term values (eV), oscillator strengths and charge distributions calculated for the unoccupied orbitals of SiF_4.

orbital assignment	term value	Q_{out} (%)	Q_{int} (%)	Q_{Si} (%)	Q_F (%)	Q_C (%)	Q_H (%)	oscillator strength	orbital type
$1a_1^*$	4.34	50.3	30.3	8.2	6.2	5.0	0.3	2.89×10^{-3}	mixed
$1e^*$	3.32	38.5	30.8	14.1	9.5	3.6	3.5	1.00×10^{-2}	anti.
$2a_1^*$	2.66	70.7	17.9	2.7	6.5	1.4	0.3	1.77×10^{-3}	mixed
$2e^*$	1.90	72.4	7.4	14.3	3.3	1.1	1.4	1.13×10^{-2}	mixed
$3a_1^*$	1.80	82 1	3.6	6.9	4.7	2.6	0.1	4.12×10^{-3}	mixed
$4a_1^*$	1.55	92.3	4.3	1.5	1.7	0.2	0.0	1.37×10^{-3}	Ryd. (p+d)
$5e^*$	1.07	92.6	2.0	4.0	0.7	0.4	0.3	3.22×10^{-3}	Ryd. (p)
$6a_1^*$	1.04	84.5	1.6	6.8	3.8	3.2	0.1	5.30×10^{-3}	mixed
$11a_1^*$	0.67	89.8	1.7	4.1	1.9	2.4	0.1	3.47×10^{-3}	mixed
$16a_1^*$	0.46	94.6	1.2	2.1	0.8	1.3	0.0	1.73×10^{-3}	Ryd. (s+p)

Table 2.4.7: Term values (eV), oscillator strengths and charge distributions calculated for the unoccupied orbitals of $SiCH_3F_3$.

orbital assignment	term value	Q_{out} (%)	Q_{int} (%)	Q_{Si} (%)	Q_F (%)	Q_C (%)	Q_H (%)	oscillator strength	orbital type
$1b_2^*$	3.32	39.2	36.3	10.4	3.3	5.0	5.8	3.71×10^{-3}	anti.
$2a_1^*$	2.57	61.8	19.7	7.9	4.8	2.7	3.1	3.00×10^{-3}	mixed
$3a_1^*$	2.12	72.5	15.5	5.4	1.6	3.9	1.1	3.12×10^{-3}	mixed
$2b_2^*$	1.98	74.6	8.8	11.7	1.9	1.5	1.6	4.33×10^{-3}	mixed
$3b_2^*$	1.58	87.7	6.3	4.3	1.1	0.4	0.2	9.73×10^{-4}	mixed
$6a_1^*$	1.30	86.3	5.6	4.4	1.2	1.5	1.0	1.79×10^{-3}	mixed
$7a_1^*$	1.11	93.0	3.8	1.4	0.1	1.4	0.3	8.36×10^{-4}	Ryd. (p+d)
$4b_2^*$	1.10	93.5	2.1	3.0	0.4	0.7	0.3	1.07×10^{-3}	Ryd. (p)
$11a_1^*$	0.78	94.1	2.4	2.0	0.4	0.7	0.4	8.63×10^{-4}	Ryd. (p+d)
$3b_1^*$	0.94	93.6	3.6	0.7	0.8	1.1	0.3	7.21×10^{-4}	Ryd. (p)

Table 2.4.8: Term values (eV), oscillator strengths and charge distributions calculated for the unoccupied orbitals of $Si(CH_3)_2F_2$.

orbital assignment	term value	Q_{out} (%)	Q_{int} (%)	Q_{Si} (%)	Q_F (%)	Q_C (%)	Q_H (%)	oscillator strength	orbital type
$1a_1^*$	3.27	60.0	28.7	4.4	0.5	4.4	2.0	4.51×10^{-3}	mixed
$1e^*$	2.64	65.9	23.2	2.0	0.5	7.0	1.4	7.41×10^{-3}	mixed
$2e^*$	2.30	73.7	18.4	2.1	0.1	4.8	0.9	3.49×10^{-3}	mixed
$2a_1^*$	2.23	74.1	11.4	8.2	0.9	3.9	1.5	1.37×10^{-3}	mixed
$4a_1^*$	1.46	88.5	4.0	3.1	0.1	4.2	1.2	1.73×10^{-3}	mixed
$3e^*$	1.39	85.8	6.6	4.0	0.2	2.5	1.0	3.82×10^{-3}	mixed
$4e^*$	1.38	83.8	7.0	5.2	0.2	2.8	1.0	4.75×10^{-3}	mixed
$5a_1^*$	1.12	90.0	1.8	5.8	0.1	2.3	0.0	1.57×10^{-3}	Ryd. (p)
$9e^*$	0.61	94.2	2.6	1.8	0.0	1.0	0.4	1.70×10^{-3}	Ryd. (p)
$13a_1^*$	0.45	92.5	1.3	3.4	0.1	2.6	0.1	1.38×10^{-3}	Ryd. (s+f)

Table 2.4.9: Term values (eV), oscillator strengths and charge distributions calculated for the unoccupied orbitals of $Si(CH_3)_3F$.

2.4.3.1. Si 2*p* pre-edge

Numerous unoccupied levels, most very close to threshold, were found by the MS-Xα calculations for all five fluoromethylsilane molecules with energy searches to within 0.05 Rydbergs of the ionization thresholds using the converged Si 2*p* transition state potentials. Oscillator strengths (see section 2.1) were calculated for transitions from the Si 2*p* levels terminating at the identified virtual levels.

orbital assignment	term value	Q_{out} (%)	Q_{inter} (%)	Q_{Si} (%)	Q_C (%)	Q_H (%)	oscillator strength	orbital type
$1t_2^*$	2.09	79.4	15.7	0.5	3.2	1.1	6.98×10^{-4}	mixed
$2t_2^*$	1.44	89.6	8.4	0.6	0.8	0.5	1.28×10^{-3}	mixed
$3t_2^*$	1.11	88.7	8.2	1.5	0.9	0.7	1.97×10^{-3}	mixed
$4t_2^*$	0.93	93.8	4.3	0.9	0.7	0.2	1.37×10^{-3}	Ryd. (p+f)
$6t_2^*$	0.68	94.5	3.6	1.1	0.4	0.4	1.44×10^{-3}	Ryd. (d)
$7t_2^*$	0.60	96.7	2.2	0.5	0.5	0.1	6.82×10^{-4}	Ryd. (p)
$10t_2^*$	0.46	97.1	1.8	0.7	0.2	0.2	9.03×10^{-4}	Ryd. (d)
$14t_2^*$	0.33	98.3	1.0	0.5	0.1	0.1	5.80×10^{-4}	Ryd. (d)
$8a_1^*$	0.19	99.7	0.3	0.0	0.0	0.0	9.58×10^{-4}	Ryd. (s)
$9a_1^*$	0.15	98.9	0.0	0.5	0.7	0.0	4.56×10^{-4}	Ryd. (s)

Table 2.4.10: Term values (eV), oscillator strengths and charge distributions calculated for the unoccupied orbitals of $Si(CH_3)_4$.

All of the unoccupied orbitals were used to construct the theoretical Si $2p$ pre-edge photoabsorption spectra. Calculated eigenvalues, oscillator strengths and charge distributions of the ten unoccupied orbitals calculated to have the greatest oscillator strengths for the five fluoromethylsilane molecules are given in Table 2.4.6 - Table 2.4.10. The numbering of the virtual orbitals in Table 2.4.6 Table 2.4.10 begins at one for the virtual orbital manifolds of each symmetry to facilitate comparisons between molecules. The simulated Si $2p$ pre-edge spectra presented in Fig. 2.4.5 were calculated using the eigenvalues of the unoccupied levels, the corresponding oscillator strengths, a Si $2p$ spin-orbit splitting of 0.61 eV and a statistical 2:1 intensity ratio convoluted with a Lorentzian line shape with a half height width of 0.25 eV.

Agreement between theory and experiment varies from molecule to molecule, but is generally reasonably good. The MS-Xα results are not expected to identically reproduce the spectra, but rather to aid as guides in assigning the more obvious spectral features. When the calculated spectra reproduce the general shape of the experimental spectra, good agreement is thought to exist between the two data sets. The agreement between theory and experiment for

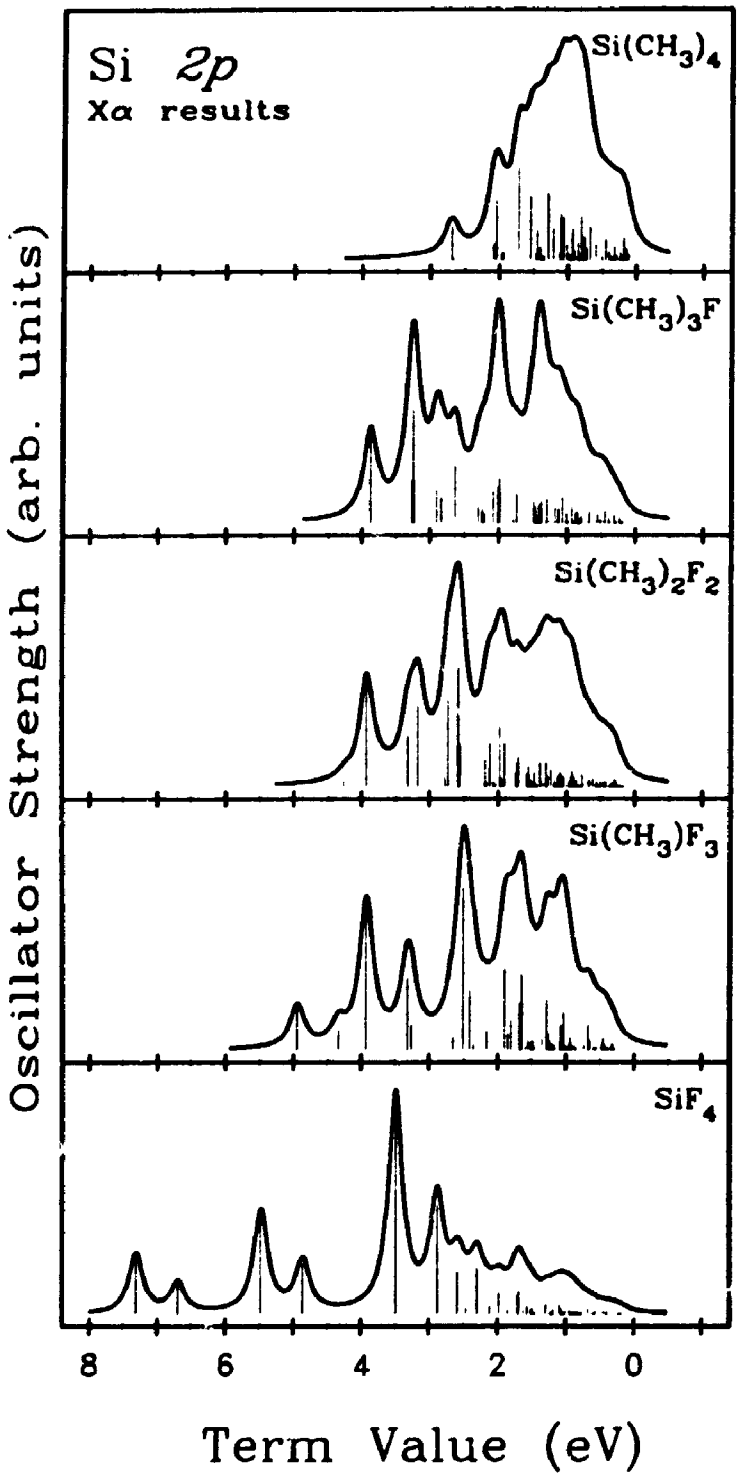

Figure 2.4.5: Simulated Si 2*p* pre-edge photoabsorption spectra for the fluoromethylsilane compounds constructed from the eigenvalues and oscillator strengths from the MS-Xα calculations.

the Si 2*p* spectrum of $SiCH_3F_3$ (Fig. 2.4.2 and Fig. 2.4.5) is good, with theory reproducing the number, positions and relative intensities of the peaks very well, especially if the position of the first doublet in the theoretical spectrum were shifted to overlap more strongly with the remainder of the spectrum. The line widths of the peaks in the simulated spectra are not a very good match for the experimental peaks and tend to skew the overall shape of the spectra. The 0.25 eV linewidth used in the simulation, which is considerably narrower than the ~0.4 eV experimental linewidth was selected to highlight the positions of the individual peaks. For $Si(CH_3)_2F_2$ (Fig. 2.4.5) below 3.5 eV, the number, intensity and positions of the peaks in the theoretical spectrum also match the experimental results reasonably well. Above 3.5 eV, resonances appear to be missing from the theoretical spectrum. Agreement is not quite as good for $Si(CH_3)_3F$ (Fig. 2.4.5) where the first two virtual levels need to be shifted by ~0.5 eV in order to reproduce the experimental spectrum. For $Si(CH_3)_4$, agreement between theory and experiment is also reasonably good, with the theoretical spectrum reproducing the general shape of the Si 2*p* pre-edge spectrum. Agreement is perhaps the poorest for SiF_4. Apart from the 2:1 intensity problem noted earlier for the first doublet (1-2), if the second spin-orbit doublet (3-4) were shifted by ~1eV to higher energy, then the number and position of the peaks, albeit not their intensities, would agree reasonably well with experiment.

The calculations roughly reproduce the convergence of peaks from SiF_4 to $Si(CH_3)_4$ noted earlier . Thus, the theoretical (experimental) range of term values (Table 2.4.1 (*c*) - Table 2.4.5 (*c*) and Fig. 2.4.5) decreases from 6.70 eV (4.96 eV) for SiF_4 to 4.34 eV (4.08 eV) for $SiCH_3F_3$ to 3.67 eV (4.05 eV) for $Si(CH_3)_2F_2$ to 3.27 eV (3.45 eV) for $Si(CH_3)_3F$ to 3.08 eV (3.46 eV) for $Si(CH_3)_4$. The differences between the predicted and observed shifts can be attributed to inaccuracies in the Xα method in dealing with the strong perturbations of the potential caused by the strongly electronegative ligands. The calculations also underestimate the intensity

of the first virtual orbital (usually an a_1^* orbital) to the total oscillator strength. This is best seen in the SiF_4 and $SiCH_3F_3$ spectra in Fig. 2.4.5.

Assignments of the experimental Si $2p$ spectra are given in Table 2.4.1 (a) - Table 2.4.5 (a) based on the simulated spectra from the MS-Xα parameters and considering the orbital characters from the charge distributions summarized in Table 2.4.6 - Table 2.4.10. Calculated orbitals with most of their charge density in the atomic spheres ($\Sigma Q_{\text{atomic}} > 50\%$) are assigned as antibonding orbitals while those with most of their charge density in the outersphere ($Q_{\text{out}} > 90\%$) are assigned as Rydberg orbitals. Orbitals with intermediate charge density distributions are assigned as orbitals with mixed antibonding-Rydberg character. The division is somewhat arbitrary, but a comparison of the assignments of the orbital characters based on the MS-Xα calculated charge distributions with the solid state spectra[148] indicates that in previous interpretations[109] too many virtual orbitals were being assigned as Rydberg orbitals. Comparison of the spectra of the solid compounds with those of the gas phase compounds provide an experimental measure of the valence/Rydberg character of the orbitals.[12,84,148]

The assignment of the pre-edge spectrum of SiF_4 will be described in detail before presenting a few select features from the other spectra. In SiF_4, the first two unoccupied levels ($1a_1^*$ and $1t_2^*$) have relatively large contributions from the intersphere region and significant contributions from the Si and F atomic spheres. This is characteristic of molecular orbitals with bonding or antibonding character and hence the first two levels, the $1a_1^*$ and $1t_2^*$ orbitals respectively, are assigned as Si-F antibonding orbitals. The third virtual orbital, $2a_1^*$, is calculated to have a charge distribution which is intermediate between that expected of an antibonding level and that of a Rydberg level. The $2a_1^*$ orbital is therefore assigned as an orbital of mixed valence - Rydberg character. The $2t_2^*$, $1e^*$ and $3a_1^*$ virtual orbitals of SiF_4 are also assigned as orbitals with mixed antibonding-Rydberg character. The remaining unoccupied orbitals in Table 2.4.6 are assigned

as Rydberg orbitals based on their charge distributions. The assignment for the Si 2*p* pre-edge absorption spectrum of SiF_4 based on the above MS-Xα results is similar to that proposed previously by Friedrich *et al.*[84] The assignment is summarized in Table 2.4.1. Peaks 1 and 2 on the SiF_4 absorption spectrum in Fig. 2.4.2 are assigned to correspond to transitions from the spin orbit split Si 2*p* orbitals into the $1a_1^*$ virtual orbital. Peak 3 corresponds to the $2p_{3/2}$ component of an excitation to the $1t_2^*$ orbital while 4 has the corresponding $2p_{1/2}$ component overlapped with the $2p_{3/2}$ component of the transition to the $2a_1^*$ orbital. Peak 5 has contributions from the $2p_{1/2}$ component of the $2a_1^*$ mixed orbital and the $2p_{3/2}$ component of the $2t_2^*$ and $1e^*$ mixed character orbitals. Peak 6 has contributions from the $2p_{1/2}$ components of these mixed orbitals plus the $3t_2^*$ orbital with Rydberg character. The other peaks in the absorption spectrum are assigned as transitions to Rydberg orbitals as indicated in Table 2.4.1. The valence/Rydberg characters of the terminating orbitals are in good accord with the assignments based on a comparison with the experimental spectra of the solid compounds.[148] While transitions to Rydberg orbitals are not expected to contribute significant intensity to the pre-edge photoabsorption spectra of molecules with strong potential barriers, it has been suggested recently that transitions from core orbitals to Rydberg levels may have appreciable intensity for non-hydride molecules since the Rydberg wavefunctions can penetrate into the inner well of the molecular potential.[90]

The proposed ordering of the first two unoccupied levels in SiF_4, $3a_1^*$ and $4t_2^*$, is consistent with previous calculations.[84] Furthermore, the separation between the $1a_1^*$ and $1t_2^*$ levels is similar in both calculations, even though different theoretical methods were used. The ordering is also consistent with a recent DV-Xα calculation for SiF_4 which found a_1^* and t_2^* virtual orbitals below the ionization threshold.[152] The assignment of the multiplet structure in the Si 2*p* pre-edge absorption spectrum of SiF_4 is in agreement with one previously reported

assignment[84] but differs from the assignment of Bodeur *et al.*[108] In their assignment of the Si 2*p* pre-edge region of SiF_4, Bodeur *et al* propose that, upon excitation of the Si 2*p* core electron, the molecule undergoes a distortion to a C_{3v} trigonal bipyramidal excited state which results in the splitting of the t_2^* antibonding orbital into three orbitals of lower symmetry, an a_1^* and two e^* orbitals, and results in the multiplet of peaks observed below the Si 2*p* threshold. These MS-Xα results indicate that Si 2*p* → Rydberg transitions have appreciable intensity in SiF_4 and can account for the additional bands in the Si 2*p* absorption spectrum without invoking large deformations[108] of the molecular geometry in order to account for all of the peaks.

Term values, oscillator strengths and calculated charge distributions for the virtual orbitals of the other fluoromethylsilane molecules are given in Table 2.4.7 – Table 2.4.10 and assignments of the eight peaks (six spin-orbit doublets) are given in Table 2.4.2 (*a*) – Table 2.4.5 (*a*). Most of the unoccupied orbitals have large contributions to the charge distribution from the outersphere region indicating that they are either Rydberg orbitals or mixed antibonding/Rydberg orbitals. For example, in $SiCH_3F_3$ only the $1e^*$ virtual orbital has a large enough contribution from the atomic spheres to be classified as an antibonding orbital. For $Si(CH_3)_2F_2$, only the $1b_2^*$ virtual orbital has been classified as an antibonding orbital (Table 2.4.8). After substitution of three methyl groups the outersphere contribution to all virtual orbitals is large and thus for $Si(CH_3)_3F$ and $Si(CH_3)_4$, all peaks correspond to transitions to mixed antibonding-Rydberg or Rydberg virtual orbitals.

2.4.3.2. Si 2*p* continuum

Silicon 2*p* cross sections for the five fluoromethylsilane molecules were calculated using the appropriate Si 2*p* transition state potentials. The resulting theoretical cross sections along with the partial channel contributions are presented

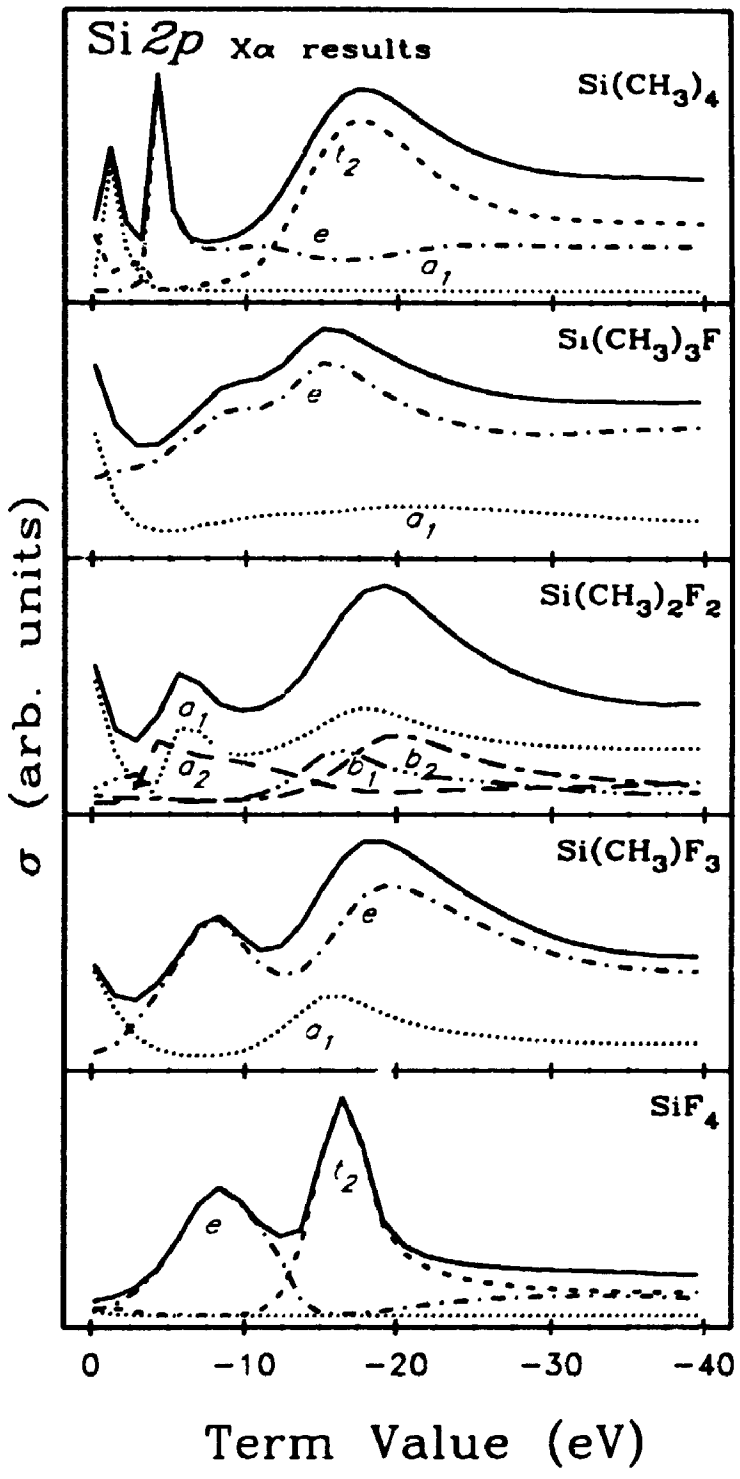

Figure 2.4.6: Theoretical Si 2*p* cross sections of the fluoromethylsilane compounds from the MS-Xα calculations.

in Fig. 2.4.6. Different outgoing channels are allowed for the ionized Si 2*p* photoelectron in the five molecules as a result of the three different symmetry groups; T_d for SiF_4 and $Si(CH_3)_4$; C_{3v} for $SiCH_3F_3$ and $Si(CH_3)_3F$; and C_{2v} for $Si(CH_3)_2F_2$. Symmetry channels contributing to theoretical cross section maxima are indicated on the figure and corresponding assignments of the experimentally observed resonances are provided in Table 2.4.1 (*b*) - Table 2.4.5 (*b*).

Agreement between the calculated cross sections and the experimental Si 2*p* spectra ranges from good to excellent. The intensities and positions of the experimentally observed resonances in the Si 2*p* continuum spectrum of $Si(CH_3)_2F_2$ are well reproduced in the theoretical spectrum. The calculated spectra for $SiCH_3F_3$ and $Si(CH_3)_3F$ have maxima at approximately the same positions as those observed experimentally (Fig. 2.4.3), but the relative intensities are not in quantitative agreement. The theoretical results for SiF_4 and $Si(CH_3)_4$ are in good agreement with the experimental results, reproducing both the number and approximate energies of the resonances. These theoretical results were used to assign features in the Si 2*p* continuum spectra of the fluoromethylsilane molecules. Eigenphase sum changes were used along with Kriele's criterion that a cross section enhancement must be accompanied by a change in the eigenphase sum of $\geq 0.3\pi$ over <6 eV in order to classify it as a *shape resonance.*[153] Eigenphase sum changes accompanying the cross section enhancements are summarized in Table 2.4.1 (*b*) - Table 2.4.5 (*b*).

The five theoretical Si 2*p* continuum cross sections in Fig. 2.4.6 are all relatively similar, exhibiting peaks near threshold, ~5-9 eV above threshold, and ~17-20 eV above threshold. The trends in both experimental and theoretical intensities are very important in obtaining a physical interpretation of all three resonances. The peak near threshold in the theoretical spectra consists of a peak in the ka_1 symmetry channel for all five fluoromethylsilane molecules, with contributions from the kb_2 channel in $Si(CH_3)_2F_2$. This is not consistent with a previous report

for $Si(CH_3)_4$ where the resonance near threshold was assigned as a transition from the Si $2p$ orbitals into an e^* virtual level.[142] The previous assignment was based upon potential barrier model arguments, while we do not invoke this model to explain these resonances. Sudden changes in the eigenphase sums accompany all of the low energy cross section maxima, satisfying Kriele's criterion for a shape resonance.[153] The intensities of the theoretical resonances near threshold increase with the number of methyl ligands in the molecule. This is consistent with the experimental spectra (Fig. 2.4.3), where the relative intensity of the first cross section enhancement above the Si $2p$ threshold increases as the number of methyl groups in the compound increases. This observation in both the theoretical and experimental results suggests that the resonances slightly above the Si $2p$ threshold in the photoabsorption spectra of the five fluoromethylsilane molecules are related to the presence of the Si – C bonds. These resonances are possibly due to transitions into Si – C antibonding orbitals lying just above threshold. The pre-edge calculations are consistent with this assignment, since only the Si – F antibonding orbitals were found in the bound state. The split resonance near threshold in the calculated Si $2p$ continuum cross section of $Si(CH_3)_4$ is also consistent with this assignment, since in tetrahedral symmetry the Si – C antibonding orbitals split into two components. These low energy resonances are therefore assigned as shape resonances due to Si – C virtual orbitals. Similar assignments have been proposed for low energy resonances in the CF_3X [14] molecules. Antibonding C–F orbitals above threshold in CF_3X molecules were found to be responsible for low energy resonances in a valence electron partial cross section study.

Medium energy resonances, ~5-9 eV above threshold, occur in the $k\sigma$ symmetry channels of the four T_d and C_{3v} molecules, and in the ka_1 and ka_2 channels in $Si(CH_3)_2F_2$. The ke representation of the T_d and C_{3v} groups transforms as the ka_1 and ka_2 representations of the C_{2v} symmetry group, and

hence the medium energy resonance can be said to occur in the *ke* channel for all five fluoromethylsilane molecules. This assignment is consistent with previous results for SiF_4 [84,85,147,152,154] and $Si(CH_3)_4$,[142] where the resonances ~5 eV above threshold were assigned as resonances in the *ke* channels. The calculated medium energy cross section enhancements are all accompanied by changes in the eigenpha. ° sums, as indicated in Table 2.4.1 (*b*) – Table 2.4.5 (*b*), and hence they correspond to shape resonances according to Kriele's criteria.[153] Intensity patterns in theoretical cross sections of the second continuum peak are consistent with the experimental results, with a decrease in relative intensity as the fluorine ligands are replaced with methyl ligands. The intensity of the medium energy peak in the theoretical spectrum of $Si(CH_3)_4$ is anomalous but it is thought to be the result of splitting of the Si–C antibonding orbital as described above. The medium energy cross section enhancements above the Si 2*p* edges of the fluorine containing fluoromethylsilane molecules are assigned to be due to trapping of the *d* continuum channels by the potential barriers created by the strongly electronegative fluorine atoms. They are therefore assigned to be shape resonances due to ligand induced potential barriers. The intensity pattern of the medium energy resonances are consistent with this assignment, since the intensity is largest for SiF_4 and smallest for $Si(CH_3)_3F$. The electropositive methyl groups present a lower barrier for trapping the *d* waves and hence the intensity of the resonances are proportional to the number of fluorine atoms.

The high energy resonances, ~20 eV above threshold, in the calculated cross sections of the fluoromethylsilane molecules occur in the kt_2 symmetry channels, or in corresponding channels for molecules with other than T_d symmetry, for all five molecules except $Si(CH_3)_4$. The energies of the cross section maxima for each of the symmetry channels are summarized in Table 2.4.1 (*b*) – Table 2.4.5 (*b*). Only the kt_2 channel of SiF_4 and the *ke* channel of $SiCH_3F_3$ exhibit shape resonance behavior[153] with sudden changes in their eigenphase sums. This

assignment is consistent with previous studies which have identified a resonance in the kt_2 channel ~20 eV above the Si 2*p* ionization threshold in SiF_4.[84,85,147,152,154] Previously, results from other silicon spectra were used to assign the cross section maximum approximately 20 eV beyond the Si 2*p* threshold in the Si 2*p* spectrum of $Si(CH_3)_4$ as a resonance in the kt_2 channel. This previous assignment was not based upon theoretical calculations, but rather on a comparison with spectra of other tetrahedral silicon compounds. The origin of the high energy resonances occurring at the same approximate energy in the Si 2*p* photoabsorption spectra of all five fluoromethylsilane molecules is not apparent from either the combined experimental or theoretical data. Photoabsorption spectra above the Si 2*p* ionization edges of other silicon compounds exhibit similarly shaped peaks in the same energy region.[142,154] A calculated Si 2*p* spectrum for atomic silicon also has a broad peak centered ~20 eV above the ionization threshold.[154] The peak position of the high energy peak does not vary significantly in any of the compounds, hence it cannot logically be attributed to any bond length dependence. The similarities between different molecular and even the atomic cross sections therefore suggest that these higher energy peaks, ~20 eV above the Si 2*p* threshold are the result of a delayed onset of the $2p \rightarrow \varepsilon d$ transition, in agreement with previous results for SiH_4 and atomic silicon.[71,154]

2.4.3.3. Si 2*s* pre-edge

In a method analogous to the one used to calculate the theoretical Si 2*p* pre-edge spectra, unoccupied levels were identified with energy searches to within 0.05 Rydbergs of the Si 2*s* ionization thresholds using converged Si 2*s* transition state potentials for all five fluoromethylsilane molecules. Eigenvalues and oscillator strengths from the MS-Xα calculations were used to construct the theoretical spectrum after convolution with a Lorentzian line shape with a half height width of 1.0 eV. The simulated Si 2*s* pre-edge spectra are presented in Fig. 2.4.7.

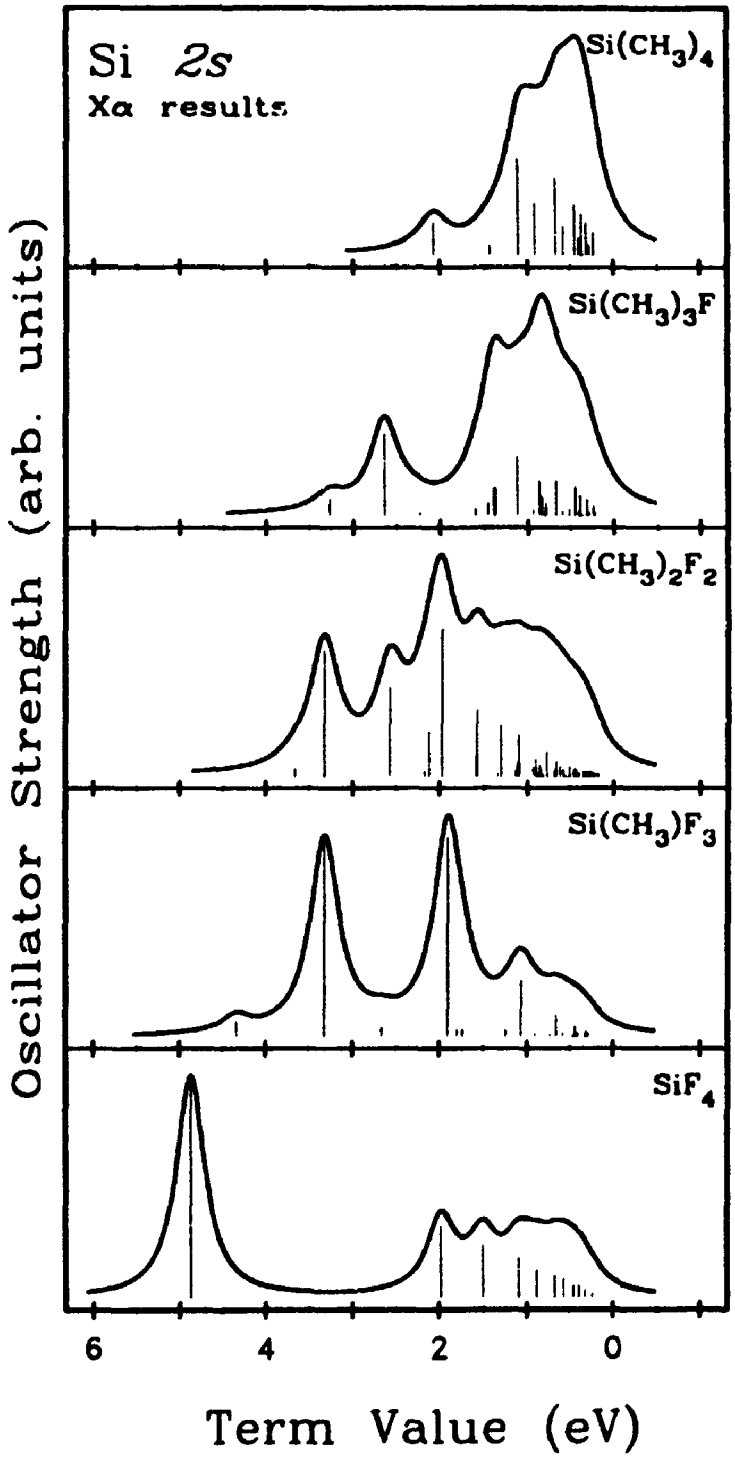

Figure 2.4.7: Simulated Si 2*s* pre-edge photoabsorption spectra for the fluoromethylsilane compounds constructed from the eigenvalues and oscillator strengths from the MS-Xα calculations.

Experimental photoabsorption spectra of the Si 2*s* pre-edge regions of the fluoromethylsilane compounds in Fig. 2.4.4 are generally simple exhibiting only one or two peaks. The theoretical Si 2*s* spectra in Fig. 2.4.7 roughly reproduce this simplicity with two groups of peaks, one at higher term value and the other closer to threshold. The peaks at higher term value gradually merge with the peaks closer to threshold as the number of methyl ligands in the molecule is increased. The intensity of the higher term value peaks also decreases with a decreasing number of fluorine ligands. This roughly reproduces, albeit exaggerates, the experimental trend observed, where the intensity of the peak closer to threshold increases with the number of methyl ligands in the compound.

The MS-Xα calculations indicate that transitions from the Si 2*s* levels into antibonding and mixed antibonding-Rydberg orbitals produce the more intense peaks while transitions into orbitals with Rydberg character result in less intense contributions to the spectra. The assignments of the experimental spectra are summarized in Table 2.4.1 (*c*) - Table 2.4.5 (*c*) for SiF_4 - $Si(CH_3)_4$ respectively.

2.4.3.4. Si 2*s* continuum

The Si 2*s* continuum cross sections of the five fluoromethylsilane molecules were calculated using the Si 2*s* transition state potentials. Resulting cross sections and partial channel contributions are presented in Fig. 2.4.8. It is difficult to compare the theoretical curves with the experimental data owing to the weak nature of the Si 2*s* continuum features and the poor signal to noise ratio of the experimental data (Fig. 2.4.4). The positions of the experimental and theoretical cross section maxima are given in Table 2.4.1 (*c*) - Table 2.4.5 (*c*) along with assignments of the contributing channels. For SiF_4 (Table 2.4.1 (*c*)) and $Si(CH_3)_4$ (Table 2.4.5 (*c*)) only the kt_2 outgoing channel is allowed by the electric dipole selection rules.[151] The positions of the resonances in the theoretical

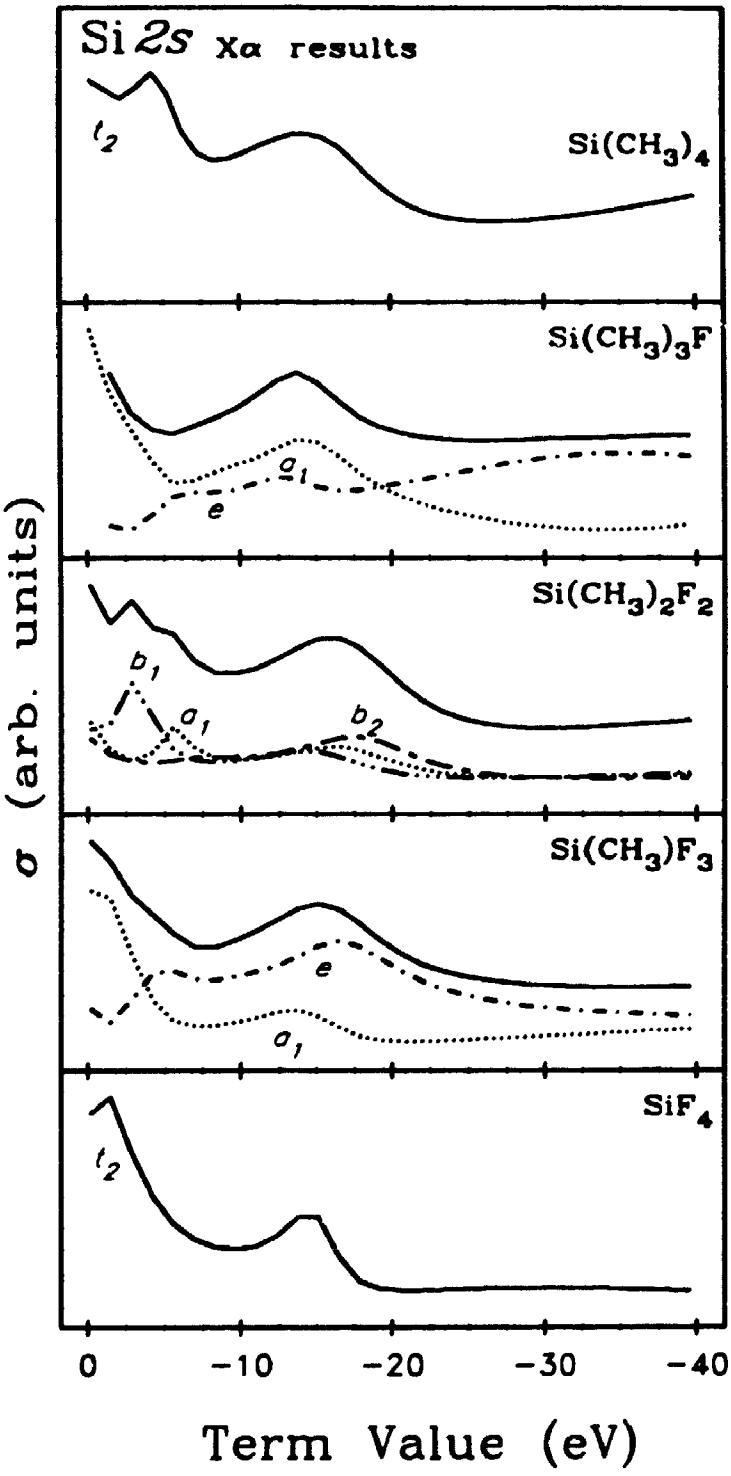

Figure 2.4.8: Theoretical Si 2*s* cross sections of the fluoromethylsilane compounds from the MS-Xα calculations.

cross sections correlate reasonably well with the theoretical positions of the high energy resonances above the Si $2p$ ionization edges.

2.5. RESULTS: Chloromethylsilane Compounds, $Si(CH_3)_xCl_{4-x}$

2.5.1. Experimental Photoabsorption Spectra

Photoabsorption spectra of the five chloromethylsilane molecules are presented in Fig. 2.5.1 over the photon energy range 100 - 220 eV which encompasses the discrete and continuum regions of the Si 2*p*, Si 2*s* and Cl 2*p* edges for all five molecules. The $Si(CH_3)_4$ spectrum was terminated at a photon energy of 200 eV since it has no Cl 2*p* ionization edge. Ionization edges for the Si 2*p* and Si 2*s* core levels of each molecule are indicated on the experimental curves, with the flag at lower energy corresponding to the averaged Si 2*p* ionization potential and the higher energy mark indicating the Si 2*s* ionization edge. The values used were from available core level photoelectron spectra in the literature.[145]

The spectra in Fig. 2.5.1 illustrate several features of the core-level photoabsorption spectra of the chloromethylsilane molecules. First, the spectra are all similar with series of strong absorption peaks below the Si 2*p* ionization edges (~100–110 eV) and much broader structure above the Si 2*p* edges. A single relatively strong absorption peak, with some fine structure, is observed below each Si 2*s* edge and weak structure is seen in the Si 2*s* continua, although it is stronger than the corresponding structure in the spectra of the fluoromethylsilane compounds. Below the Cl 2*p* edges, series of sharp peaks are seen merging into the continua which exhibit maxima at or just above threshold. Second, the Si 2*p*, Si 2*s* and Cl 2*p* spectra are all superimposed on the decreasing valence cross section as evidenced by the sloping cross section below the Si 2*p* pre-edge structure. The valence cross sections are not as noticeable as in the fluoromethylsilane compounds, where the strongly sloping background from the fluorine inner-valence orbital ionization continua dominates the photoabsorption spectrum of SiF_4 (Fig. 2.4.1). Finally, only the spectrum for $Si(CH_3)_4$ has a noticeable "step" at ~140 eV due to improper normalization of the second order C 1*s* photoabsorption.

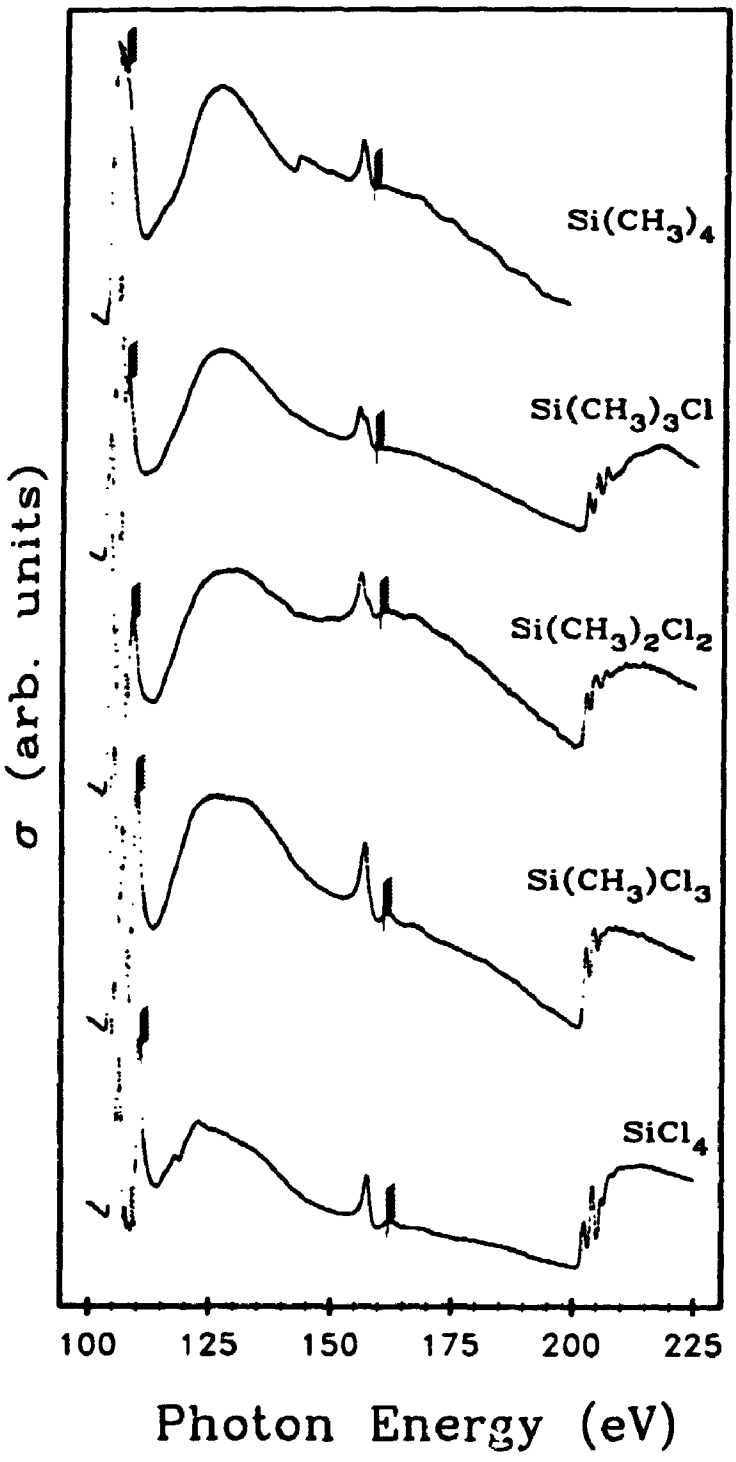

Figure 2.5.1: Photoabsorption spectra of the chloromethylsilane compounds around the Si 2*p*, Si 2*s* and Cl 2*p* ionization edges.

Resonances in the discrete and continuum regions of the Si 2*p*, Si 2*s* and Cl 2*p* core-level ionization edges are discussed in detail in the following sections. The photoabsorption spectra of the Si 2*p* core-levels of the chloromethylsilane compounds are rich in structure, with numerous discrete and continuum resonances.

2.5.1.1. Si 2*p* pre-edge spectra

High resolution photoabsorption spectra of the Si 2*p* pre-edge regions of the five chloromethylsilane molecules are presented in Fig. 2.5.2. The spin-orbit split Si 2*p* ionization potentials are indicated by the broken lines on the figure. Values for the Si 2*p* ionization potentials and the positions of the indicated features are given in the tables in this section. These spectra exhibit similar trends to those seen for the fluoromethylsilane molecules in the preceding section. First, the range of term values decreases by ~0.7 eV with each substitution of a methyl ligand for a chlorine atom around the central silicon atom from 5.9 eV in $SiCl_4$ to 3.15 eV in $Si(CH_3)_4$. The empty orbitals into which the Si 2*p* electrons are excited are therefore closer to the vacuum level for the chloromethylsilane molecules with a larger number of methyl ligands. It is surprising that the term values of the first absorption features in the Si 2*p* pre-edge photoabsorption spectra of the chloromethylsilane molecules are always greater than those for the corresponding fluoromethylsilane molecules (compare Tables 2.4.1 (*a*) - 2.4.5 (*a*) with 2.5.1 (*a*) 2.5.5 (*a*)). The first unoccupied orbitals in the chloromethylsilane molecules are therefore more strongly bound than the corresponding orbitals in the fluoromethylsilane molecules. Second, in a manner analogous to that seen for the fluoromethylsilane molecules, the relative intensities of the first pair of absorption peaks are roughly proportional to the number of chlorine atoms in the molecule. The 1-2 spin-orbit doublet is the most intense feature in the spectra of $SiCl_4$ and $SiCH_3Cl_3$ but is of equal intensity to other features in the $Si(CH_3)_2Cl_2$ Si 2*p* pre-edge spectrum and is

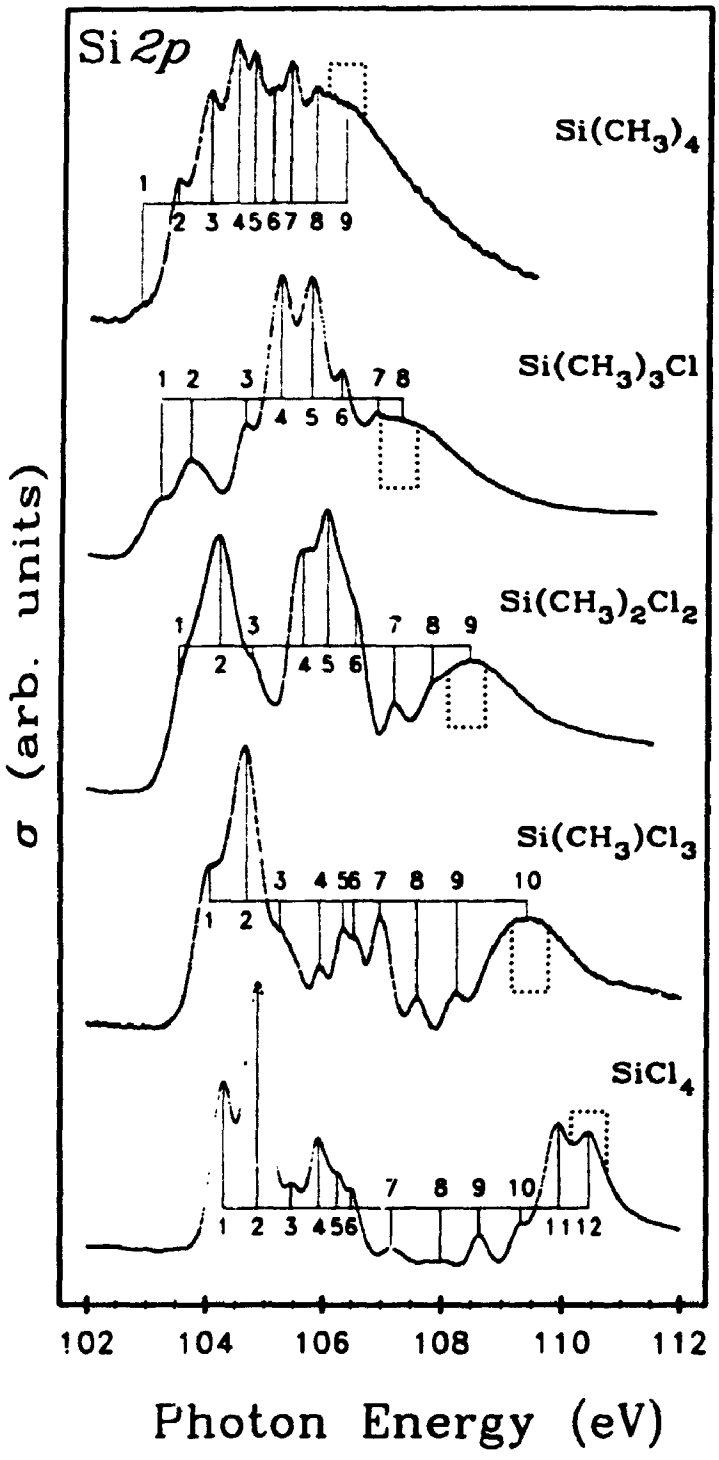

Figure 2.5.2: Photoabsorption spectra of the Si 2*p* pre-edge regions of the chloromethylsilane compounds.

of much lower intensity in the $Si(CH_3)_3Cl$ photoabsorption spectrum. There is also a spin-orbit doublet peak whose relative intensity follows the number of methyl groups in the molecules. Peaks 5-7 in the Si $2p$ photoabsorption spectrum of $Si(CH_3)Cl_3$, 4-6 in $Si(CH_3)_2Cl_2$ and 4-5 in $Si(CH_3)_3Cl$ increase in relative intensity with the number of methyl ligands, as well as shifting closer to threshold. The Si $2p$ pre-edge photoabsorption spectra of the chloromethylsilane molecules are similar to each other and to the corresponding spectra for the fluoromethylsilane molecules. The spectra of $Si(CH_3)_3Cl$ and $Si(CH_3)_3F$ are very similar, but as the electronic structure of these molecules are dominated by the three methyl ligands this is not unexpected.

The Si $2p$ pre-edge photoabsorption spectrum of $SiCl_4$ shown in Fig. 2.5.2, has been studied in detail in several previous reports,[90,108,118,149,152] and the spectrum of the condensed sample has also been measured.[155] The spectrum consists of an intense spin-orbit split peak (1-2) at low photon energy followed ~2 eV above by a series of peaks (3-6) with medium intensity and a pair of strong absorption peaks near threshold (11-12). There are also some very weak peaks (7-10) at intermediate photon energies. The positions (photon energies) and term values of the 12 peaks labelled on the $SiCl_4$ Si $2p$ pre-edge spectrum in Fig. 2.5.2 are given in Table 2.5.1 (*a*) along with the Si $2p_{3/2}$ and Si $2p_{1/2}$ ionization edge positions and a comparison with the available previous results. There is a good correlation between the peak positions presented here and these reported earlier by Fomichev et al.[118] The correlation is not as good for the other previous results of Zimkina et al.[10]

The labeled peaks in the $SiCl_4$ Si $2p$ pre-edge spectrum (Fig. 2.5.2) have been grouped into spin-orbit split pairs by considering the term values of the peak positions with respect to both the Si $2p_{3/2}$ and Si $2p_{1/2}$ ionization edges (see Table 2.5.1 (*a*)). Using the criteria that the term values of the $2p_{3/2}$ and $2p_{1/2}$ components of a spin-orbit pair differ by no more than 0.1 eV, eight spin-orbit

(a) Si 2p pre-edge

peak label	energy (eV)	energy (eV)†	energy (eV)‡	term value (eV)		assignments		
				$Si2p_{3/2}$	$Si2p_{1/2}$	resonance		$Si2p_{3/2} \rightarrow$
1	104.30	103.96	103.0	5.87	6.46	a		$1a_1^*$
2	104.88	104.57	103.5	5.29	5.88	b	a	
3	105.46	105.15	-	4.71	5.30	c	b	
4	105.93	105.60	104.7	4.24	4.83	d	c	$1t_2^*$
5	106.25	-	-	3.92	4.51		?	-
6	106.49	106.00	105.2	3.68	4.27	e	d	
7	107.17	106.80	-	3.00	3.59		e	-
8	107.99	107.50	107.1	2.18	2.77	f		$3t_2^*$
9	108.63	108.18	108.5	1.54	2.13	g	f	
10	109.32	108.80	-	0.85	1.44	h	g	
11	109.95	109.40	-	0.22	0.81	i	h	$8e^*$
12	110.45	109.90	-	−0.28	0.31		i	-
$Si2p_{3/2}$	110.16	-	-	-	-	-	-	-
$Si2p_{1/2}$	110.77	-	-	-	-	-	-	-

† Ref. 118
‡ Ref. 10

(b) Si 2p continuum

peak label	energy (eV)	term value (eV)	calc. term value (eV)	phase shift (π)	symmetry channel
1	111.5	−0.9	−0.5	0.5	ke
2	115.2	−4.6			
3	117.2	−6.9	−9.3	1.6	kt_2
4	119.7	−9.1			
5	122.5	−11.9	−13.4	0.8	ke
6	134.0	−23.4	−18.5	0.5	kt_2

(c) Si 2s

peak label	energy (eV)	term value (eV)	Si 1s term value (eV)§	calc. term value (eV)	phase shift (π)
1	154.4	7.4			-
2	156.8	5.0	4.8	3.88	-
Si2s	161.8	-	-	-	-
3	161.9	-0.1	-0.4	-0.1	0.5
4	168.0	-7.2	-7.2	-9.3	1.6
5	173.2	-11.4	-11.3		
6	181.5	-19.7	-21.4	-18.5	0.5

§ Ref. 120

Table 2.5.1: Energies, term values and assignments of the discrete and continuum resonances in the Si 2*p* and 2*s* photoabsorption spectra of $SiCl_4$

pairs can be identified; 1-2, 2-3, 4-6, 6-7, 8-9, 10-11, and 11-12. The intensity of peak 4 is much larger than that of its spin-orbit paired peak, 6, which is not consistent with the other peaks in the pre-edge spectrum of $SiCl_4$ where the $2p_{3/2}$ and $2p_{1/2}$ peaks are of comparable intensity. It is therefore likely that peak 4 also has contributions from the Si $2p_{1/2}$ component of another pair of peaks, which would necessarily also involve a peak with a position close to peak 3. The pair 3-4 has therefore also been identified. Peak 5 could be the Si $2p_{1/2}$ component with an unresolved Si $2p_{3/2}$ component between peaks 3 and 4. The nine spin-orbit split resonances assigned to the Si $2p$ pre-edge photoabsorption spectrum of $SiCl_4$ based on the above arguments are summarized in Table 2.5.1 and indicated with the letters a–i. While it is possible that some of the spin-orbit pairs identified could result from spurious spacing of adjacent peaks by ~0.6 eV, the intensity patterns of the peaks are consistent with the assignment of 9 or 10 spin-orbit split discrete resonances to the Si $2p$ pre-edge photoabsorption spectrum of $SiCl_4$.

It seems unlikely that better photon resolution will be able to resolve the Si $2p$ pre-edge photoabsorption spectrum of $SiCl_4$ any more clearly than the spectrum presented in Fig. 2.5.2. The peaks in the $SiCl_4$ photoabsorption spectrum, which have half-height widths of $\gtrsim$0.3 eV, are considerably broader than the ~0.1 eV photon resolution used to measure the spectrum. The observed breadth of the peaks probably results from vibrational broadening of the core hole state as observed in the Si $2p$ photoelectron spectrum of $SiCl_4$.[156] The Si $2p$ photoelectron lines of $SiCl_4$ were found to have a FWHM (full-width at half maximum) of ~0.3 eV, with most of that width resulting from unresolved vibrational states (see Chapter 3). The spacing of the Si–Cl vibrational levels, estimated to be ~0.065 eV (from the equivalent-core model[157]), is on the same order as the lifetime limited natural line width of the Si $2p$ core hole which was found to be ~0.045 eV for SiH_4.[146] Based on observations of similar linewidths in the Si $2p$ photoelectron spectrum of SiF_4,[146,156] similar natural linewidths are expected for $SiCl_4$. Even

with much better photon resolution it will therefore not be possible to resolve any of the overlapping transitions assigned in the Si 2*p* pre-edge photoabsorption spectrum of $SiCl_4$ presented here.

The Si 2*p* pre-edge photoabsorption spectrum of $SiCH_3Cl_3$ is also presented in Fig. 2.5.2 with the Si 2*p* ionization edges indicated on the figure by the broken lines. A photoabsorption spectrum of the Si 2*p* pre-edge region of $SiCH_3Cl_3$ has been reported previously by Fomichev et al with similar resolution[118] and it is in very good overall agreement with the spectrum reported here. The Si 2*p* pre-edge photoabsorption spectra of $SiCl_4$ and $SiCH_3Cl_3$ are similar in overall shape as well. A pair of strong absorption peaks (1-2) are observed at low photon energy followed by peaks of medium intensity (3-7), two weak peaks at intermediate photon energy and a relatively strong absorption maximum at threshold. The principal difference between the overall Si 2*p* pre-edge spectra of $SiCl_4$ and $SiCH_3Cl_3$ is the extent of the pre-edge spectrum, from the position of the first resonance to the ionization edge. The range of term values in the $SiCl_4$ pre-edge spectrum is ~0.7 eV greater than the corresponding range in the $SiCH_3Cl_3$ spectrum where the peaks are therefore more closely spaced. Positions (photon energies) and term values of the ten peaks indicated on the $SiCH_3Cl_3$ spectrum in Fig. 2.5.2 are summarized in Table 2.5.2 (*a*) along with the Si $2p_{3/2}$ and Si $2p_{1/2}$ ionization energies. Peak positions from the previously reported $SiCH_3Cl_3$ Si 2*p* pre-edge photoabsorption spectrum are also included for comparison.[118] In Fomichev's spectrum, peaks 4-6 were not individually resolved and hence only the averaged value was reported for their positions. An error in the previous data is apparent upon comparison of the term values in Table 2.5.2 as the differences between the two sets of data shift from 0.46 eV for peak 1 to 0.7 eV for peak 10. A error in the calibration function used for the monochromator in the previous study is probably responsible for the differences. The correspondence between the final peak position in the Si 2*p* pre-edge photoabsorption spectra with the Si 2*p* ionization potentials measured

(a) Si 2p pre-edge

peak label	energy (eV)	energy (eV)†	term value (eV)		assignments		
			$Si2p_{3/2}$	$Si2p_{1/2}$	resonance		$Si2p_{3/2} \rightarrow$
1	104.06	103.7	5.10	5.71	a		$1a_1^*$
2	104.68	104.2	4.48	5.09	b	a	$2a_1^*$
3	105.26	104.95	3.90	4.51	c	b	$1e^*$
4	105.95	-	3.21	3.82	d	c	$3a_1^*$
5	106.34	105.8	2.82	3.43	e		$4a_1^*$
6	106.53	-	2.63	3.24		d	-
7	106.97	106.4	2.19	2.80	f	e	$5a_1^*$
8	107.58	107.0	1.58	2.19	g	f	$8a_1^*$
9	108.25	107.55	0.91	1.52		g	-
10	109.40	108.7	-0.24	0.37		h	-
$Si2p_{3/2}$	109.16	-	-	-	-	-	-
$Si2p_{1/2}$	109.77	-	-	-	-	-	-

† Ref. 118

(b) Si 2p continuum

peak label	energy (eV)	term value (eV)	calc. term value (eV)	phase shift (π)	symmetry channel
1	111.0	−0.4	−0.5	0.5	ke
2	122.0	−12.4	−13.4	1.0,0.5	$ke+ka_1$
3	133.5	−23.9	−19.5	0.2,1.0	$ke+ka_1$

(c) Si 2s

peak label	energy (eV)	term value (eV)	Si 1s term value (eV)‡	calc. term value (eV)	phase shift (π)	assignment
1	154.0	6.8			-	
2	156.0	4.8	4.7	4.48	-	a_1^*
3	157.4	3.4		3.11	-	e^*
Si2s	160.8	-	-	-	-	-
3	161.1	−0.3	−0.7	−1.0	0.6	ke
4	166.4	−5.6	−6.8	−8.3	0.5	ka_1
5	174.0	−13.2		−12.4	0.8	ke
6	181 1	−20.3	−20.4			

‡ Ref. 120

Table 2.5.2: Energies, term values and assignments of the discrete and continuum resonances in the Si 2*p* and 2*s* photoabsorption spectra of $SiCH_3Cl_3$

by photoelectron spectroscopy[145] for all of the chloromethylsilane compounds indicates that the data presented here is accurately calibrated.

The labelled peaks in the $SiCH_3Cl_3$ Si $2p$ pre-edge spectrum have been grouped into spin-orbit pairs by considering the term values of the peak positions with respect to the Si $2p_{3/2}$ and Si $2p_{1/2}$ ionization edges (see Table 2.5.2 (a)). Seven pairs of peaks are easily identified using the 0.1 eV criterion; 1-2, 2-3, 3-4, 4-6, 5-7, 7-8 and 8-9. In addition, there is probably a peak located between peaks 9 and 10 on the spectrum that corresponds to the Si $2p_{3/2}$ component of peak 10. The broad asymmetric peak across the Si $2p$ ionization threshold could easily accommodate such a peak. Line widths of the resonances in the Si $2p$ pre-edge photoabsorption spectrum of $SiCH_3Cl_3$ are similar to those observed for $SiCl_4$ and the same explanation based on the spacing of the vibrational levels and the natural linewidth of the Si $2p$ core hole is expected to hold.

The Si $2p$ pre-edge photoabsorption spectrum of $Si(CH_3)_2Cl_2$ is also presented in Fig. 2.5.2 with the Si $2p$ ionization potentials flagged by the dashed lines. The overall shape of the spectrum is quite different from the other chloromethylsilane compounds. Two strong absorption maxima (peaks 1-3 and 4-6) are observed centered approximately 4 eV and 2 eV below the Si $2p$ ionization edge. Weak peaks (7-8) are observed closer to threshold and a broad peak of moderate intensity spans the ionization threshold region. Positions (photon energies) and term values of the nine peaks indicated on the $Si(CH_3)_2Cl_2$ spectrum in Fig. 2.5.2 are given in Table 2.5.3 (a). The only previously reported Si $2p$ pre-edge photoabsorption spectrum of $Si(CH_3)_2Cl_2$ was published by Fomichev et al and is very similar to the spectrum reported here.[118] Positions for the peaks from the previous study are included in Table 2.5.3 (a) for comparison and a fairly good correlation with the present results is seen. The range of term values is decreased by ~0.6 eV from $SiCH_3Cl_3$, squeezing the spectrum closer to the ionization threshold.

Spin-orbit split resonances were identified by comparing term values with respect to both the Si $2p_{3/2}$ and Si $2p_{1/2}$ ionization edges and applying the selection criterion that the term values differ by no more than 0.1 eV for two peaks to be

(a) Si 2p pre-edge

peak label	energy (eV)	energy (eV)†	term value (eV)		assignments		
			$Si2p_{3/2}$	$Si2p_{1/2}$	resonance		$Si2p_{3/2} \rightarrow$
1	103.54	103.35	4.55	5.16	a		$1a_1^*, 2a_1^*$
2	104.22	103.95	3.87	4.48	b	a	$1b_2^*, 1b_1^*$
3	104.78	104.50	3.31	3.92		b	-
4	105.66	105.35	2.43	3.04	c		$2b_2^*$
5	106.06	105.70	2.03	2.64	d	c	$2b_1^*$
6	106.54	106.10	1.55	2.16	e	d	$3b_1^*$
7	107.20	106.85	0.89	1.50	f	e	$4b_1^*$
8	107.82	107.60	0.27	0.88	g	f	$8a_1^*$
9	108.46	108.10	−0.37	0.24		g	-
$Si2p_{3/2}$	108.09	-	-	-	-	-	-
$Si2p_{1/2}$	108.70	-	-	-	-	-	-

† Ref. 118

(b) Si 2p continuum

peak label	energy (eV)	term value (eV)	calc. term value (eV)	phase shift (π)	symmetry channel
1	110.0	−1.5	−0.5	0.9, 0.2	$ka_1 + ka_2$
2	123.4	−14.9	−12.7	1.3, 0.1, 0.4	$ka_1 + ka_2 + kb_2$
3	127.6	−19.1	−18.2	1.3, 0.5, 0.2	$ka_1 + kb_1 + kb_2$

(c) Si 2s

peak label	energy (eV)	term value (eV)	Si 1s term value (eV)‡	calc. term value (eV)	phase shift (π)	assignment
1	152.9	6.8		3.3	-	a_1^*
2	155.2	4.5	4.6	2.9	-	a_1^*
3	156.8	2.9	3.3	1.3	-	e^*
Si2s	159.7	-	-	-	-	-
4	161.7	−2.0	−1.3	−2.0	0.8	kb_2
5	167.1	−7.4	−6.8	−4.2,−8.3	0.9,0.6	ka_1, kb_1
6	174.0	−14.3		−11.4	0.8	ka_1
7	181.0	−21.3	−21.5	−18.5	0.1	kb_2

‡ Ref. 120

Table 2.5.3: Energies, term values and assignments of the discrete and continuum resonances in the Si 2p and 2s photoabsorption spectra of $Si(CH_3)_2Cl_2$

considered a spin-orbit pair. Only five spin-orbit split resonances are evident from the data in Table 2.5.3 (*a*); 1-2, 2-3, 6-7, 7-8, and 8-9. This leaves peaks 4 and

5 unassigned, so even though the two peaks are separated by only 0.4 eV they have also been assigned as a spin-orbit split resonance. Given the broad lines observed in this spectrum, the positions of these peaks could be in error. Peaks 5-6 have also been assigned as a spin-orbit split doublet to account for the intensity of peak 6 and also because slightly offset peaks at position 5 could give rise to the broadened peak shape observed. The seven resonances assigned to the Si $2p$ pre-edge photoabsorption spectrum of $Si(CH_3)_2Cl_2$ are summarized in Table 2.5.3 (a).

While the broad and unresolved peaks in the first two absorption bands would suggest that the resolution of the $Si(CH_3)_2Cl_2$ Si $2p$ pre-edge photoabsorption spectrum is considerably poorer than for $SiCl_4$ or $SiCH_3Cl_3$, the shape of peak 7 is very similar to peak 8 in the spectrum of $SiCH_3Cl_3$ indicating similar spectral resolution. Slightly offset overlapping peaks could account for the poor resolution in the first two absorption bands.

A representative Si $2p$ pre-edge photoabsorption spectrum of $Si(CH_3)_3Cl$ is also given in Fig. 2.5.2 with the dashed lines indicating the Si $2p$ ionization edges. While the spectrum is quite different from the spectra of the other chloromethylsilane compounds, the progression in the spectrum from $Si(CH_3)_2Cl_2$ is apparent. Relative to the spectrum of $Si(CH_3)_2Cl_2$, the intensity of the first peak (1-2) has decreased significantly while the intensities of the other peaks have increased. The range in term values is reduced by a further $\sim$0.8 eV from that in $Si(CH_3)_2Cl_2$, forcing the peaks to overlap more noticeably. The positions (photon energies) and term values of the eight positions marked on the figure are summarized in Table 2.5.4 (a) together with the Si $2p_{3/2}$ and Si $2p_{1/2}$ ionization potentials. Also included in Table 2.5.4 are peak positions from the previously reported Si $2p$ pre-edge photoabsorption spectrum of $Si(CH_3)_3Cl$ which are lower than the values reported here but otherwise in good agreement with these values.[118]

(a) Si 2p pre-edge

peak label	energy (eV)	energy (eV)†	term value (eV)		assignments		
			$Si2p_{3/2}$	$Si2p_{1/2}$	resonance		$Si2p_{3/2} \rightarrow$
1	103.22	102.80	3.73	4.34	a,b		$3a_1^*$
2	103.73	103.40	3.22	3.83		a,b	-
3	104.64	104.30	2.31	2.92	c		$6a_1^*$
4	105.23	104.85	1.72	2.33	d	c	$11a_1^*$
5	105.77	105.35	1.18	1.79	e	d	$14a_1^*$
6	106.28	105.85	0.67	1.28	f	e	Ryd.
7	106.90	106.65	0.05	0.66	g	f	Ryd.
8	107.31	-	−0.36	0.25		g	-
$Si2p_{3/2}$	106.95	-	-	-	-	-	-
$Si2p_{1/2}$	107.56	-	-	-	-	-	-

† Ref. 118

(b) Si 2p continuum

peak label	energy (eV)	term value (eV)	calc. term value (eV)	phase shift (π)	symmetry channel
1	108.2	−0.8	−0.5	0.2, 0.1	$ka_1 + ke$
2	115.2	−7.8	−6.3	0.5,1.0	$ke+ka_1$
3	125.7	−18.3	−18.0	0.5,0.2	$ke+ka_1$

(c) Si 2s

peak label	energy (eV)	term value (eV)	Si 1s term value (eV)‡	calc. term value (eV)	phase shift (π)	assignment
1	154.6	4.0	4.2	2.16	-	a_1^*
2	155.6	3.0	2.8	1.37	-	a_1^*
Si2s	158.6	-	-	-	-	-
3	160.5	−1.9	−2.0	−1.0	0.3	ke
4	166.2	−7.6	−7.3	−5.0	0.7,0.3	$ke+ka_1$
5	173.7	−15.1		−8.3	1.5	ke
6	180.0	−21.4	−22.5	−20.5	0.0	ka_1

‡ Ref. 120

Table 2.5.4: Energies, term values and assignments of the discrete and continuum resonances in the Si 2*p* and 2*s* photoabsorption spectra of $Si(CH_3)_3Cl$

Spin-orbit split resonances were identified by comparing the term values of peaks with respect to both the Si $2p_{3/2}$ and Si $2p_{1/2}$ ionization edges. Five pairs of peaks were found to meet the criteria that the term values for the $2p_{3/2}$ and $2p_{1/2}$ components of the spin-orbit split pair differ by no more than 0.1 eV; 1-2, 3-4,

4-5, 5-6, and 6-7. Peaks 7-8 may also form a spin-orbit split pair and while the separation between the peaks is only 0.41 eV, the broad shape of peak 8 makes it difficult to identify its position. The broad unresolved peaks 1-2 may also contain a second overlapping spin-orbit split resonance leading to the broad lines observed. This assignment is supported by an asymmetry on the high photon energy side of peak 2 which is probably due to a slightly offset overlapping peak. A summary of the seven resonances assigned to the Si 2*p* pre-edge spectrum of $Si(CH_3)_3Cl$ is given in Table 2.5.4 (*a*).

The Si 2*p* pre-edge photoabsorption spectrum of $Si(CH_3)_4$ was discussed in detail in section 2.4.2.1 and will not be repeated here. Several trends are apparent from the above discussion of the Si 2*p* pre-edge photoabsorption spectra of the chloromethylsilane compounds in Fig. 2.5.2 beyond the trends in the intensities and term values noted at the beginning of this section. The two groups of resonances at low photon energy in $SiCl_4$, 1-2 and 3-6, appear to merge to form one band in the mixed chloromethylsilane molecules; peaks 1-5 in $SiCH_3Cl_3$, 1-3 in $Si(CH_3)_2Cl_2$ and 1-2 in $Si(CH_3)_3Cl$. Additional absorption peaks also appear in $SiCH_3Cl_3$ with respect to $SiCl_4$ at intermediate energies (between the first strong peaks and the ionization threshold) and grow in intensity with each substitution of a chlorine atom with a methyl group. Finally, weak absorption peaks are observed near threshold in the Si 2*p* pre-edge photoabsorption spectra for all of the chloromethylsilane compounds; peaks 7-10 in $SiCl_4$, 8-9 in $SiCH_3Cl_3$, 7-8 in $Si(CH_3)_2Cl_2$, 6-8 in $Si(CH_3)_3Cl$ and 8-9 in $Si(CH_3)_4$. These peaks probably result from transitions into Rydberg orbitals.

2.5.1.2. Si 2*p* continuum spectra

Photoabsorption spectra of the discrete and continuum regions of the Si 2*p* ionization edges of the chloromethylsilane molecules over the photon energy range 100 - 150 eV are presented in Fig. 2.5.3. The intensities of the spectra have been

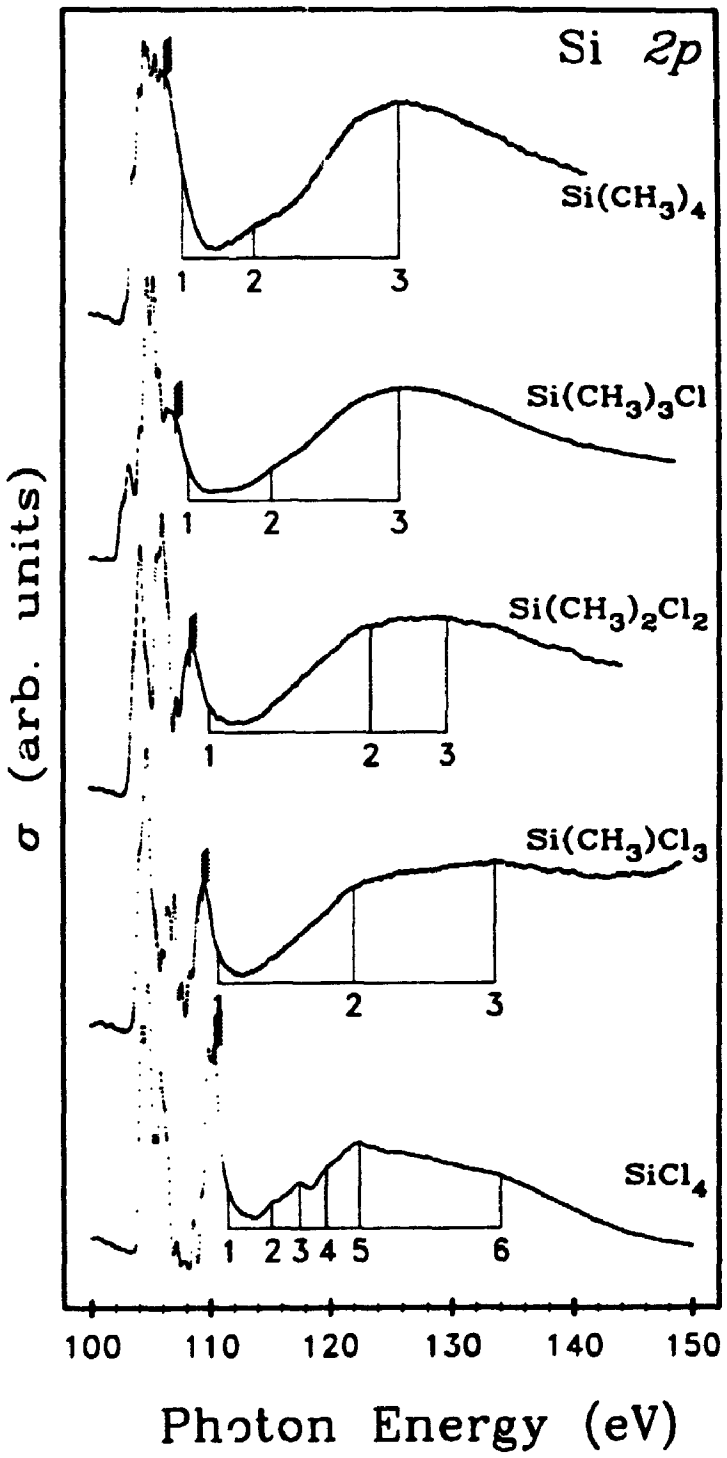

Figure 2.5.3: Photoabsorption spectra of the Si 2*p* regions of the chloromethylsilane compounds.

normalized to arbitrary values to make best use of the space on the figure. Pre-edge regions of the Si 2*p* spectra have been included on the figure to provide a relative measure of the intensities of the continuum resonances. The Si 2*p* continuum regions of $SiCl_4$ [88,90,108,10,149] and $Si(CH_3)_4$ [108,109,142,149,150] have been discussed in several previous studies. The Si 2*p* spectrum of $Si(CH_3)_4$ was also presented in section 2.4.2.2 of this thesis and is included here only for comparison with the other results.

The continuum regions of the Si 2*p* photoabsorption spectra of the chloromethylsilane compounds have much less structure than the discrete regions. Six features are identified in the $SiCl_4$ spectrum while only three features are noted in the Si 2*p* continuum regions of the photoabsorption spectra of the other chloromethylsilane compounds. The positions (photon energies) and term values of the features indicated on Fig. 2.5.3 are summarized in parts (*b*) of Table 2.5.1 - Table 2.5.4 for $SiCl_4$ - $Si(CH_3)_3Cl$ and in Table 2.4.5 for $Si(CH_3)_4$. The Si 2*p* continuum photoabsorption spectra of the chloromethylsilane compounds in Fig. 2.5.3 are considerably different from the spectra of the analogous fluorine containing molecules (Fig. 2.4.3). In particular, while two well resolved resonances are observed for all of the fluorine containing fluoromethylsilane molecules (peaks 2 and 3 in Fig. 2.4.3), strongly overlapping peaks are observed for the chloromethylsilane spectra (peaks 2 and 3 in Fig. 2.5.3).

The continuum regions of the photoabsorption spectra all have cross section maxima very close to the Si 2*p* thresholds (peaks 1 in Fig. 2.5.3). Some of the intensity for these peaks could result from the discrete features tailing into the continuum. Since the peaks extend ~2 eV above threshold for all of the chloromethylsilane compounds, the peaks are assigned as continuum resonances just above the Si 2*p* ionization threshold. It is difficult to establish accurate positions for the broad and overlapping peaks in the Si 2*p* continuum spectra of the chloromethylsilane compounds and positions and term values reported in

Table 2.5.1 (*b*) - Table 2.5.4 (*b*) are therefore prone to fairly large errors. This is especially evident in the Si 2*p* continuum spectrum of $Si(CH_3)_2Cl_2$ where it is very difficult to identify the position of the maxima for any of the peaks.

The Si 2*p* continuum photoabsorption spectrum of $SiCl_4$ exhibits five additional features at higher energy. The peaks labeled 5 and 6 on the $SiCl_4$ spectrum of Fig. 2.5.3 appear to be similar to the peaks labeled 2 and 3 on the spectra of the other chloromethylsilane molecules on the same figure. Peaks 2-4 on the $SiCl_4$ photoabsorption spectrum however, have no apparent analogs in the spectra of the other chloromethylsilane molecules or in the spectra of the fluoromethylsilane compounds (Fig. 2.4.3). The intensity of the peak at position 5 in the $SiCl_4$ spectrum decreases in $SiCH_3Cl_3$ (where it is peak 2) and becomes almost indiscernible from the background in the spectra of $Si(CH_3)_2Cl_2$ and $Si(CH_3)_3Cl$. The intensity of this peak appears to follow the number of Cl atoms in the molecule in the same manner that the second peak in the Si 2*p* continuum spectra of the fluoromethylsilane molecules followed the number of fluorine atoms in the molecule. The Cl atoms do not form as strong a barrier to the escape of the Si 2*p* photoelectron as the F atoms do as evidenced by the weak broad nature of the continuum resonances assigned to result from the presence of the Cl atoms compared with the strong and narrow resonances observed for the fluorine containing molecules (Fig. 2.4.3). The second peak in the Si 2*p* continuum spectrum of $Si(CH_3)_3Cl$ has a similar term value, -7.8 eV, as the peak observed in the $Si(CH_3)_4$ spectrum, -7.3 eV, and is probably due to the methyl ligands rather than the Cl atom. There may be a weak peak between positions 2 and 3 in the $Si(CH_3)_3Cl$ spectrum due to the Cl atom which is manifested as a broadening of the spectrum compared to the $Si(CH_3)_4$ spectrum.

A very broad peak is observed in the Si 2*p* continuum photoabsorption spectra of all five of the chloromethylsilane compounds ~20 eV above threshold. The relative intensity of this resonance with respect to the pre-edge features remains

fairly constant for all of the chloromethylsilane molecules. A similar high-energy resonance was noted for the fluoromethylsilane molecules is section 2.4.2.2. The constant shape and position of the resonance suggests that it results from a delayed onset of the Si $2p \rightarrow \epsilon d$ channel due to a centrifugal barrier created by the $\ell/(\ell+1)$ term in the radial Schrödinger equation in section 2.1. Similar effects have been seen in the $2p$ photoabsorption spectra of several atoms and molecules.[71,154]

2.5.1.3. Si 2*s* pre-edge spectra

Photoabsorption spectra of the discrete and continuum regions of the Si 2*s* ionization edges of the chloromethylsilane molecules are presented in Fig. 2.5.4. Linear baselines, determined from the background intensities at photon energies of 150 and 190 eV have been subtracted from the spectra to align the spectra on the figure. While the Si 2*s* features are much less intense than the corresponding Si 2*p* features, the Si 2*s* spectra of the chloromethylsilane compounds are of much better quality than the Si 2*s* absorption spectra of the analogous fluoromethylsilane compounds (Fig. 2.4.4). The Si 2*s* ionization thresholds of the chloromethylsilane compounds are indicated on the five spectra in Fig. 2.5.4. The positions (photon energies) and term values of the features indicated on Fig. 2.5.4 are included in Table 2.5.1 (*c*) - Table 2.5.4 (*c*) for $SiCl_4$ - $Si(CH_3)_3Cl$ and in Table 2.4.5 (*c*) for $Si(CH_3)_4$. The discrete regions of the Si 2*s* photoabsorption spectra of the chloromethylsilane compounds are very similar in their simplicity. Only 1 - 4 peaks can be identified in the pre-edge regions of the chloromethylsilane spectra. All of the pre-edge features are very broad (half-height widths $\gtrsim$2.5 eV) which is a reflection of the the short lifetime of the Si 2*s* hole state due to the efficient Coster-Kronig transitions.[8]

The Si 2*s* pre-edge photoabsorption spectrum of $SiCl_4$ in Fig. 2.5.4 has one very strong peak with a term value of 5.0 eV and a much weaker peak with a term value of 7.4 eV (Table 2.5.1 (*c*)) which is manifested as a broad asymmetric leading

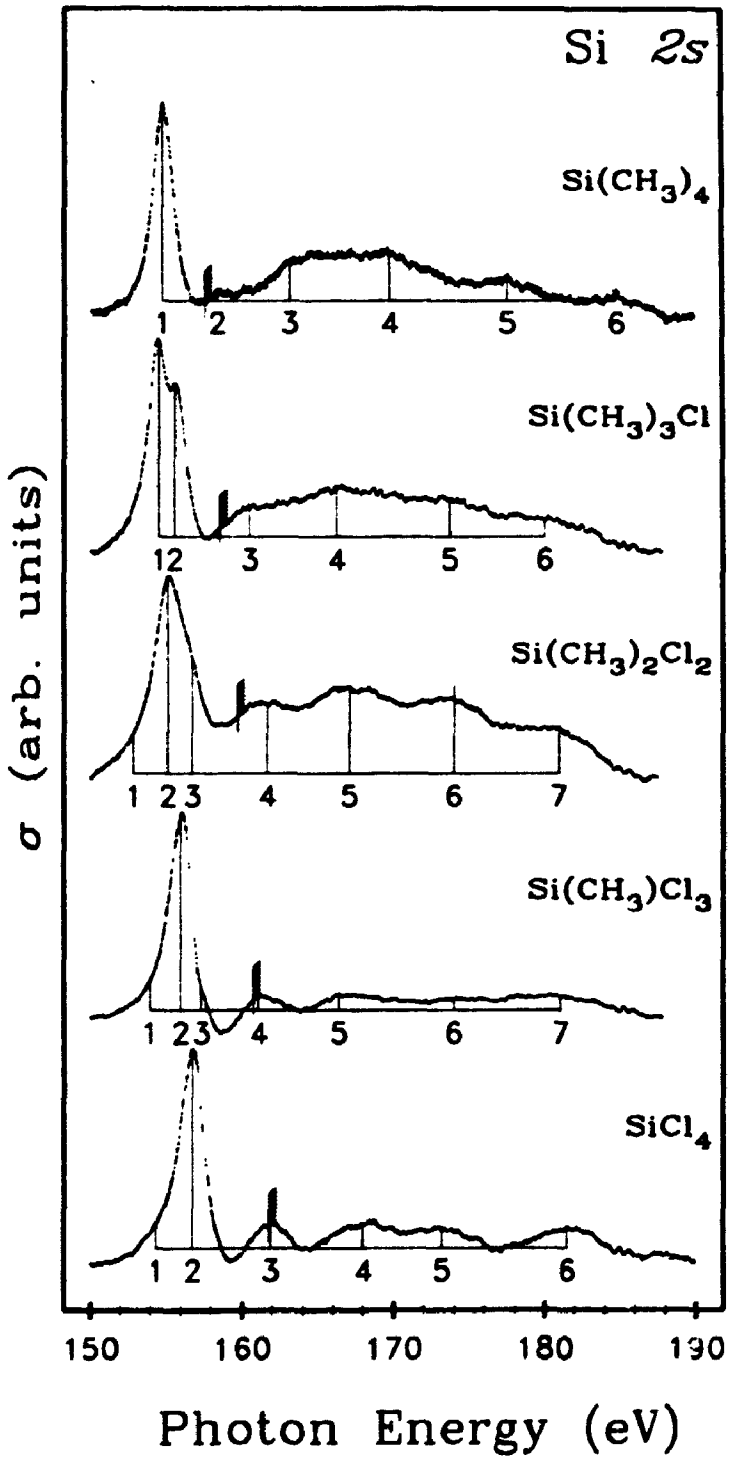

Figure 2.5.4: Photoabsorption spectra of the Si 2*s* regions of the chloromethylsilane compounds.

tail for the larger peak. The Si 2*s* pre-edge photoabsorption spectrum of $Si(CH_3)_4$ (Fig. 2.5.4) also has one strong peak, with a term value of 2.8 eV (Table 2.4.5 (*c*)). Unlike the peak in the $SiCl_4$ spectrum, this peak has a symmetric shape and there are therefore no other obvious peaks in the discrete portion of the Si 2*s* photoabsorption spectrum of $Si(CH_3)_4$. In the tetrahedral $SiCl_4$ and $Si(CH_3)_4$ molecules, dipole selection rules allow only for transitions to t_2^* final states from the a_1 Si 2*s* levels. The strong peaks in the Si 2*s* pre-edge photoabsorption spectra of $SiCl_4$ and $Si(CH_3)_4$ are therefore assigned as electronic transitions to virtual molecular orbitals of t_2^* symmetry. The relatively large intensity of the peaks indicates that the virtual orbitals populated are probably antibonding orbitals. The weak peak at a term value of 7.4 eV in the $SiCl_4$ spectrum could either be a transition to a t_2^* virtual orbital with a small oscillator strength, a forbidden transition to a virtual orbital with a different symmetry (probably a_1^*) or an artifact of the baseline subtraction.

Photoabsorption spectra of the discrete regions of the Si 2*s* ionization edges of the mixed chloromethylsilane molecules shown in Fig. 2.5.4 appear to be admixtures of the $SiCl_4$ and $Si(CH_3)_4$ spectra. The shape of the Si 2*s* pre-edge peak in the $SiCH_3Cl_3$ spectrum is very similar to the peak in the $SiCl_4$ spectrum, with a strong absorption maximum at a term value of 4.8 eV and a weaker shoulder at a term value of 7.5 eV. There is also a shoulder on the high photon energy side of the strong peak (feature 3 in the $SiCH_3Cl_3$ spectrum in Fig. 2.5.4) at a term value of 3.3 eV. In the Si 2*s* pre-edge photoabsorption spectrum of $Si(CH_3)_2Cl_2$, the intensity of the shoulder on the high photon energy side of the strongest peak is enhanced resulting in a marked broadening of the peak shape. Three peaks are assigned to the Si 2*s* spectrum of $Si(CH_3)_2Cl_2$ as shown in Fig. 2.5.4. Positions and term values of the three peaks are summarized in Table 2.5.3 (*c*). The Si 2*s* pre-edge photoabsorption spectrum of $Si(CH_3)_3Cl$ exhibits two distinct peaks with term values of 4.0 and 3.0 eV (Table 2.5.4 (*c*)). These peaks are analogous to the

two higher photon energy peaks in the other mixed chloromethylsilane compounds with the higher energy peak due to the Cl atom and the peak with a term value of 3.0 eV resulting from the methyl ligands. The intensities of the two peaks are inconsistent with this assignment since the peak assigned to the Si–Cl antibonding orbital would be expected to be weaker than the peak correlated with the three methyl ligands. Trends in the relative intensities of the two peaks in the other mixed chloromethylsilane compounds support the assignment however, as does a consideration of the term values of the two peaks across the series of the five molecules.

The term values of the peaks in the Si 2*s* pre-edge photoabsorption spectra assigned to result from transitions to the Si–Cl and Si–C antibonding orbitals are consistent with, although not identical to, the term values of peaks in the Si 2*p* pre-edge spectra which were assigned to result from the the same orbitals. In section 2.5.1.1 the Si–Cl resonances were found to occur with the highest term values (~5.0 eV in $SiCl_4$ to ~3.5 eV for $Si(CH_3)_3Cl$) while the resonances attributed to methyl ligands were found with lower term values (~2.5 eV for $SiCH_3Cl_3$ to ~1.8 eV for $Si(CH_3)_4$). A similar trend is identified here for resonances below the Si 2*s* ionization edges of the chloromethylsilane compounds where the term values of the resonances attributed to the Si–Cl orbitals are ~1.0 eV greater than the term values for peaks assigned to the Si–C antibonding orbitals. Term values for all of the resonances also decrease with increasing methyl substitution for the Si 2*s* pre-edge spectra.

A similar trend was also identified in the discrete portions of the Si 1*s* spectra of the chloromethylsilane molecular series.[119,120] Two peaks were observed in the Si 1*s* pre-edge photoabsorption spectra of the mixed chloromethylsilane compounds, the lower energy one (higher term value) assigned to transitions into antibonding orbitals arising from the Si–Cl bonds and the one closer to threshold resulting from transitions into Si–C antibonding orbitals. The intensity pattern of the

peaks, which are better resolved than the Si 2*s* peaks owing to the longer lifetimes of the Si 1*s* hole compared the Si 2*s* core hole, is also consistent with the spectra presented here. The two peaks below the Si 1*s* edge were found to have the same intensity for $Si(CH_3)_3Cl$ with the methyl peak being weaker for the other mixed compounds.

2.5.1.4. Si 2*s* continuum spectra

Continuum regions of the Si 2*s* photoabsorption spectra of the chloromethylsilane molecules are also included in Fig. 2.5.4. The spectra have a more complex structure than either the corresponding Si 2*p* continuum photoabsorption spectra (Fig. 2.5.3) or the Si 2*s* spectra of the analogous fluoromethylsilane compounds in Fig. 2.4.4. The energies and term values of the features indicated on Fig. 2.5.4 are summarized in Table 2.5.1 (*c*) - Table 2.5.4 (*c*) for $SiCl_4$ to $Si(CH_3)_3Cl$ and in Table 2.4.5 (*c*) for $Si(CH_3)_4$. The Si 2*s* continuum spectra in Fig. 2.5.4 are all similar, exhibiting four or five weak absorption maxima with half-height widths of ~2–4 eV. The peaks in the Si 2*s* continuum photoabsorption spectra of $SiCl_4$ and $Si(CH_3)_2Cl_2$ are well defined resulting in fairly accurate positions and term values. For the three other chloromethylsilane molecules, the positions (and term values) of the peaks are not as well defined due to the very weak maxima in the absorptions spectra.

The term values of the peaks in the Si 2*s* continuum regions of the chloromethylsilane compounds appear to correlate fairly well with the term values of the peaks above the Si 2*p* ionization edges. In the spectra of $SiCl_4$, for example, four peaks are observed above the Si 2*s* edge with term values of −0.1, −7.2, −11.4 and −19.7 eV (Table 2.5.1 (*c*)). These positions correlate well with the peaks observed above the Si 2*p* edge with term values of −0.9, −6.9, −11.9 and −23.4 eV (Table 2.5.1 (*c*)). Similar correlations are seen for the other chloromethylsilane molecules where only one peak above each of the Si 2*s* ionization edges of $SiCH_3Cl_3$,

$Si(CH_3)_2Cl_2$ and $Si(CH_3)_4$ does not have a peak with the same term value above the Si $2p$ ionization edge.

An excellent correlation is also seen with the term values for the Si $1s$ ionization edges of the chloromethylsilane molecules which have been reported recently.[89,119,120] Term values of the peaks observed in the photoabsorption spectra above the Si $1s$ ionization edges of the chloromethylsilane compounds are included in Table 2.5.1 (c) - Table 2.5.4 (c).[120] For $SiCl_4$ for instance, a one to one correspondence is seen between the peaks observed above the Si $2s$ and Si $1s$ ionization edges. Moreover, the term values of the four corresponding peaks are all within 0.7 eV. A similar correspondence is found for the other compounds although some of the peaks identified in the Si $2s$ photoabsorption spectra have no analogs in the Si $1s$ photoabsorption spectra. In particular, the intermediate energy peaks observed ~13–15 eV above the Si $2s$ ionization edges in the photoabsorption spectra of the mixed chloromethylsilane compounds were not identified in the Si $1s$ photoabsorption spectra.

2.5.1.5. Cl $2p$ spectra

The Cl $2p$ pre-edge photoabsorption spectra of the chlorine containing chloromethylsilane compounds are shown in Fig. 2.5.5. The spectra all consist of a set of well defined resonances below the Cl $2p$ ionization edges split by the 1.6 eV Cl $2p$ spin-orbit splitting.[145] The Cl $2p_{3/2}$ and Cl $2p_{1/2}$ ionization edges of the chloromethylsilane compounds are indicated by the dashed lines on the spectra in Fig. 2.5.5. Positions (photon energies) and term values with respect to both the Cl $2p_{3/2}$ and Cl $2p_{1/2}$ ionization edges of the features indicated on the figure are summarized in Table 2.5.5. The Cl $2p$ ionization potentials of $SiCl_4$, $SiCH_3Cl$, $Si(CH_3)_2Cl_2$ and $Si(CH_3)_3Cl$ were obtained from previously reported

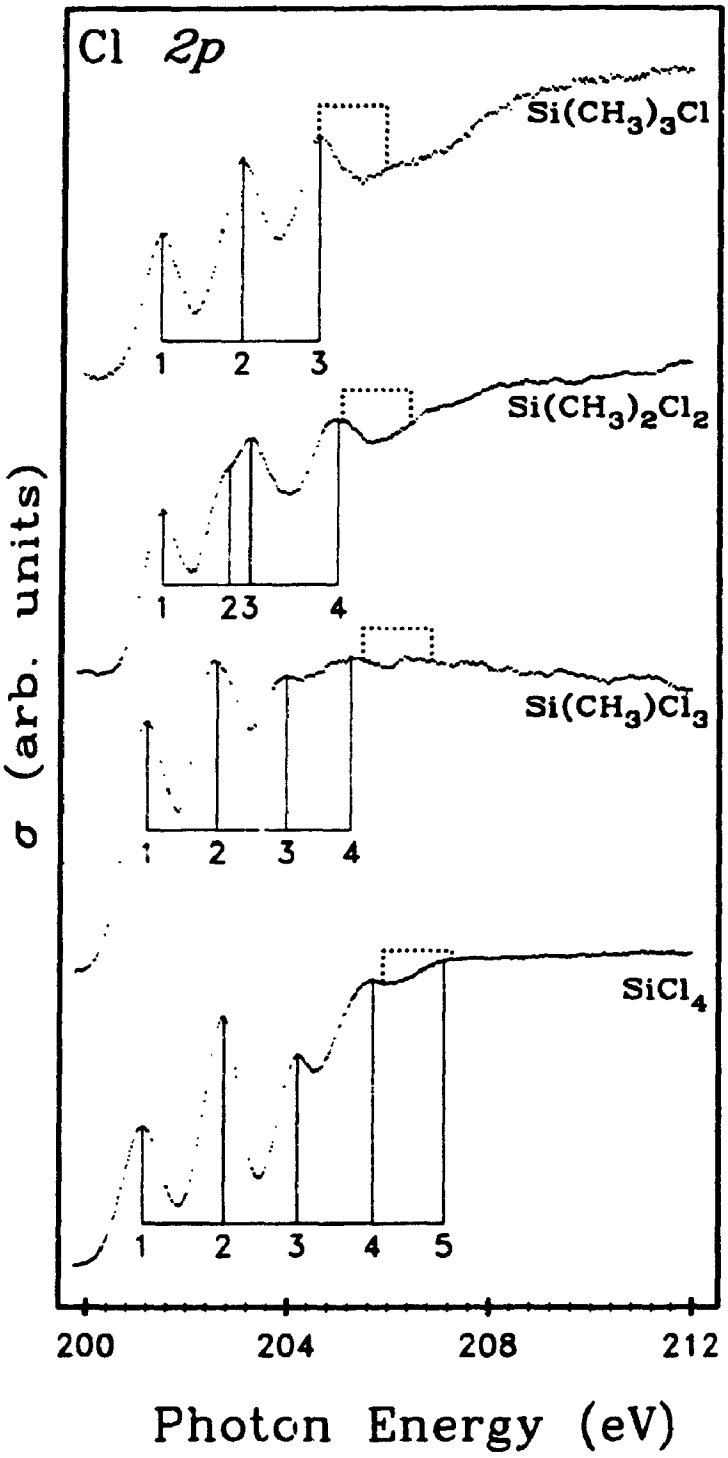

Figure 2.5.5: Photoabsorption spectra of the Cl 2*p* regions of the chloromethylsilane compounds.

(a) $SiCl_4$

peak label	energy (eV)	term value (eV)		Cl 1s term value (eV)†	resonance	
		$Cl2p_{3/2}$	$Cl2p_{1/2}$		$Cl2p_{3/2} \rightarrow$	$Cl2p_{1/2} \rightarrow$
1	201.3	5.6	7.2		a	
2	203.2	3.7	5.3	4.6	b	a
3	204.9	2.0	3.6	2.9	c	b
4	206.7	0.2	1.8		d	c
5	208.3	−1.4	0.2			d
$Cl2p_{3/2}$	206.9	-	-	-	-	-
$Cl2p_{1/2}$	208.5	-	-	-	-	-

(b) $SiCH_3Cl_3$

peak label	energy (eV)	term value (eV)		Cl 1s term value (eV)†	resonance	
		$Cl2p_{3/2}$	$Cl2p_{1/2}$		$Cl2p_{3/2} \rightarrow$	$Cl2p_{1/2} \rightarrow$
1	201.4	5.1	6.7		a	
2	203.0	3.4	5.0	3.6	b	a
3	204.6	1.8	3.4	2.5	c	b
4	206.1	0.3	1.9			c
$Cl2p_{3/2}$	206.4	-	-	-	-	-
$Cl2p_{1/2}$	208.0	-	-	-	-	-

(c) $Si(CH_3)_2Cl_2$

peak label	energy (eV)	term value (eV)		Cl 1s term value (eV)†	resonance	
		$Cl2p_{3/2}$	$Cl2p_{1/2}$		$Cl2p_{3/2} \rightarrow$	$Cl2p_{1/2} \rightarrow$
1	201.7	4.2	5.8		a	
2	203.3	2.7	4.3		b	a
3	203.8	2.2	3.8	2.3	c	b
4	205.8	0.1	1.7			c
$Cl2p_{3/2}$	205.9	-	-	-	-	-
$Cl2p_{1/2}$	207.5	-	-	-	-	-

(d) $Si(CH_3)_3Cl$

peak label	energy (eV)	term value (eV)		Cl 1s term value (eV)†	resonance	
		$Cl2p_{3/2}$	$Cl2p_{1/2}$		$Cl2p_{3/2} \rightarrow$	$Cl2p_{1/2} \rightarrow$
1	201.7	3.7	5.3		a	
2	203.5	1.8	3.4	1.5	b	a
3	205.3	0.0	1.6			b
$Cl2p_{3/2}$	205.3	-	-	-	-	-
$Cl2p_{1/2}$	206.9	-	-	-	-	-

† Ref. 120

Table 2.5.5: Energies, term values and resonance assignments for the discrete and continuum resonances in the Cl 2*p* photoabsorption spectra of $SiCl_4$, $SiCH_3Cl_3$, $Si(CH_3)_2Cl_2$ and $Si(CH_3)_3Cl$.

photoelectron spectra of the molecules.[158] The peaks have been grouped into spin-orbit split resonances by comparing their term values with respect to the two Cl $2p$ ionization edges.

The maximum term values from the Cl $2p$ pre-edge spectra of the chloromethylsilane compounds are seen to decrease with each substitution of a methyl group for a chlorine atom. The term values of the first peaks in the Cl $2p$ pre-edge spectra correlate very well with the term values of the first resonances below the Si $2p$ ionization edges for the four chlorine containing chloromethylsilane compounds. This result implies a transferability of term values between the ionization edges of the different atoms in the compound.

Photoabsorption spectra of the Cl $1s$ ionization edges of the chloromethylsilane compounds have also been reported previously[120] and the term values of the peaks in the discrete regions of the spectra have been included in Table 2.5.5. A reasonably good correlation between the term values of the resonances below the Cl $2p$ and Cl $1s$ ionization edges is seen.

The shape of the Cl $2p$ pre-edge spectra is quite different from the shape of the Si $2p$ pre-edge spectrum. The "edge-jump" appears to overlap with the Cl $2p$ pre-edge structure in a fashion similar to the K-edge spectra of first row elements. In the Si $2p$ spectra on the other hand, there is no well defined "edge jump" at threshold, making it much easier to identify the weak pre-edge peaks close to the ionization threshold. This is consistent with the trend seen in the $2p$ photoabsorption spectra of the second row hydride molecules[72] where the "edge-jump" becomes more predominant across the series SiH_4, PH_3, H_2S, HCl and Ar.

2.5.2. DISCUSSION: Assignment Using MS-Xα Results

Theoretical cross sections of the discrete and continuum regions of the Si $2p$ and Si $2s$ ionization edges were calculated using the MS-Xα method and the

results are presented here. The theoretical results are used in conjunction with the trends noted in the previous sections to assign the peaks in the spectra of the chloromethylsilane compounds.

2.5.2.1. Si 2*p* pre-edge

Virtual electronic levels of the chloromethylsilane compounds were identified in the Si 2*p* pre-edge MS-Xα calculations by fine mesh energy searches to within 0.05 Rydbergs of the ionization thresholds using the converged Si 2*p* transition state potentials. Oscillator strengths were calculated for all of the virtual electronic levels found and the eigenvalues and corresponding oscillator strengths of the virtual levels were used to construct simulated Si 2*p* pre-edge spectra. The calculated eigenvalues, oscillator strengths and charge distributions for the ten virtual orbitals with the greatest oscillator strengths are given in Tables 2.5.3 - 2.5.9 for $SiCl_4$ - $Si(CH_3)_3Cl$ and in Table 2.4.10 for $Si(CH_3)_4$. The simulated Si 2*p* pre-edge spectra of the chloromethylsilane molecules presented in Fig. 2.5.6 were constructed using the eigenvalues of the virtual orbitals as the term values and the corresponding oscillator strengths for transitions to these virtual levels for the intensity of the peaks. A Si 2*p* spin-orbit splitting of 0.61 eV with a statistical 2:1 intensity ratio was used with a Lorentzian line shape with a half-height width of 0.25 eV to convolute with the line positions and intensities to approximate the experimental spectra.

There is generally reasonable agreement of the theoretical Si 2*p* pre-edge spectra in Fig. 2.5.6 with the experimental spectra in Fig. 2.5.2. The overall shape of the theoretical spectra, as defined by the positions and intensities of the peaks, are similar to the experimental spectra for all of the chloromethylsilane molecules albeit some of the peaks are shifted relative to their experimental counterparts. The 0.25 eV linewidth used to approximate the peak shape is not a good match to the experimental linewidths resulting in a difference in the appearance of the

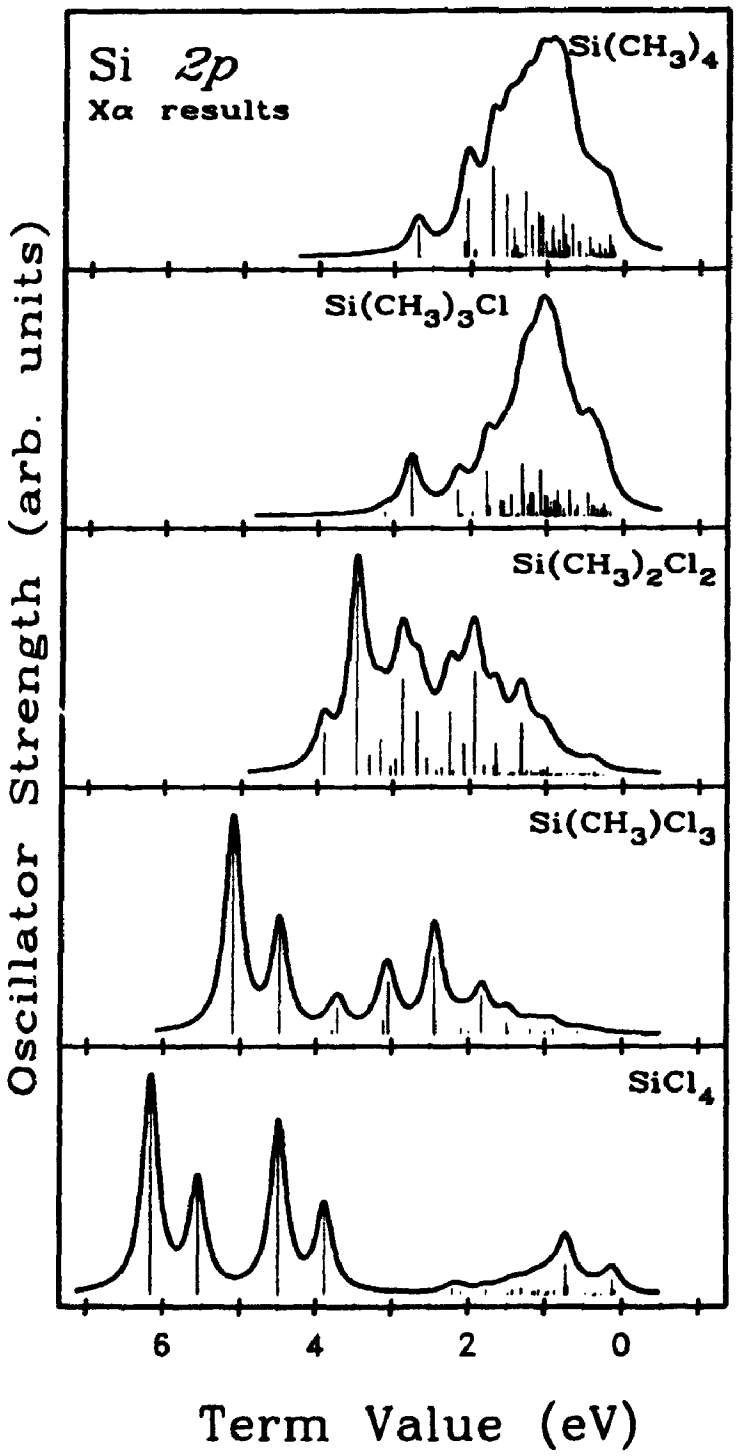

Figure 2.5.6: Simulated Si 2*p* pre-edge photoabsorption spectra of the chloromethylsilane compounds constructed from the eigenvalues and oscillator strengths from the MS-Xα calculations.

experimental and theoretical spectra. The linewidth of 0.25 eV was chosen to highlight the positions of the peaks and to prevent too much overlap between spin-orbit pairs. The 2:1 statistical area ratio used for the theoretical Si $2p_{3/2}$ to Si $2p_{1/2}$ peak areas is also in poor agreement with some of the peaks in the experimental spectra.

The calculated term values for the lowest energy virtual electronic states roughly reproduce the convergence of the experimental term values noted in section 2.4.1. The theoretical(experimental) term values for the lowest state decrease from 5.55(5.87) eV for $SiCl_4$ to 4.49(5.10) eV for $SiCH_3Cl_3$, 3.31(4.55) eV for $Si(CH_3)_2Cl_2$, 3.23(3.73) eV for $Si(CH_3)_3Cl$ and 2.66(3.46) eV for $Si(CH_3)_4$. The differences between the calculated and observed shifts noted in section 2.4.3.1 for the fluoromethylsilane compounds are also apparent for the chloromethylsilane molecules and can be attributed to inaccuracies in the Xα method in dealing with the strong perturbation of the potential caused by the fluorine and chlorine ligands. The theoretical results however, still provide a good basis for assigning the intense resonances in the Si 2p pre-edge spectra.

The numbering of the virtual orbitals begins at one for the manifolds of virtual orbitals of each symmetry. This facilitates a comparison of virtual orbitals between different molecules since it is the symmetry and character of the virtual orbital which is of interest, rather than its numerical label. The characters of the virtual orbitals are determined by the charge distributions. Orbitals with small contributions to the total charge from the outersphere region (that region of space not included inside the intersphere and atomic sphere regions) are assumed to be antibonding orbitals, those with intermediate outersphere charges are classified as mixed antibonding – Rydberg orbitals, and virtual orbitals with large outersphere charges ($Q_{out} > 90\%$) are classified as Rydberg orbitals.

Three resonances are easily assigned in the Si 2p pre-edge photoabsorption spectrum of $SiCl_4$. Three virtual molecular orbitals with relatively large oscillator

orbital assignment	term value	Q_{out} (%)	Q_{int} (%)	Q_{Si} (%)	Q_{Cl} (%)	oscillator strength	orbital type
$1a_1^*$	5.55	6.7	9.0	23.7	60.6	2.59×10^{-2}	anti
$1t_2^*$	3.88	4.9	22.6	34.9	37.6	2.02×10^{-2}	anti.
$3t_2^*$	1.60	80.1	16.0	0.5	3.4	7.83×10^{-4}	mixed
$4t_2^*$	1.16	89.3	8.0	0.4	2.3	6.43×10^{-4}	Ryd (p)
$6t_2^*$	0.82	98.4	1.0	0.1	0.4	5.46×10^{-4}	Ryd (f)
$7t_2^*$	0.70	94.0	4.1	0.3	1.5	7.89×10^{-4}	Ryd (p)
$11t_2^*$	0.47	96.5	2.3	0.2	1.0	6.28×10^{-4}	Ryd (p)
$18t_2^*$	0.27	99.4	0.3	0.1	0.3	5.17×10^{-4}	Ryd (f)
$7e^*$	0.14	97.6	1.1	0.3	0.9	8.91×10^{-4}	Ryd (g)
$8e^*$	0.13	99.7	0.2	0.0	0.1	3.74×10^{-3}	Ryd (d)

Table 2.5.6: Term values (eV), oscillator strengths and charge distributions calculated for the unoccupied orbitals of $SiCl_4$.

strengths were identified by the MS-Xα calculations and they correlate very well with the three strong bands in the experimental photoabsorption spectrum (Fig. 2.5.2). The calculated spectrum is also in good agreement with a previous MS-Xα calculation, altnough the previous calculation did not include the orbitals very close to threshold which contribute significant intensity to the spectrum.[90] Based on the eigenvalues and oscillator strengths for $SiCl_4$, summarized in Table 2.5.6, resonances in the Si 2*p* pre-edge photoabsorption spectrum assigned as *a*, *d*, and *h* in Table 2.5.1 are assigned to transitions from the Si 2*p* electron into the $1a_1^*$ antibonding orbital, $1t_2^*$ antibonding orbital and an $8e^*$ Rydberg *d* orbital respectively. In addition to these three assignments, resonance *f* from Table 2.5.1 can be assigned as a transition terminating at the $3t_2^*$ mixed antibonding – Rydberg virtual orbital. The MS-Xα calculation does not provide a clear assignment for the other peaks observed in the $SiCl_4$ Si 2*p* pre-edge photoabsorption spectrum, although the calculations indicate that transitions to virtual orbitals with high Rydberg characters can contribute appreciable intensity to the spectrum. The additional peaks are therefore tentatively assigned as transitions to Rydberg orbitals. This assignment is in reasonably good agreement with the Si 2*p* pre-edge

absorption spectrum of solid $SiCl_4$,[155] where the three main bands found in the gas phase spectrum are present but the weaker structure is absent. The absorption peak at threshold remains in the solid state spectrum, but the fine structure is no longer visible (i.e. no doublet), suggesting that the peaks at threshold in the gas phase spectrum are due to transitions into Rydberg orbitals with an underlying continuum resonance.

The assignment given above is also in good agreement with some previous work, although it is at odds with Bodeur et al's assignment.[108] In their study of the Si $2p$ pre-edge spectrum of $SiCl_4$, Bodeur et al assigned the peaks to transitions into final states of C_{2v} symmetry due to Jahn-Teller distortions in the Si $2p^{-1}$ excited state. Contrary to the assignments of Bodeur et al, these distortions are not required to explain the number of lines observed in the spectrum as contour diagrams of low angular momentum Rydberg orbitals have shown that they can penetrate the chlorine cage to result in substantial intensity for transitions from core levels into these orbitals.[90] The assignment of the Si $2p$ pre-edge photoabsorption spectrum of $SiCl_4$ given above is in good agreement with results from DV-Xα calculations, where the three bands were assigned to transitions into orbitals of a^*, t_2^* and e^* symmetry.[152]

The MS-Xα calculations provide assignments for most of the peaks in the experimental Si $2p$ pre-edge photoabsorption spectrum of $SiCH_3Cl_3$. Based on the eigenvalues and oscillator strengths summarized in Table 2.5.7, the first strong absorption band in the experimental spectrum is assigned to electronic transitions from the Si $2p$ core levels to the $1a_1^*$ antibonding orbital overlapping with weaker transitions to the $2a_1^*$ mixed antibonding – Rydberg virtual orbitals. The second band, which was attributed to the Si–CH_3 antibonding orbitals in section 2.5.1.1, is assigned to transitions into the $1e^*$ antibonding orbital and the $3a_1^*$ and $4a_1^*$ mixed character orbitals. Finally, the weaker transitions closer to threshold are assigned to transitions into the $5a_1^*$ mixed character orbital and the $8a_1^*$ Rydberg orbital.

orbital assignment	term value	Q_{out} (%)	Q_{inter} (%)	Q_{Si} (%)	Q_{Cl} (%)	Q_{C} (%)	Q_{H} (%)	oscillator strength	orbital type
$1a_1^*$	4.49	8.8	9.8	26.3	51.7	3.3	0.1	2.46×10^{-2}	anti.
$2a_1^*$	3.18	57.3	36.2	0.4	5.0	1.1	0.0	5.35×10^{-4}	mixed
$1e^*$	3.11	7.5	23.4	33.7	33.6	0.8	1.1	3.28×10^{-3}	anti.
$3a_1^*$	2.44	40.5	33.4	7.5	14.5	4.2	0.3	6.13×10^{-3}	mixed
$4a_1^*$	1.84	60.9	14.5	10.4	8.5	5.6	0.3	9.00×10^{-3}	mixed
$5a_1^*$	1.49	87.8	8.1	1.6	2.1	0.4	0.0	8.11×10^{-4}	mixed
$6a_1^*$	1.40	89.6	5.8	1.3	1.7	1.5	0.0	4.00×10^{-4}	Ryd. (s)
$7a_1^*$	1.06	92.4	5.4	0.6	1.0	0.6	0.0	3.43×10^{-4}	Ryd. (p)
$8a_1^*$	0.90	91.0	4.6	1.7	1.9	0.8	0.0	1.45×10^{-3}	Ryd. (d)
$13a_1^*$	0.58	95.2	2.5	0.8	1.1	0.4	0.0	7.33×10^{-4}	Ryd. (d)

Table 2.5.7: Term values (eV), oscillator strengths and charge distributions calculated for the unoccupied orbitals of $SiCH_3Cl_3$.

The assignment of the experimental spectrum is summarized in Table 2.5.2 (a). Oscillator strengths obtained from the MS-Xα calculations do not predict any significant intensity at the Si 2p threshold. The broad peak at threshold, peak 10 in the Si 2p pre-edge spectrum of $SiCH_3Cl_3$ Fig. 2.5.2, is therefore likely due to a continuum resonance just above the Si 2p threshold rather than discrete resonances. This assignment is consistent with the broad shape of the resonance and the spectra of the other chloromethylsilane compounds.

The Si 2p pre-edge spectrum of $Si(CH_3)_2Cl_2$ is difficult to assign using the MS-Xα results since the calculated spectrum in Fig. 2.5.6 consists of numerous overlapping bands producing a broad and unresolved theoretical spectrum. By dividing the transitions with significant oscillator strengths into two groups based on their eigenvalues (Table 2.5.8), however, an assignment of the experimental absorption spectrum can be obtained. The first group of peaks in the experimental spectrum, which were assigned to result from Si–Cl antibonding orbitals in the previous section are assigned to transitions into the $2a_1^*$ antibonding orbital overlapping with transitions into the $1a_1^*$, $1b_2^*$ and $1b_1^*$ mixed antibonding – Rydberg virtual orbitals. The second experimental absorption band (peaks 4-6 in

orbital assignment	term value	Q_{out} (%)	Q_{inter} (%)	Q_{Si} (%)	Q_{Cl} (%)	Q_{C} (%)	Q_{H} (%)	oscillator strength	orbital type
$1a_1^*$	3.31	40.7	43.9	4.53	8.6	2.3	0.1	3.02×10^{-3}	mixed
$2a_1^*$	2.87	24.4	15.4	23.2	33.6	2.6	0.7	1.34×10^{-2}	anti.
$1b_2^*$	2.56	46.3	37.9	5.7	5.8	2.0	2.4	2.50×10^{-3}	mixed
$3a_1^*$	2.43	61.3	30.1	1.0	4.6	2.4	0.6	6.80×10^{-4}	mixed
$1b_1^*$	2.36	60.5	30.4	1.1	5.7	1.8	0.4	1.17×10^{-3}	mixed
$2b_2^*$	2.08	33.1	24.7	22.2	18.6	0.2	1.2	4.39×10^{-3}	anti.
$2b_1^*$	1.65	67.2	22.6	3.1	4.7	2.1	0.4	4.44×10^{-3}	mixed
$3b_1^*$	1.33	74.2	10.8	7.2	5.3	2.3	0.3	7.18×10^{-3}	mixed
$4b_1^*$	1.07	90.4	7.1	0.7	0.9	0.9	0.0	7.07×10^{-4}	Ryd. (p)
$8a_1^*$	1.03	86.9	8.3	1.6	1.6	0.1	0.0	8.44×10^{-4}	Ryd. (p)

Table 2.5.8: Term values (eV), oscillator strengths and charge distributions calculated for the unoccupied orbitals of $Si(CH_3)_2Cl_2$.

Fig. 2.5.2) are assigned to overlapping transitions into the $2b_2^*$ antibonding and $2b_1^*$ and $3b_1^*$ mixed antibonding – Rydberg virtual orbitals. Finally, the weak peaks superimposed upon the broad continuum resonance are assigned to transitions into the $4b_1^*$ and $8a_1^*$ Rydberg orbitals. The strong broad absorption band across the ionization threshold is assigned to a continuum resonance at the ionization threshold since the MS-Xα calculation predicts very little intensity at threshold.

orbital assignment	term value	Q_{out} (%)	Q_{inter} (%)	Q_{Si} (%)	Q_{Cl} (%)	Q_{C} (%)	Q_{H} (%)	oscillator strength	orbital type
$3a_1^*$	2.17	22.3	15.0	31.2	27.9	2.5	1.2	2.98×10^{-3}	anti.
$6a_1^*$	1.19	88.6	7.9	0.8	1.1	1.3	0 3	2.48×10^{-3}	mixed
$8a_1^*$	0.86	90.7	8.3	0.3	0.2	0.4	0.1	1.22×10^{-3}	Ryd. (d+f)
$11a_1^*$	0.71	93.3	3.9	0.9	0.6	1.0	0.2	2.83×10^{-3}	Ryd. (p)
$7e^*$	0.70	90.2	5.4	2.0	1.1	0.9	0.3	1.23×10^{-3}	Ryd. (p)
$12a_1^*$	0.61	94.9	4.0	0.5	0.2	0.4	0.0	1.23×10^{-3}	Ryd. (d+f)
$14a_1^*$	0.48	95.5	2.2	0.8	0.4	1.2	0.1	2.52×10^{-3}	Ryd. (p)
$11e^*$	0.48	92.6	3.6	1.9	0.9	0.9	0.2	1.20×10^{-3}	Ryd. (p)
$15a_1^*$	0.42	96.9	2.2	0.4	0.1	0.3	0.0	1.19×10^{-3}	Ryd. (d+f)
$20a_1^*$	0.26	97.9	0.9	0.5	0.2	0.6	0.0	1.42×10^{-3}	Ryd. (p)

Table 2.5.9: Term values (eV), oscillator strengths and charge distributions calculated for the unoccupied orbitals of $Si(CH_3)_3Cl$.

The shape of the experimental Si 2*p* pre-edge spectrum of $Si(CH_3)_3Cl$ is well reproduced by the theoretical spectrum constructed with the eigenvalues and oscillator strengths from the MS-Xα calculation. Most of the virtual orbitals in Table 2.5.9 have large charge distributions from the outersphere, which is consistent with Rydberg orbitals, a large number of which contribute to total cross section as evidenced by the number of vertical lines in the $Si(CH_3)_3Cl$ theoretical spectrum in Fig. 2.5.6. This situation makes it difficult to assign the peaks in the experimental spectrum to transitions into individual virtual orbitals. The first doublet in the experimental spectrum can be readily assigned to result from electronic transitions from the Si 2*p* orbitals into the $3a_1^*$ antibonding orbital plus overlapping weaker transitions. The low energy shoulder on the strongest peaks in the photoabsorption spectrum of $Si(CH_3)_3Cl$ in Fig. 2.5.2 is assigned to the $6a_1^*$ mixed character virtual orbitals and the stronger peaks are assigned to transitions into the $11a_1^*$ and $14a_1^*$ Rydberg orbitals. The weaker peaks closer to threshold are generically assigned as transitions into Rydberg orbitals. The Rydberg character predicted for the strong peaks in the Si 2*p* pre-edge photoabsorption spectrum of $Si(CH_3)_3Cl$ is at odds with the assignments for the other chloromethylsilane compounds where only the small peaks near threshold were assigned as Rydberg transitions. A photoabsorption spectrum of the solid phase of $Si(CH_3)_3Cl$ would help confirm the assignment.

2.5.2.2. Si 2*p* continuum

Cross sections for the Si 2*p* continuum regions of the five chloromethylsilane molecules were calculated using the converged Si 2*p* transition state potentials. The resulting theoretical cross sections are presented in Fig. 2.5.7 complete with the partial symmetry channel contributions to the cross sections. The three different symmetries of the chloromethylsilane molecules; T_d for $SiCl_4$ and $Si(CH_3)_4$, C_{3v} for $SiCH_3Cl_3$ and $Si(CH_3)_3Cl$ and C_{2v} for $Si(CH_3)_2Cl_2$ allow

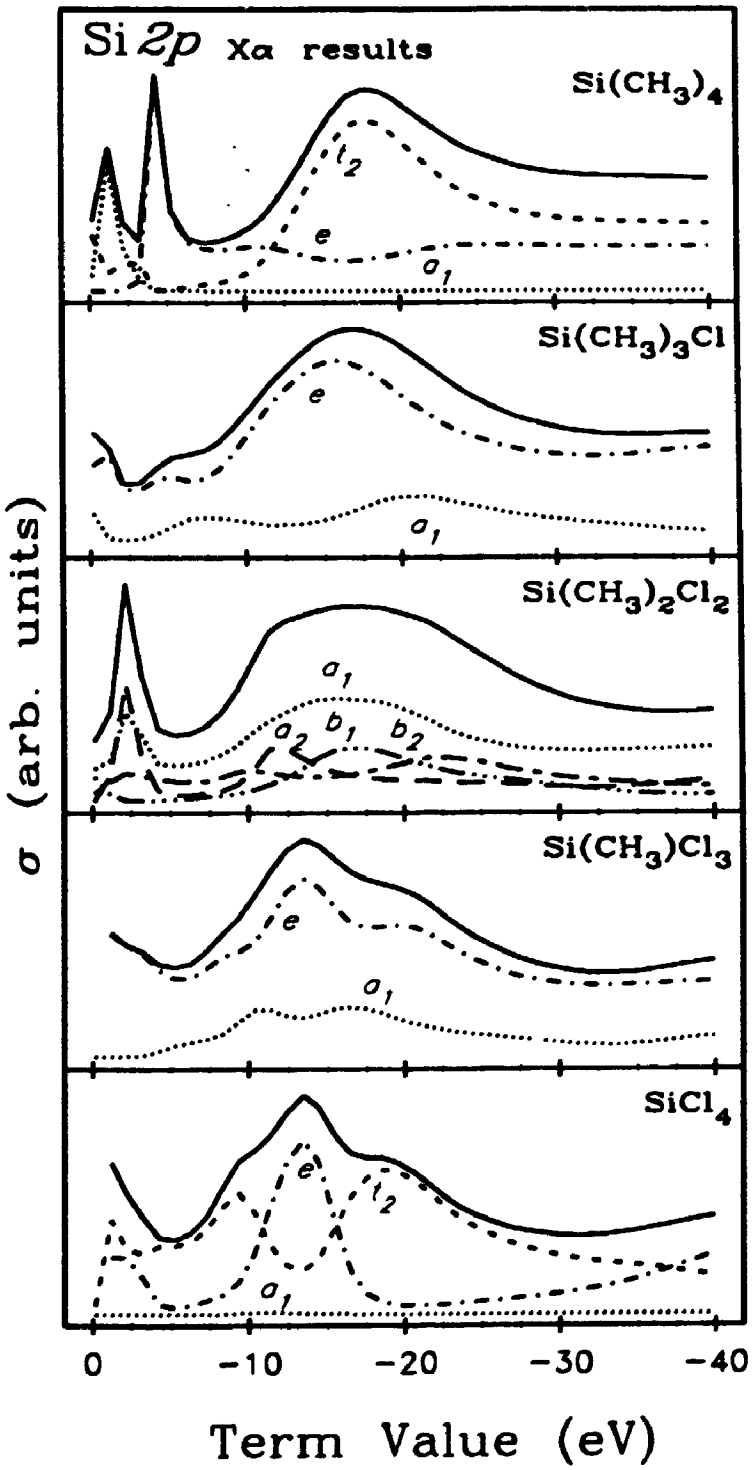

Figure 2.5.7: Theoretical Si 2*p* cross sections of the chloromethylsilane compounds from the MS-Xα calculations.

different outgoing channels from the Si 2*p* core electrons based on the electric dipole selection rules.[151] The symmetry channels contributing to the resonances in the theoretical cross sections are indicated on the curves in Fig. 2.5.7 and summarized in part (*b*) of Table 2.5.1 - Table 2.5.4 for $SiCl_4$ to $Si(CH_3)_3Cl$ respectively and in Table 2.4.5 for $Si(CH_3)_4$.

The calculated cross sections of the chloromethylsilane molecules in Fig. 2.5.7 are in good agreement with the experimental Si 2*p* continuum cross sections (Fig. 2.5.3), reproducing the shape of the spectra with little discrepancy. The spectra do not separate neatly into three resonances as did the spectra for the fluoromethylsilane compounds, so the correlations between the calculated and experimental spectra will be discussed on a molecule by molecule basis. Eigenphase sum changes are used to determine whether a resonance satisfies Kriele's criterion: that a cross section enhancement must be accompanied by a change $\geq 0.3\pi$ in the eigenphase sum of the partial symmetry channel containing the enhancement to be classified as a *shape resonance*.[153] The eigenphase sum changes at the calculated cross section enhancements are summarized in the tables and discussed in the following section.

The cross section for $SiCl_4$ in Fig. 2.5.7 reproduces all of the major features in the experimental spectrum with a cross section enhancement at threshold and three main peaks above threshold. All of the peaks in the theoretical spectrum satisfy Kriele's criteria[153] for shape resonances since the eigenphase sum changes are all $\geq 0.5\pi$ as summarized in Table 2.5.1 (*b*). Also given in the table are the symmetry channels contributing to the cross section maxima along with the term values. The ke symmetry channel is calculated to contribute most of the intensity to the resonance at threshold and the strong shape resonance $\sim$13 eV above threshold. The kt_2 splits around the strong ke resonance to give the two shape resonances above and below it.

The Si 2*p* continuum photoabsorption spectrum of $SiCH_3Cl_3$ is also well reproduced by the MS-Xα calculated cross sections with three principal peaks with contributions from both the ka_1 and ke outgoing channels. The resonance at threshold occurs in the ke channel which also contributes most of the intensity to the higher energy resonances with the rest contributed by the ka_1 channel. The term values, eigenphase sum changes and symmetry channels of the calculated cross section maxima are given in Table 2.5.2 (*b*). Except for the contributions from the ke channel to the higher energy resonance, the eigenphase sum changes of all of the resonance satisfy Kriele's criteria and are hence labelled shape resonances.[153]

The four allowed symmetry channels, ka_1, ka_2, kb_1 and kb_2. for the Si 2*p* continuum cross sections of the C_{2v} symmetry group molecule $Si(CH_3)_2Cl_2$ all contribute significant intensity to the total cross section as illustrated in Fig. 2.5.7. The low energy resonance (at threshold) is shifted slightly into the continuum by the MS-Xα calculation and has significant contributions from both the ka_1 and ka_2 symmetry channels with a minor contribution from the kb_2 channel. Only the ka_1 channel satisfies the criteria for a shape resonance as seen by the eigenphase sum changes in Table 2.5.3 (*b*). Further above the edge, the ka_1, ka_2 and kb_2 symmetry channels contribute to form roughly two resonances, one ~13 eV above the Si 2*p* threshold and the other ~18 eV above. The eigenphase sum changes of the contributing symmetry channels are summarized in Table 2.5.3 (*b*).

The MS-Xα calculated Si 2*p* continuum spectrum of $Si(CH_3)_3Cl$ is also in good agreement with the corresponding experimental spectrum. A weak resonance at threshold, which is not a shape resonance, has contributions from both the ka_1 and ke symmetry channels. Another weak resonance ~6 eV above threshold has shape resonance contributions from both symmetry channels. At higher energy, the ke channel exhibits a shape resonance which contributes most of the intensity to the broad feature observed experimentally 18 eV above threshold.

Although it does not appear so at first glance, the Si $2p$ continuum spectra of the fluoromethylsilane and chloromethylsilane compounds are similar in nature. The resonance at threshold has overlapping contributions from both the Si−Cl and Si−C bonds in the chloromethylsilane spectra while only the Si−C bonds contributed intensity to this resonance in the fluoromethylsilane compounds. At higher energies, Si−C bonds result in a weak resonance ~7 eV above threshold and the Si−Cl bonds in a stronger resonance ~12 eV above threshold. These Si−Cl resonances overlap with the higher energy Si $2p \rightarrow \epsilon d$ resonances ~20 eV above threshold. The presence of the electronegative F and Cl atoms therefore narrow and split the resonances above the ionization edge. The effect is more pronounced in the spectra of the fluoromethylsilane compounds (Fig. 2.4.6) where the splitting is greater, separating the resonances resulting from the Si−F and Si−C bonds. In the chloromethylsilanes, the effect is not as strong since the Cl atoms do not perturb the potential around the Si atom as much as the fluorine atoms do and the Si−Cl resonances therefore overlap with the Si−C resonances and the higher energy Si $2p \rightarrow \epsilon d$ resonance.

2.5.2.3. Si $2s$ pre-edge

In a method analogous to the one used to construct the simulated Si $2p$ pre-edge spectra from the calculated parameters, the eigenvalues of unoccupied levels were identified with energy searches to within 0.05 Rydbergs of the vacuum level using the converged MS-Xα Si $2s$ transition state potentials for all of the chloromethylsilane molecules. The resulting eigenvalues were used to calculate oscillator strengths and both used to construct theoretical Si $2s$ pre-edge absorption spectra. The line positions (eigenvalues) and intensities (oscillator strengths) were convoluted with Lorentzian line shapes with half-height widths of 1.0 eV and the resulting theoretical spectra are presented in Fig. 2.5.8

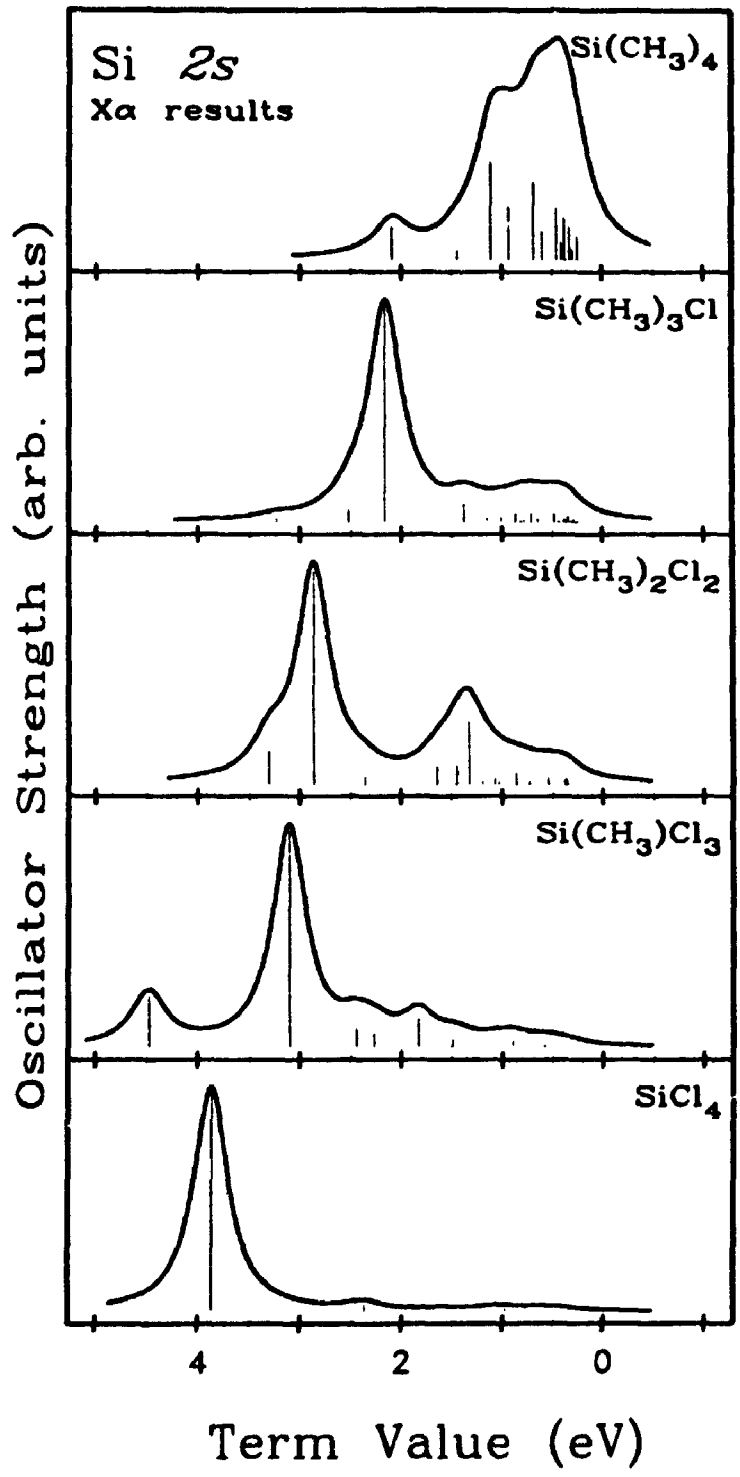

Figure 2.5.8: Theoretical Si 2*s* pre-edge absorption spectra of the chloromethylsilane compounds constructed from the eigenvalues and oscillator strengths from the MS-Xα calculations.

The theoretical Si 2*s* pre-edge photoabsorption spectra in Fig. 2.5.8 are in reasonable agreement with the experimental spectra in Fig. 2.5.4, where the spectra of the chlorine containing molecules are dominated by one strong absorption band. The 1 eV linewidth used for the Lorentzian lineshape convolution with the calculated eigenvalues and oscillator strengths does not properly approximate the true linewidth. The narrower linewidth was deliberately chosen to highlight the positions of individual bands in the theoretical spectrum. Eigenvalues of the major peaks in the theoretical spectra are included in Table 2.5.1 (*c*) to Table 2.5.4 (*c*) together with the symmetries of the virtual orbitals. The MS-Xα calculations reproduce the shift in term values of the main peak with replacement of Cl atoms by methyl ligands. The experimental(theoretical) values shift from 5.0(3.9) eV in $SiCl_4$ to 4.8(3.11) eV in $SiCH_3Cl_3$, 4.5(2.9) eV in $Si(CH_3)_2Cl_2$, 4.0(2.2) eV in $Si(CH_3)_3Cl$ and 2.8(1.1) eV in $Si(CH_3)_4$. The calculations overestimate the shift of the peak positions as was observed for the peaks below the Si 2*p* edge. The virtual orbitals responsible for the main peaks in the Si 2*s* pre-edge photoabsorption spectra of the chloromethylsilane compounds were found to be orbitals with antibonding character.

The MS-Xα calculations do not reproduce the behavior of the second peak in the Si 2*s* pre-edge, which was assigned to result from electronic transitions of the Si 2*s* electron into the Si−C antibonding orbitals in section 2.5.1.3. There is a systematic increase in the relative intensities of peaks ~1−2 eV above the main Si−Cl peaks in the theoretical spectra of $SiCl_4$, $SiCH_3Cl_3$ and $Si(CH_3)_2Cl_2$. In the theoretical spectrum of $Si(CH_3)_3Cl$, however, the intensity of peaks above the main line are greatly decreased. Transitions to orbitals with primarily mixed antibonding-Rydberg and Rydberg character were found to account for most of the intensity observed in these peaks above the Si−Cl main lines.

2.5.2.4. Si 2*s* continuum spectra

The Si 2*s* continuum cross sections of the chloromethylsilane molecules were calculated using the converged MS-Xα Si 2*s* transition state potentials. The resulting cross sections and partial symmetry channel contributions to the total cross section are presented in Fig. 2.5.9. Term values of the main features in the calculated cross sections along with the corresponding changes in the eigenphase sums and the contributing symmetry channels are summarized in Table 2.5.1 (*c*) – Table 2.5.4 (*c*) for $SiCl_4$ to $Si(CH_3)_3Cl$ and in Table 2.4.5 (*c*) for $Si(CH_3)_4$. At first glance, the calculated Si 2*s* cross sections are not in agreement with the experimental Si 2*s* continuum photoabsorption spectra (Fig. 2.5.4) for the chloromethylsilane compounds. Upon more careful consideration, however, the agreement is not as poor as it first appears.

In the Si 2*s* continuum region of $SiCl_4$, for example, good agreement is found between the calculated positions of the resonances and the positions observed in the experimental spectrum (Table 2.5.1 (*c*)). The calculated positions of the low and high energy resonances, −0.1 eV and −18.5 eV respectively, are in agreement with the experimentally observed positions of −0.1 and−19.7 eV. The medium energy resonance found in the calculated cross section at −9.3 eV is observed experimentally as two resonances split about that energy, at −7.2 and −11.4 eV. All of the calculated resonances are found in the kt_2 symmetry channel by the selection rules[151] for the a_1 type Si 2*s* orbitals in the T_d molecule $SiCl_4$. The three calculated resonances are also found to obey Kriele's criteria for shape resonances[153] since the eigenphase sums are found to change by $\geq 0.3\pi$ at the positions of the resonances.

Agreement between theory and experiment is not as obvious for $SiCH_3Cl_3$ where the three peaks observed at lower energies in the experimental Si 2*s* continuum photoabsorption spectrum are reproduced by the MS-Xα calculations, but the higher energy resonance at ~20.3 eV is not. The relative calculated

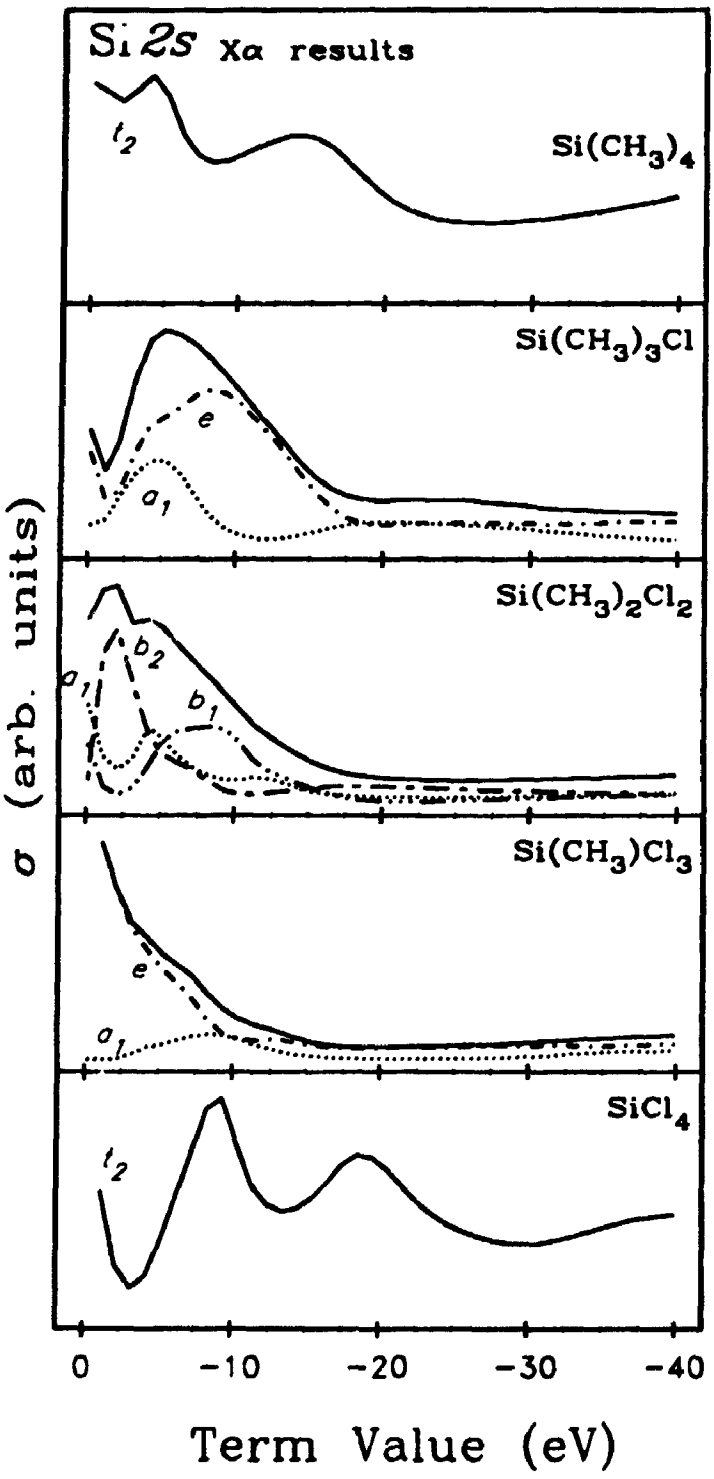

Figure 2.5.9: Theoretical Si 2*s* cross sections of the chloromethylsilane compounds from the MS-Xα calculations.

intensities of the lower energy resonances are not in agreement with the experimental intensities, but the positions of the peaks in the theoretical cross section, −1.0, −8.3, and −12.4 eV, are in good agreement with the experimental values of −0.3, −5.6, and −13.2 eV (Table 2.5.2 (*c*)). Changes in the eigenphase sums indicate that all of the above peaks in the MS-Xα cross section meet Kriele's criteria for shape resonances[153] and the assignment to symmetry channels is summarized in Table 2.5.2 (*c*).

While the Si 2*s* theoretical cross section of $Si(CH_3)_2Cl_2$ in Fig. 2.5.9 does not look at all like the experimental spectrum in Fig. 2.5.4, the positions of the five resonances in the ka_1, kb_1 and kb_2 symmetry channels, summarized in Table 2.5.3 (*c*), are similar to the experimental resonance positions. Apart from the weak high energy resonance at −18.5 eV in the MS-Xα calculations, the eigenphase sums at the positions of the other resonances show changes of $>0.3\pi$. The peaks observed in the experimental spectrum are therefore assigned as shape resonances in the symmetry channels indicated in Table 2.5.3 (*c*).

A similar correlation between the calculated and experimental resonance positions is seen for the Si 2*s* continuum region of $Si(CH_3)_3Cl$ as summarized in Table 2.5.4 (*c*). The shape of the calculated MS-Xα cross sections in Fig. 2.5.9 is also in reasonable agreement with the shape of the experimental spectrum in Fig. 2.5.4 with a broad unresolved "hump" centered ~10 eV above the Si 2*s* ionization threshold. Positions, symmetries and eigenphase sum changes of the theoretical resonances are included in Table 2.5.4 (*c*). Except for the high energy peak in the ka_1 channel at −20.5 eV, all of the resonances meet the criteria to be classified as shape resonances.

The MS-Xα calculated Si 2*s* continuum cross section for $Si(CH_3)_4$ (Fig. 2.5.9) is in good agreement with the experimental photoabsorption spectrum (Fig. 2.5.4) and reproduces the positions and intensities of the first three resonances quite well. Because of the dipolar selection rules, all of the calculated resonances for

the tetrahedral molecule, $Si(CH_3)_4$, are found in the kt_2 symmetry channels. The calculated term values and eigenphase sum changes at those positions are summarized in Table 2.4.5 (c). From these values, the resonances at -4.2 eV and -14.4 eV are found to be shape resonances while those at lower term values, -0.1 eV, and higher term values -40.0 eV do not meet Kriele's criteria.

Overall, the calculated Si $2s$ absorption peak positions are shown to be in reasonable agreement with the experimental spectra, reproducing the number and positions of the experimentally observed resonances. The relative intensities of the calculated absorption peaks do not show the same degree of agreement with the experimental data. The MS-Xα calculations are essential for the assignment of the experimentally observed absorption peaks to their appropriate symmetry channels.

2.6. RESULTS: Chlorosilane compounds, SiH_xCl_{4-x}

2.6.1. Experimental photoabsorption spectra

Photoabsorption spectra of the four available chlorosilane molecules are presented in Fig. 2.6.1 over the photon energy range 100–225 eV which encompasses the discrete and continuum regions of the Si 2*p*, Si 2*s* and Cl 2*p* ionization edges for all of the molecules. A sample of SiH_3Cl was not available and hence the experimental photoabsorption spectra of SiH_3Cl are not reported here. The photoabsorption spectrum of SiH_4 was terminated at a photon energy of 200 eV since no Cl 2*p* structure is present in the spectrum of this molecule. Ionization edges for the Si 2*p* and Si 2*s* core levels for each of the molecules are indicated on the experimental data curves with the flag at lower energy corresponding to the weighted averaged Si 2*p* ionization potential and the higher energy mark at ~160 eV indicating the Si 2*s* ionization edges. The Si 2*p* ionization potential values were obtained from the Si 2*p* photoelectron spectra of $SiCl_4$, SiH_2Cl_2 and SiH_4 reported in chapter 4 of this thesis. The Si 2*p* ionization threshold for $SiHCl_3$ was obtained from a previously reported Si 2*p* photoelectron spectrum of the molecule.[158] Values have not been reported for the Si 2*s* ionization edges of these molecules and hence the method used to estimate the Si 2*s* ionization potential from the Si 2*p* ionization potential and the Si 2*p* – Si 2*s* splitting of 51.2 eV used for the fluoromethylsilane molecules was repeated.[118,142]

Several features of the chlorosilane molecules are obvious in the wide range scans in Fig. 2.6.1. The spectra share many overall similarities with a series of strong absorption peaks below the Si 2*p* ionization edges (~100 eV), broader structure above the Si 2*p* ionization edges, relatively sharp and strong absorption below the Si 2*s* ionization edges (~160 eV) followed by weak oscillatory behaviour above the Si 2*s* ionization edges. In the chlorine containing chlorosilane compounds, series of sharp peaks are also seen merging into the continua which

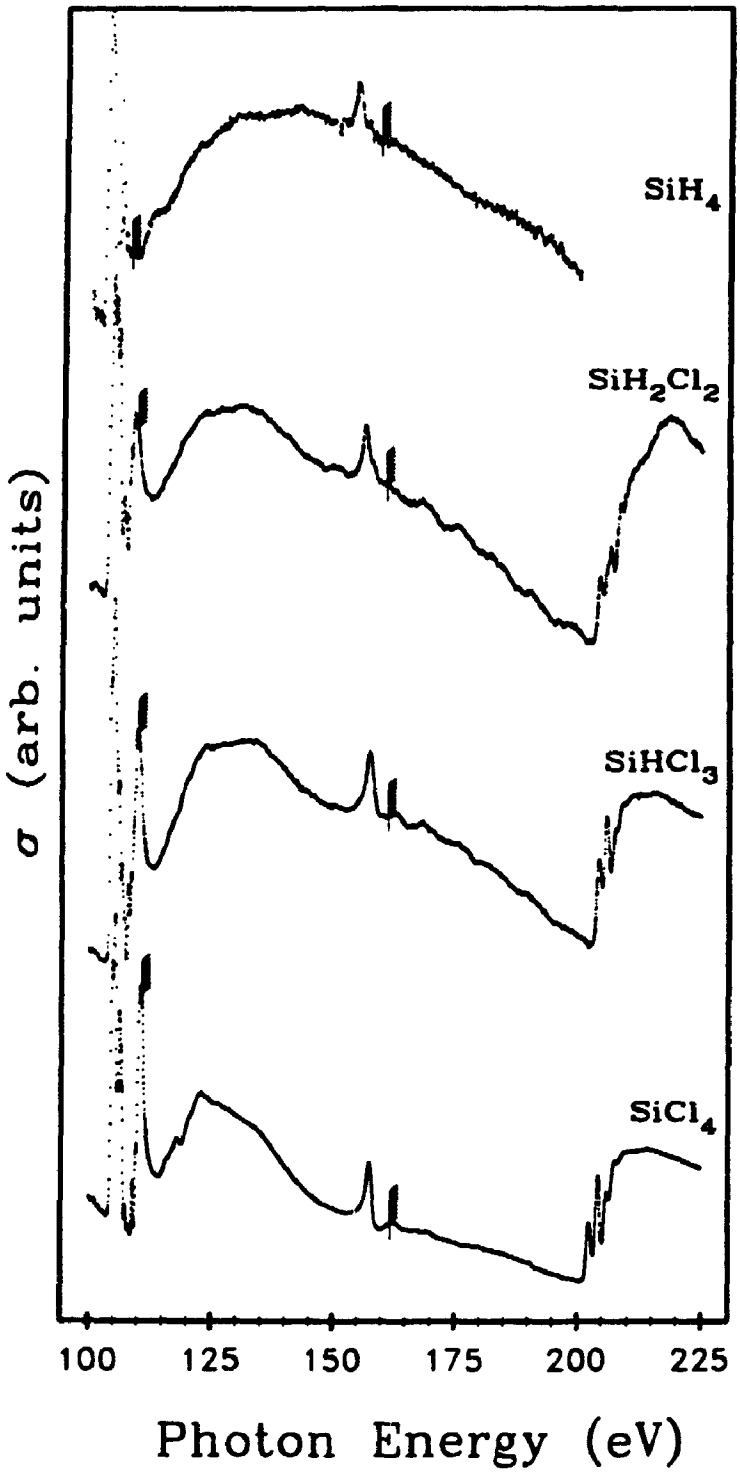

Figure 2.6.1: Photoabsorption spectra of the Si 2*p*, Si 2*s* and Cl 2*p* regions of the chlorosilane compounds.

exhibit maxima at or just above threshold. The discrete and continuum structure for all of the edges are superimposed upon a decreasing background from the inner valence levels of the molecules. The decreasing background is not as dominant as in the fluoromethylsilane compounds where absorption by the fluorine inner-valence orbitals significantly affected the shape of the absorption spectrum.

Resonances in the discrete and continuum regions of the Si 2*p*, Si 2*s* and Cl 2*p* core-level ionization edges are discussed in detail in the following section. The spectra are further compared and contrasted with the spectra of the chloromethylsilane and fluoromethylsilane compounds presented in the previous sections.

2.6.1.1. Si 2*p* pre-edge spectra

High resolution photoabsorption spectra of the Si 2*p* pre-edge regions of the chlorosilane molecules are presented in Fig. 2.6.2. The two components of the spin-orbit split Si 2*p* ionization potentials are indicated by the dashed lines on the photoabsorption spectra. Values for the Si 2*p* ionization potentials and the positions of the indicated features are given in the tables in this section. Similar trends to those noted for the fluoromethylsilane and chloromethylsilane molecules in the preceding sections are seen in these spectra.

The term values of the first resonance below the Si 2*p* ionization edges of the chlorosilane compounds tend to decrease slightly with substitution of a H for a Cl ligand around the central Si atom. The decrease in term values from 5.9 eV for $SiCl_4$ to 4.8 for SiH_4, is not as pronounced as in the spectra of the fluoromethylsilane and chloromethylsilane molecules where much larger changes in the term values for the first peak were observed. The different behavior for the chlorosilane compounds is a reflection of the different effects of the methyl ligands and the hydride ligand on the electronic structure surrounding the Si atom. Methyl ligands are electron donating and therefore increase the valence electron

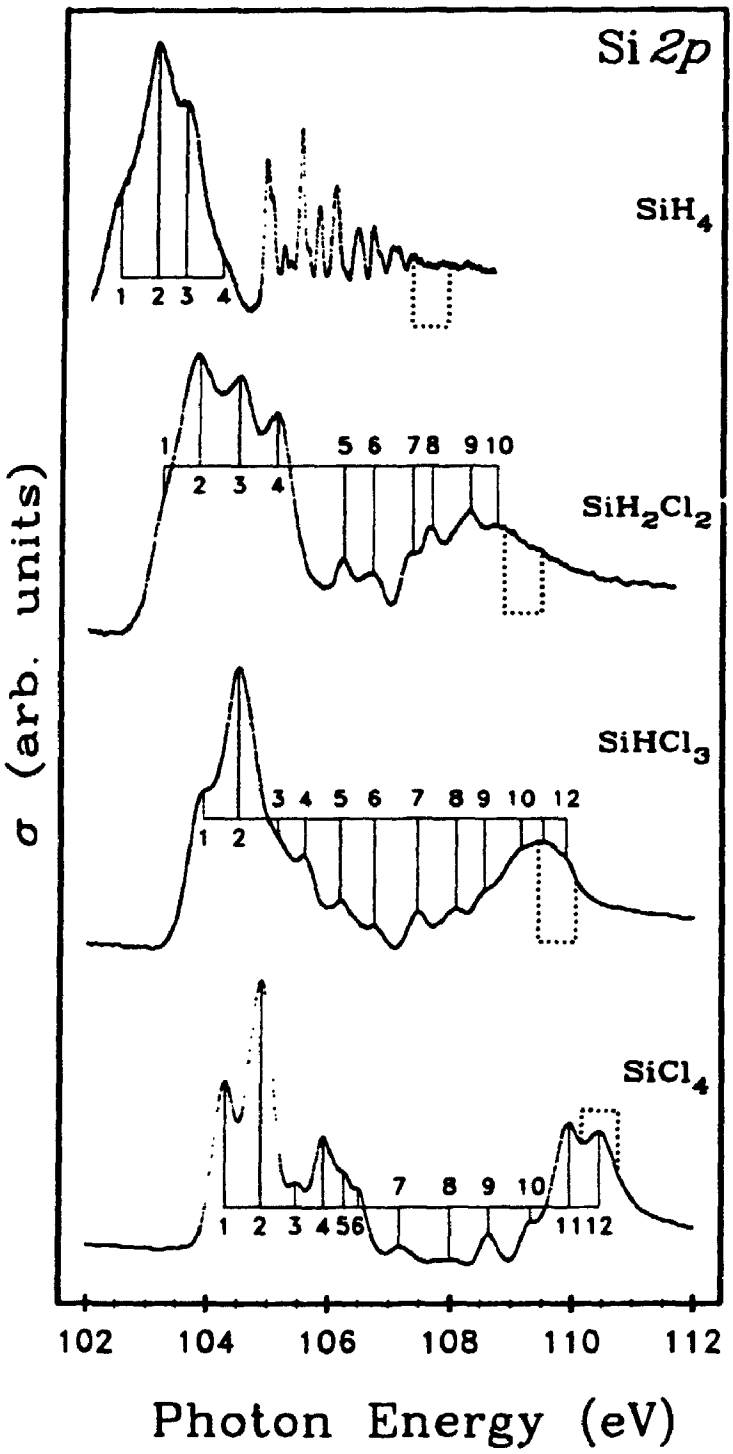

Figure 2.6.2: Photoabsorption spectra of the Si 2*p* pre-edge regions of the chlorosilane compounds.

density around the central atom. Hydride ligands, conversely, do not perturb the electronic structure of the moieties to which they are bound as significantly. The effect of replacing an electron withdrawing Cl atom with a H atom on the electron density around the Si atom is therefore less pronounced than the replacement with a methyl group. This primarily affects the core level binding energies, where electron withdrawing groups such as F and Cl atoms shift the Si $2p$ binding energy higher while electron donating groups such as CH_3 (and to a lesser extent H) shift it to lower values. The shift in the Si $2p_{3/2}$ binding energy from $SiCl_4$ (110.16 eV) to SiH_4 (107.31) of ~2.8 eV is larger than the ~1.0 eV shift in term values for the first peak in the absorption spectra. Different shifts for the ionization potential and term values of the lowest energy photoabsorption feature are observed here because the Si $2p$ pre-edge absorption spectrum probes the virtual electronic structure of a molecule, while the change in binding energy is a function of the electron density around the atomic center being ionized. Obviously the electron density around the Si atom is perturbed to a greater extent than is the virtual electronic structure upon replacement of a Cl with a H. The virtual electronic structure of a molecule is dependent upon many factors including bond strength and the presence or absence of antibonding orbitals in these molecules and does not strictly reflect the electronic density around the central atom.

There are no peaks whose relative intensities follow the number of ligands of a specific type in these spectra as were observed for the fluoromethylsilane and chloromethylsilane compounds. It is, however, interesting to compare the Si $2p$ pre-edge spectra of $SiHCl_3$ and SiH_2Cl_2 with the spectra of the analogous $SiCH_3Cl_3$ and $Si(CH_3)_2Cl_2$ to elucidate the different effects of the methyl and hydride ligands on the spectra. The spectra of $SiHCl_3$ (Fig. 2.6.2) and $SiCH_3Cl_3$ (Fig. 2.5.2) are similar, but the band (5–7) observed in the spectrum of $SiCH_3Cl_3$ which was attributed to the Si–CH_3 bond is absent from the $SiHCl_3$ spectrum. This observation strongly supports the previous assignment of this band to the Si–CH_3

antibonding orbital. The Si 2*p* pre-edge spectra of SiH_2Cl_2 and $Si(CH_3)_2Cl_2$ are not as similar as the spectra of the trichloro species, but only one broad intense band (1–4) is observed in the SiH_2Cl_2 spectrum whereas two bands (1–3 and 4–6) were seen in the $Si(CH_3)_2Cl_2$ spectrum in Fig. 2.5.2. This observation provides further supporting evidence for the previous assignment of the band with peaks 4–6 as being due to the Si–C antibonding orbitals. The structure of the first band in the Si 2*p* absorption spectrum of the SiH_2Cl_2 is considerably broader than the corresponding band in the $Si(CH_3)_2Cl_2$ spectrum. Contributions from the Si–H antibonding orbitals which are apparent as the broad peaks in the Si 2*p* pre-edge photoabsorption spectrum of SiH_4, therefore appear to be overlapping with peaks from transitions to the Si–Cl antibonding orbitals.

Apart from the very narrow peaks at intermediate photon energy in the Si 2*p* pre-edge photoabsorption spectrum of SiH_4, peaks in the Si 2*p* pre-edge photoabsorption spectra of the chlorosilane molecules are all relatively broad and only partially resolved. This indicates that vibrational broadening due to the excitation of the Si–Cl and Si–H vibrational modes are responsible for the observed breadth of the peaks as in the chloromethylsilane molecules. The spectrum of SiH_4 is a special case and will be discussed in detail.

The Si 2*p* pre-edge photoabsorption spectrum of $SiCl_4$ was discussed in detail in the previous section on the chloromethylsilane molecules and will not be discussed again here. Three bands of considerable intensity were identified, peaks 1-2, 4–6 and 11-12 and the spectrum is repeated in Fig. 2.6.2 for purposes of comparison.

A high resolution Si 2*p* pre-edge photoabsorption spectrum of $SiHCl_3$ is presented in Fig. 2.6.2. This spectrum has not been reported previously. The positions and term values of the features identified on the spectrum are summarized in Table 2.6.1 (*a*) along with the Si $2p_{3/2}$ and Si $2p_{1/2}$ ionization energies from the low resolution photoelectron spectrum of the molecule. As noted previously, the spectrum is very similar to that of $SiCH_3Cl_3$ (Fig. 2.5.2)

(a) Si 2p pre-edge

peak label	energy (eV)	term value (eV)		assignments		
		$Si2p_{3/2}$	$Si2p_{1/2}$	resonance		$Si2p_{3/2} \rightarrow$
1	103.92	5.52	6.13	a		$1a_1^*$
2	104.50	4.94	5.55	b	a	$1e^*$, $2a_1^*$
3	105.11	4.33	4.94		b	-
4	105.60	3.84	4.45	c		$3a_1^*$
5	106.18	3.26	3.87	d	c	$4a_1^*$
6	106.74	2.70	3.31	e	d	Ryd.
7	107.44	2.00	2.61	f	e	Ryd.
8	108.08	1.36	1.97		f	-
9	108.54	0.90	1.51	g		Ryd.
10	109.14	0.30	0.91		g	-
11	109.50	0.06	0.67	h		Ryd.
12	109.89	−0.45	0.16		h	-
$Si2p_{3/2}$	109.44	-	-	-	-	-
$Si2p_{1/2}$	110.05	-	-	-	-	-

(b) Si 2p continuum

peak label	energy (eV)	term value (eV)	calc. term value (eV)	phase shift (π)	symmetry channel
1	111.2	−1.4	−1.0	0.5	ke
2	116.5	−6.7	−8.3	0.9,0.4	ke+ka_1
3	122.7	−12.9	−13.9	0.6,0.5	ke+ka_1
4	134.4	−24.6	−18.5	0.9	ke

(c) Si 2s

peak label	energy (eV)	term value (eV)	calc. term value (eV)	phase shift (π)	symmetry
1	154.2	6.9	5.42	-	a_1^*
2	155.8	5.3	4.07, 3.87	-	e^*, a_1^*
3	158.7	2.4	2.88 ,2.64	-	a_1^*,e^*
Si2s	161.1	-	-	-	-
4	161.2	−0.1	−0.5	0.6	ke
5	167.2	−6.1	−6.7	0.3,1.7	ka_1 + ke
6	175.1	−14.0	−12.4	0.3,1.4	ke+ka_1
7	182.6	−21.5	−18.5	0.6	ke

Table 2.6.1: Energies, term values and assignments of the discrete and continuum resonances in the Si 2*p* and 2*s* photoabsorption spectra of $SiHCl_3$

with the exception of the missing Si−C band. By comparing the term values of

the peak positions with respect to both the Si $2p_{3/2}$ and Si $2p_{1/2}$ ionization edges, the peaks can be readily grouped into spin orbit split resonances. Eight such pairs are easily identified by selecting pairs with term values that differ by $\leq$0.1 eV and are labelled with lower case letters in Table 2.6.1 (a). The intensity ratios of the peaks are not inconsistent with the assignment given, but spurious pairings could result from coincidental spacing of peaks by ~0.6 eV. The strong peaks observed with relatively large term values (peaks 1−3) are assumed to result from electronic transitions from the Si $2p$ levels into antibonding orbitals while the weaker peaks result from transitions into Rydberg orbitals. The assignment will be discussed in further detail in the discussion section with the aid of MS-Xα calculations.

The high resolution Si $2p$ pre-edge photoabsorption spectrum of SiH_2Cl_2 is also presented in Fig. 2.6.2 for the first time. Peak positions and corresponding term values are summarized in Table 2.6.2 along with values for the Si $2p_{3/2}$ and Si $2p_{1/2}$ ionization potentials from chapter 4. Spin-orbit split resonances were identified by comparing the term values with respect to both the Si $2p_{3/2}$ and Si $2p_{1/2}$ ionization thresholds. Five spin-orbit pairs were found to within 0.1 eV of threshold: 1-2, 2-3, 3-4, 6-7 and 8-9. In order to account for the sharp peak at position 5, a spin-orbit pair 5-6 was also included. The broad asymmetric shape of peak 6 is not inconsistent with this assignment. In addition, to account for the relatively strong intensity and asymmetric shape of peak 9, as well as the presence of peak 10, a further pair 9-10 was also identified. The general shape of the spectrum, with strong absorption peaks well below the Si $2p$ ionization edges followed by weaker peaks leading up to the edge is consistent with the $SiHCl_3$ spectrum and a similar assignment of transitions to antibonding orbitals and Rydberg orbitals respectively probably holds.

A high resolution photoabsorption spectrum of the discrete regions of the Si $2p$ ionization edges of SiH_4 is also presented in Fig. 2.6.2. To highlight the complex structure in the finely spaced absorption lines near threshold, the spectrum is also

(a) Si 2p pre-edge

peak label	energy (eV)	term value (eV)		assignments		
		$Si2p_{3/2}$	$Si2p_{1/2}$	resonance		$Si2p_{3/2} \rightarrow$
1	103.25	5.62	6.23	a		$1a_1^*$
2	103.83	5.04	5.65	b	a	$1b_1^*$, $2a_1^*$
3	104.49	4.38	4.99	c	b	$1b_2^*$
4	105.10	3.77	4.38		c	
5	106.23	2.64	3.25	d		$3a_1^*$
6	106.71	2.16	2.77	e	d	$2b_2^*$
7	107.34	1.53	2.14		e	
8	107.67	1.20	1.81	f		$5a_1^*$ + Ryd.
9	108.30	0.57	1.18	g	f	$3a_2^*$ + Ryd.
10	108.75	0.12	0.73		g	
$Si2p_{3/2}$	108.87	-	-	-	-	-
$Si2p_{1/2}$	109.48	-	-	-	-	-

(b) Si 2p continuum

peak label	energy (eV)	term value (eV)	calc. term value (eV)	phase shift (π)	symmetry channel
1	110.5	−1.2	−2.2	0.5	ka_1
2	116.7	−7.4	−4.2,−7.3	1.4,0.6	$kb_1 + ka_2$
3	121.7	−12.4	−12.4	0.8	ka_1
4	133.9	−24.6	−18.5	0.4, 0.1	$ka_1 + kb_1$

(c) Si 2s

peak label	energy (eV)	term value (eV)	calc. term value (eV)	phase shift (π)	symmetry
1	154.4	6.9	5.61,5.20	-	b_1^*,a_1^*
2	155.5	5.3	3.32	-	b_1^*
Si2s	160.5	-	-	-	-
3	160.6	−0.1			
4	166.7	−6.2	−5.2,−7.3	0.9,0.9	$ka_2 + kb_1$
5	174.4	−13.9	−13.4	0.1	kb_1
6	183.0	−22.5			

Table 2.6.2: Energies, term values and assignments of the discrete and continuum resonances in the Si 2*p* and 2*s* photoabsorption spectra of SiH_2Cl_2.

presented on a larger scale in Fig. 2.6.3 where 21 absorption lines are indicated and the Si 2*p* ionization potentials are marked with dashed lines. The positions and term values of the indicated features on Fig. 2.6.3 and values for the Si 2*p* ionization

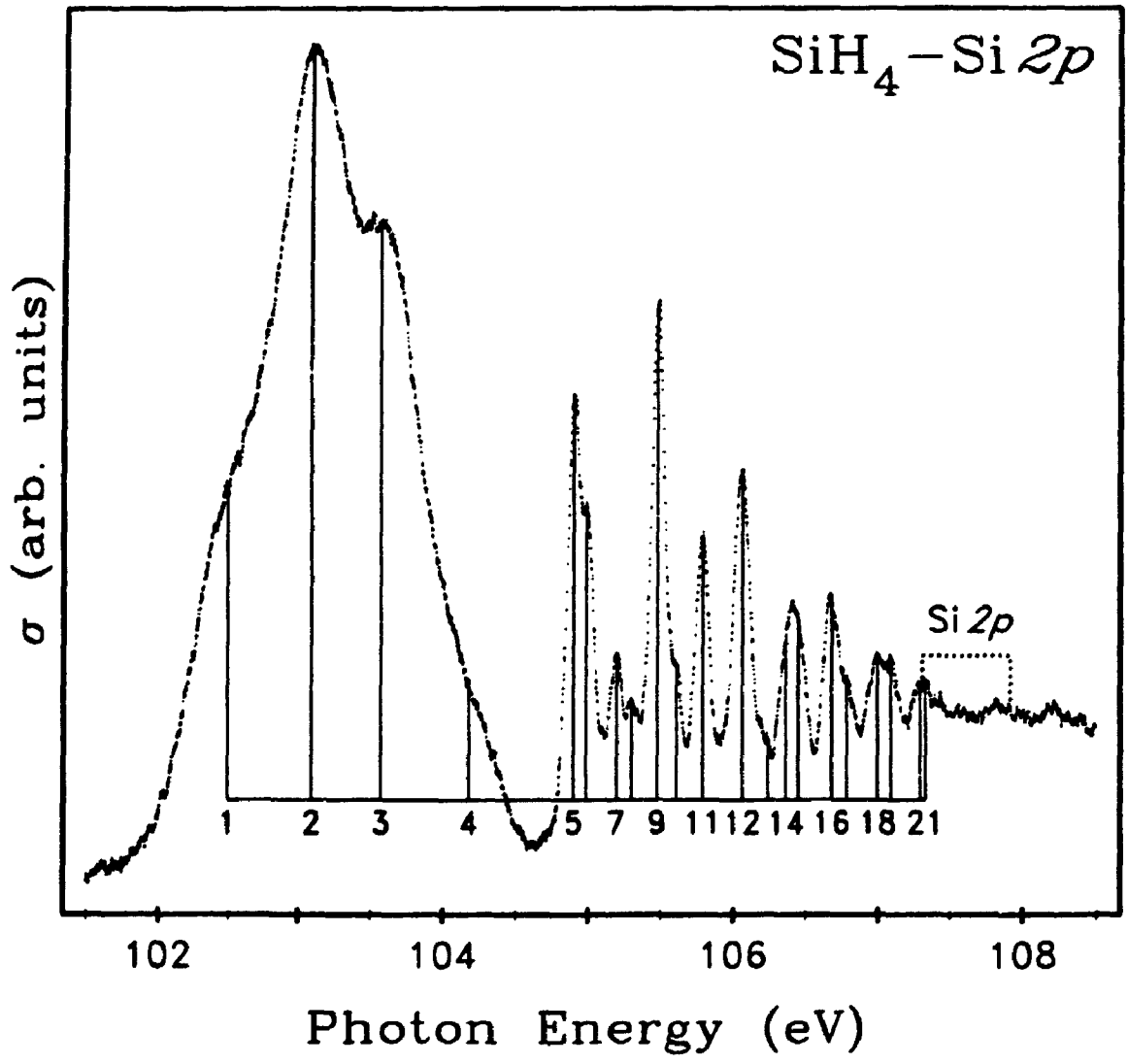

Figure 2.6.3: High resolution photoabsorption spectrum of the Si2*p* pre-edge region of SiH_4.

(a) Si 2p pre-edge

peak label	energy (eV)	term value (eV)		assignments		
		$Si2p_{3/2}$	$Si2p_{1/2}$	resonance		$Si2p_{3/2} \rightarrow$
1	102.49	4.82	5.43	a		$1t_2^*$
2	103.09	4.22	4.83	b	a	$1a_1^*$
3	103.57	3.74	4.35	c	b	$1e^*$
4	104.18	3.13	3.74		c	-
5	104.90	2.41	3.02	d		Ryd.
6	104.99	2.32	2.93	e		Ryd.
7	105.20	2.11	2.72	f		vib.
8	105.30	2.01	2.62			vib.
9	105.48	1.83	2.44	g	d	Ryd.
10	105.61	1.70	2.31	h	e	Ryd.
11	105.79	1.52	2.13	i	f	Ryd.
12	106.06	1.25	1.86	j	g	Ryd.
13	106.24	1.07	1.68		h	Ryd.
14	106.37	0.94	1.55	k	i	Ryd.
15	106.45	0.86	1.47	l		Ryd.
16	106.68	0.63	1.24	m	j	Ryd.
17	106.79	0.52	1.13	n		Ryd.
18	107.00	0.31	0.92		k	-
19	107.09	0.22	0.83		l	-
20	107.30	0.01	0.62		m	-
21	107.33	-0.02	0.59		n	-
$Si2p_{3/2}$	107.31	-	-	-	-	-
$Si2p_{1/2}$	107.92	-	-	-	-	-

(b) Si 2p continuum

peak label	energy (eV)	term value (eV)	calc. term value (eV)	phase shift (π)	symmetry channel
1	112.2	−4.5	−9.3	0.6	ke
2	119.6	−11.9	−13.4	1.1	kt_2

(c) Si 2s

peak label	energy (eV)	term value (eV)	Si 1s term value (eV)†	calc. term value (eV)	phase shift (π)
1	154.3	4.6	4.5	4.22	-
2	156.6	2.3	2.8	2.20	-
3	157.8	1.1	1.2	1.11	-
Si2s	158.9	-	-	-	-
4	162.0	−3.1		−1.2	0.0

† Ref. 117

Table 2.6.3: Energies, term values and assignments of the discrete and continuum resonances in the Si 2p and 2s photoabsorption spectra of SiH_4

potential (from chapter 3) are summarized in Table 2.6.3 (*a*). High resolution spectra of the Si 2*p* pre-edge absorption spectra of SiH_4 have been reported previously.[71-74] The spectrum reported here is in excellent agreement with the previously reported spectra obtained at slightly higher photon resolutions. Term values of the observed peaks vary somewhat in the previous reports because until very recently, the Si 2*p* ionization potentials had not been accurately measured by photoelectron spectroscopy. The Si 2*p* ionization potentials reported in Table 2.6.3 are from the very high resolution Si 2*p* core level photoelectron spectrum reported in Chapter 3, and are the most accurately determined values to date.

The Si 2*p* pre-edge photoabsorption spectrum of SiH_4 consists of two parts which will be considered separately: a broad overlapping band at low photon energy and a series of sharp absorption lines closer to threshold. The broad band has been assigned to result from transitions of the Si 2*p* electrons into antibonding orbitals because it is observed in both the gas phase and solid state spectra.[71,74] The presence of an excited electron in an antibonding orbital can result in a large change in the equilibrium nuclear geometry of the molecule, resulting in the excitation of numerous vibrational states and the broad lines observed. The sharper lines close to threshold result from excitations into Rydberg orbitals which do not significantly change the bonding properties of the molecule and hence less vibrational broadening is observed. These sharp lines are washed out in the solid state spectrum.[71,74] The broad bands in the Si 2*p* absorption spectrum of SiH_4 centered at $h\nu \sim 103$ eV are assigned to two overlapping spin-orbit split resonances based on both the differences in term values with respect to the Si $2p_{3/2}$ and Si $2p_{1/2}$ ionization edges (Table 2.6.3 (*a*)). Peaks 1-2 and 3-4 form two obvious spin-orbit split resonances based strictly on their term values. The intensities of the four unresolved bands are not consistent with this assignment however, as the Si $2p_{1/2}$ component of the 1-2 resonance is about twice as intense as the Si $2p_{3/2}$ component whereas the Si $2p_{3/2}$ component of the second resonance resonance is

approximately four times larger than the corresponding $2p_{1/2}$ component. This band could possibly be assigned with a third resonance, 2-3, overlapping with the other two resonances. While peaks 2 and 3 are separated by only 0.48 eV (not the 0.61 eV Si $2p$ spin-orbit splitting value), the broad unresolved nature of the band could contain the necessary peaks for the third unresolved resonance. The assignment of the broad band will be discussed in more detail in the discussion section with the aid of results from the MS-Xα calculations.

The assignment of the sharp structure to Rydberg series has been carried out previously[71-74] but the assignments are at odds with one another. At least 11 spin-orbit split pairs of Rydberg lines can be identified from the term values of the peaks positions with respect to both the Si $2p_{3/2}$ and Si $2p_{1/2}$ ionization thresholds. The spin-orbit split resonances are identified by letters in the "resonance" columns of Table 2.6.3 (a). To help clarify the assignment of the many lines in the Si $2p$ pre-edge photoabsorption spectrum of SiH_4, the term values of the resonances assigned in Table 2.6.3 (a) have been used to determine effective quantum numbers, $n - \delta$, for the Rydberg orbitals according to the relationship[159]

$$n - \delta = \left(\frac{109734}{TV}\right)^{\frac{1}{2}} \tag{2.6.1}$$

where n is the true quantum number of the Rydberg level, δ the quantum defect and TV the term value of the feature in units of cm^{-1}. The results are summarized in Table 2.6.4.

Three spin-orbit split series, A–C are assigned to the spectrum based on the effective quantum number values in Table 2.6.4. The Si $2p_{3/2}$ members of each series are identified by the subscripted labels, i.e. A_1, A_2, ..., and the Si $2p_{1/2}$ components are identified with the primed label, i.e. A'_1, A'_2, ..., in Table 2.6.4. No attempt is made at this point to identify the azimuthal quantum numbers of the Rydberg series. Peaks 7 and 8 are assigned as vibrational components of the strong peaks 5 and 6 as they are separated by 0.31 eV which is consistent with

peak number	term values (eV)	term values (cm^{-1})	$(109\ 734/TV)^{1/2}$	assignment Si $2p_{3/2} \Rightarrow$	assignment Si $2p_{1/2} \Rightarrow$
5	2.41	19 438	2.376	A_1	-
6	2.32	18 712	2.422	B_1	-
7	2.11	17 018	2.539	*vib*-A_1	-
8	2.01	16 212	2.602	*vib*-B_1	-
9	1.83	14 760	2.727	C_1	A_1'
10	1.70	13 711	2.829	-	B_1'
11	1.52	12 260	2.992	*vib*-C_1	*vib*-A_1'
12	1.25	10 082	3.299	A_2	C_1'
13	1.07	8 630	3.566	B_2	-
14	0.94	7 582	3.804	C_2	*vib*-C_1'
15	0.86	6 936	3.978	*vib*-A_2	-
16	0.63	5 081	4.647	B_3, C_3	A_2'
17	0.52	4 194	5.115	-	B_2'
18	0.31	2 500	6.625	C_5	C_2'
19	0.22	1 774	7.865	C_6	*vib*-A_2'
20	0.01	81	36.87	-	B_3', C_3'

Table 2.6.4: Rydberg assignment of the sharp lines in the Si $2p$ pre-edge photoabsorption spectrum of SiH_4. The peak number column refers to the assignment given on figure 2.6.3 and in Table 2.6.3.

the vibrational splitting observed in the photoelectron spectrum of SiH_4.[146,156] Several other peaks are assigned to have vibrational contributions as indicated in Table 2.6.4. The high resolution Si $2p$ photoabsorption spectrum of SiD_4 would help confirm this assignment, but to the best of my knowledge it has not been previously reported. The assignment given in Table 2.6.4 accounts for every peak observed, sometimes with more than one Rydberg orbital assigned to a given peak. It should be noted that the assignments are based strictly on an empirical comparison of the effective quantum numbers and are not rigorous. The three series used to assign the Rydberg structure are consistent with the s, p, and d Rydberg series assigned to the spectrum by previous workers,[73-74] although the detailed assignments of the peaks to individual series differs from the previous work. This difference may be due in part to inaccuracies in the Si $2p$ ionization potentials used in the previous studies yielding inaccurate term values

and resulting in errors in the effective quantum numbers used to assign the series. Also, previous workers did not assign as many vibrational bands to the absorption spectrum. The Si 2*p* photoelectron spectrum of SiH_4 given in Chapter 3 indicates that strong vibrational side-bands should be observed for the Rydberg orbitals.

2.6.1.2. Si 2*p* continuum spectra

Photoabsorption spectra of the Si 2*p* discrete and continuum regions of the chlorosilane molecules over the photon energy range 100 to 150 eV are presented in Fig. 2.6.4. The pre-edge region is included to provide a measure of the relative intensities of the continuum resonances. The spectra are all presented on arbitrary intensity scales to maximize the use of the available space on the figure. The Si 2*p* photoabsorption spectrum of $SiCl_4$ was the subject of the previous section (2.5.1.2) and is included here to complete the series. The Si 2*p* continuum region of SiH_4 has also been the subject of previous reports[74,75,152] but is included here to highlight the trends observed in the chlorosilane molecular series.

The Si 2*p* continuum spectra of the chlorosilane molecules are all relatively simple with only a few broad peaks in each spectrum. The spectra of the chlorine containing compounds are similar, with peaks at or near threshold followed by peaks ~7,~12, and ~24 eV above threshold. The SiH_4 spectrum is considerably different than the spectra of the other chlorosilanes, exhibiting two weak peaks ~5 eV and ~12 eV above threshold superimposed upon a very broad background peak that has a maximum ~25 eV above the Si 2*p* ionization threshold. The H atoms surrounding the Si atom are not expected to perturb the potential sufficiently to support shape resonances in the continuum and the two peaks observed are therefore probably due to doubly excited or ionized states of SiH_4.

Successive additions of Cl atoms around the Si atom are expected to increasingly perturb the potential and change the Si 2*p* continuum absorption spectrum from the atomic-like spectrum of SiH_4 to the spectrum of $SiCl_4$, where

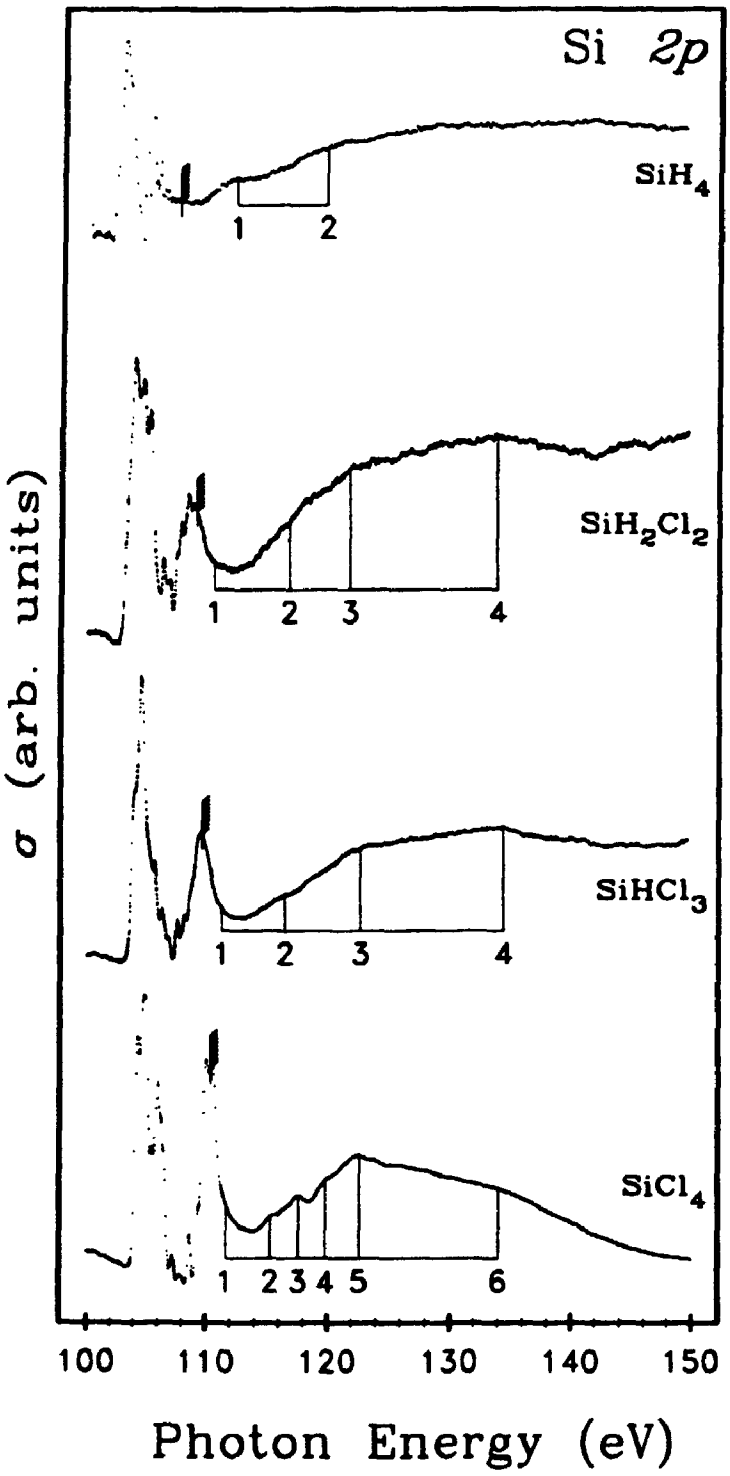

Figure 2.6.4: Photoabsorption spectra of the Si 2*p* regions of the chlorosilane compounds.

fairly strong and distinct resonances are observed. The spectra of $SiHCl_3$ and SiH_2Cl_2 do appear to be intermediate between the spectra of $SiCl_4$ and SiH_4, exhibiting some resonances in the continuum which are not as well defined as they are in the $SiCl_4$ spectrum. Unfortunately, the spectrum of SiH_3Cl is not available but it would be expected to be even more atomic-like and it would complete the chlorosilane molecular series. The fairly constant positions of the first three peaks in the spectra of $SiHCl_3$ and SiH_2Cl_2, and the presence of similar peaks in the $SiCl_4$ spectrum suggest that they result from the Si−Cl bonds or the perturbation of the potential around the central Si atom by the electronegative Cl ligands. The higher energy resonance ~25 eV above the Si 2*p* ionization edge observed for all of the molecules probably results from a delayed Si $2p \rightarrow \epsilon d$ onset as discussed previously for the fluoromethylsilane and chloromethylsilane molecules. The shape of the high energy resonance is strongly dependent on the nature of the ligands (F, Cl, CH_3, or H) around the central Si atom. For SiH_4 the high energy peak is very broad extending over ~50 eV as evidenced by the shape of the SiH_4 absorption spectrum in Fig. 2.6.1, while for SiF_4 it is much narrower, extending over only ~15 eV as seen in Fig. 2.4.1. The Cl and CH_3 ligands have an intermediate effect on the shape of the high energy resonance. It is narrower for in the Si 2*p* spectra of $SiCl_4$ and $Si(CH_3)_4$ than in the SiH_4 spectrum but broader than in the SiF_4 spectrum.

It is also informative to compare the Si 2*p* continuum photoabsorption spectrum of the mixed chlorosilane compounds with the spectra of the analogous chloromethylsilane compounds (Fig. 2.5.3). The spectra of $SiHCl_3$ and $SiCH_3Cl_3$ are very similar reflecting their similar electronic structure. The spectra of SiH_2Cl_2 and $Si(CH_3)_2Cl_2$ are quite different however, since the resonances due to the Cl and CH_3 ligands overlap strongly in the $Si(CH_3)_2Cl_2$ spectrum, rounding out the above edge spectrum. The positions of the Si−Cl resonance (peak 3) are therefore more clearly seen in the SiH_2Cl_2 spectrum.

2.6.1.3. Si 2*s* pre-edge spectra

Photoabsorption spectra of the Si 2*s* pre-edge and continuum regions of the chlorosilane spectra are presented in Fig. 2.6.5. Linear baselines determined from the background intensities at 150–190 eV have been subtracted from the spectra for presentation purposes. The SiH_4 spectrum was measured using a double ion chamber (the others measured by direct photoabsorption in a gas cell) which did not have an adequate dynamic range, and hence the spectrum is quite noisy. The spectrum is sufficiently well-defined to show the main features of the Si 2*s* absorption. The Si 2*s* ionization thresholds of the chloromethylsilane molecules are indicated on the spectra in Fig. 2.6.5.

The Si 2*s* pre-edge absorption spectra of the chlorosilane molecules are all relatively simple with two or three absorption peaks. All of the spectra are dominated by one strong absorption peak with surrounding peaks of lesser intensity. The pre-edge region of the Si 2*s* photoabsorption spectrum of $SiHCl_3$ is very similar to the $SiCl_4$ spectrum with a strong peak asymmetrically broadened on the low photon energy side. In addition, a small peak on the high side of the main peak has appeared which fills in some of the intensity between the main peak and threshold. The positions of the features indicated on the $SiHCl_3$ spectrum, as well as the value used for the Si 2*s* ionization potential are listed in Table 2.6.1 (*c*). The Si 2*p* pre-edge photoabsorption spectrum of SiH_2Cl_2 also has one strong peak with a shoulder at lower energy. The spectrum is very similar to $Si(CH_3)_2Cl_2$ Si 2*s* pre-edge spectrum. The positions and term values of the peaks in the SiH_2Cl_2 spectrum are listed in Table 2.6.2 (*c*) along with the Si 2*s* ionization energy. The shift to lower photon energy (higher term value) of the main peak on going from $SiHCl_3$ to SiH_2Cl_2 is consistent with the shift observed for the first peak below the Si 2*p* ionization threshold.

Below the Si 2*s* edge of SiH_4, one broad strong peak followed by two much weaker peaks closer to threshold are observed. The peak positions and term values

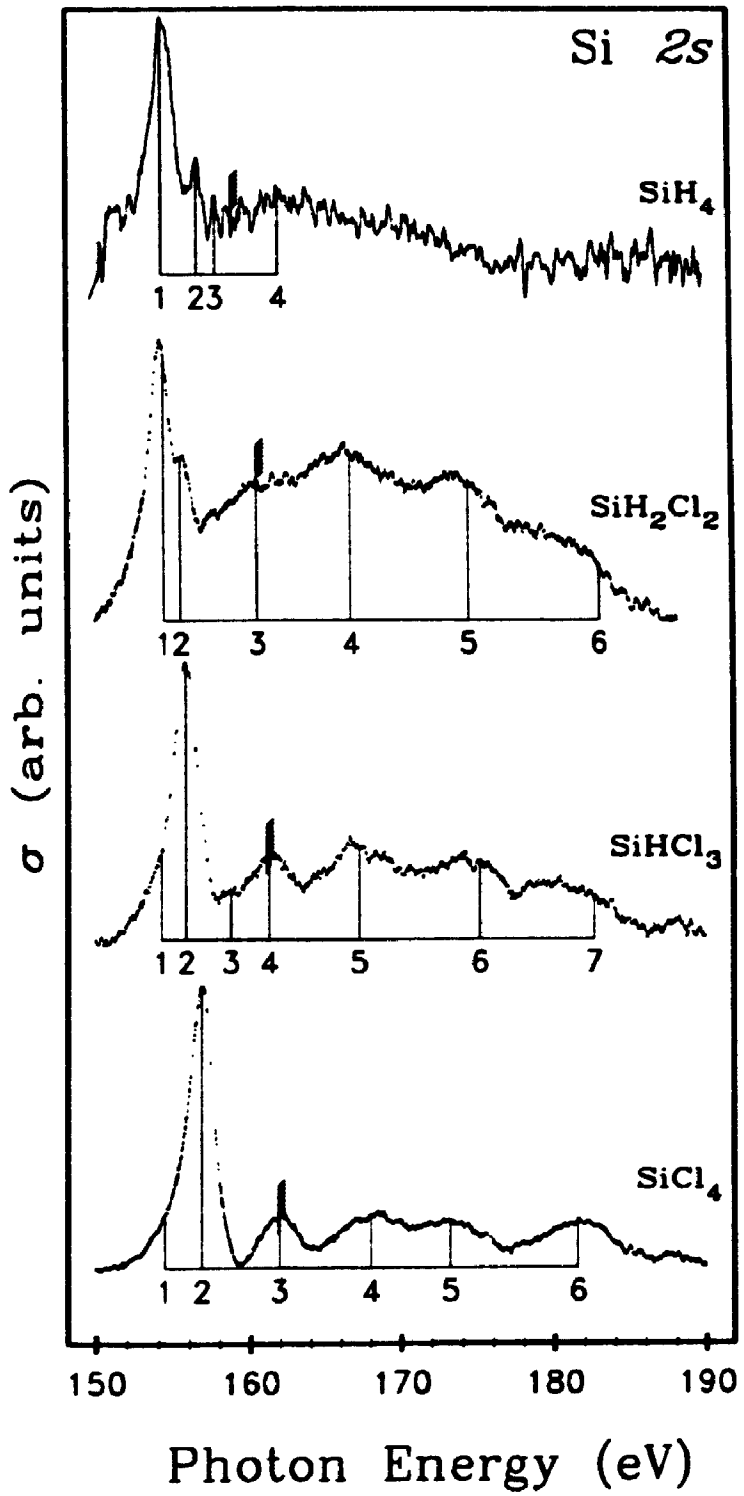

Figure 2.6.5: Photoabsorption spectra of the Si 2*s* regions of the chlorosilane compounds.

are given in Table 2.6.3 (c) as is the Si 2*s* ionization potential for SiH_4. The strong peak probably corresponds to a Si 2*s* → Si−H antibonding orbital transition, and the term value of 4.6 eV is of the same magnitude as the term value of the first broad absorption band below the Si 2*p* ionization edge at 4.82 eV. The weaker peaks probably result from Si 2*s* → Rydberg transitions and again, the term values are consistent with the term values observed for the sharp peaks below the Si 2*p* ionization threshold. Furthermore, the peaks identified in the Si 2*p* pre-edge spectrum with similar term values to those of the peaks below the Si 2*s* ionization edge, peaks 6 and 13 in Table 2.6.3 (*a*) and Fig. 2.6.3 with term values of 2.3 eV and 1.1 eV respectively, were identified as members of the same Rydberg series (B) in Table 2.6.4. From the Si 2*s* orbital, only transitions to p-type Rydberg orbitals are allowed by the electric dipole selection rules. Rydberg series B in Table 2.6.4 is therefore assigned to the n*p* Rydberg series based on the observations for the Si 2*s* pre-edge spectrum. The low intensities of peaks 6 and 13 in Fig. 2.6.3 are also consistent with this assignment since 2*p* → n*p* transitions are forbidden and not expected to have significant intensities based on the selection rules for electronic transitions ($\Delta\ell = \pm 1$).

In a previously reported Si 1*s* photoabsorption spectrum of SiH_4,[117], a photoabsorption spectrum very similar to the Si 2*s* photoabsorption spectrum was observed and the term values of the features are summarized in Table 2.6.3 (*c*). The same assignment proposed above for the Si 2*s* spectrum was given for the Si 1*s* spectrum in the previous work[117] confirming the assignment of the Si 2*s* photoabsorption spectrum.

2.6.1.4. Si 2*s* continuum spectra

Spectra of the continuum regions of the chlorosilane molecules are also presented in Fig. 2.6.5. The spectra of the chlorine containing compounds are all similar with the same number of peaks at almost identical positions. Above

the SiH_4 Si 2*s* ionization edge, however, very little structure is observed due to the low signal to noise ratio. One peak ~3.1 eV above the Si 2*s* ionization edge of SiH_4 is tentatively assigned to the spectrum (Table 2.6.3 (*c*)). The H atoms are not capable of supporting any virtual molecular orbitals in the continuum and so this peak is probably due to a multielectron excited or ionized state.

For the two mixed chlorosilane compounds, the term values of the peaks in the Si 2*s* continuum photoabsorption spectra appear to correlate fairly well with the term values of the peaks observed above the Si 2*p* ionization edges. In the $SiHCl_3$ spectra for instance, four peaks are identified above both the Si 2*p* (Table 2.6.1 (*b*)) and Si 2*s* (Table 2.6.1 (*c*)) ionization edges with term values within ~1.0 eV of each other. For the Si 2*p* and Si 2*s* continuum spectra of SiH_2Cl_2 a similar correlation is observed (Table 2.6.2 (*b*) and (*c*)). A similar correspondence was also noted for the chloromethylsilane molecules.

In a previous study of the Si 1*s* photoabsorption spectrum of SiH_4[117], numerous features were observed above the Si 1*s* ionization edge. The spectrum was reported with a much higher signal to noise ratio than the Si 2*s* photoabsorption spectrum presented in Fig. 2.6.5 and features were identified up to 77.0 eV above threshold. Only doubly excited states were found to contribute intensity above the ionization edge, which is consistent with the assignment given above. In addition, a weak feature was identified 1.4 eV above the ionization threshold, in a position very similar to the feature identified 1.2 eV above threshold in the Si 2*s* photoabsorption spectrum reported here.

2.6.1.5. Cl 2*p* spectra

The Cl 2*p* photoabsorption spectra of the chlorine containing chlorosilane compounds are shown in Fig. 2.6.6. The spectrum of $SiCl_4$, which was discussed in detail in section 2.5.1.5, is included for comparison with the spectra of the chlorosilane compounds. The Cl 2*p* photoabsorption spectrum of $SiHCl_3$ is almost

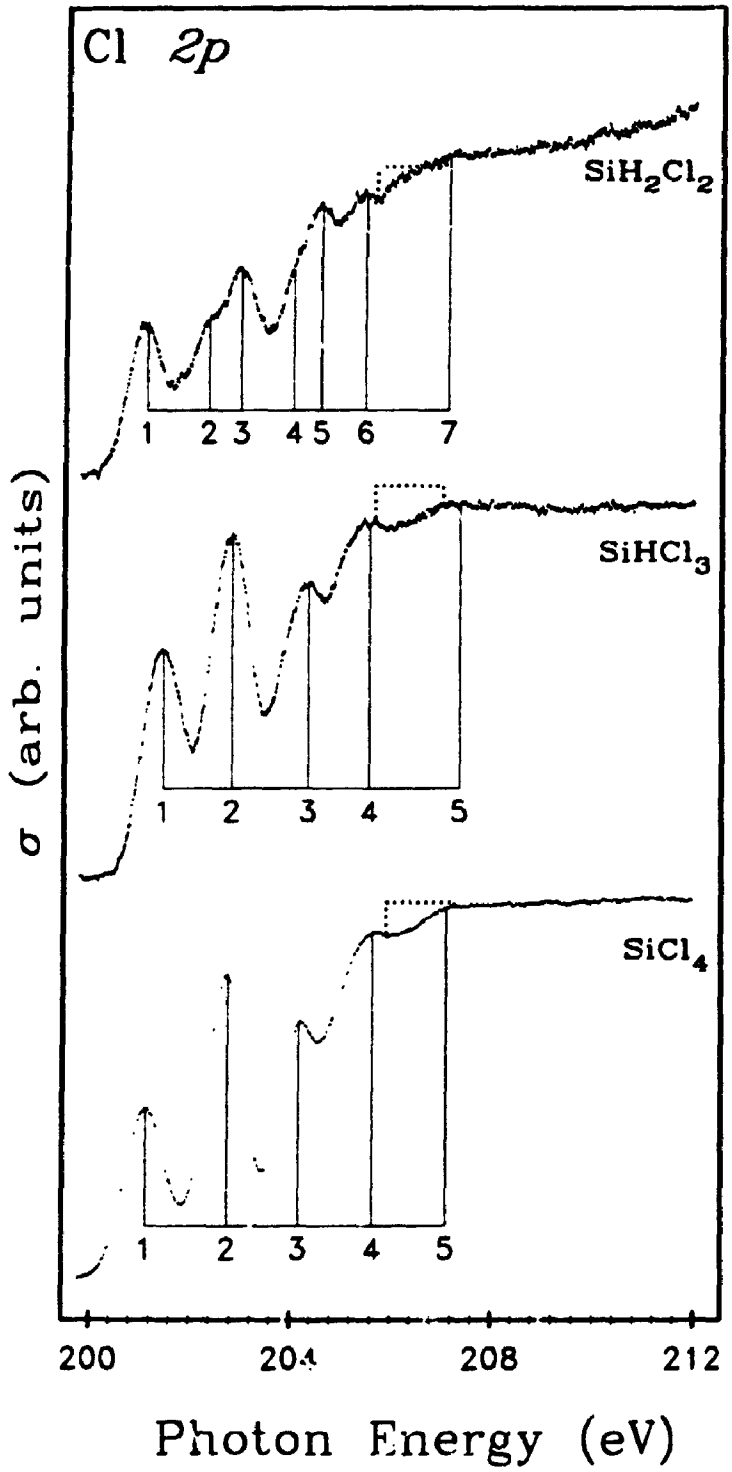

Figure 2.6.6: Photoabsorption spectra of the Cl 2*p* regions of the chlorosilane compounds

(a) $SiHCl_3$

peak label	energy (eV)	term value (eV)		resonance	
		$Cl2p_{3/2}$	$Cl2p_{1/2}$	$Cl2p_{3/2} \rightarrow$	$Cl2p_{1/2} \rightarrow$
1	201.7	4.9	6.5	a	
2	203.2	3.4	5.0	b	a
3	205.0	1.6	3.2	c	b
4	206.4	0 2	1.8	d	c
5	208.6	−2.0	−0.4		d
$Cl2p_{3/2}$	206.6	-	-	-	-
$Cl2p_{1/2}$	208.2	-	-	-	-

(b) SiH_2Cl_2

peak label	energy (eV)	term value (eV)		resonance	
		$Cl2p_{3/2}$	$Cl2p_{1/2}$	$Cl2p_{3/2} \rightarrow$	$Cl2p_{1/2} \rightarrow$
1	201.3	5.3	6.9	a	
2	202.7	3.9	5.5		a
3	203.5	3.1	4.7	b	
4	204.7	1.9	3.5	c	
5	205.2	1.4	3.0		b
6	206.4	0.2	1.8	d	c
7	208.3	−1.7	−0.1		d
$Cl2p_{3/2}$	206.6	-	-	-	-
$Cl2p_{1/2}$	208.2	-	-	-	-

Table 2.6.5: Energies, term values and assignments of the discrete resonances in the Cl 2*p* photoabsorption spectra of $SiHCl_3$ and SiH_2Cl_2

identical to the $SiCl_4$ spectrum, exhibiting the same number of peaks with very similar positions and intensities to the peaks observed in the $SiCl_4$ spectrum. The Cl 2*p* pre-edge photoabsorption spectrum of SiH_2Cl_2 has a different manifold of peaks than that observed for $SiCl_4$ and $SiHCl_3$.

Values of the Cl 2*p* ionization potentials could not be found in the literature for the two mixed chlorosilane compounds, and so the values were estimated from the photoabsorption spectrum. Since the spectra of $SiHCl_3$ and $SiCl_4$ are very similar, the Cl $2p_{3/2}$ ionization potential is assumed to lie ~0.2 eV above the feature 4 in Fig. 2.6.6 as it does for $SiCl_4$ (Table 2.5.5 (*a*)), yielding a Cl $2p_{3/2}$ ionization potential of 206.6 eV. The Cl $2p_{3/2}$ ionization potential of SiH_2Cl_2 is expected

to be ~0.2 eV above the spectral feature 6 in Fig. 2.6.3, also yielding a Cl $2p_{3/2}$ ionization potential of 206.6 eV. Ionization potentials for the $2p_{1/2}$ component of the spin-orbit split core levels were obtained by adding the 1.6 eV Cl $2p_{3/2}$ – Cl $2p_{1/2}$ spin orbit splitting from previous studies.[145] Term values of the peak positions in Fig. 2.6.6 were calculated using the above ionization energies, and all of the values are summarized in Table 2.6.5. The peaks have also been grouped into spin-orbit split pairs by considering their term values with respect to both of the Cl 2*p* ionization edges.

The assignment of the Cl 2*p* photoabsorption spectrum of $SiHCl_3$ is obviously the same as that for the Cl 2*p* spectrum of $SiCl_4$, with four spin-orbit split resonances (Table 2.6.5 (*a*)). The position of peak 5 is fairly uncertain and the peak maximum could be closer to the threshold and thus form a spin-orbit doublet with peak 4. It is interesting that while the Cl 2*p* spectra of $SiCl_4$ and $SiHCl_3$ appear to be very similar, the maximum term value for $SiCl_4$ is 5.6 eV but only 4.9 eV for $SiHCl_3$. The substitution of a H for a Cl compresses the spectrum closer to threshold in $SiHCl_3$. For the Cl 2*p* photoabsorption spectrum of SiH_2Cl_2, four spin-orbit split resonances have also been identified and the assignment is summarized in Table 2.6.5 (*b*). The pattern of partially overlapping bands in the spectrum is similar to the pattern observed in the Cl 2*p* photoabsorption spectrum of $Si(CH_3)_2Cl_2$ (Fig. 2.5.5) although the term values are different. The Cl 2*p* spectrum of SiH_2Cl_2 shows the same trends observed for the Si 2*p* ad Si 2*s* spectra where the term value of the first feature is larger than the corresponding term values for the $SiHCl_3$ spectra.

2.6.2. DISCUSSION: Assignment Using MS-Xα Results

Theoretical cross sections of the discrete and continuum regions of the Si 2*p* and Si 2*s* ionization edges of the chlorosilane molecules were calculated using the MS-Xα method. The theoretical results are used in conjunction with trends noted

in the preceding sections to assign both the narrow pre-edge peaks and the broader continuum peaks for all of the chlorosilane compounds.

2.6.2.i. Si 2*p* pre-edge

Using the methods described in the previous sections, numerous unoccupied levels were identified just below the vacuum level by energy searches for eigenvalues in the converged MS-Xα Si 2*p* transition state potentials of the chlorosilane molecules. Oscillator strengths were calculated for each of the eigenvalues and the results used to simulate the Si 2*p* pre-edge photoabsorption spectra. The eigenvalues were assumed to be equal to the term values and the oscillator strengths to the relative intensities of the peaks, which were convoluted with spin-orbit split Lorentzian line shapes with 0.25 eV half-height widths, 0.61 eV spin-orbit splittings, and 2:1 statistical $2p_{3/2}$:$2p_{1/2}$ intensity ratios to provide the simulated Si 2*p* photoabsorption spectra for the chlorosilane molecules which are presented in Fig. 2.6.7. Calculations were completed for SiH_3Cl to complete the molecular series, even though experimental data is not available for comparison. The MS-Xα results for $SiCl_4$, which were discussed in section 2.5.2.1 are also included in Fig. 2.6.7 for comparison.

Agreement between theory and experiment is rather good considering that only semiquantitative results are expected from the MS-Xα method. The calculations yield the best results for the Si 2*p* pre-edge spectra of $SiHCl_3$ and SiH_4 where the theoretical spectra are very similar in overall shape to the experimental Si 2*p* pre-edge spectra in Fig. 2.6.7. Less quantitative agreement between the theoretical and experimental spectra is observed for SiH_2Cl_2, but the calculations do reproduce the increase in the first term value from the $SiHCl_3$ spectrum which was noted in the experimental data. The theoretical Si 2*p* pre-edge spectrum of SiH_3Cl cannot be compared with experimental results since a sample of SiH_3Cl was not available.

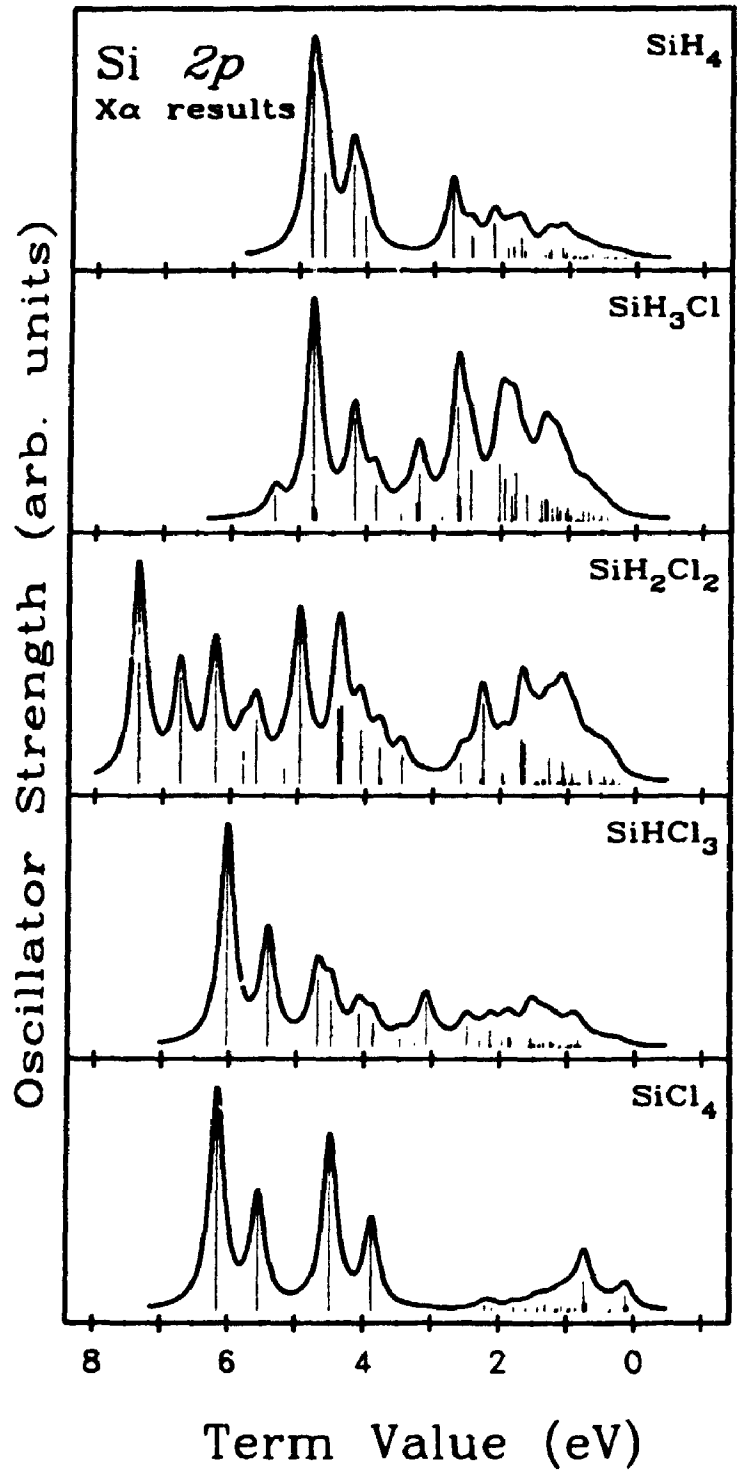

Figure 2.6.7: Simulated Si 2*p* pre-edge photoabsorption spectra for the chlorosilane compounds constructed from the eigenvalues and oscillator strengths from the MS-Xα calculations.

orbital assignment	term value	Q_{out} (%)	Q_{inter} (%)	Q_{Si} (%)	Q_{Cl} (%)	Q_H (%)	oscillator strength	orbital type
$1a_1^*$	5.43	7.5	19.3	23.3	47.4	2.5	2.71×10^{-2}	anti.
$1e^*$	4.08	7.8	33.0	29.9	28.7	0.6	8.58×10^{-3}	anti.
$2a_1^*$	3.88	30.4	42.3	15.7	10.5	1.1	6.12×10^{-3}	anti.
$3a_1^*$	2.86	52.5	36.0	5.2	4.2	2.1	1.13×10^{-3}	mixed
$4a_1^*$	2.48	43.4	35.6	5.8	11.4	3.9	5.71×10^{-3}	mixed
$5a_1^*$	1.53	84.6	10.0	2.1	2.7	0.7	2.14×10^{-3}	Ryd. (d)
$6a_1^*$	1.35	88.1	6.1	1.9	2.0	1.8	1.04×10^{-3}	Ryd. (s)
$7a_1^*$	1.25	90.1	7.4	0.8	1.4	0.3	1.31×10^{-3}	Ryd. (p)
$5e^*$	1.22	89.1	8.2	5.6	2.1	0.0	1.10×10^{-3}	Ryd. (p)
$7e^*$	0.93	91.5	6.7	0.3	1.4	0.0	1.18×10^{-3}	Ryd. (d)

Table 2.6.6: Term values (eV), oscillator strengths and charge distributions calculated for the unoccupied orbitals of $SiHCl_3$.

The calculated Si $2p$ pre-edge spectrum of $SiHCl_3$, while in reasonable agreement with the experimental spectrum, does not provide an unequivocal assignment. The first strong doublet observed in the experimental spectrum (Fig. 2.6.2) is assigned to the $2p \rightarrow 1a_1^*$ transition. The numbering of the virtual orbitals used here begins at one for the first virtual level of each symmetry representation to allow easy comparison between different molecules of the same or different symmetries. The calculated eigenvalue of the $1a_1^*$ virtual orbital (Table 2.6.6), 5.43 eV, is in excellent agreement with the experimental term value of 5.52 eV (Table 2.6.1 (a)) as are the relative calculated and experimental intensities. The resonance assigned to overlap with the first spin-orbit doublet has contributions from the $1e^*$ and $2a_1^*$ antibonding orbitals according to the MS-Xα calculations, while the $3a_1^*$ and $4a_1^*$ mixed character orbitals probably contribute intensity in the region of peaks 4–6 in the experimental photoabsorption spectrum (Fig. 2.6.2). The remaining calculated virtual orbitals have primarily Rydberg character and hence the remaining peaks in the experimental photoabsorption spectrum are assigned to transitions from the Si $2p$ levels to orbitals with Rydberg character.

orbital assignment	term value	Q_{out} (%)	Q_{inter} (%)	Q_{Si} (%)	Q_{Cl} (%)	Q_H (%)	oscillator strength	orbital type
$1a_1^*$	6.74	6.9	33.6	22.9	31.4	5.2	1.92×10^{-2}	anti.
$1b_1^*$	5.62	6.0	44.1	29.0	20.2	0.6	1.17×10^{-2}	anti.
$2a_1^*$	5.21	13.1	56.0	20.6	6.6	3.6	3.02×10^{-3}	anti.
$1b_2^*$	4.36	11.1	49.6	25.5	7.6	6.2	1.42×10^{-2}	anti.
$3a_1^*$	3.80	35.5	49.1	6.2	6.0	3.0	6.71×10^{-3}	anti.
$2b_2^*$	3.46	41.2	50.3	2.3	4.2	2.0	5.45×10^{-3}	anti.
$5a_1^*$	1.96	57.9	32.1	2.3	6.6	1.0	1.99×10^{-3}	mixed
$3b_2^*$	1.65	71.2	18.2	4.4	3.2	3.0	7.26×10^{-3}	mixed
$9a_1^*$	1.08	85.0	10.9	1.4	2.6	0.2	3.97×10^{-3}	Ryd. (d)
$15a_1^*$	0.67	96.8	2.3	0.3	0.6	0.0	2.41×10^{-3}	Ryd. (p)

Table 2.6.7: Term values (eV), oscillator strengths and charge distributions calculated for the unoccupied orbitals of SiH_2Cl_2.

While the agreement between the theoretical and experimental spectra is not as good for SiH_2Cl_2, an assignment of the Si $2p$ pre-edge spectrum can also be made using the MS-Xα results. The strong peaks in the theoretical Si $2p$ pre-edge spectrum of SiH_2Cl_2 above 4 eV term value (Fig. 2.6.7) and the strong peaks in the experimental Si $2p$ pre-edge spectrum at low photon energy (peaks 1–4 in Fig. 2.6.2) are obviously related. The MS-Xα calculations indicate that these peaks result from electronic transitions of the Si $2p$ electrons into the $1a_1^*$, $1a_2^*$, $2a_1^*$, and $1b_2^*$ virtual orbitals which have antibonding character based on their calculated charge distributions (Table 2.6.7). The three resonances assigned to the strong broad set of peaks in the experimental spectrum are therefore assigned as electronic transitions from the Si $2p$ levels into these orbitals as indicated in Table 2.6.2 (a). Peaks 5 and 6, which have moderate intensity in the experimental Si $2p$ photoabsorption spectrum, are assigned to transitions into the $3a_1^*$ and $2b_2^*$ antibonding orbitals which were found to have lower oscillator strengths. Finally, the $5a_1^*$ and $3b_2^*$ orbitals, which have mixed antibonding - Rydberg character are assigned to account for the absorption intensity closer to threshold along with overlapping transitions into orbitals with primarily Rydberg character.

orbital assignment	term value	Q_{out} (%)	Q_{inter} (%)	Q_{Si} (%)	Q_H (%)	oscillator strength	orbital type
$1t_2^*$	4.21	29.4	41.6	16.9	12.0	4.03×10^{-2}	anti.
$1a_1^*$	4.04	61.7	13.1	16.1	7.2	1.87×10^{-2}	mixed
$1e^*$	2.12	69.2	24.6	4.6	1.6	1.55×10^{-2}	mixed
$2a_1^*$	1.83	85.0	4.0	4.3	6.8	4.97×10^{-3}	Ryd. (s)
$3t_2^*$	1.31	97.7	1.1	0.7	0.4	2.23×10^{-3}	Ryd. (d)
$2e^*$	1.10	92.7	5.7	1.3	0.4	4.45×10^{-3}	Ryd. (d)
$3a_1^*$	1.05	92.1	2.4	1.3	4.4	1.49×10^{-3}	Ryd. (s)
$6t_2^*$	0.75	99.0	0.4	0.3	0.4	1.01×10^{-3}	Ryd. (d)
$3e^*$	0.67	97.0	2.3	0.6	0.0	1.97×10^{-3}	Ryd. (d)
$4e^*$	0.45	98.5	1.1	0.3	0.0	1.05×10^{-3}	Ryd. (d)

Table 2.6.8: Term values (eV), oscillator strengths and charge distributions calculated for the unoccupied orbitals of SiH_4.

The calculated Si $2p$ pre-edge absorption spectrum of SiH_4 in Fig. 2.6.7 is in very good agreement with the experimental spectrum in Fig. 2.6.2 with strong absorption bands ~4 eV below threshold and numerous weaker absorptions leading up to the ionization threshold. The strong bands ~4 eV below the ionization threshold result from overlapping transitions of the Si $2p$ electrons into the $1t_2^*$ antibonding orbital and $1a_1^*$ orbital of mixed character according to the calculated eigenvalues and charge distributions presented in Table 2.6.8. It is possible that transitions to the $1e^*$ orbital, which is calculated to have a mixed antibonding-Rydberg character (Table 2.6.8) may also contribute to the broad band in the SiH_4 absorption spectrum, but further theoretical calculations would be required to confirm this assignment. The calculated ordering of the $1t_2^*$ and $1a_1^*$ virtual orbitals is at odds with a previous assignment which had the t_2^* virtual orbital above the a_1^* ($\sigma - 4s$) virtual orbital[74] based on CI ab initio calculations. The assignment given here is in good agreement with DV-Xα calculations performed recently for SiH_4 [152] which found a t_2^* virtual orbital below the a_1^* orbitals, both assigned to the broad absorption band in the Si $2p$ pre-edge photoabsorption spectrum of SiH_4. Both of the previous calculations support the assignment of

only two absorption bands to the broad and intense band in the Si $2p$ pre-edge rather than the three resonances postulated in section 2.6.1.1 where the assignment was made based on the shape of the absorption band. Schwarz has noted that the intensity ratio of the $2p_{3/2}$ and $2p_{1/2}$ components of the second row hydrides are very sensitive to the interaction between the excited electron in the virtual orbital and the core hole.[72]

The MS-Xα calculations confirm the assignment of the sharp absorption lines at higher energies to $2p \rightarrow$ Rydberg transitions. Although the ordering of the orbital energies are not expected to yield exact results, the MS-Xα calculations predict that the first Rydberg peaks result from transitions into an n$d(e)$ Rydberg state followed by transitions into ns and n$d(t_2)$ Rydberg orbitals. Based on the MS-Xα results, therefore, the A_i series in Table 2.6.4 is assigned to the n$d(e)$ Rydberg series, the B_i series to the ns Rydberg series and peaks C_i to the n$d(t_2)$ Rydberg series. The assignments based on the MS-Xα results are at variance with the assignment of the B_i peaks to the np Rydberg series based on the observation of peaks with similar term values in the Si $2s$ pre-edge spectrum. The ordering of the Rydberg orbitals in the MS-Xα calculations $d(e) > s > d(t_2)$ is identical to the ordering predicted by the CI calculations although the previous report did not identify as many vibrational bands in the spectra as in the assignment given here.

2.6.2.2. Si $2p$ continuum

Silicon $2p$ ionization cross sections for the chlorosilane molecules were calculated using the MS-Xα method and the appropriate Si $2p$ transition state potentials. The resulting theoretical cross sections along with the partial symmetry channel contributions to the cross sections are presented in Fig. 2.6.8. The $SiCl_4$ cross section, which was discussed in the previous section 2.5.2.2 is included for purposes of comparison as is the calculated cross section for SiH_3Cl for which

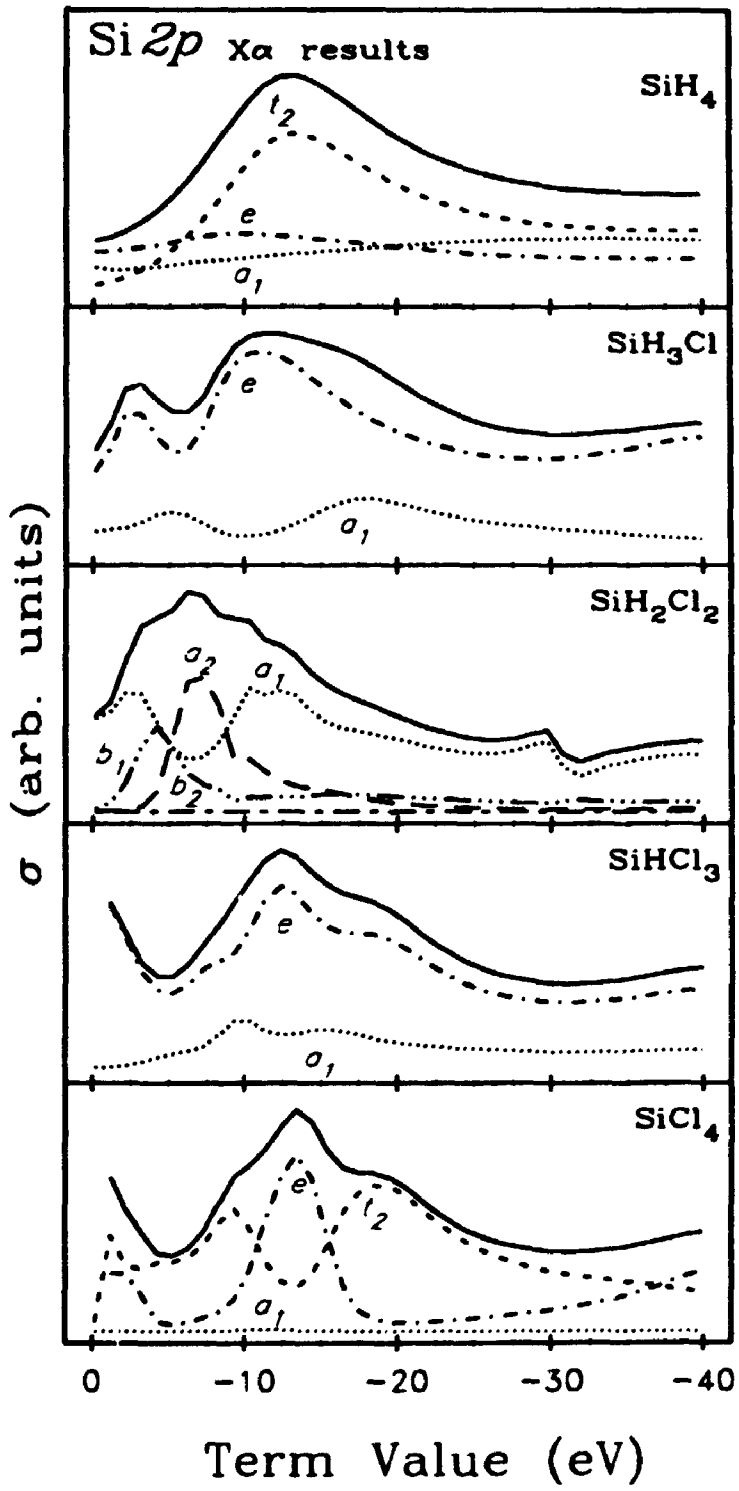

Figure 2.6.8: Theoretical Si 2*p* cross sections of the chlorosilane compounds from the MS-Xα calculations.

no experimental data is available. Different outgoing symmetry channels are allowed for the ionized Si 2*p* electron in the three different ground state symmetries represented by the chlorosilane molecules; T_d for $SiCl_4$ and SiH_4, C_{3v} for $SiHCl_3$ and SiH_3Cl and C_{2v} for SiH_2Cl_2. The principal symmetry channels contributing to the cross sectional maxima in the five chlorosilane molecules are indicated on Fig. 2.6.8 and summarized in Table 2.6.1 (*b*) for $SiHCl_3$, Table 2.6.2 (*b*) for SiH_2Cl_2, and Table 2.6.3 (*b*) for SiH_4.

The calculated cross sections are in reasonably good agreement with the experimental Si 2*p* continuum photoabsorption spectra of the chlorosilanes in Fig. 2.6.4. The similarity between the experimental $SiHCl_3$ and $SiCl_4$ Si 2*p* spectra is reproduced by the MS-Xα calculations as is the presence of only one broad resonance above the Si 2*p* ionization edges of SiH_4. The calculated SiH_4 cross section is very atomic-like with a delayed onset of the $2p \rightarrow kt_2$ producing a broad peak ~14 eV above the ionization threshold. A weaker peak is also seen in the *ke* symmetry channel ~10 eV above threshold. The kt_2 and *ke* symmetry channels transform as the *d* orbitals (d_{xy}, d_{xz}, and d_{yz}) and (d_{z^2} and $d_{x^2-y^2}$) respectively, and the kt_2 and *ke* symmetry channels therefore correspond to the $2p \rightarrow \epsilon d(t_2)$ and $2p \rightarrow \epsilon d(e)$ channels respectively. Contributions from the $2p \rightarrow ka_1$ channel, which transforms as $2p \rightarrow \epsilon s$ are smaller than the contributions from the $2p \rightarrow \epsilon d(t_2) + \epsilon d(e)$ which is consistent with previous calculations for the Si atom.[147] The dominance of the *d* channels over the *s* channel is also consistent with the dominance of $\Delta\ell = +1$ over $\Delta\ell = -1$ outgoing channels noted for atomic ionization cross sections[160] and is highlighted by these calculations. The eigenphase sums of the kt_2 and *ke* symmetry channels change by 1.1π and 0.6π respectively at the positions of the cross section enhancement, satisfying Kriele's criteria for a shape resonance.[153] This shape resonance must be due to centrifugal barriers in the kt_2 and *ke* channels giving rise to the delayed onset observed in numerous $\ell > 2$ final states. The broad absorption peak above the SiH_4 Si 2*p*

ionization edge is therefore shown to be due to a delayed onset in the $2p \rightarrow \epsilon d$ channels. The other weaker peaks at lower energy have been assigned to doubly excited states based on similar observations above the Si 1s ionization edge.[117]

In the MS-Xα calculated Si 2p cross section of SiH_3Cl (Fig. 2.6.8), the strong kt_2 shape resonance observed above the Si 2p edge of SiH_4 divides into two separate resonances by the perturbation of the atomic-like potential in SiH_4 by the electronegative Cl ligands. Upon lowering the molecular symmetry from T_d to C_{3v}, the t_2 representation is split into the e and a_1 representations[151] both of which are seen to have two cross section maxima at similar energies (Fig. 2.6.8). The division of the resonance in the kt_2 symmetry channel of the Si 2p continuum is preserved for the rest of the chlorosilane molecules.

In the calculated Si 2p cross section for SiH_2Cl_2, for example, the division of the resonance is present in the ka_1 symmetry channel (the t_2 representation in the T_d symmetry group transforms as the $a_1 + b_1 + b_2$ representations in the molecule with C_{2v} symmetry). Positions of the maxima in the partial symmetry channels of the calculated Si 2p cross section of SiH_2Cl_2 are summarized in Table 2.6.2 (*b*) together with the accompanying shift in the eigenphase sum. Although the shape of the calculated Si 2p cross section of SiH_2Cl_2 is not in good agreement with the shape of the experimental spectrum (Fig. 2.6.4), the term values of the calculated cross section maxima are in good accord with the experimental term values as seen in Table 2.6.2 (*b*). Most of the observed maxima meet the eigenphase sum change required to be classified as shape resonances. The resonance found in the ka_2 channel is also preserved in the calculated cross sections of $SiHCl_3$ and $SiCl_4$. This resonance is observed as the strong peak in the $k\epsilon$ symmetry channels of the two remaining chlorosilane molecules.

The divided kt_2 resonance can also be seen in the $k\epsilon$ and ka_1 symmetry channels of the calculated $SiHCl_3$ Si 2p cross section. An additional peak is found in the $k\epsilon$ symmetry channel very near to the ionization threshold. The calculated

positions of the cross section maxima for $SiHCl_3$ are in very good agreement with the positions of the experimentally observed resonances as tabulated in Table 2.6.1 (*b*). The symmetry channels of the peaks in the calculated Si 2*p* cross sections of $SiHCl_3$ are also given in the table along with the corresponding eigenphase sum changes. All of the peaks are seen to satisfy Kriele's criteria for shape resonances.[153]

Comparing the calculated Si 2*p* cross sections of the chlorosilane molecules in Fig. 2.6.8 with the calculated cross sections of the analogous chloromethylsilane molecules in Fig. 2.5.7, only small differences are found. The cross sections of $SiHCl_3$ and $SiCH_3Cl_3$ are virtually identical with similar peak positions and intensities. For the remaining compounds, however, the Si 2*p* cross sections of the chloromethylsilanes are similar to those for the analogous chlorosilane compounds, only shifted to higher term values with some additional structure near threshold. The term value of the strong high energy resonance is −13.4 eV in the SiH_4 cross section but −17.5 eV for $Si(CH_3)_4$. There are also additional peaks near threshold in the chloromethylsilane cross sections when compared to the analogous chlorosilane cross sections. These peaks in the calculated Si 2*p* cross sections appear to be due to Si−C antibonding orbitals which are shifted into the continuum in the MS-Xα calculation by the electropositive methyl ligands around the central Si atom.

2.6.2.3. Si 2*s* pre-edge spectra

Simulated Si 2*s* pre-edge absorption spectra have been constructed for the chlorosilane molecules from the eigenvalues of the virtual orbitals identified in the converged Si 2*s* transition state potential and the oscillator strengths calculated for transitions to these orbitals. The eigenvalues and oscillator strengths were convoluted with Lorentzian lineshapes with half-height widths of 1.0 eV and the resulting simulated Si 2*s* pre-edge photoabsorption spectra are presented in

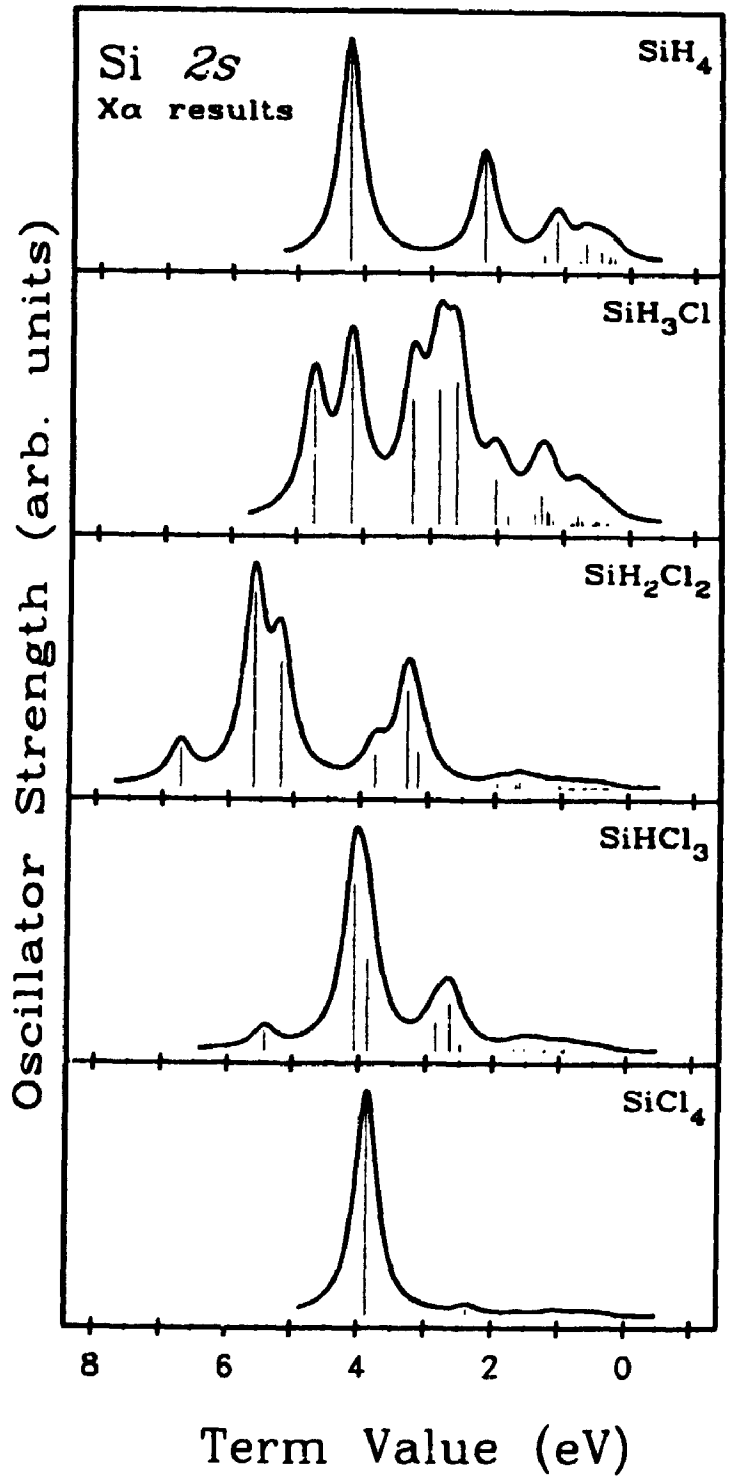

Figure 2.6.9: Simulated Si 2*s* pre-edge photoabsorption spectra for the chlorosilane compounds constructed from the eigenvalues and oscillator strengths from the MS-Xα calculations.

Fig. 2.6.9. The simulated $SiCl_4$, spectrum which was discussed in detail in section 2.5.2.3, is presented for comparison with the spectra of the other chlorosilane molecules as is the simulated SiH_3Cl Si 2*s* absorption spectrum.

The simulated spectra in Fig. 2.6.9 generally compare favourably with the experimental Si 2*s* pre-edge photoabsorption spectra in Fig. 2.6.5. Three peaks were found in the Si 2*s* pre-edge region of $SiHCl_3$ by the MS-Xα calculation, a weak one 5.4 eV below the Si 2*s* ionization edge, a very strong one 4.0 e below the ionization edge and one with moderate intensity 2.7 eV below the 2*s* edge. Term values and symmetries for the calculated resonance positions are summarized in Table 2.6.1 (*c*) and a good correlation is seen with the experimental term values The relative calculated intensities (oscillator strengths) of the peaks also compare favourably with the experimental intensities resulting in a close similarity between the simulated $SiHCl_3$ spectrum in Fig. 2.6.9 and the experimental spectrum in Fig. 2.6.5.

Three primary absorption bands are also present in the simulated Si 2*s* spectrum of SiH_2Cl_2 with a similar intensity pattern to the one exhibited in the $SiHCl_3$ simulated spectrum. Three peaks with similar intensities were also identified in the experimental Si 2*s* pre-edge spectrum of SiH_2Cl_2 (Fig. 2.6.5). Term values for the experimental and theoretical term values of the peak positions are given in Table 2.6.2 (*c*) along with the symmetries of the virtual orbitals. The calculated and experimental term values are not in very good agreement, differing by as much as 2 eV. A better correspondence is seen between the spacing of the experimental and calculated peak positions. The MS-Xα calculations reproduce the shift of the main peak to higher term value from $SiHCl_3$ to SiH_2Cl_2 which is observed in the experimental data. The very weak peaks close to threshold in the calculated spectra of SiH_2Cl_2 and $SiHCl_3$ are not identified in the experimental spectra but even if they are present, they would be impossible to pick out of the background without much higher signal to noise.

All of the absorption peaks identified in the Si 2*s* pre-edge absorption spectra of the mixed chlorosilane compounds are due to transitions from the Si 2*s* to antibonding orbitals in the virtual molecular orbital manifold. Only one transition to an antibonding orbital was found in the calculated Si 2*s* spectrum of SiH_4, a t_2^* orbital with a term value of 4.2 eV. This is in very good agreement with the strong peak observed 4.6 eV below the Si 2*s* ionization edge of SiH_4. The other peaks in the calculated Si 2*s* pre-edge absorption spectrum are due to transitions of the Si 2*p* electrons into Rydberg orbitals with t_2 symmetry. The calculated eigenvalues of the Rydberg orbitals are also in very good agreement with the experimental term values given in Table 2.6.3 (*c*). The MS-Xα calculations therefore support the assignment of the n*p* Rydberg series (*p* orbitals transform as the t_2 representation in the T_d symmetry group) to the smaller peaks in the experimental Si 2*s* pre-edge absorption spectrum.

2.6.2.4. Si 2*s* continuum spectra

The Si 2*s* continuum cross sections of the chlorosilane molecules, calculated using the appropriate converged Si 2*s* transition state potentials are given in Fig. 2.6.10. The contributing partial symmetry channels are indicated on the curves for each compound.

The calculated resonance positions for $SiHCl_3$ are in reasonable agreement with the term values of the peak positions observed in the experimental spectrum as seen in Table 2.6.1 (*c*). Eigenphase sum changes around the indicated positions satisfy the requirements for shape resonances.[153] The agreement is not as good for the calculated cross sections and experimental Si 2*s* continuum photoabsorption spectrum for SiH_2Cl_2. The two calculated resonance positions are summarized in Table 2.6.2 (*c*) and compare well with two of the experimentally observed peak positions. There are no cross section maxima at the positions of the high and low energy peaks observed in the experimental spectrum. The shape of the calculated

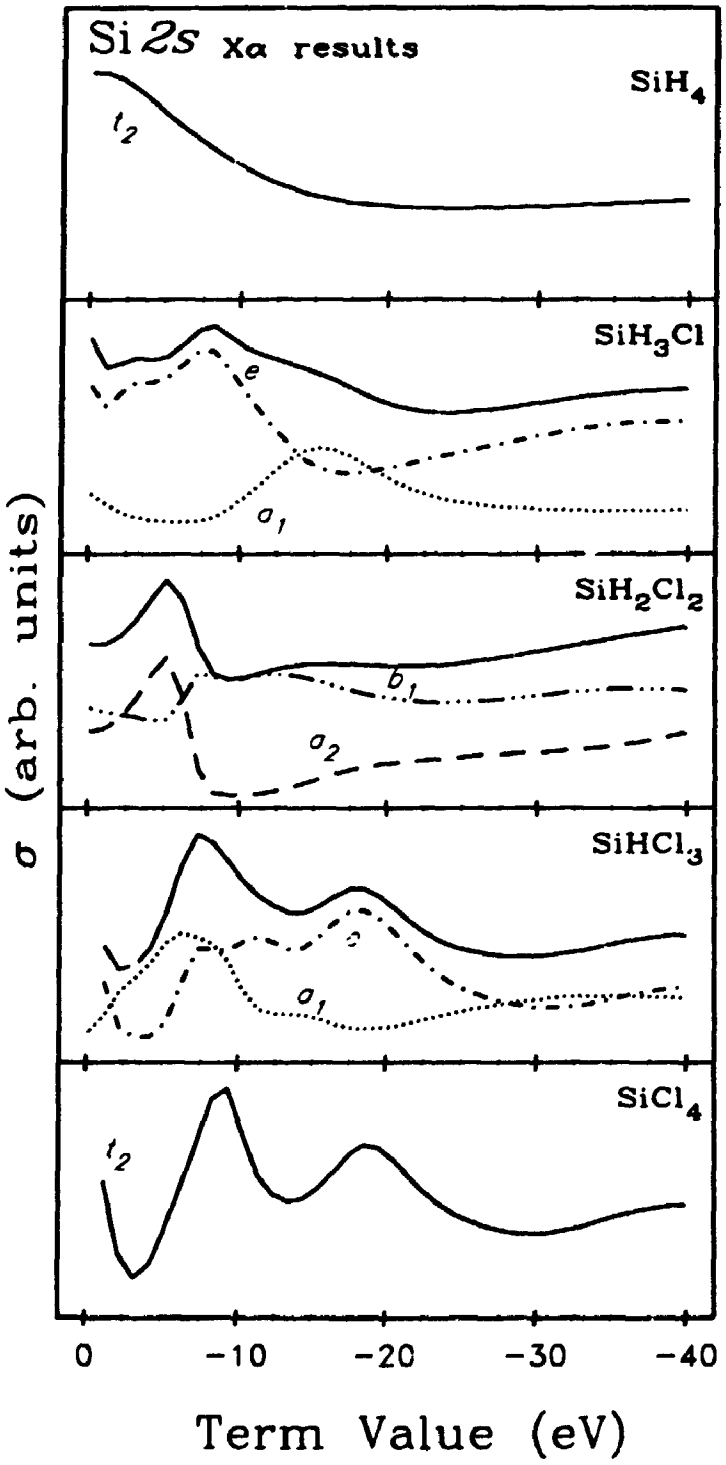

Figure 2.6.10: Theoretical Si 2*s* cross sections of the chlorosilane compounds from the MS-Xα calculations.

Si 2*s* cross section of SiH_4 (Fig. 2.6.10) is in good accord with the experimental spectrum in Fig. 2.6.5, exhibiting only a decreasing cross section from the Si 2*s* ionization threshold.

2.7. CONCLUSIONS

Silicon $2p$ and $2s$ core level absorption spectra of the fluoromethylsilane molecules, $Si(CH_3)_xF_{4-x}$; $x = 0 \rightarrow 4$, the chloromethylsilane compounds, $Si(CH_3)_xCl_{4-x}$; $x = 0 \rightarrow 4$, and the chlorosilane compounds, SiH_xCl_{4-x}; $x = 0 \rightarrow 4$ have been reported and compared with previous results where available. Chlorine $2p$ core level absorption spectra were also reported for the chlorine containing molecules. The Si $2s$ spectra were found to be less complicated than the $2p$ spectra in all cases. Pre-edge and continuum features were assigned with the aid of MS-Xα calculations in conjunction with trends observed in the spectra of the five related molecules.

Peaks in the experimental Si $2p$ pre-edge photoabsorption spectra were assigned to result from transitions of the Si $2p$ electrons into virtual orbitals of valence and/or Rydberg character. Eigenvalues and oscillator strengths from MS-Xα calculations were compared with experimental spectra and used to assign the character and symmetries of the final-state orbitals for the electronic transitions. The degree of valence (antibonding) character of the virtual state orbital manifold was found to generally decrease across the series F > Cl > H > CH_3. Peaks resulting from transitions into Si–F or Si–Cl and Si–CH_3 antibonding orbitals were identified in the experimental spectra of the fluoromethylsilane and chloromethylsilane molecules. Intensities of these peaks were observed to roughly follow the number of bonds of that type in the molecule. A convergence of the peaks towards threshold was also noted as the number of methyl ligands in the molecule was increased. For the chlorosilane molecules, final state orbitals of Si–Cl and Si–H antibonding character were identified but found to result in overlapping peaks in the experimental Si $2p$ photoabsorption spectra of the mixed compounds.

The series of sharp lines below the Si $2p$ ionization threshold of SiH_4 were assigned to transitions into three Rydberg series with considerable vibrational structure based on the effective quantum numbers and MS-Xα calculations. The

MS-Xα calculations were found to nicely reproduce the relative positions of the virtual valence and Rydberg orbitals in SiH_4. Oscillator strengths for transitions into orbitals with strong Rydberg character in the mixed chlorosilane compounds and the chloromethylsilane and fluoromethylsilane compound form the MS-Xα calculations were found to be smaller than values for transitions to antibonding and mixed antibonding – Rydberg orbitals, but still significant.

The Si 2*p* continuum regions of the absorption spectra exhibited three absorption maxima for all five of the fluoromethylsilane molecules, one near threshold and others ~5 and ~20 eV above threshold. The two lower energy resonances were assigned to shape resonances for all five fluoromethylsilane molecules. The intensity of the peak at ~5 eV was found to be roughly proportional to the number of fluorine ligands in the molecule and the resonance near threshold roughly proportional to the number of methyl ligands. The relative intensity of the high energy resonance, however, was found to be independent of the ligands. The low energy resonances were found to be shape resonances due to virtual orbitals resulting from transitions into Si - C antibonding orbitals lying just above the Si 2*p* ionization threshold. This assignment was consistent with both the experimental data and previous results for other molecules. The medium energy resonances were assigned as shape resonances due to ligand induced potential barriers owing to the electronegative barrier created by the fluorine ligands surrounding the central silicon atom trapping the *d* continuum channel. The changing intensity of the medium energy resonance as fluorine ligands were replaced with methyl ligands supported this assignment. The high energy resonance was assigned as an atomic-like delayed onset based on the observation of resonances at similar energies for other silicon compounds as well as atomic silicon. According to the MS-Xα calculations, the resonance near threshold occurs in the ka_1 channel for all five molecules. The resonance ~5 eV above threshold is always in the *ke* channel, except for $Si(CH_3)_2F_2$ where it is in the

ka_1 and kb_1 channels, which in C_{2v} symmetry correspond to the ke channel of the C_{3v} and T_d symmetries. The higher energy resonance, ~20 eV above threshold, occurs in the kt_2 channel for SiF_4 and corresponding channels for $SiCH_3F_3$ and $Si(CH_3)_2F_2$. In the other two molecules, $Si(CH_3)_3F$ and $Si(CH_3)_4$, this resonance was calculated to be in the ke symmetry channel.

Continuum regions of the Si 2*p* photoabsorption spectra of the chloromethylsilane compounds were not clearly resolved into individual absorption bands. Four resonances were identified in the spectra however, one at or near threshold, and three others in the continuum with term values of approximately −7.0 eV, −12.0 eV and −20 eV. Intensities of the resonances were not found to vary clearly with the numbers of ligands of a given type, but by considering both the experimental and theoretical Si 2*p* continuum absorption cross sections several conclusions could be drawn. The resonance at threshold was found to have overlapping contributions from both Si−Cl and Si−C antibonding orbitals. The resonances −7 eV and −12 eV above threshold were found to depend on the presence of methyl and chlorine ligands respectively. The resonances ~12 eV above the edge were assigned as shape resonances due to ligand induced potential barriers owing to the electronegative barrier created by the chlorine ligands surrounding the central silicon atom trapping the *d* continuum channel. The higher energy resonance observed in all of the spectra ~20 eV above the ionization edge was assigned to result from a delayed onset of the Si $2p \rightarrow \epsilon d$ ionization channel as noted for the fluoromethylsilane compounds.

The Si 2*p* continuum spectra of the chlorosilane compounds were in good agreement with the assignments given for the chloromethylsilane compounds. Three resonances were observed in the spectra of the chlorine containing compounds, one near threshold and two others further above threshold. The intensity of the resonance at threshold was observed to be sensitive to the number of chlorine atoms in the molecule. The Si−Cl antibonding orbital contribution

to the resonance at threshold in the spectra of the chloromethylsilane compounds was therefore clearly demonstrated in the spectra of the chlorosilane compounds. The intensity of the resonance at intermediate energies was found to be dependent upon the number of chlorine atoms in the molecule, as in the chloromethylsilane spectra. The delayed-onset nature of the high energy resonance was also clearly demonstrated in the spectra of the chlorosilane compounds.

Absorption spectra of the Si 2*s* discrete and continuum regions were found to be much weaker than the corresponding 2*p* regions. Relative intensities of the features were considerably larger for the chloromethylsilane and chlorosilane spectra than for the fluoromethylsilane spectra. The discrete regions of the spectra were similar for all of the molecules with only one or two broad resonances resolved. Transitions to antibonding Si–F, Si–Cl, Si–C and Si–H orbitals were assigned to all account for the strong peaks. Term values of the peak positions compared favourably with the term values of the peaks assigned to antibonding orbitals below the Si 2*p* ionization edges. The weak absorption structure in the Si 2*s* continuum regions of the fluoromethylsilane were not considered but MS-Xα calculations were used to assign the features in the chlorosilane and chloromethylsilane spectra.

2.8. REFERENCES

1. A.P. Hitchcock, J. Electron Spectrosc. Rel. Phenom. 25, 245 (1982), updated 1991.
2. A. Bianconi, "XANES Spectroscopy", in: *X-Ray Absorption: Princliples, Applications, Techniques of EXAFS, SEXAFS and XANES*, ed. D.C. Koningsberger and R. Prins (John Wiley and Sons, Toronto, 1988) p. 573.
3. A.P. Hitchcock, Phys. Scr. T31, 159 (1990).
4. E.A. Stern, "Theory of EXAFS", in: *X-ray Absorption: Principles, Applications, Techniques of EXAFS, SEXAFS and XANES*, ed. D.C. Koningsberger and R. Prins (John Wiley and Sons, Toronto, 1988) p. 3.
5. D.E. Sayers and B.A. Bunker, "Data Analysis", in: *X-ray Absorption: Principles, Applications, Techniques of EXAFS, SEXAFS and XANES*, ed. D.C. Koningsberger and R. Prins (John Wiley and Sons, Toronto, 1988) p. 211.
6. W.H.E. Schwarz, Agnew. Chem. Internat. Edit. 13, 454 (1974).
7. F.C. Brown, "Inner-Shell Threshold Spectra", in: *Synchrotron Radiation Research*, ed. H. Winick and S. Doniach (Plenum Pre s, New York, 1980) p. 61.
8. J. Berkowitz, *Photoabsorption, Photoionization and Photoelectron Spectroscopy* (Academic Press, New York, 1979).
9. R.E. La Villa and R.D. Deslattes, J. Chem Phys. 44, 4399 (1966).
10. T.M. Zimkina and A.S. Vinogradov, J. Phys. Paris Colloq. 32, C4-3 (1971).
11. V.I. Nefedov, Z. Struk. Khim. 11, 272 (1970).
12. M.A. Robin, *Higher Excited States of Polyatomic Molecules*, Vol. 1 (Academic Press, New York, 1974).

13. J.L. Dehmer, J. Chem. Phys. 56, 4496 (1972).

14. J.D. Bozek, G.M. Bancroft, J.N. Cutler, K.H. Tan, B.W. Yates and J.S. Tse, Chem. Phys. 132, 25 (1989).

15. B.W. Yates, K.H. Tan, G.M. Bancroft, L.L. Coatsworth and J.S. Tse, J. Chem. Phys. 83, 4906 (1985).

16. B.W. Yates, K.H. Tan, G.M. Bancroft, L.L. Coatsworth, J.S. Tse and G.J. Schrobilgen, J. Chem. Phys. 84, 3603 (1986).

17. B.W. Yates, K.H. Tan, G.M. Bancroft and J.S. Tse, J. Chem. Phys. 85, 3840 (1986).

18. J.E. Bice, K.H. Tan, G.M. Bancroft and J.S. Tse, Inorg. Chem. 26, 4106 (1987).

19. K.H. Sze and C.E. Brion, Chem. Phys. 137, 353 (1989).

20. B. Sonntag, J. Phys. 39, C4 (1978).

21. R. Haensel, C. Keitel, P. Schreiber and C. Kunz, Phys. Rev. 188, 1375 (1969).

22. C.E. Wight, C.E. Brion and M.J. Van der Wiel, J. Electron Spectroc. Relat. Phenom. 1, 457 (-731972).

23. R.B. Kay, Ph.E. Van der Leeuw and M.J. Van der Wiel, J. Phys. B 10, 2513 (1977).

24. A.P. Hitchcock and C.E. Brion, J. Electron Spectrosc. Relat. Phenom. 18, 1 (1980).

25. J.L. Dehmer and D. Dill, Phys. Rev. Lett. 35, 213 (1975).

26. J.W. Davenport, Phys. Rev. Lett. 36, 945 (1976).

27. T.N. Rescigno and P.W. Langhoff, Chem. Phys. Lett. 51, 65 (1977).

28. J.L. Dehmer, "Shape Resonances in Molecular Fields" in: *Resonance and Related Chemical Dynamics*, ed. D.G. Truhlar, Am. Chem. Soc. Ser. 263 (Am. Chem. Soc., Washington, 1984) p. 139.

29. P.W. Langhoff, "Molecular Photoionization Resonances: A Theoretical Chemist's Prespective" in: *Resonance and Related Chemical Dynamics*, ed. D.G. Truhlar, Am. Chem. Soc. Ser. 263(Am. Chem. Soc., Washington, 1984) p. 113.

30. A.P. Hitchcock, S. Beaulieu. T. Steel, J. Stöhr and F. Sette, J. Chem. Phys. 80, 3927 (1984).

31. F. Sette, J. Stöhr and A.P. Hitchcock, Chem. Phys. Lett. 110, 517 (1984).

32. F. Sette, J. Stöhr and A.P. Hitchcock, J. Chem. Phys. 81, 4906 (1984).

33. J.A. Horslry, J. Stöhr, A.P. Hitchcock, D.C. Newbury, A.L. Johnson and F. Sette, J. Chem. Phys. 83, 6099 (1985).

34. A.P. Hitchcock, D.C. Newbury, I. Ishii, J. Stöhr, J.A. Horsley, R.D. Redwing, A.L. Johnson and F. Sette, J. Chem. Phys. 85, 4849 (1986).

35. I. Ishii, R. McLaren, A.P. Hitchcock and M.B. Robin, J. Chem. Phys. 87, 4344 (1987).

36. J. Stöhr, J.L. Gland, W. Eberhardt, D. Outka, R.J. Madix, F. Sette, R.J. Koestner and U. Doebler, Phys. Rev. Lett 51, 2414 (1983).

37. J. Stöhr, F. Sette and A.L. Johnson, Phys. Rev. Lett. 53, 1684 (1984).

38. M.N. Piancastelli, D.W. Lindle, T.A. Ferret and D.A. Shirley, J. Chem. Phys. 86, 2765 (1987).

39. A.P. Hitchcock and J. Stöhr, J. Chem. Phys. 87, 3253 (1987).

40. M.N. Piancastelli, D.W. Lindle, T.A. Ferret and D.A. Shirley, J. Chem. Phys. 87, 3255 (1987).

41. J.A. Sheehy, T.J. Gil, C.L. Winstead, R.E. Farr.n and P.W. Langhoff, J. Chem. Phys. 91, 1796 (1989).

42. J.S. Tse, J. Chem. Phys. 89, 920 (1988).

43. B.M. Addison-Jones, K.H. Tan, B.W. Yates, J.N. Cutler, G.M. Bancroft and J.S. Tse, J. Electron Spectrosc. Relat. Phenom. 48, 155 (1989).

44. M. Nakamura, M. Sasanuma, S. Sato, M. Watanabe, H. Yamashita, Y. Iguchi, A. Ejiri, S. Nakai, S. Yamaguchi, T. Sagawa, Y. Nakai and T. Oshio, Phys. Rev. 178, 80 (1969).

45. M.J. Van der Wiel, Th.M. El-Sherbini and C.E. Brion, Chem. Phys. Lett. 7, 161 (1970).

46. D.A. Shaw, G.C. King, F.H. Read and D. Cvejanović, J. Phys. B 15, 1785 (1982).

47. D.W. Lindle, C.M. Truesdale, P.H. Kobrin, T.A. Ferrett, P.A. Heimann, U. Becker, H.G. Kerkhoff and D.A. Shirley, J. Chem. Phys. 81, 5375 (1984).

48. M. Tronc, G.C. King, R.C.Bradford and F.H. Read, J. Phys. B 9, L555 (1976).

49. D.A. Shaw, G.C. King, D. Cvejanović and F.H. Read, J. Phys. B 17, 2091 (1984).

50. W.H.E. Schwarz and R.J. Buenker, Chem. Phys. 13, 153 (1976).

51. I. Harrison and G.C. King, J. Electron Spectrosc. Relat. Phenom. 43, 155 (1987).

52. X.-M. Tong and J.-M. Li, J. Phys. B 22, 1531 (1989).

53. R.N.S. Sodhi, C.E. Brion and R.G. Cavell, J. Electron Spectrosc. Relat. Phenom. 34, 373 (1984).

54. W. Zhang, K.H. Sze, C.E. Brion, X.M. Tong and J.M. Li, Chem. Phys. 140, 265 (1990).

55. C.T. Chen, Y. Ma and F. Sette, Phys. Rev. A 40, 6737 (1989).

56. C.T. Chen and F. Sette, Rev. Sci. Instrum. 60, 1616 (1989).

57. C.T. Chen and F. Sette, Phys. Scr. T31, 119 (1990).

58. P.A. Heimann, F. Senf, W. McKinney, M. Howells, R.D. van Zee, L.J. Medhurst, T. Lauritzen, J. Chin, J. Meneghetti, W. Gath, H. Hogrefe and D.A. Shirley, Phys. Scr. T31, 127 (1990).

59. M. Domke, C. Xue, A. Uschmann, T. Mandel, E. Hudson, D.A. Shirley and G. Kaindl, Chem. Phys. Lett. 173, 122 (1990).

60. Y. Jugnet, F.J. Himpsel, Ph. Avouris and E.E. Koch, Phys. Rev. Lett. 53, 198 (1984).

61. A.P. Hitchcock and C.E. Brion, J. Electron Spectrosc. Relat. Phenom. 10, 317 (1977).

62. I. Ishii and A.P. Hitchcock, J. Electron Spectrosc. Relat. Phenom. 46, 55 (1988).

63. M.B. Robin, I. Ishii, R. McLaren and A.P. Hitchcock, J. Electron Spectrosc. Relat. Phenom. 47, 53 (1988).

64. Y. Ma, F. Sette, G. Meigs, S. Modesti and C.T. Chen, Phys. Rev. Lett. 63, 2044 (1989).

65. H. Rabus, D. Arvanitis, M. Domke, A. Puschmann, L. Wenzel, G. Comelli, G. Kaindl and K. Baberschke, Phys. Scr. T31, 131 (1990).

66. F.X. Gadea, H. Köppel, J. Schirmer, L.S. Cederbaum, K.J. Randall, A.M. B. . .haw, Y. Ma, F. Sette and C.T. Chen, Phys. Rev. Lett. 66, 883 (1991).

67. R.E. Farren, J.A. Sheehy and P.W. Langhoff, Chem. Phys. Lett. 177, 307 (1991).

68. W. Eberhardt, R.-P. Haelbich, M. Iwan, E.E. Koch and C. Kunz, Chem. Phys. Lett. 40, 180 (1976).

69. M. Tronc, G.C. King and F.H. Read, J. Phys. B 12, 137 (1979).

70. A.P. Hitchcock, M. Popock and C.E. Brion, Chem. Phys. Lett. 49, 125 (1977).

71. W. Hayes and F.C. Brown, Phys. Rev. A 6, 21 (1972).

72. W.H.E. Schwarz, Chem. Phys. 11, 217 (1975).

73. W. Hayes, F.C. Brown and A.B. Kunz, Phys. Rev. Lett. 27, 774 (1971).

74. H. Friedrich, B. Sonntag, P. Rabe, W. Butscher and W.H.E. Schwarz, Chem. Phys. Lett. 64, 360 (1979).

75. G. Cooper, T. Ibuki and C.E. Brion, Chem. Phys. 140, 147 (1990).

76. E.B. Zarate, G. Cooper and C.E. Brion, Chem. Phys. 148, 289 (1990).

77. J. Hormes, U. Kuetgens and I. Ruppert, J. Phys. 47, C8-569 (1986).

78. R. Szargan, K.H. Hallmeier,A. Meisel and E. Hartmann, "Core Excited States in the XUV Absorption Spectra of Boron, Carbon, Silicon and Titanium Fluorides. $X\alpha_{MT}$ Calculations", in: *Core Excited States in the XUV*, 1980, p. 805.

79. J.A. Stephens, D. Dill and J.L. Dehmer, J. Chem. Phys. 84, 3638 (1986).

80. W. Zhang, G. Cooper, T. Ibuki and C.E. Brion, Chem. Phys. 137, 391 (1989).

81. W. Zhang, G. Cooper, T. Ibuki and C.E. Brion, Chem. Phys. 151, 343 (1991).

82. W. Zhang, G. Cooper, T. Ibuki and C.E. Brion, Chem. Phys. 151, 357 (1991).

83. A.S. Vinogradov and T.M. Zimkina, Opt. Spect. 31, 288 (1971).

84. H. Friedrich, B. Pittel, P. Rabe, W.H.E. Schwarz and B. Sonntag, J. Phys. B 13, 25 (1980).

85. A.A. Pavlychev, A.S. Vinogradov, T.M. Zimkina, D.E. Onopko and S.A. Titov, Opt. Spect. 52, 302 (1982).

86. M.Ya. Amusya, A.A. Pavlychev, A.S. Vinogradov, D.E. Onopko and S.A. Titov, Opt. Spect. 53, 91 (1982).

87. D L. Mott, Phys. Rev. 144, 94 (1966).

88. T.A. Carlson, W.A. Svensson, M.O. Krause, T.A. Whitley, F.A. Grimm, G.V. Wald, J.W. Taylor and B.P. Pullen, J. Chem. Phys. 84, 122 (1986).

89. S. Bodeur, J.L. Ferrer, I. Nenner, P. Millie, M. Benfatto and C.R. Natoli, J. Phys. 48, C9-1117 (1987).

90. J.S. Tse, Z.F. Liu, J.D. Bozek and G.M. Bancroft, Phys. Rev. A 39, 1791 (1989).

91. B.M. Addison, K.H. Tan, G.M. Bancroft and F. Cerrina, Chem. Phys. Lett. 129, 468 (1986).

92. T.A. Ferrett, D.W. Lindle, P.A. Heimann, M.N. Piancastelli, P.H. Kobrin, H.G. Kerkhoff, U. Becker, W.D. Brewer and D.A. Shirley, J. Chem. Phys 89, 4726 (1988).

93. K.H. Sze and C.E. Brion, Chem. Phys. 140, 439 (1990).

94. J.S. Tse, Chem. Phys. Lett. 163, 392 (1989).

95. G. Cooper, K.H. Sze and C.E. Brion, J. Am. Chem. Soc. 111, 5051 (1989).

96. E. Ruhl and A.P. Hitchcock, J. Am. Chem. Soc. 111, 5069 (1989).

97. A.P. Hitchcock, A.T. Wen and E. Ruhl, J. Electron Spectrosc. Relat. Phenom. 51, 653 (1990).

98. G.C. Cooper, K.H. Sze and C.E. Brion, J. Am. Chem. Soc. 112, 4121 (1990).

99. A.P. Hitchcock, A.T. Wen and E. Ruhl, Chem. Phys. 147, 51 (1990).

100. A.P. Hitchcock, J.A. Horsley and J. Stöhr, J. Chem. Phys. 85, 4835 (1986).

101. K.H. Sze, C.E. Brion, X.M. Tong and J.M. Li, Chem. Phys. 115, 433 (1987).

102. A.P. Hitchcock, S. Bodeur and M. Tronc, Chem. Phys. 115, 93 (1987).

103. K.H. Sze, C.E. Brion, M. Tronc, S. Bodeur and A.P. Hitchcock, Chem. Phys. 121, 279 (1988).

104. A.P. Hitchcock and M. Tronc, Chem. Phys. 121, 265 (1988)

105. N. Kosugim, S. Bodeur and A.P. Hitchcock, J. Electron Spectrosc. Relat. Phenom. 51, 103 (1990).

106. C. Dezarnaud, M. Tronc and A.P. Hitchcock, Chem. Phys. 142, 455 (1990).

107. G. Cooper, E.B. Zarate, R.K. Jones and C.E. Brion, Chem. Phys. 150, 251 (1991).

108. S. Bodeur, I. Nenner and P. Millie, Phys. Rev. A 34, 2986 (1986).

109. J.D. Bozek, G.M. Bancroft and K.H. Tan, Chem. Phys. 145, 131 (1990).

110. A.P. Hitchcock and C.E. Brion, J. Electron Spectrosc. Relat. Phenom. 14, 417 (1978).

111. F.C. Brow, R.Z. Bachrach and A. Bianconi, Chem. Phys. Lett. 54, 425 (1978).

112. R.N.S. Sodhi and C.E. Brion, J. Electron Spectrosc. Relat. Phenom. 37, 97 (1985).

113. E. Ishiguro, S. Iwata, A. Mikuni, Y. Suzuki, H. Kanamori and T. Sasaki, J. Phys. B 20, 4725 (1987).

114. Z.F. Liu, J.N. Cutler, G.M. Bancroft, K.H. Tan, R.G. Cavell and J.S. Tse, Chem. Phys. Lett. 172, 421 (1990).

115. S. Bodeur and I. Nenner, J. Phys. 47, C8-79 (1986).

116. S. Bodeur, P. Millié, E. Lizon á Lugrin, I. Nenner, A. Filipponi, F. Boscherini and S. Mobilio, Phys. Rev. A 39, 5075 (1989).

117. S. Bodeur, P. Millié and I. Nenner, Phys. Rev. A 41, 252 (1990).

118. V.A. Fomichev, T.M. Zimkina, A.S. Vinogradov and A.M. Evdokimov, J. Struct. Chem. 11, 626 (1970).

119. J. Hormes, R. Chauvistre, U. Keutgens, U. Fischer and I. Ruppert, J. Phys. 48, C9-1113 (1987).

120. J.L. Ferrer, S. Bodeur and I. Nenner, J. Electron Spectrosc. Relat. Phenom. 52, 711 (1990).

121. R. Haensel, C. Keitel, P. Schreiber and C. Kunz, Phys. Rev. 188, 1375 (1969).

122. K.H. Johnson, Advan. Chem. Phys. 7, 143 (1973).

123. T.W. Davenport, *Ph. D. Thesis*, University of Pennsylvania, USA (1976).

124. J.C. Slater and K.H. Johnson, Phys. Rev. B 5, 844 (1971).

125. D.A. Case and M. Karplus, Chem. Phys. Lett. 39, 33 (1976).

126. D.A. Case, Ann. Rev. Phys. Chem. 33, 151 (1982).

127. J.C. Slater, Phys. Rev. 81, 385 (1951).

128. R.S. Wallace, *Ph.D. Thesis*, Boston Universtiy Graduate School (1980).

129. D. Dill and J.L. Dehmer, J. Chem. Phys. 61, 692 (1974).

130. R. Rempfer, H. Operhammer and N. Auner, J. Am. Chem. Soc. 108, 3893 (1986).

131. P.W. Allen and L.E. Sutton, Acta Cryst. 3, 46 (1950) and references therein.

132. L.O. Brockway and F.T. Wall, J. Am. Chem. Soc. 56, 2373 (1934).

133. R.C. Mackler, J.H. Bailey and W. Gordy, J. Chem. Phys. 21, 1710 (1953).

134. R. Wellington and M.C.L. Gerry, J. Molec. Spectrosc. 60, 117 (1976).

135. R. Kewley, P.M. McKinney and A.G. Robiette, J. Molec. Spectrosc. 34, 390 (1970).

136. D.R.J. Boyd, J. Chem. Phys. 23, 922 (1955).

137. K. Schwarz, Phys. Rev. B 5, 2466 (1972).

138. J.G. Norman, J. Chem. Phys. 61, 4630 (1974).

139. W. Rösch, W.G. Klemperer and K.H. Johnson, Chem. Phys. Lett. 23, 149 (1973).

140. F. Herman, A.R. Williams and K.H. Johnson, J. Chem. Phys. 61, 3508 (1974).

141. L. Latter, Phys. Rev. 99, 510 (1955).

142. R.N.S. Sodhi, S. Daviel, C.E. Brion and G.G.B. de Souza, J. Electron Spectrosc. Relat. Phenom. 35, 45 (1985).

143. P. Kelfve, B. Blomster, H. Siegbahn, K. Siegbahn, E. Sanhueza and O. Goscinski, Phys. Scr. 21, 75 (1980).

144. W.B. Perry and W.L. Jolly, Chem. Phys. Lett. 17, 611 (1972).

145. J.E. Drake, C. Riddle, and L. Coatsworth Can. J. Chem. 53, 3602 (1975).

146. J.D. Bozek, G.M. Bancroft, J.N. Cutler and K.H. Tan, Phys. Rev. Lett. 65, 2757 (1990).

147. A.A. Pavlychev, A.S. Vinogradov, T.M. Zimkina, D.E. Onopko and S.A. Titov, Opt. Spec. 47, 40 (1979).

148. C.R. Wen and R.A. Rosenberg, J. Chem. Phys., *submitted.*

149. J.D. Bozek, K.H. Tan, G.M. Bancroft and J.S. Tse, Chem. Phys. Lett. 138, 33 (1987).

150. G.G.B. de Souza, P. Morin and I. Nenner, J. Chem. Phys. 83, 492 (1985).

151. G. Herzberg, *Molecular Spectra and Structure*, Vol. 3 (D. Van Nostrand Company Inc., Toronto, 1967).

152. H. Iishikawa, K. Fujima, H. Adachi, E. Miyauchi and T. Fujii, J. Chem. Phys., *submitted.*

153. J. Kriele, A. Schweig and W. Thiel, Chem. Phys. Lett. 108, 259 (1984).

154. A.A. Pavlychev, A.S. Vinogradov and T.M. Zimkina, Opt. Spectrosc. 52, 139 (1982).

155. R.A. Rosenberg, *unpublished results.*

156. J.D. Bozek, G.M. Bancroft and K.H. Tan, Phys. Rev. A 43, 3597 (1991).

157. K. Nakamoto, *Infrared and Raman Spectra of Inorganic and Coordination Compounds* (Wiley, Toronto, 1986), 4th ed.

158. W.L. Jolly, K.D. Bomben and C.J. Eyermann, At. Data Nucl. Data Tables 31, 433 (1984).

159. W.C. Ermler and R.S. Mulliken, J. Molec. Spect. 61, 100 (1976).

160. U. Fano and F. Cooper, Rev. Mod. Phys. 40, 441 (1968).

CHAPTER 3.
Vibrational Fine Structure in the Si 2p photoelectron spectra of simple gaseous molecules

3.1. INTRODUCTION

Photoelectron spectroscopy is both an important analytical method and an area of intense fundamental research. Photoelectron spectroscopy was first performed using nearly monochromatic line photon sources, which remain important for the analytical methods. The fundamental research is driven by the increasing availability of high-resolution tunable photon sources, namely synchrotrons. Photoelectron spectroscopy using synchrotron radiation sources is a relatively new field with the first reports appearing in 1972.[1,2] Second generation synchrotron light sources and advances in monochromator design have continued to open new areas of research for photoelectron spectroscopy and the next generation of synchrotron light sources, presently being developed,[3] promise to continue the trend.

The photoelectron effect is a dipole interaction where the energy of an incident photon is used to eject bound electrons from atoms, molecules or solid samples. Photoelectron spectroscopy is performed by analyzing the kinetic energies of the ejected photoelectrons. The kinetic energy of the ejected electron, E_k, and the energy of the ionizing radiation, $h\nu$, are related by Einstein's energy conservation relation for the photoelectric effect:[4]

$$E_k = h\nu - (E_f - E_0) \qquad (3.1.1)$$

where E_0 is the total energy of the initial state of the sample, usually (but not always) the ground electronic state, and E_f is the total energy of the sample after

the ejection of the photoelectron. The kinetic energy of the ionized sample is much smaller than the kinetic energy of the electron because of the large mass difference. When more than one non-degenerate electron is available for ejection from the sample, a series of kinetic energies, $E_k(j)$, and final state energies, $E_f(j)$, are appropriate in Eq. (3.1.1). The *ionization energy*, $I(j)$, of the ejected electron, j, is the energy difference between the total energies of the j^{th} final state and the initial state:

$$I(j) = E_f(j) - E_0 \tag{3.1.2}$$

In Koopmans' theorem,[5] which assumes that the photoelectric event is a one-electron process with no interaction between the ionized electron and the remaining electrons in the sample, the ionization energy is equal to the binding energy of the electron, $E_b(j)$, and the eigenvalue of the j^{th} orbital of the initial state of the sample:

$$I(j) = E_b(j) = -\epsilon_j \tag{3.1.3}$$

The binding energy in Koopmans' theorem is referenced to the vacuum level and does not account for any electron relaxation in the ionized sample. Combining the above equations yields,

$$h\nu = E_b(j) + E_k(j) \tag{3.1.4}$$

which directly relates the known photon energy, the measured kinetic energy of the photoelectron and its binding energy.

In a photoelectron spectrum, peaks are observed at characteristic binding energies. The ejected electrons are energy analyzed over the range $0 \leq E_k(j) \leq h\nu$ and counted for each kinetic energy range. If the photon beam is monochromatic and of known energy, Eq. (3.1.4) can be used to relate the kinetic energies $E_k(j)$ with the binding energies $E_b(j)$. Peaks in the photoelectron spectrum are associated with the atomic or molecular orbitals in the sample with ionization potentials less than the incident photon energy. In the historical development

of photoelectron spectroscopic techniques, photon sources in two different energy ranges have been used. Ultraviolet photoelectron spectroscopy (UPS), developed by Turner and Al-Joboury at Imperial College, London, England,[6] typically uses a helium discharge lamp to generate photons to ionize the valence molecular orbitals in a sample. The He I line at 21.22 eV and the He II line at 40.81 eV, which have very narrow natural linewidths of a few millivolts, have enough energy to eject electrons from the outer orbitals of matter. X-ray photoelectron spectroscopy (XPS), developed in Uppsala, Sweden, by Siegbahn and coworkers,[7] usually employs Al K_α and Mg K_α radiation with energies of 1486 and 1253 eV respectively, as the source of ionizing photons. The higher energy photons used in XPS are capable of ionizing the core electrons of atoms in molecules and solids. Siegbahn and coworkers found that the binding energies of core electrons from a given atom are sensitive to the chemical environment of the atom and coined the term "electron spectroscopy for chemical analysis" (ESCA) to describe the analytical technique. Unmonochromatized Al K_α and Mg K_α radiation have line widths of $\sim$1.0 eV (Ref. 8) resulting in photoelectron lines with widths of $\gtrsim$1 eV. When a monochromator is employed, excitation bandwidths as narrow as 0.25 eV [6,9] can be achieved, but typically only $\gtrsim$0.3 eV resolution is achieved. Monochromatization of the lines results in a significant loss in light intensity which reduces the photoelectron current from the sample and becomes the limiting factor for the achievable resolution.

The availability of monochromatized synchrotron radiation fills in the gap in the excitation energy between the He I and He II lines around 20-40 eV and the Al and Mg Kα lines above 1000 eV. More significantly for this study, the high intensity from the present day synchrotrons allows us to select a very narrow bandwidth of ionizing radiation and still have enough photon flux to get a measurable photoelectron current from the sample. The very high resolution

in this work is unparalleled in previous photoelectron spectra and is seen to be critical for resolving the vibrational fine structure in the photoelectron spectra.

High resolution photoelectron spectroscopy has been widely used in the past eight years to resolve and characterize surface chemical shifts of the narrow core levels of metals and semiconductors,[10,11] and more recently to characterize the ligand field splitting of the Sn 4*d* core level of Sn metal.[11] Total instrumental (photon plus electron) resolutions of < 0.2 eV are essential for such studies. Prior to this work photoelectron spectra of molecular core-levels with binding energies of >30 eV have not been obtained with total instrumental resolutions of ≤0.1 eV. High resolution photoabsorption spectra (photon resolution <0.1 eV) for both solid films[12] and gases[13] below 225 eV were obtained before the high resolution photoelectron spectra because of the much lower incident radiation intensities required. A number of other high resolution photoabsorption spectra have been obtained recently using monochromatized synchrotron radiation with photon energies up to 150 eV as reported in Chapter 2, and more recently up to 400 eV.[14] Many more high resolution "absorption" spectra of gases have also been obtained up to 700 eV in the last ten years using electron energy loss spectroscopy.[15]

In contrast to the above examples, very few high resolution molecular core level photoelectron spectra have been obtained using synchrotron radiation. Spectra taken with laboratory sources have already shown the great potential of such high resolution studies. For example, over fifteen years ago, Gelius *et al*[16,17] partially resolved the C–H vibrational splitting (symmetric stretch) for the C 1*s* level of CH_4 using a monochromatized Al Kα source. More recently, they completely resolved this splitting[18] with an improved instrument which gave experimental contributions to the line width of 0.23 eV and a total C 1*s* width of 0.3 eV. Over ten years ago, Bancroft *et al*[19] resolved the ligand field splittings on a number of low lying core *d* levels (binding energies <27 eV) using He I and He II sources. They

suggested[20,21] that similar splittings would be resolved on many deeper narrow *p*, *d*, and *f* core levels. A high resolution Si 2*p* photoelectron spectrum of $SiCl_4$ taken with monochromatized synchrotron radiation ($\Delta E_{photon} \approx 0.2$ eV) with an overall resolution of 0.33 eV was reported recently, but, no fine structure was observed.[22]

High resolution core level photoelectron spectra are simpler than absorption spectra, and provide fundamentally important information for the future development of all core level spectroscopies (i.e. absorption, photoelectron, Auger, and fluorescence) of free molecules, adsorbates on surfaces, and solids. For example, inherent core level linewidths need to be measured to help fully interpret the photoelectron spectra of surfaces which are complicated by surface core level shifts and disorder broadening associated with various adsorbate covered surfaces.[16,23] In addition, these widths are required to study the chemical dependence of core level lifetimes and linewidths in free molecules and surfaces.[16,24] Equally important, such high resolution measurements are urgently required for several reasons: to aid in the complete interpretation of the complex pre-edge absorption spectra of free molecules,adsorbates and surfaces[25]; to stringently test the core equivalent model which has been widely used to interpret core level binding energies[26] and vibrational broadenings of core level photoelectron,[27–31] photoabsorption[32] and X-ray emission spectra[33]; and to study vibrational band intensities as a function of excitation energy where shape resonances are expected to affect the intensity distribution of bands within the vibrational manifold.[34]

Vibrational fine structure in molecular core-level spectroscopy was first resolved in the C1*s* photoelectron spectrum of CH_4 reported by Siegbahn.[17] The spectrum was measured with a monochromatized Al K_α source yielding a total experimental resolution of ~0.4 eV and it was observed to be noticeably asymmetric exhibiting three unresolved vibrational bands of decreasing intensity.[17] The resolution of the spectrometer was subsequently slightly improved and the vibrational progression was resolved into its individual bands.[18] Prior to

Siegbahn's measurements, core-level photoelectron bands were not expected to exhibit vibrational fine structure[35,36] since core orbitals are generally considered non-bonding orbitals and, based on trends observed in the vibrational structure accompanying valence photoelectron bands, photoelectron bands of non-bonding orbitals were not expected to exhibit vibrational fine structure.[37]

Numerous other examples of vibrational fine structure have since been observed in core level spectra using a variety of different experimental techniques. Absorption techniques (photoabsorption, electron energy loss, and photoelectron spectroscopies) and emission techniques (X-ray emission, Auger, and autoionization spectroscopies) have both been used to study the vibrational bands observed in core level spectroscopy. In absorption-type experiments, the core ionized molecule is the final state of the experiment. The attenuation of the incident radiation or the energy of the ejected photoelectron contains information about the nature of the core hole created, including information about the vibrational levels of the core hole state. In emission techniques, photons or electrons emitted in the process of filling the core hole are analyzed for that same information, hence the core ionized molecule is the initial state of these systems. The techniques used to study the vibrational structure accompanying core hole creation or filling are all limited or complicated by the nature of the initial or final states of the experiment.

At very high experimental resolutions, vibrational bands are often observed on the core to bound transitions (usually core $\rightarrow$ antibonding) in the pre-edge region of photoabsorption (PAS) and electron energy loss (EELS) spectra.[38,39] The intensities and spacing of the vibrational bands are influenced by both the core hole and the presence of the excited electron in an empty orbital of the valence shell of the molecule. The bonding properties of the molecule, and hence the vibrational manifold of the core excitation are affected by these excited electrons.

Vibrational fine structure has been resolved in the N1$s \rightarrow 1\pi_g^*$ transition in the pre-edge of the N1s absorption spectrum of N_2 by both EELS[39,40] and very recently by PAS.[14,38,41] Spectral features resulting from excitations of the C1s electron into an antibonding π^* orbital also exhibit vibrational structure for the simple carbon compounds, CO,[42,43] CH_4,[43,44] C_2H_2,[44,45] C_2H_4,[38,41,44–46] and C_6H_6[45,47] and the spectra have been resolved by both techniques. When vibrational structure is observed for the non-bonding Rydberg levels[48] it is possible to estimate the effect of the core hole on the bonding properties of the molecule since the Rydberg orbitals do not interact with the molecule appreciably.

X-ray emission,[49,50] Auger,[51–53] and autoionization[52,54] spectra are often complicated by interference between the finite lifetime of the core hole state and its vibrational structure.[55–57] Emission studies of vibrations in core levels have concentrated primarily on simple diatomics such as N_2,[49,51,54] CO,[49,52,58] NO,[49] O_2,[49,53] and simple hydrides such as H_2O,[59] NH_3,[60] and H_2S.[61] One particular experimental advantage of the emission techniques is that a highly monochromatic excitation source is not usually required and often laboratory sources can be used.

The difficulties involved in obtaining vibrationally resolved core level photoelectron spectra are primarily experimental. A highly monochromatic light source with much greater intensity than needed for photoabsorption spectroscopy is required to resolve vibrational bands spaced <0.3 eV apart at energies of usually >100–300 eV. This requirement has prevented core level photoelectron spectra from being obtained with resolved vibrational structure in all but the simplest of compounds, CH_4[17,18,62] and SiH_4.[63,64] Using monochromatized Al K_α sources, the bandwidth of the incident radiation has previously been limited to >0.3 eV. With the use of a high resolution monochromator and a synchrotron radiation source, core level photoelectron spectra can be used to study changes in the intensities of the vibrational bands as a function of energy of the incident light. With the other techniques listed above, vibrational structure appears only at discrete levels

of fixed energy and therefore they cannot be used for such studies. Theoretical calculations have indicated that the relative intensities of vibrational bands within a photoelectron line should be affected by shape resonances in both valence and core levels.[65] Vibrationally resolved studies of valence photoelectron bands have confirmed this prediction in numerous systems[66,67] but to date there have been no reports of analogous studies performed using core level photoelectron spectroscopy. The recent commissioning of new high resolution monochromators[38,41,68] and the future availability of new high brightness synchrotrons should facilitate such measurements in core levels. Overall, photoelectron spectroscopy can provide information about the nature of the core hole ion that is not available from other techniques owing to the lack of interaction between the ejected electron and the core hole ion. In addition, it should be possible to obtain vibrationally resolved cross sections.

Vibrational fine structure observed in core level spectra results from differences in the equilibrium nuclear geometries of the initial and final states of the electronic excitation, ionization or de-excitation process which creates or fills a core hole. In the photoelectron experiment for instance, the initial state is the ground vibrational state of the ground electronic state of the molecule. Under the Born-Oppenheimer approximation, which presumes separability of the nuclear and electronic parts of the wavefunction describing the molecule, the photoionization process involves only an electronic transition. The nuclear geometry of the final state remains unchanged from that of the initial state (neutral molecule) in the photoionization process (sudden approximation). The *equilibrium* nuclear geometry of the final state, however, may be different from the nuclear geometry of the initial state due to electronic reorganization resulting from the incomplete screening of the positive nucleus by the core hole. In quantum mechanical terms, changes in the equilibrium nuclear geometry upon ionization allow for non-zero overlap between the vibrational ground state of the initial electronic state, $v'' = 0$,

and higher vibrational states of the final electronic state, $v' = 0, 1, 2, \ldots, n$. Franck-Condon (FC) factors, defined as the square of the overlap integral between vibrational states of the initial and final electronic states of the transition, can be used to calculate the relative intensities of the individual vibrational bands in the manifold observed. Franck-Condon factors can be calculated only if the potential energy surfaces of the initial and final electronic states are known.

The spacings of the vibrational levels in the ionic core hole state often change from those of the neutral ground state as determined by the change in the potential energy surface of the final state. When vibrational structure is resolved for the core hole state, energies of the vibrational levels can be determined and used in the calculation of the potential energy surface of the core hole state. Individual vibrational states are usually not resolved in core level photoelectron spectroscopy but rather the photoelectron line is asymmetrically broadened by contributions from unresolved vibrational bands.[17] In this situation, vibrational energy levels can be obtained by several different means; by deconvolution of the peak shape, a process which does not always yield one unique result; from theoretical calculations, which are often difficult and time-consuming; or by use of the equivalent-cores approximation which often yields accurate results. In the equivalent-cores model, physical properties of the core hole ion state of a molecule are approximated by the properties of a molecule in which the core ionized atom, Z, is replaced by one with an additional proton, Z+1. Removal of a core electron from the molecule has approximately the same effect on the valence electrons, and hence most of the chemical properties of the molecule, as the addition of a proton to the nucleus of the ionized atom. This is the basis of the equivalent-cores approximation. The equivalent-cores model has been applied to estimate core electron binding energy shifts using Jolly's thermodynamic interpretation,[69,70] and to aid in the assignment of core level pre-edge spectral features.[14,45,48,71] The model has also been applied to approximate the potential energy surfaces of final states

of core ionizations to estimate core level linewidths[72,73] or to calculate parameters describing the vibrational fine structure of the core ionized states.[14,53,74] Previous experimental[17,64] and theoretical[75–77] studies have established the applicability of the equivalent-cores approximation in the determination of vibrational energy levels for core ionized molecules.

In the majority of the previous reports of vibrational fine structure observed in core level spectroscopy, the K shell spectra of simple diatomic, triatomic or hydride molecules of first row elements, C, N, O, and F, were examined for vibrational structure. Broad lines observed in the photoelectron spectra of molecular and atomic C, N, and O adsorbates on a Ni(100) substrate have been attributed to vibrational broadening.[28,29,31,74] Vibrational structure was observed in the LVV Auger spectrum of H_2S in one of the few studies of vibrational effects in core level spectra of non-first row elements.[61]

A rather simple photoelectron spectrometer has been constructed specifically for high resolution gas phase core-level studies of volatile and involatile compounds using monochromatized synchrotron radiation. Following a discussion of the spectrometer and a characterization of the resolution and transmission efficiency obtained, vibrationally resolved photoelectron spectra of the Si $2p$ core-levels of eleven silicon molecules are presented: SiH_4, $C_2H_5SiH_3$, $(CH_3)_2SiH_2$, $(CH_3)_3SiH$, $(CH_3)_4Si$, SiF_4, $SiCl_4$, $(CH_3)_3SiCl$, $(CH_3)_3SiI$, Cl_2SiH_2 and CH_3SiF_3. All of the spectra exhibit vibrational structure and extensive use of the equivalent-cores approximation is made to estimate the energies of the vibrational levels. Experimental resolution plays a crucial role in the observation of vibrational structure and we will show that photon resolutions of $\leq$0.2 eV are required to resolve even the simplest structure. Accurate adiabatic Si $2p_{3/2}$ ionization potentials are also reported for all of the compounds.

3.2. EXPERIMENTAL

Samples of the eleven compounds used in this study were obtained commercially and liquid samples were degassed with repeated freeze-pump-thaw cycles. The samples were then introduced directly into the gas cell of the spectrometer at pressures of between 0.5 and 1.0 torr. Constant sample pressures were maintained over the time required to accumulate data for each spectrum.

With the exception of the very high resolution spectra of SiH_4, SiF_4 and $Si(CH_3)_4$, all of the photoelectron spectra reported here were measured with photons from the CSRF Mark IV Grasshopper monochromator.[78] A 900 groove/mm grating was used in the monochromator, yielding a minimum practical photon resolution of 0.12 Å with 20 μm slit widths (0.16 eV at 130 eV photon energy). Intensities at these resolutions are comparable to those obtained from a typical He I lamp ($\sim 10^{10}$ photons per second). Monochromator slit widths were varied to yield the desired photon resolutions. For the highest resolution spectra of SiH_4, SiF_4 and $Si(CH_3)_4$, undulator radiation was used as the excitation source. Photons from the undulator on the Aladdin storage ring were monochromatized using a 2400 groove/mm grating in a 6 m toroidal grating monochromator (TGM)[79] with an excitation bandwidth (aberration limited) of $\sim$ 0.090 eV at 135 eV photon energy.

As in previous photoelectron studies of gases,[80] the photon beam emerging from the monochromator exit slit is refocussed to the gas cell in the photoelectron chamber. A two stage differential pumping system and a high vacuum gate valve with a rectangular glass light guide (1mm $\times$ 10mm $\times$ 200mm) supported in a copper tube is used to isolate the optical elements of the beamline from the high pressure interaction region. The light guide results in almost five orders of magnitude differential pumping, so that the entire beamline is at pressures of less than 2×10^{-10} torr with pressures in the sample chamber of $\sim10^{-5}$ torr.

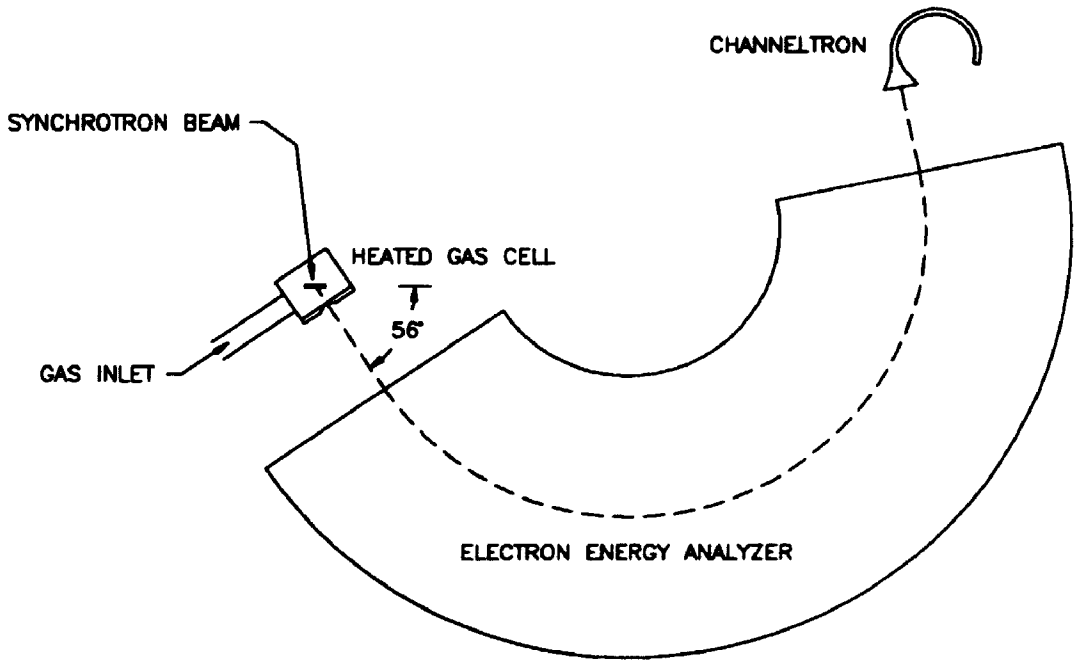

Figure 3.2.1: A schematic diagram of the photoelectron spectrometer based on the McPherson ESCA 36 electron energy analyzer shown in the plane perpendicular to the direction of propagation of the synchrotron beam.

A schematic diagram of the photoelectron spectrometer is shown in Fig. 3.2.1. A large (36 cm mean radius) McPherson electron energy analyzer (from the University of Alberta) provided the required high resolution and high transmission capabilities.[81] The analyzer was oriented on a frame so that the synchrotron beam is directed across the length of the analyzer slit, and so that electrons are taken off at a pseudo-magic angle ($\Theta_x = 55.8°$, $\Theta_y = 34.2°$, $\Theta_z = 90°$) calculated assuming a 90 % polarization of the synchrotron light. The photoelectron angular distribution measured with polarized radiation and a randomly oriented target is given by,[82]

$$\frac{\partial\sigma}{\partial\Omega} = \frac{\sigma}{4\pi}\left[1 + \frac{\beta}{2}\left(3\cos^2\theta - 1\right)\right] \tag{3.2.1}$$

where σ is the photoelectron cross section, β the asymmetry parameter, and θ the angle between the direction of the photoelectron and the polarization vector of the radiation, $\vec{E}$. For partially polarized incident radiation such as synchrotron radiation, Eq. (3.2.1) becomes:

$$\frac{\partial\sigma}{\partial\Omega} = \frac{\sigma}{4\pi}\left[1 - \frac{\beta}{4}\left(3\cos^2\theta_z - 1\right) - 3\rho\left(3\cos^2\theta_x - \cos^2\theta_y\right)\right] \tag{3.2.2}$$

where ρ is the polarization of the incident radiation, $\rho = (I_y - I_x)/I_0$. The size of the McPherson electron energy analyzer dictated the only practical geometry would be for it to be mounted in the xy plane relative to the direction of the propagation of the synchrotron light as the z-direction. The angular distribution of the photoelectron then simplifies to

$$\frac{\partial\sigma}{\partial\Omega} = \frac{\sigma}{4\pi}\left[1 + \frac{\beta}{4}\left(1 + 3\rho\cos 2\theta_x\right)\right] \tag{3.2.3}$$

For light polarizations of other than 90 % the photoelectron intensities will be dependent upon β,[83] albeit only slightly since the polarization of the incident radiation does not change rapidly with photon energy. The effect of the polarization of the incident radiation on the measured cross section is illustrated in Table 3.2.1 where the term $(1 + 3\rho\ \cos\ 2\theta_x)\ /\ 4$ from Eq. (3.2.3) is shown for some representative angles and polarizations. The term should go to zero

in the best case, and then the β term in Eq. (3.2.3) will not contribute to the photoelectron cross section. At the $\theta_x = 55.8°$ geometry, if the degree of light polarization were only 80%, the β term will contribute a ~3% error to the measured cross section.

θ_x	$(1 + 3\,\rho\,\cos 2\theta_x)/4$				
(deg.)	$\rho = 1.0$	$\rho = 0.95$	$\rho = 0.9$	$\rho = 0.85$	$\rho = 0.8$
51.0	0.094	0.102	0.110	0.117	0.125
52.0	0.069	0.078	0.087	0.096	0.105
53.0	0.043	0.054	0.064	0.074	0.085
54.0	0.018	0.030	0.041	0.053	0.065
54.5	0.006	0.018	0.030	0.042	0.055
55.0	−0.007	0.006	0.019	0.032	0.042
55.5	−0.019	−0.005	0.008	0.022	0.035
55.6	−0.021	−0.008	0.006	0.019	0.033
55.8	−0.026	−0.012	**0.002**	0.015	0.029
56.0	−0.031	−0.017	−0.003	0.011	0.025
56.2	−0.036	−0.022	−0.007	0.007	0.021
56.4	−0.041	−0.026	−0.012	0.003	0.017
57.0	−0.055	−0.040	−0.025	−0.009	0.006
58.0	−0.079	−0.062	−0.046	−0.029	−0.013
59.0	−0.102	−0.084	−0.067	−0.049	−0.032
60.0	−0.125	−0.106	−0.087	−0.069	−0.050

Table 3.2.1: Values of the term $(1 + 3\rho \cos 2\theta_x)/4$ for a variety of angles (θ_x) and light polarizations (ρ).

The synchrotron beam from the glass light guide entered the gas cell through another aligned light guide 2 cm in length. Electrons exiting from a 1 mm exit slit on the gas cell, travelled into the analyzer through a 3 mm slit and a baffles arrangement common to the McPherson 36 electron spectrometer. A 1 mm exit slit on the analyzer gave an approximate resolution[81] $\Delta E/E$ of 1/760 or 1.3×10^{-3}. This resulted in an electron resolution of 0.04 eV at a kinetic energy of 30 eV; and this electron resolution or better was used for all of our spectra. The gas cell was heated by a resistance heater for involatile samples.

The McPherson analyzer and the sample chamber were each pumped by 330 l/sec Balzers turbomolecular pumps. Pressures in the gas cell of 0.1 torr (as measured by an MKS capacitance manometer) resulted in pressures of $\sim 10^{-5}$ and $\sim 10^{-7}$ torr in the sample and analyzer chambers respectively.

Electrons emerging from the energy analyzer were detected with a channeltron electron detector biased to a positive voltage of ~2500 V at the front end and grounded at the back. The channeltron detector was linked to a specially designed amplifier-discriminator based on the Amptec A-101 chip. TTL pulses from the A-101 were stored in a frequency counter unit in a Biodata Microlink frame interfaced with a Zenith Z-158 PC microcomputer. A second counter was used to measure a signal proportional to the electron current in the Aladdin storage ring. Due to limitations in the frequency counters, dwell times of one second were used for each channel in the data acquisition. The computer also controlled the kinetic energy scanning of the electron energy analyzer through a Biodata Microlink interface unit and McPherson high stability power supply. The energy of the electrons transmitted by the spherical sector analyzer is proportional to the voltages applied to the spheres, V, plus an offset equal to the work function, ϕ, of the spectrometer:[82,83]

$$E_k = sV\left(1 + \frac{E_k}{E_k + 2m_0c^2}\right) + \phi \qquad (3.2.4)$$

where s is the constant of proportionality and the relativistic term $E_k/\left(E_k + 2m_0c^2\right)$ is vanishingly small for low kinetic energies ($\lesssim 10^{-4}$ for $E_k <$ 100 eV), and hence ignored here. The work function is usually zero for gas phase spectra, but situations exist where charging of the gas cell may necessitate the introduction of a work function value, so it was included in the program. A custom data acquisition computer program was coded in the "C" programming language (~5000 lines) with some additional low level input/output routines written in 8088 Assembler language. The program included real time data acquisition capabilities with adjustable parameters to control the spectrometer and a user manipulated

graphical display of the electron energy spectrum. After entry of the appropriate parameters for the spectrum, the data acquisition program proceeded by setting the energy of the electrons transmitted through the energy analyzer by changing the voltages on the spheres according to Eq. (3.2.4), accumulating electron counts for one second, and then proceeding on to the next electron energy. The program included multi-scanning capabilities allowing a spectrum to be acquired over a period of up to several hours.

A lens system was intentionally not employed in this spectrometer. Especially for high temperature non-conductors, previous experience with both the lens based Leybold LHS-11 system and the McPherson ESCA 36 strongly indicated that *differential* charging is one of the most difficult problems to overcome in obtaining high resolution gas phase spectra. Charge induced shifting of the electron energy spectrum as a function of time seriously degrades the resolution of the spectrum. Previous experience has shown that the basic McPherson system could give the necessary high resolution for the most difficult involatile gas phase molecules.[20,21]

Vibrational structure in the photoelectron spectra was deconvoluted using a non-linear least-squares method[84] employing a linear combination of Gaussian and Lorentzian line shapes. A single peak shape (half height width and Gauss/Lorentz ratio) split by the Si $2p$ spin-orbit coupling and vibrational splitting was used to describe the lineshape for all of the experimental spectra. A modified deconvolution program was coded (in the "C" language) which allowed only one photoelectron line (the vibrational ground-state Si $2p_{3/2}$ line) with spin-orbit splitting and vibrational splitting. Experimental spectra were therefore described by eight parameters,

1. the energy (position) of the Si $2p_{3/2}$, $v' = 0$ photoelectron line,
2. the intensity of the Si $2p_{3/2}$, $v' = 0$ photoelectron line,
3. the full width at half maximum (FWHM) of the photoelectron peak,

4. the Gaussian/Lorentzian ratio in the linear combination of Gaussian and Lorentzian lineshape used in the deconvolution,
5. the Si $2p_{3/2}$ - Si $2p_{1/2}$ splitting,
6. the Si $2p_{3/2}$ - Si $2p_{1/2}$ splitting intensity ratio,
7. the vibrational level separation for each vibrational series identified, and
8. the intensity ratios of the peaks within a vibrational series.

Anharmonic factors were not included in the fitting procedure, since only a small number of vibrational states were observed in most of the Si $2p$ photoelectron spectra. In cases where more vibrational states were found they were not individually resolved and anharmonic factors could not be determined.

3.3. RESULTS and DISCUSSION

3.3.1. Characterization of the Photoelectron Spectrometer

The electron energy spectra of the Xe $N_{4,5}OO$ and Kr $M_{4,5}NN$ Auger lines were measured to characterize the resolution and transmission of the electron spectrometer and to determine the spectrometer constant, s from Eq. (3.2.4). Using a line of known kinetic energy, an accurate spectrometer constant, s_{acc} can be determined by,

$$s_{acc} = \frac{E_k(acc)\,s}{E_k(meas)} \tag{3.3.1}$$

where $E_k(meas)$ is the measured kinetic energy of the line, $E_k(acc)$ the true kinetic energy of the line, and s the spectrometer constant used to measure the spectrum. The Xe $N_{4,5}00$ and Kr $M_{4,5}NN$ Auger spectra have been reported previously at very high resolution[85] and provide useful standards for determining the operating parameters and characteristics for the new spectrometer. Kinetic energies of the intense Xe NOO and Kr MNN Auger lines are given in Table 3.3.1 and Table 3.3.2 respectively and compared with the values from Ref. 85. The agreement between the two sets of values is within ±0.10 eV which is the accuracy limit given for the values in Ref. 85.

The Xe $N_{4,5}OO$ and Kr $M_{4,5}NN$ Auger spectra in Fig. 3.3.1 and Fig. 3.3.2 respectively confirm the high resolution of the electron spectrometer. The resolution observed in Auger electron spectra does not depend on the bandwidth of the excitation source and is therefore a sensitive probe of the resolution of the electron energy analyzer. The spectra in Fig. 3.3.1 and Fig. 3.3.2 are of comparable quality to the previously published Xe NOO and Kr MNN Auger spectra[85] measured with an electron energy analyzer with better resolution ($\Delta E/E = 1/1800$). The doublet peaks in the Kr MNN Auger spectrum in Fig. 3.3.2 at 52.4 and 51.5 eV have been resolved to the baseline with linewidths of ~0.17 eV in a spectrum with higher digital resolution (more points). Similar spectra of

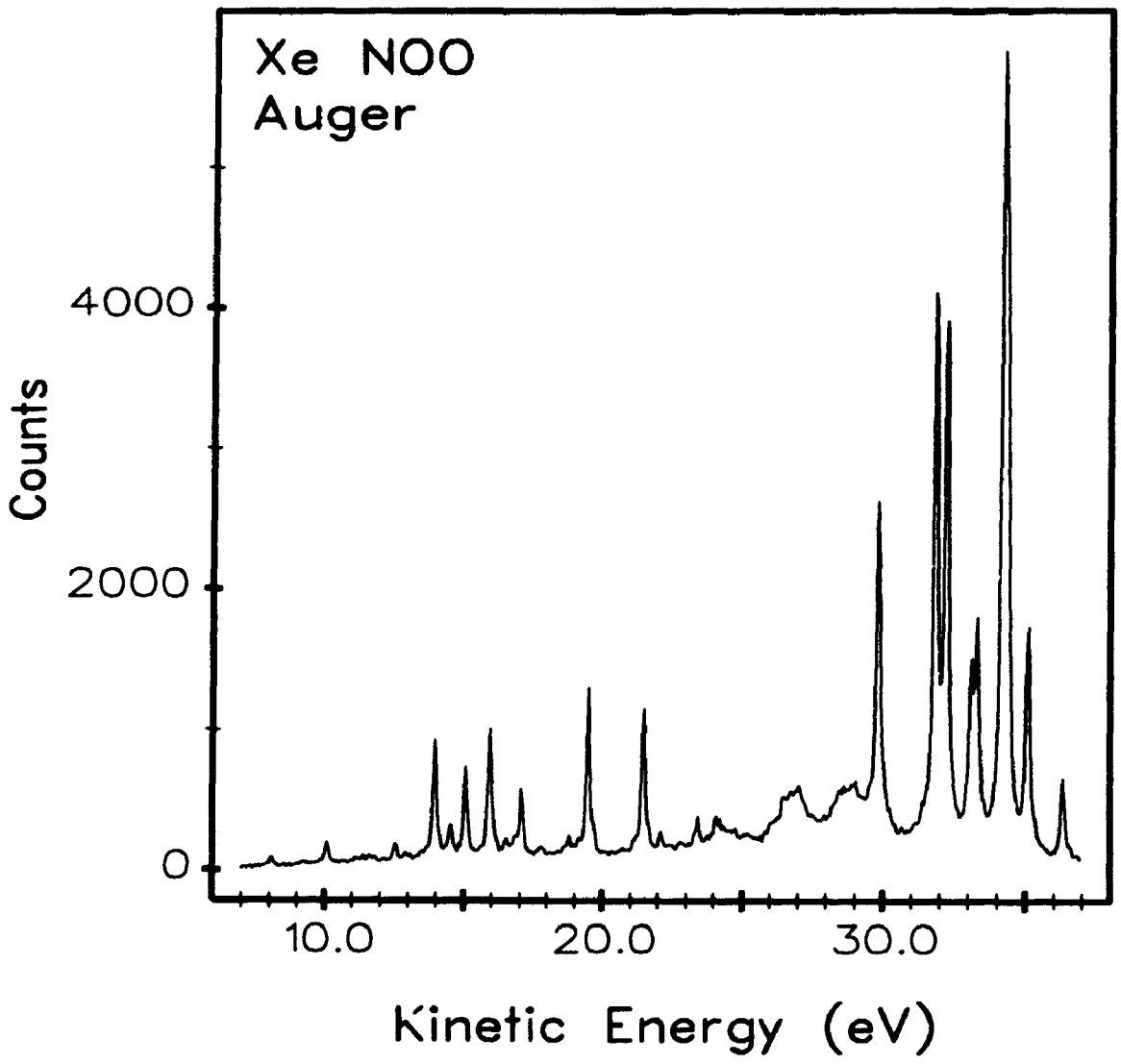

Figure 3.3.1: Xenon $N_{4,5}OO$ Auger spectrum following photoionization of the Xe $4d$ levels at $h\nu = 94$ eV. The positions of the peaks are given in Table 3.3.1.

individual lines in the Xe NOO Auger spectrum were found to have linewidths of 0.13 eV, which approaches the expected lifetime width[86] of ~0.13 eV, and show that the electron resolution obtained is better than 0.06 eV.

peak label	KE_{BOZEK} (eV)	KE_{WERME} (eV)	ΔKE (eV)	I_{BOZEK}/I_{WERME}
1	36.23	36.20	−0.03	1.0180
2	35.00	34.99	−0.01	1.4497
3	34.23	34.21	−0.02	2.7229
4	34.09	34.07	−0.02	0.8704
5	33.22	33.21	−0.01	1.8499
6	33.02	32.99	−0.03	0.9141
7	32.11	32.09	−0.02	1.9536
8	31.73	31.71	−0.02	0.9289
9	29.74	29.73	−0.01	1.1877
15	22.02	22.04	0.02	1.4298
16	21.39	21.44	0.05	0.8180
18	19.42	19.45	0.03	0.7031
19	19.04	19.07	0.03	0.3230
20	18.66	18.74	0.08	0.7417
21	17.68	17.28	−0.40	1.5032
22	16.97	17.02	0.05	0.8761
23	16.74	16.78	0.04	0.8955
24	15.86	15.92	0.06	0.5667
25	14.98	15.05	0.07	0.5275
26	14.42	14.48	0.06	0.7961
27	13.88	13.95	0.07	0.4554
28	12.44	12.54	0.10	0.3312
29	9.97	10.07	0.10	0.1220
30	7.96	8.08	0.12	0.0819

Table 3.3.1: Kinetic energies of peaks in the Xe-NOO Auger spectrum in Fig. 3.3.1 compared with values from Ref. 85. The peak labels are consistent with those given in Ref. 85. Ratios of the intensities of the peaks from the spectrum in Fig. 3.3.1 and the Xe-NOO spectrum in Ref. 85 are also included in the table and discussed in the text with respect to the transmission of the electron spectometer.

The Auger spectra in Fig. 3.3.1 and Fig. 3.3.2 have not been corrected for the transmission of the spherical sector analyzer. To estimate the transmission of the analyzer as a function of kinetic energy, the relatively intense and well resolved Auger peaks in Fig. 3.3.1 and Fig. 3.3.2 were fit with Lorentzian/Gaussian lines to determine their areas. Auger spectra from Ref. 85 were digitized (with a 300 dot per inch scanner) and also fit with peaks to obtain standard areas for comparison. Significant errors in the peak areas are introduced by fitting the broad-scan Auger

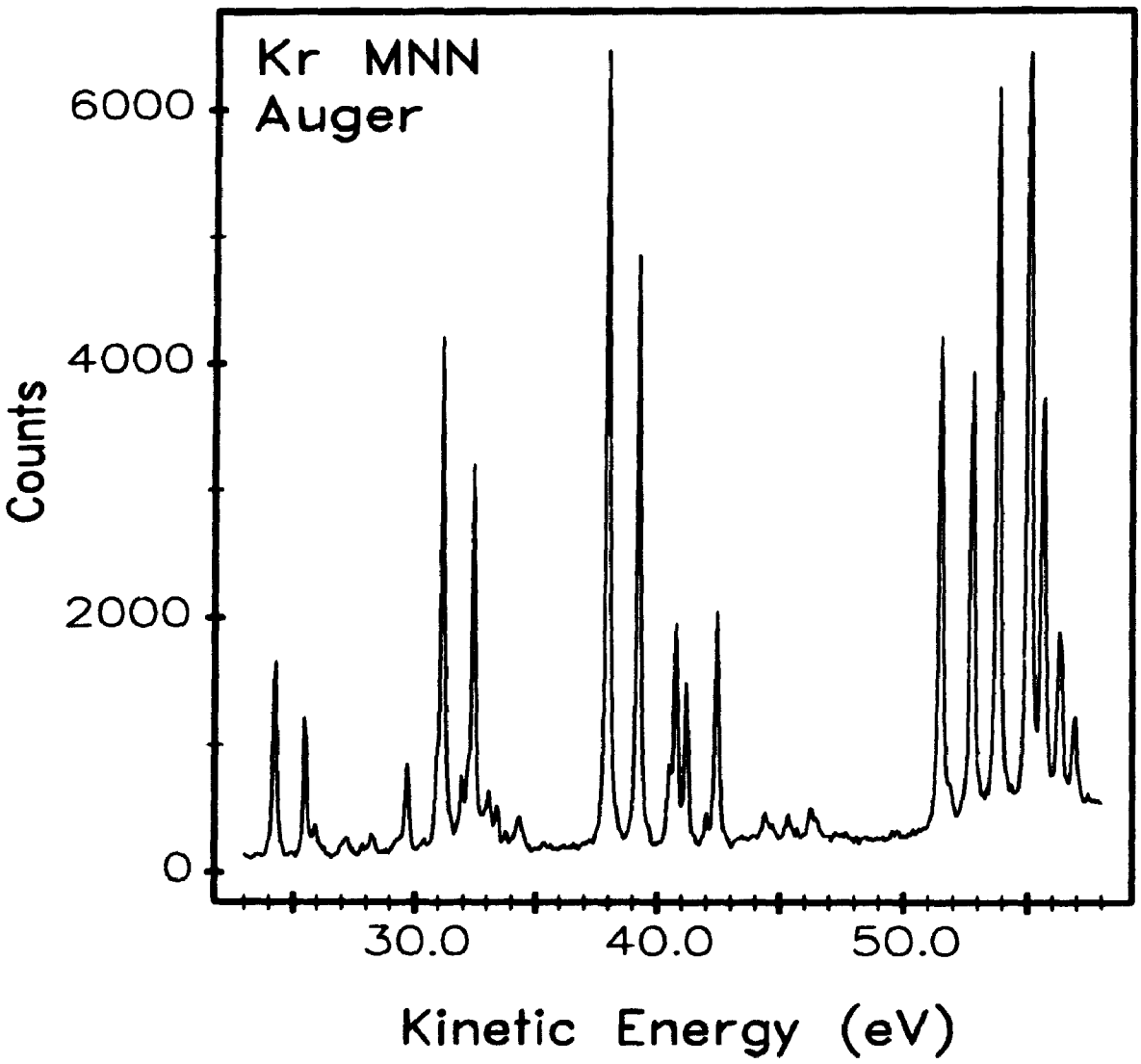

Figure 3.3.2: Krypton $M_{4,5}NN$ Auger spectrum following photoionization of the Kr 3*d* levels at $h\nu$ = 177 eV. The positions of the peaks are given in Table 3.3.2.

spectra which were measured with only 500 data points resulting in the sharp peaks being described by only a few data points. Significant errors are also present in the areas determined from the digitized spectra of Werme *et al.*[85] It was felt that the errors would be less than those obtained by simply measuring the peak heights,

peak label	KE_{BOZEK} (eV)	KE_{WERME} (eV)	ΔKE (eV)	I_{BOZEK}/I_{WERME}
1	56.54	56.51	−0.03	1.6905
2	55.95	55.94	−0.01	1.2721
3	55.28	55.26	−0.02	0.8362
4	54.71	54.70	−0.01	1.0000
6	53.46	53.45	−0.01	0.9989
7	52.41	52.41	−0.00	0.8920
8	5[illegible]3	52.00	0.47	1.2293
10	51.16	51.15	−0.01	0.9963
11	46.[illegible]5	46.09	−0.06	0.4514
12	45.91	45.88	−0.03	0.5930
13	45.36	45.00	−0.36	0.1523
14	45.00	44.34	−0.66	0.3982
16	44.35	43.86	−0.49	0.4602
17	44.06	43.45	−0.61	0.4240
18	43.63	43.18	−0.45	0.8504
20	42.09	42.14	0.05	0.9052
21	41.66	41.69	0.03	0.6254
23	40.84	40.89	0.05	0.7277
24	40.41	40.46	0.05	1.0160
25	40.14	40.19	0.05	0.9653
27	38.87	38.71	−0.16	0.9626
30	37.61	37.67	0.06	0.9835
31	33.93	34.03	0.10	1.7137
33	33.06	33.13	0.07	1.3540
34	32.69	32.78	0.09	2.8977
35	32.06	32.14	0.08	0.7096
36	31.83	31.91	0.08	4.6449
37	31.58	31.67	0.09	1.2871
40	30.81	30.89	0.08	0.6393
41	30.57	30.64	0.07	1.9553
43	29.31	29.39	0.08	1.2805
44	28.93	28.86	−0.07	2.1442
46	27.90	27.91	0.01	1.0393
50	25.55	25.64	0.09	1.1307
51	25.14	25.23	0.09	0.8463
52	23.88	23.98	0.10	0.8278

Table 3.3.2: Kinetic energies of peaks in the Kr-MNN Auger spectrum in Fig. 3.3.2 compared with values from Ref. 85. The peak labels are consistent with those given in Ref. 85. Ratios of the intensities of the peaks from the spectrum in Fig. 3.3.2 and the Kr-MNN spectrum in Ref. 85 are also included in the table and discussed in the text with respect to the transmission of the electron spectometer.

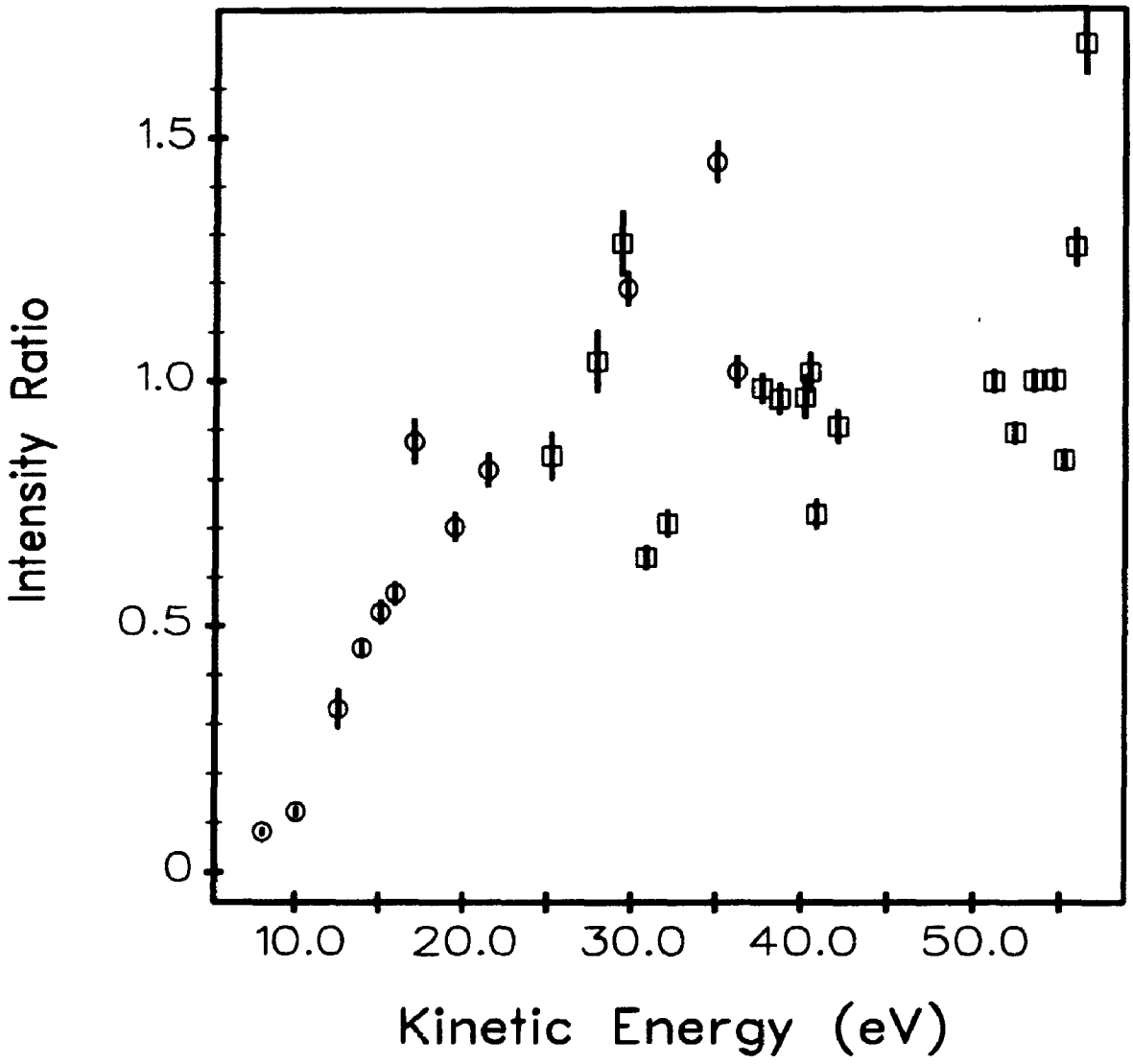

Figure 3.3.3: Ratios of peak areas from the Xe $N_{4,5}OO$ (○) and Kr $M_{4,5}N$ (⊔) Auger spectra in Fig. 3.3.1 and Fig. 3.3.2 versus values from the spectra in Ref. 85 as a function of kinetic energy.

since the true peak maxima could easily be missed in the kinetic energy scan using only 500 data points. The peak areas from both sets of data, normalized to the total area of all peaks in the spectra, were used to determine the intensity ratios (I_{BOZEK}/I_{WERME}) of the peaks in the Auger spectra in Fig. 3.3.1 and Fig. 3.3.2

which are given in Table 3.3.1 and Table 3.3.2 for the Xenon and Krypton spectra respectively. These ratios are plotted as a function of kinetic energy for the intense and well-resolved peaks in Fig. 3.3.3. While there is considerable scatter in the data in Fig. 3.3.3, the general trend is that the transmission rises from ~0.1 at 10 eV to ~1.0 at 20 eV and appears to level off at 1.0 above 20 eV. This indicates that above kinetic energies of 20 eV, the electron spectrometer should give fairly constant transmission. No cross section studies were performed for this thesis, and hence an accurate description of the transmission of the electron spectrometer is not crucial. The transmission function determined does have implications for this work however, making it difficult to measure high resolution core-level spectra with kinetic energies of < 20 eV. Since the experimental resolution of photoelectron spectra depends on the photon bandwidth as well as the electron energy resolution, a trade-off must be made between the low throughput of the electron energy analyzer at lower kinetic energies and the degrading photon resolution with higher photon energies.

Photoelectron spectra of the Xe 4*d* and Kr 3*d* core levels have been measured to better understand the effects of photon bandwidth and electron energy resolution on the overall resolution of the photoelectron lines. The Xe 4*d* photoelectron spectrum in Fig. 3.3.4 was measured with a photon energy, $h\nu$ = 94 eV and a photon resolution, $\Delta h\nu$ = 0.09eV. The excellent quality of the Xe 4*d* photoelectron spectrum confirms the very high electron and photon resolutions of the photoelectron spectrometer as a whole. The signal to background ratios in this, and most other spectra approaches 100:1. The spectrum was deconvoluted with a spin-orbit split doublet with a 1.984 eV splitting (from Ref. 82) and 1:1.5 statistical intensity ratio for the Xe $4d_{3/2}$:Xe $4d_{5/2}$ peak intensities. The description of the peak obtained from a non-linear least squares fit to the experimental data has a half-height width of 0.187 eV and an 13% Gaussian - 87% Lorentzian linear combination peak shape. It is apparent that the total width of 0.187 eV is the

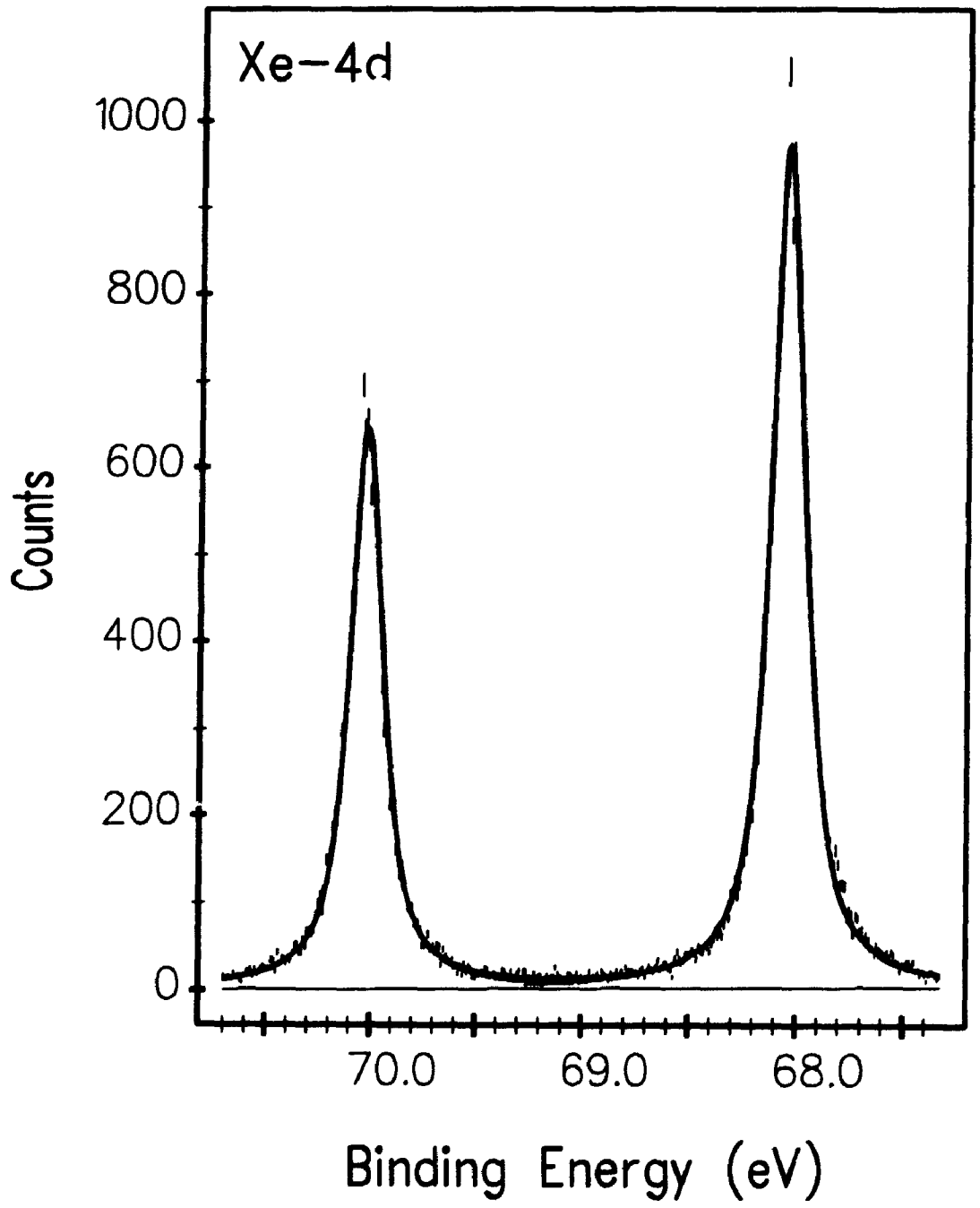

Figure 3.3.4: Photoelectron spectrum of the Xe 4*d* core levels measured with a photon energy $h\nu = 94$ eV. The spectrum is deconvoluted with a spin-orbit split doublet with 1.984 eV separation and 1:1.5 intensity ratio, a 0.13 Gaussian/Lorentzian peak shape and a FWHM of 0.187 eV.

narrowest yet reported for the Xe 4*d* core level. Generally, the spectrometer contribution to the observed linewidth is approximated by a Gaussian lineshape of width Γ_G and the lifetime limited contribution to the total width by a Lorentzian lineshape of width Γ_L . Assuming that the FWHM value obtained from the fitting procedure (which uses a linear combination of Gaussian and Lorentzian lineshapes) approximates the width of the true function describing the lineshape, a Voigt function with width Γ_V, the Lorentzian line width can be obtained from the expression:[82]

$$\frac{\Gamma_L}{\Gamma_V} = 1 - \left(\frac{\Gamma_G}{\Gamma_V}\right)^2 - 0.114\left(1 - \frac{\Gamma_G}{\Gamma_V}\right)\left(\frac{\Gamma_G}{\Gamma_V}\right)^2 \qquad (3.3.2)$$

With an experimental contribution to the linewidth of $\Gamma_G = 0.097$ eV, a value is obtained for Γ_L of 0.13 eV, slightly larger than the 0.11 eV natural linewidth value given previously[82], but in good accord with another previous value.[86] The Lorentzian and Gaussian linewidths can also be extracted from the Gaussian fraction and total width using the figures in Ref. 87. A value of 0 , eV is obtained for the Xe 4*d* natural linewidth using this method. A more accurate natural linewidth could be obtained by fitting the spectrum with a lineshape described by a convolution of a Lorentzian line representing the lifetime limited linewidth with a Gaussian line representing the experimental contributions to the observed peak.

The Kr 3*d* photoelectron spectrum in Fig. 3.3.5 was measured with a photon energy, $h\nu = 130$ eV and a photon resolution, $\Delta h\nu = 0.20$eV. The spectrum was deconvoluted with a spin-orbit split doublet with a 1.243 eV splitting (from Ref. 82) and 1:1.5 statistical intensity ratio for the Kr $3d_{3/2}$:Kr $3d_{5/2}$ peak intensities. A small peak is observed in the experimental data in Fig. 3.3.5 slightly above the Kr $3d_{3/2}$ photoelectron line which corresponds to one of the weak Kr *MNN* Auger peaks shown in Fig. 3.3.2. The description of the peak obtained from a non-linear least squares fit to the experimental data has a half-height width of 0.26 eV and an 45% Gaussian - 55% Lorentzian linear combination peak

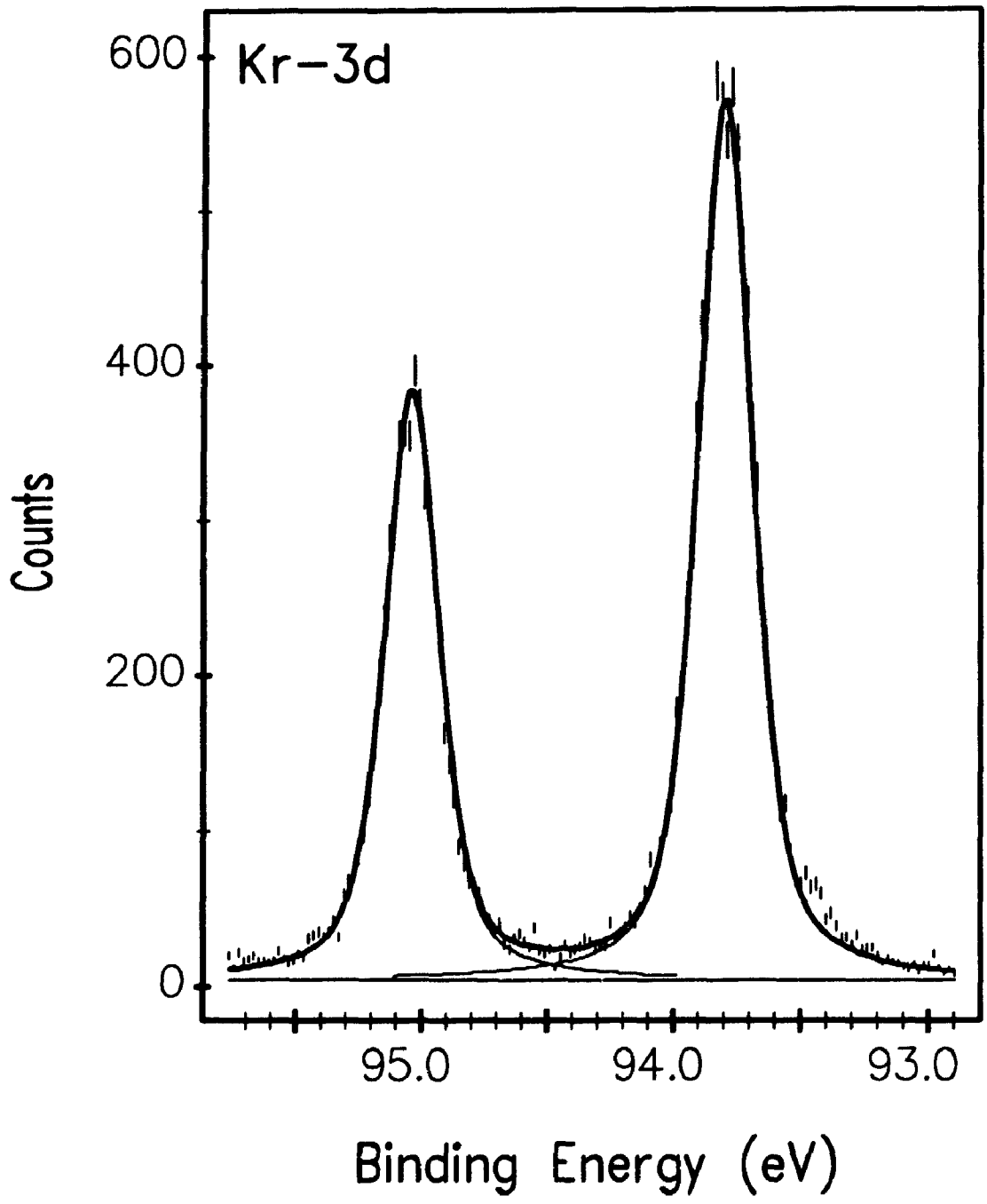

Figure 3.3.5: Photoelectron spectrum of the Kr 3*d* core levels measured with a photon energy, $h\nu = 130$ eV. The spectrum is deconvoluted with a spin-orbit split doublet with 1.243 eV separation and 1:1.5 intensity ratio, a 0.45:0.55 Gaussian/Lorentzian peak shape and a FWHM of 0.26 eV.

shape. Using the approximate Eq. (3.3.2) and a Γ_G of 0.21 eV, a value of 0.08 eV is obtained for the natural linewidth of the Kr 3*d* photoelectron lines which is again in good accord with the 0.090 eV value reported earlier.[82] Comparing the Gaussian components of the lineshapes fit to the Xe 4*d* and Kr 3*d*, 11% and 45% respectively, it is found that the Gaussian component is higher in the Kr 3*d* spectrum where the experimental contribution to the linewidth is larger than the lifetime limited natural linewidth. The Γ_G (experimental) to Γ_L (natural) ratios in the Xe 4*d* and Kr 3*d* photoelectron spectra are ~1:1 and ~3:1 respectively. This is a general trend observed for many atomic and molecular photoelectron lines. The Gaussian fraction of the lineshape can therefore be used as a rough measure of the experimental/natural contributions to the linewidth .

3.3.2. Vibrationally Resolved Si 2*p* Core-Level Photoelectron Spectra

Experimental Si 2*p* photoelectron spectra of the eleven compounds studied are presented in the following figures and the experimental and lineshape parameters summarized in the tables for several different experimental resolutions. The experimental resolutions given were calculated from the formal photon and electron energy resolutions using $\Gamma^2_{experimental} = \Gamma^2_{photon} + \Gamma^2_{electron}$, where Γ represents the resolution or bandwidth. The experimental resolution in these spectra was varied by changing only the photon resolution, since the resolution of the electron energy analyzer is determined by the fixed entrance and exit slits. The very high resolution ($\Delta E \leq 0.1$ eV) photoelectron spectra for SiH_4, SiF_4, and $Si(CH_3)_4$ were measured by Jeff Cutler (and kindly provided to me) using the undulator beamline since photon resolutions of that calibre were not possible with a 900 groove/mm grating in the Grasshopper monochromator.

The simulated spectra plotted as solid lines in the figures are representations of the parameters describing the spectra determined from the least-squares fit to the experimental data. As outlined previously, the spectra are described by a position

which is the adiabatic ionization energy of the $v' = 0$ vibrational level, a line shape which is defined by the full width at half maximum (fwhm) of the peak and the proportion of Gaussian component (Gauss fraction) of the line shape, the Si $2p$ spin-orbit splitting, and one or more manifolds of vibrationally split bands. The vibrational manifolds are further defined by the spacing between the vibrational bands and the relative intensities of the bands.

3.3.2.1. SiH_4

A high-resolution photoelectron spectrum of the Si $2p$ core levels of SiH_4 obtained using 135 eV photons is shown in Fig. 3.3.6. Vibrational structure is easily identified and well resolved in this spectrum. This spectrum, with total experimental line widths of 117 meV (from the fit) exhibits the narrowest core-level photoelectron linewidth observed for a molecule with vibrational structure.[10,87] The spectrum exhibits a series of three vibrational bands separated by ~0.3 eV, each split by the Si $2p$ spin-orbit splitting of ~0.6 eV. To illustrate the effect of photon resolution on the observed photoelectron spectrum, it has been measured at several different photon resolutions.

Photoelectron spectra of the Si $2p$ levels of SiH_4 measured at four different photon energy resolutions are presented in Fig. 3.3.7. The two lower resolutions were chosen to approximate the resolution of spectra measured with unmonochromatized Al K_α ($\Delta E \approx 1$ eV) and monochromatized Al K_α ($\Delta E \approx 0.3$ eV). The highest resolution spectrum in Fig. 3.3.7 (d), which is a reproduction of the spectrum in Fig. 3.3.6, was measured with a photon energy of 135 eV while the lower resolution spectra were measured at 130 eV. The effect of photon resolution on the spectrum is evident, with formal resolutions of ≤ 0.2 eV required to resolve the fine structure of the Si $2p$ photoelectron line. Using Al K_α or even monochromatized Al K_α radiation, it would be impossible to resolve the

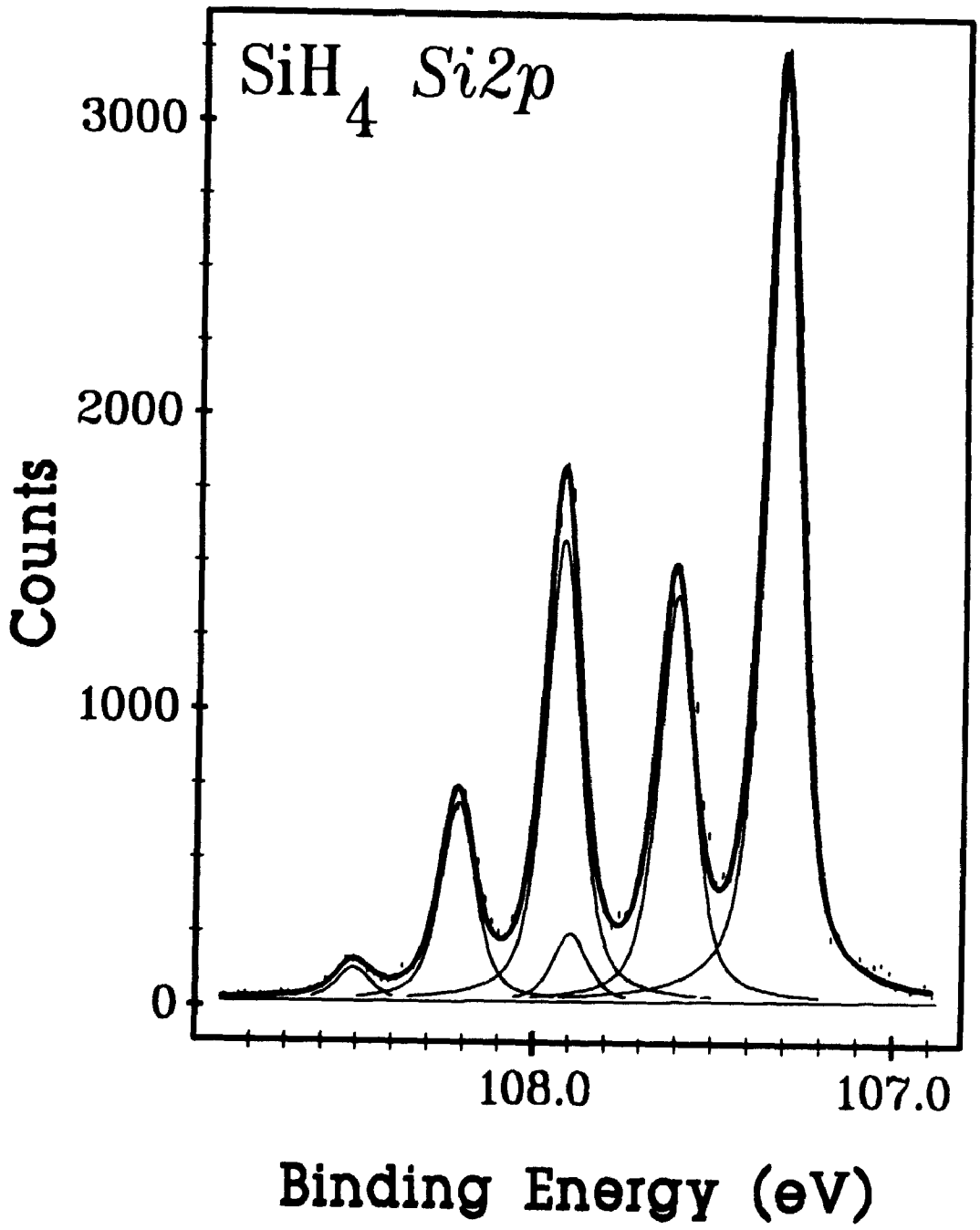

Figure 3.3.6: Experimental photoelectron spectrum of the Si $2p$ levels of silane, SiH_4, measured with an experimental resolution of 0.098 eV.

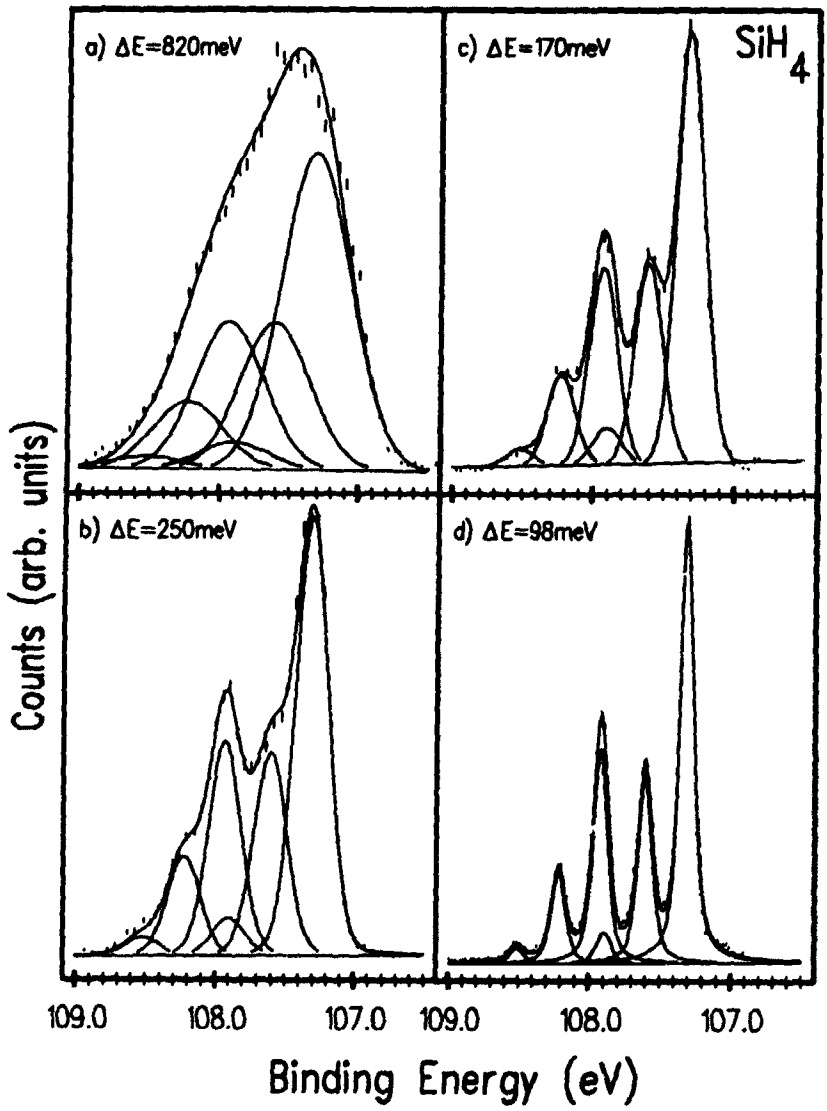

Figure 3.3.7: Experimental photoelectron spectra of the Si 2*p* levels of silane, SiH_4, measured at formal experimental resolutions of (a) 820, (b) 250, (c) 170, and (d) 98 meV. The solid curves represent parameters which describe the peak shape convoluted with the Si 2*p* spin orbit and the Si–H vibrational splittings which were determined by fitting them to the experimental data using a least-squares method as described in the text. The parameters are summarized in Table 3.3.3.

vibrational bands on the Si 2*p* photoelectron lines. The importance of high-resolution monochromatized synchrotron radiation for resolving vibrational fine structure in core-level photoelectron spectra is apparent from these spectra.

Si $2p_{3/2}$ binding energy (eV)	Experimental resolution ΔE (meV)	Observed linewidth (meV)	Gauss Fraction	Vibrational splitting (meV)	Relative intensities of vibrational bands (tot=100)
107.31(5)	98	117	0.43	293	66.3,29.1,4.6
	170	232	1.0	295	65,30,5
	250	278	0.92	295	65,30,5
	820	590	1.0	295	65,30,5

Table 3.3.3: Summary of the experimental and fitted parameters describing the Si 2*p* photoelectron spectrum of SiH_4. Fitted values were determined by a non-linear least-squares fit of the parameters to the experimental spectra, as described in section 3.2.

Each of the four SiH_4 Si 2*p* photoelectron spectra in Fig. 3.3.7 were deconvoluted using the methods described. A summary of the parameters from these fits is given in Table 3.3.3. Spin-orbit parameters for the Si 2*p* spectra of SiH_4 as well as those for the other molecules in this report, were not constrained in the deconvolution process. The spin-orbit splitting was found to be 0.612±0.005 eV in the spectra for all of the molecules. The intensity ratios of the Si $2p_{1/2}$ to Si $2p_{3/2}$ photoelectron lines were found to range from 0.45 to 0.50 for all of the samples with the exception of $SiCl_4$ where the intensity ratio was found to be 0.41. The ionization energy of SiH_4 given in Table 3.3.3, 107.31 eV, is the most accurately measured adiabatic ionization energy of the Si $2p_{3/2}$ level for this molecule since other measurements of Si 2*p* binding energies were performed using unmonochromatized Al K_α sources. Other values have been previously reported for the Si 2*p* ionization potential of SiH_4, 107.14 eV[88] and 107.31 eV,[89] measured at much lower experimental resolution (≥1.0eV). These values, however, correspond to the vertical ionization potential of SiH_4 since vibrational and spin-orbit splittings of the Si 2*p* level were not resolved previously. There is no simple

comparison between the previously reported vertical ionization potentials and the adiabatic ionization energy since the vertical ionization potential is determined by a weighted average of the individual spin-orbit and vibrational levels.

The linewidths obtained from the deconvolution of the experimental spectra and listed in Table 3.3.3, are not always consistent with the experimental resolutions which are also given. In the higher resolution spectra, ΔE=98 and 170 meV, the linewidths are greater than the formal experimental resolution owing to contributions to the linewidth from the natural lifetime limited width of the Si 2*p* core hole. The shape of the function describing the contributions of the monochromator and electron spectrometer to the total line shapes is not precisely known for the current experimental configuration, although Kr resonance Auger spectra obtained at 90 eV photon energy indicate that it is very close to Gaussian. The natural linewidth of the Si 2*p* photoelectron lines can be estimated by applying Eq. (3.3.2). For the highest resolution spectrum Γ_V = 117 meV and Γ_G = 98 meV and a natural linewidth of 33 meV is calculated. It is also possible to estimate the natural linewidth of the Si 2*p* photoelectron lines using lineshape analyses which have been described previously.[87] Assuming the experimental contribution (photon + electron) to the lineshape to be Gaussian, we obtain a natural Lorentzian linewidth of ~45 meV. Both values are in reasonable agreement with the width obtained from the high resolution photoabsorption spectrum of SiH_4,[13] but do not compare favourably with the value of 15 meV estimated by Krause.[90] A natural lifetime width of 49 meV, in excellent agreement with the value of 45 meV obtained from the lineshape analysis, is obtained using the statistical treatment of Thomas[24] with the experimental Ar 2*p* linewidth.[90] In the lower resolution spectrum (ΔE=820 meV) the linewidth is less than the formal resolution. This results from inaccuracies in the calibration of the slit widths and the inherent minimum resolution of the Grasshopper monochromator.

Vibrational splittings resulting from the Si–H symmetric stretching vibration, and the relative intensities of the vibrational bands were allowed to freely fit the experimental data for the two highest resolution SiH_4 Si $2p$ photoelectron spectra. The values obtained are very similar despite the spectra being measured at different photon energies, 130 eV and 135 eV. The Si $2p$ cross section is featureless in this energy region[91] and the vibrational band intensities are therefore not expected to change with the photon energy. Parameters determined for the ΔE=170 meV spectrum were used in the deconvolution of the lower resolution spectra with only the linewidth and Gauss fraction allowed to change in the optimization procedure. The parameters obtained reproduce the spectra very well as indicated in Fig. 3.3.7 (a) and (b).

The energy of the Si–H vibrations in Si $2p$ core ionized SiH_4, 2379 cm^{-1} determined from the photoelectron spectrum, is larger than the vibrational energy of the ground electronic state, 2180 cm^{-1} from infrared spectra,[92] indicating a change in the equilibrium nuclear geometry upon ionization of the ground state molecule. The increased vibrational energy of the core ionized state is consistent with a shortening of the Si–H bond in the ionic state. Ionization of core electrons has been found to result in a shortening of the bond in theoretical studies of core level spectra of several other hydride molecules such as CH_4,[62] NH_3[60] and H_2S.[61] The vibrational energy of the core hole ion SiH_4^+ (Si $2p^{-1}$) supports the use of the equivalent cores approximation to estimate vibrational energies in core ionized molecules. In the Z+1 analogous molecule model, the properties of a molecular ion with a core hole are presumed to be reasonably approximated by those of the analogous molecule with a Z+1 atom in the place of the one with the core hole.[26,33] The Z+1 model compound for Si $2p$ core ionized SiH_4^+ is PH_4^+. The totally symmetric vibrational frequency (ν_1) for PH_4^+ measured in the solid state has been reported as 2295 cm^{-1},[92] which is closer to the 2379cm^1 observed for SiH_4^+ (Si$2p^{-1}$) than is the ground state SiH_4 vibrational energy of 2180 cm^{-1}. The

symmetric stretching frequency of gaseous PH_3, 2327 cm^{-1} is a better value to compare with the Si−H stretching frequency of Si 2*p* ionized SiH_4 since the P−H stretching frequencies in PH_4^+ may be lowered due to hydrogen bonding with counter ions in the sample.[92] In a previous study of the vibrational excitations accompanying the C 1*s* ionization of CH_4, the first vibrational level was found to be 3154 cm^{-1} above the ground vibrational state of the core hole ion.[16−18] This value compares more favourably with the vibrational frequency of NH_4^+, 3040 cm^{-1},[92] than it does with the ground state vibrational frequency of CH_4, 2916.5 cm^{-1}.[92] For both SiH_4 and CH_4 the vibrational energies of the core hole states are more closely approximated using the Z+1 analogous molecules and ions than with the ground state molecules. Neither, however, gives exact results. The symmetric stretching frequency of PH_4^+, 2295 cm^{-1},[92] closely approximates the value observed for the Si−H stretching frequency in SiH_4^+ (Si $2p^{-1}$). The symmetric stretching frequency of PH_3 , 2327 cm^{-1},[92] can also be used to approximate the Si−H stretching frequency of SiH_4 (Si$2p^{-1}$).

The effects of post collision interaction (PCI) on the Si 2*p* photoelectron spectra presented in this study must be considered since the Si LVV Auger electrons have greater kinetic energies than the Si 2*p* photoelectrons. The slower photoelectron can be considered to be overtaken by the faster Auger electron and subsequently shield it from the positive ion. This results in a gain of energy by the Auger electron and the loss of an equal amount of energy by the photoelectron.[93] Alternatively, the photoelectron can be thought to be "shaken-down" to a lower energy state[94]. Recapture of the photoelectron by the positive ion is even possible at low kinetic energies ($\leq$2.0 eV).[95] In a recent study of the $N_5O_{23}O_{23}\ ^1S_0$ Auger line of xenon measured using photon excitation with energies near the Xe $4d_{5/2}$ threshold, the position of the line was found to shift by ~0.25 eV from 29.97±0.02 eV at photon energies above 100 eV (where PCI does not affect the spectrum) to ~30.2 eV when an excitation energy very near the Xe $4d_{5/2}$ threshold

was used.[93,96] The lineshape of the $N_5O_{23}O_{23}\ ^1S_0$ Auger peak was observed to be asymmetrically broadened with a pronounced tail on the high kinetic energy side of the peak when an excitation energy near the Xe $4d_{5/2}$ threshold was used. The peak became narrower and more symmetric with increasing photon energy. While the effects of PCI on the shape and position of photoelectron peaks have not been measured directly, they should be equal in magnitude but of the opposite sign to those observed for the Auger electron lines. The effect of PCI on the shapes and positions of the photoelectron peaks is complicated by the presence of more than one Auger decay contributing to the effect. Generally however, photoelectron lines are expected to be shifted to higher binding energy with noticeably asymmetric lineshapes if PCI plays an important role in the high resolution inner-shell spectra measured near the ionization threshold. The Si 2*p* photoelectron lines of SiH_4 however, are very symmetric, implying that PCI does not significantly affect the spectra reported here. Further studies are definitely required to assess the importance of PCI in inner-shell photoelectron spectra of molecules, but in the spectra reported here the shape and position of the peaks are not noticeably distorted.

3.3.2.2. $Si(CH_3)_4$

Photoelectron spectra of the Si 2*p* levels of tetramethylsilane, $Si(CH_3)_4$, are presented in Fig. 3.3.8 at a variety of experimental resolutions. The high resolution ΔE=99 meV spectrum (Fig. 3.3.8 (d)) was measured at a photon energy of 135 eV while the other lower resolution spectra were measured at 129 eV. The ΔE=99 meV spectrum is the highest resolution photoelectron spectrum of $Si(CH_3)_4$ reported but even at this high resolution the Si 2*p* lines appear as broad unresolved bands. The band shapes are asymmetric however, with a tailing of the band on the high binding energy side. Previously reported core level photoelectron spectra of CO and N_2 exhibited similar band shapes resulting from unresolved

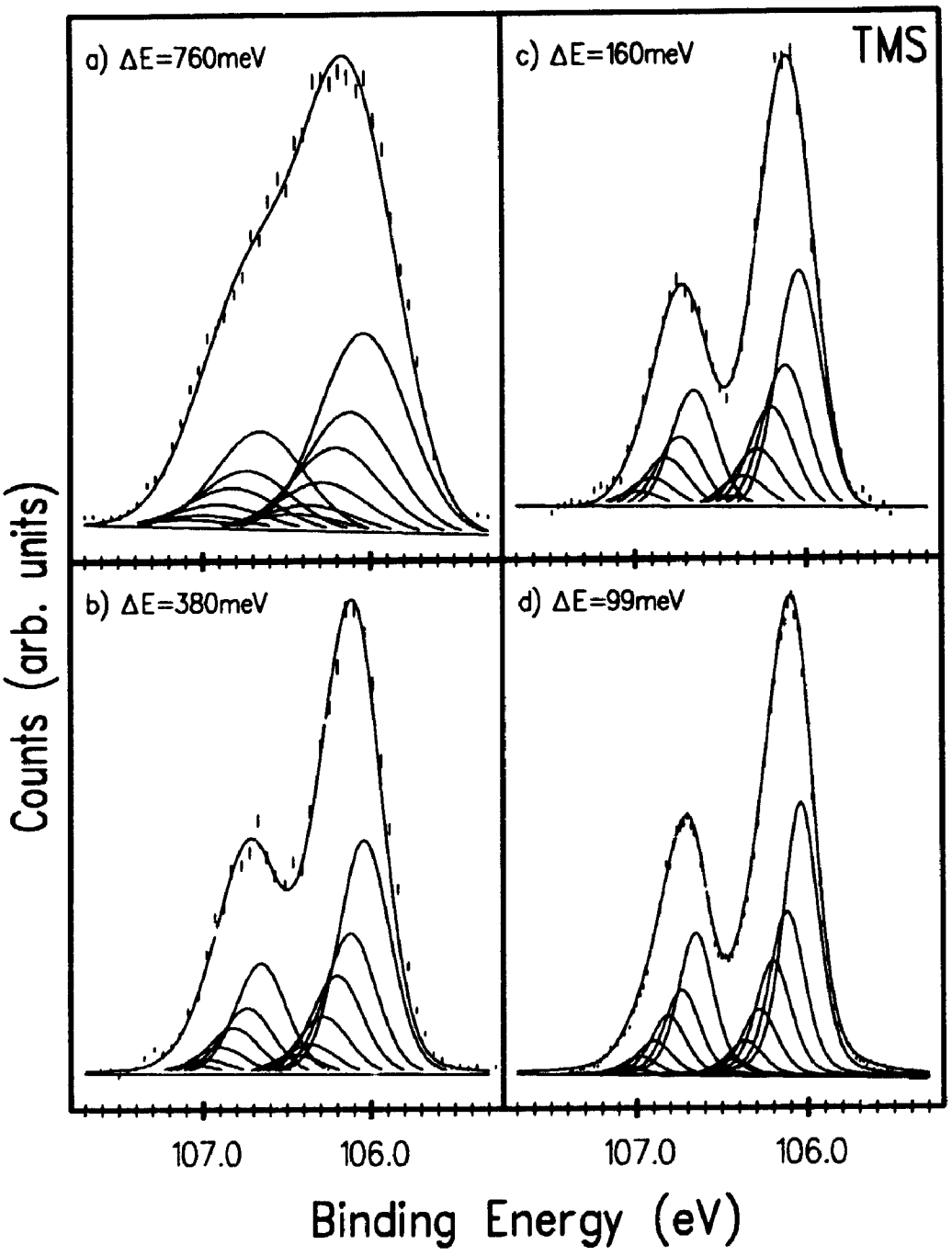

Figure 3.3.8: Experimental photoelectron spectra of the Si 2*p* levels of tetramethylsilane, $Si(CH_3)_4$, measured at formal experimental resolutions of (a) 760, (b) 380, (c) 160, and (d) 99 meV. The solid curves represent fitted parameters (Table 3.3.4) as in Fig. 3.3.7.

vibrational structure accompanying the core ionization.[17] Based on this and the accompanying observations of vibrational structure in the Si 2*p* photoelectron spectra of SiH_4 and SiF_4[64] it is proposed that the Si 2*p* photoelectron lines of $Si(CH_3)_4$ are broadened by vibrational effects.

Without resolved vibrational structure, it is difficult to fit a vibrational series to the broad Si 2*p* photoelectron lines. Using the equivalent-cores approximation however, a reasonable estimate of the vibrational energy for the Si–CH_3 stretch of the core ionized molecule can be obtained. The symmetric Si–C stretch is assumed to be the primary vibrational mode in the spectrum since the removal of a core electron can leave the molecule in an excited state of the symmetric stretch owing to the change in bond distance caused by the ionization. According to the equivalent-cores model, symmetric P–C stretching energy of $P(CH_3)_3$, 653 cm^{-1}, or $P(CH_3)_4^+$, 649 cm^{-1} (0.081 eV)[92] can be used to approximate the Si–C stretching frequency of Si 2*p* core ionized $Si(CH_3)_4$ which has a symmetric stretching vibrational energy of 593 cm^{-1} in the ground electronic state.[92]

Si $2p_{3/2}$ binding energy (eV)	Experimental resolution ΔE (meV)	Observed linewidth (meV)	Gauss Fraction	Vibrational splitting (meV)	Relative intensities of vibrational bands (tot=100)
106.04(5)	99	242	0.68	81	41,24,17,10,5,3
	160	304	1.0	81	41,25,17,10,5,3
	380	358	0.86	81	41,25,17,10,5,3
	760	614	1.0	81	41,25,17,10,5,3

Table 3.3.4: Summary of the experimental and fitted parameters describing the Si 2*p* photoelectron spectrum of $Si(CH_3)_4$. Fitted values were determined by a non-linear least-squares fit of the parameters to the experimental spectra, as described in section 3.2.

Parameters obtained from the deconvolution of the experimental Si 2*p* photoelectron spectra of $Si(CH_3)_4$ using the Si–C vibrational splitting determined above (0.081 eV) are summarized in Table 3.3.4. The adiabatic ionization potential of the Si $2p_{3/2}$ line was determined to be 106.04 eV using the vibrational manifold

illustrated in Fig. 3.3.8. Previous values 105.94,[97] 105.82,[88] and 106.02,[98] obtained using unmonochromatized Al K_α sources, are all in agreement with the value reported here.

Linewidths of the individual vibrational bands in the Si 2*p* photoelectron spectrum of $Si(CH_3)_4$ were found to be 0.242 eV (Table 3.3.4). These linewidths are much broader than those observed in the Si 2*p* photoelectron spectrum of SiH_4 where 0.117 eV lines were found to reproduce the shape of the individually resolved vibrational bands. The broader linewidths for $Si(CH_3)_4$ could be the result of either lifetime effects of the Si 2*p* core hole[35,36,24] or a incomplete description of the vibrational structure of the photoelectron spectra using only one vibrational mode. A relationship between the valence electron density surrounding the atom on which the core hole is created and the lifetime of the hole state has been proposed[35,36] and recently updated[24] to account for broadening of spectral lines corresponding to core excitations. Since the methyl ligands donate electron density to the silicon atom, illustrated by the lowering of the Si 2*p* binding energy of $Si(CH_3)_4$ relative to SiH_4, the lifetime of the Si 2*p* hole state will be shorter than that of the Si 2*p* hole state in SiH_4. The corresponding photoelectron line should therefore be broader according to the assertion that an increased Auger decay rate of the core hole will result from the increased electron density on the silicon atom thereby shorting the lifetime of the core hole state. Alternatively, the broad lines from the deconvolution of the data could be the result of an incomplete description of the vibrational states excited in the ionization process using the parameters chosen to fit the spectrum. Since the $Si(CH_3)_4$ molecule is relatively complex with 17 atoms and 16 chemical bonds, numerous other vibrational modes such as C−H stretching, CH_2 wagging, etc. could also be responsible for some of the structure in the Si 2*p* photoelectron spectrum. In high resolution photoabsorption spectra of C_2H_4 and C_6H_6 three different vibrational modes, C−H stretching, C−C stretching, and C−H bending, were identified with the aid of spectra of the deuterated

compounds.[38] These spectra are complicated however, by the creation of a core hole leading to a lowering of the molecular symmetry since the carbon atoms are no longer equivalent in the core excited species. If modes in addition to the Si−C stretch are also responsible for broadening the $Si(CH_3)_4$ Si 2*p* photoionization spectrum, the deconvolution method will increase the widths of the vibrational bands to incorporate intensity from these modes.

The ΔE=160 meV Si 2*p* photoelectron spectrum of $Si(CH_3)_4$ was also deconvoluted using a vibrational splitting of 0.081 eV. Relative band intensities determined by the fitting procedure for this spectrum are almost identical to those determined for the ΔE=99 meV spectrum (Table 3.3.4). No excitation energy dependent effects of the vibrational band intensities are observed nor expected since the Si 2*p* cross section for $Si(CH_3)_4$ is relatively constant between 130 and 135 eV.[99] The other lower resolution spectra in Fig. 3.3.8 (a) and (b) were fit using the vibrational manifold determined for the ΔE=160 meV spectrum with only the linewidth and Gauss fraction allowed to change. Parameters resulting from the procedure with these constraints describe the spectra very well as evidenced by the close correspondence between the experimental and simulated spectra in Fig. 3.3.8 (a) and (b).

3.3.2.3. $C_2H_5SiH_3$, $(CH_3)_2SiH_2$ and $(CH_3)_3SiH$

Photoelectron spectra of the Si 2*p* levels of ethylsilane, $C_2H_5SiH_3$, dimethylsilane, $(CH_3)_2SiH_2$ and trimethylsilane, $(CH_3)_3SiH$, presented in Fig. 3.3.9, Fig. 3.3.10 and Fig. 3.3.11 respectively, were measured at photon energies of 130, 129 and 129 eV and total experimental resolutions of 170, 160 and 160 meV respectively. Despite the less than optimum experimental resolution used in the measurement of these spectra (compared to the ΔE=0.1 eV resolution attained for the spectra of SiH_4, SiF_4 and $Si(CH_3)_4$) they do exhibit interesting

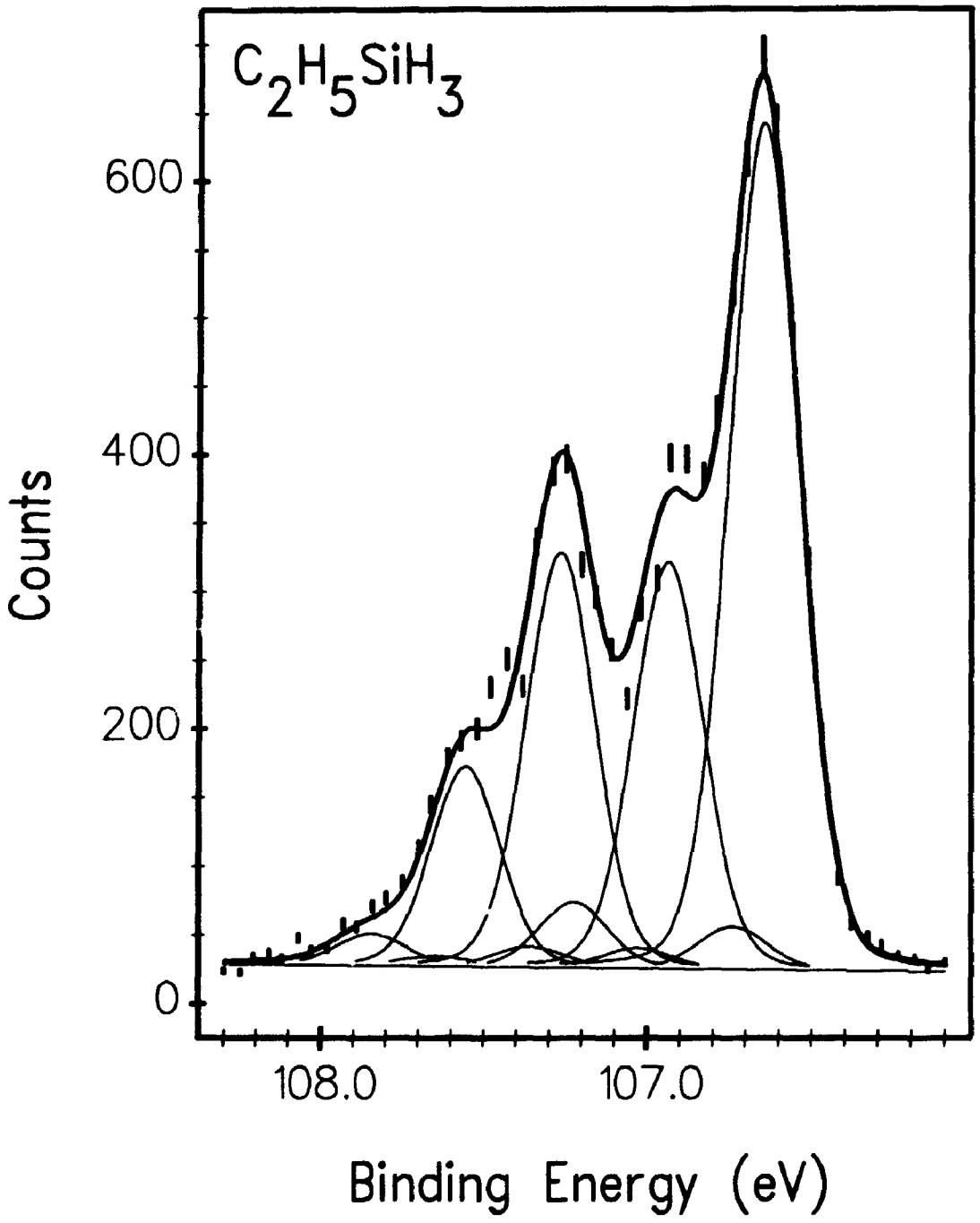

Figure 3.3.9: Experimental photoelectron spectrum of the Si 2*p* levels of ethylsilane, $C_2H_5SiH_3$, measured at a formal experimental resolution of 170 meV. The solid curves represent parameters which describe the peak shape convoluted with the Si 2*p* spin orbit and the Si–H and Si–C vibrational splittings which were determined by fitting them to the experimental data using a least-squares method as described in the text. The parameters are summarized in Table 3.3.5.

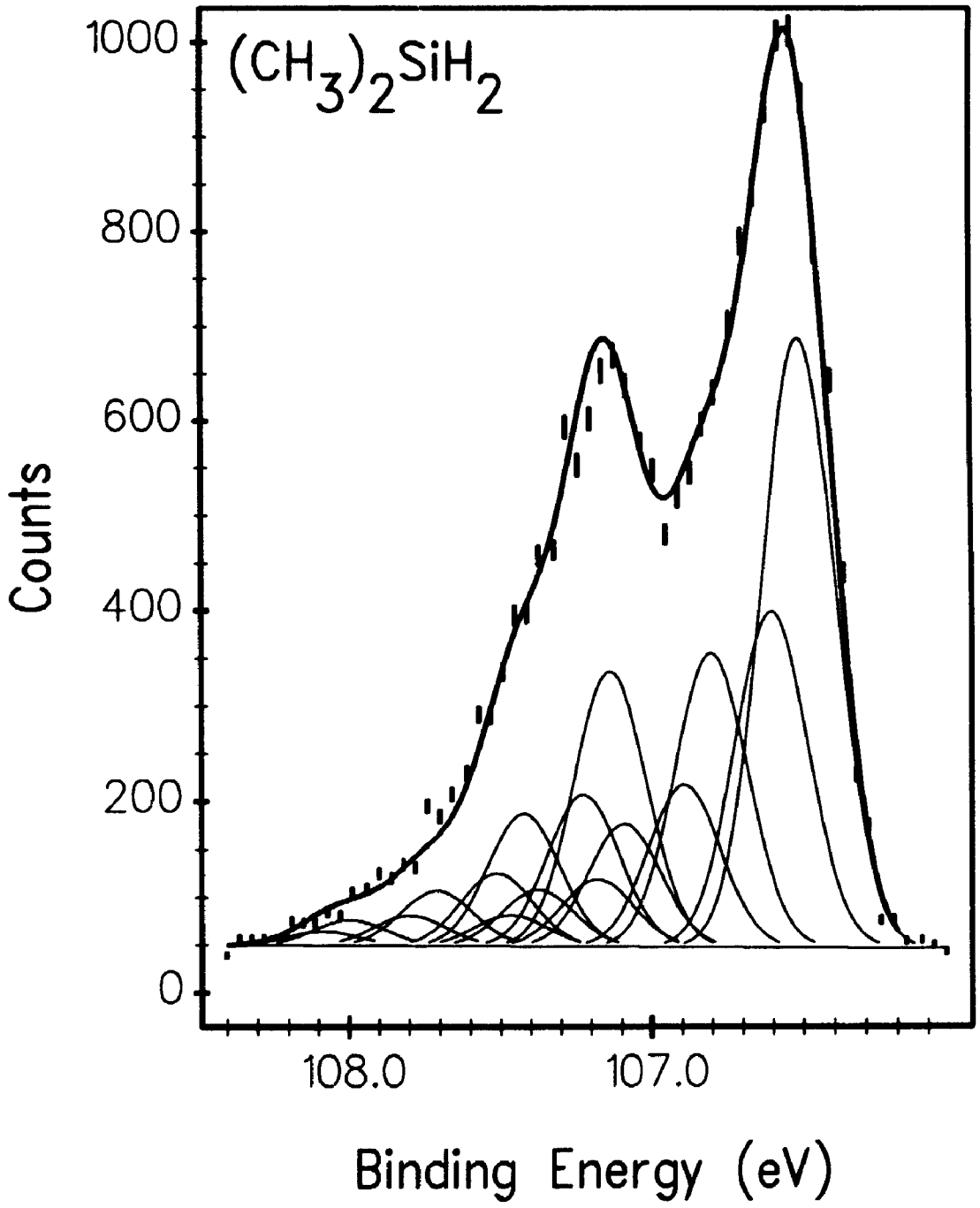

Figure 3.3.10: Experimental photoelectron spectrum of the Si 2*p* levels of dimethylsilane, $(CH_3)_2SiH_2$, measured at a formal experimental resolution of 160 meV. The solid curves represent parameters which describe the peak shape convoluted with the Si 2*p* spin orbit and the Si–H and Si–C vibrational splittings which were determined by fitting them to the experimental data using a least-squares method as described in the text. The parameters are summarized in Table 3.3.5.

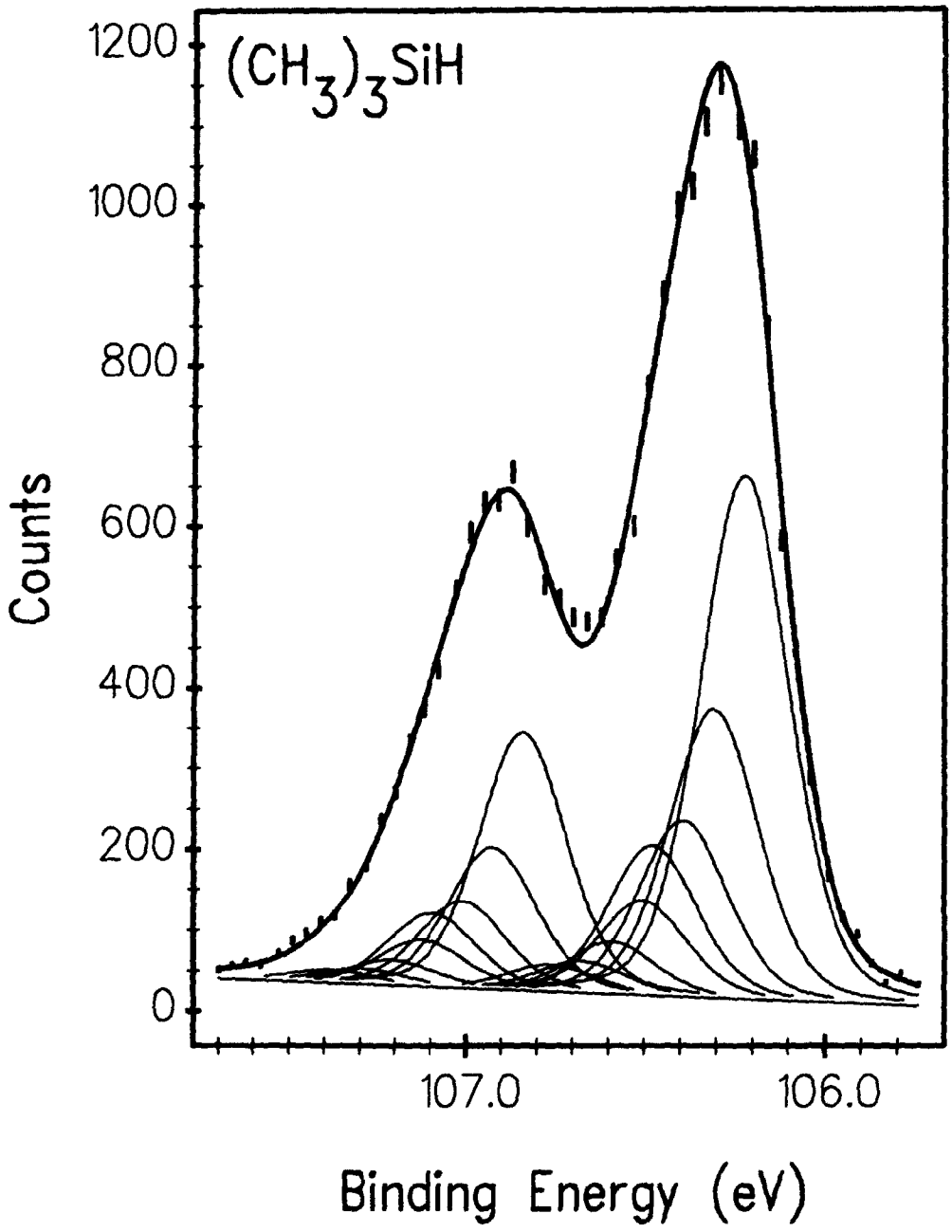

Figure 3.3.11: Experimental photoelectron spectrum of the Si 2*p* levels of trimethylsilane, $(CH_3)_3SiH$, measured at a formal experimental resolution of 160 meV. The solid curves represent parameters which describe the peak shape convoluted with the Si 2*p* spin orbit and the Si–H and Si–C vibrational splittings which were determined by fitting them to the experimental data using a least-squares method as described in the text. The parameters are summarized in Table 3.3.5

features which provide information about the nature of the Si $2p$ core hole state in these molecules.

Inspection of the spectra in Fig. 3.3.9 - Fig. 3.3.11 shows that the Si $2p$ photoelectron spectra of $C_2H_5SiH_3$ (Fig. 3.3.9) and SiH_4 (Fig. 3.3.7 (c) – obtained at the same experimental resolution) are similar. Both spectra exhibit resolved vibrational structure, although it is slightly better resolved in the spectrum of SiH_4. The Si $2p$ photoelectron spectrum of $(CH_3)_2SiH_2$ (Fig. 3.3.10) does not have resolved vibrational structure, but the highly asymmetric line shape extending over ~2.0 eV indicates that vibrational structure must be responsible for the observed broadening. Finally, the spectrum of $(CH_3)_3SiH$ in Fig. 3.3.11 appears to be very similar to the spectrum of $Si(CH_3)_4$ in Fig. 3.3.8 (c). The Si $2p$ spin orbit split lines are more completely resolved in the Si $2p$ spectrum of $Si(CH_3)_4$ than in the spectrum of $(CH_3)_3SiH$, indicating that more vibrational bands are present in the spectrum of the latter. Gradual changes in the shape of the Si $2p$ photoelectron spectra over the alkyl-silane molecular series suggest that two separate vibrational sequences cause the asymmetric line broadening in the mixed compounds. The experimental spectra of the mixed alkyl silanes were therefore deconvoluted using two vibrational sequences, one for bands corresponding to the Si–H stretch and another for bands resulting from the Si–C stretch.

Vibrational energies of suitable equivalent-cores molecules, $C_2H_5PH_3^+$, etc., could not be found and so a different method was used to estimate the Si–H and Si–C vibrational frequencies in the core ionized states of the molecules. In order to determine the appropriate vibrational splittings to use in the fitting procedure, vibrational frequencies of the ground state neutral molecules were examined. The energy of the Si–H stretch changes from 2180 cm^{-1} for SiH_4 to 2168 cm^{-1} for CH_3SiH_3, to 2143 cm^{-1} for $(CH_3)_2SiH_2$ and finally to 2123 cm^{-1} for $(CH_3)_3SiH$.[92] Rather than use these values directly to fit the vibrational structure in the photoelectron spectra, relative changes of the vibrational energies were

calculated (i.e. $\nu_{Si-H}(CH_3SiH_3)/\nu_{Si-H}(SiH_4) = 2168\ cm^{-1}/2180\ cm^{-1} = 0.9945$) and applied to the value of the Si−H stretching energy determined for the SiH_4 Si $2p$ photoelectron spectrum to determine the vibrational energy for the next molecule in the series (i.e. $\nu_{Si^*-H}(CH_3SiH_3 = \nu_{Si^*-H}(SiH_4) \times 0.9945 = 0.293\ eV$). Energies of the Si−C stretching modes were similarly determined for the core hole ions using the energy of the Si−C stretch in Si $2p$ ionized $Si(CH_3)_4$ (0.081 eV) and the sequence of symmetric Si−C stretching energies for the methyl silanes.[92] The resulting vibrational energies were used to fit the vibrational structure in the Si $2p$ photoelectron spectra in Fig. 3.3.9 - Fig. 3.3.11 and the values are summarized in Table 3.3.5. When two vibrational sequences are used to fit the photoelectron spectrum, as for the three mixed alkyl silanes, the vibrational sequences combine to yield numerous vibrational bands.

Molecule	Si $2p_{3/2}$ E_b (eV)	Exper. resolution ΔE (meV)	Observed linewidth (meV)	Gauss Fraction	Vibration splitting (meV)	Rel. intens. of vibr. bands (tot=100)
$C_2H_5SiH_3$	106.66(5)	170	248	0.85	290 94	64,31,5 95,5
$(CH_3)_2SiH_2$	106.51(5)	160	280	1.0	287 89	56,27,11,5 65,35
$(CH_3)_3SiH$	106.21(5)	160	289	0.77	284 85	85,15 46,[illegible],15,13

Table 3.3.5: Summary of the experimental and fitted parameters describing the Si $2p$ photoelectron spectra of $C_2H_5SiH_3$, $(CH_3)_2SiH_2$ and $(CH_3)_3SiH$. Fitted values were determined by a non-linear least-squares fit of the parameters to the experimental spectra, as described in section 3.2.

Parameters from the least-squares deconvolution of the experimental data result in an accurate description of the Si $2p$ photoelectron spectra of the mixed alkyl silanes as seen by the similarity of the experimental and calculated spectra in Fig. 3.3.9, Fig. 3.3.10 and Fig. 3.3.11. The combination of Si−C and Si−H stretching modes therefore appears to describe the Si $2p$ photoelectron spectra of

the mixed alkyl silanes. Even the Si 2*p* photoelectron spectrum of $(CH_3)_2SiH_2$, which extends over 2 eV (Fig. 3.3.10) is reasonably well reproduced by the fitting procedure. These results support the use of the methods described above to obtain the Si–H and Si–C vibrational energies used in the deconvolution of the experimental Si 2*p* photoelectron spectra. Parameters from the fitting procedure are summarized in Table 3.3.5. The Si 2*p* binding energies listed compare reasonably well with previous results[89]; CH_3SiH_3, 106.95 eV; $(CH_3)_2SiH_2$, 106.71 eV; $(CH_3)_3SiH$, 106.18 eV; and further illustrate the electron donating properties of the alkyl ligands.

The Si 2*p* linewidths obtained from the fitting procedure increase with the number of alkyl ligands on the central silicon atom (Table 3.3.5). The changing linewidths could be due to chemical effects on the lifetime of the core hole state or an incomplete description of the vibrational structure of the Si 2*p* bands with only two vibrational modes. The increasing linewidths of the alkyl silanes with the number of alkyl ligands parallels the increased electron density on the central silicon atom. The variation in linewidth observed here, from 0.232 eV for SiH_4, to 0.280 eV for $(CH_3)_2SiH_2$, to 0.304 eV for $Si(CH_3)_4$ (all from the $\Delta E \approx 160$ meV spectra), is large when compared to the variation in the theoretical C 1*s* linewidths of a variety of carbon compounds.[24]

The increased linewidth observed for the alkyl silanes could also be the result of vibrational modes in addition to the Si–H and Si–C stretching modes contributing to the linewidths. The molecular structures of the alkyl silane molecules are considerably more complex than that of silane. Ionization of the silicon atom could create an attractive potential for the valence electrons of the alkyl groups bonded to it thereby withdrawing electron density from the carbon atoms. The equilibrium nuclear geometries of the methyl ligands might therefore be changed by the removal of the Si 2*p* electron and bands corresponding to vibrations within the alkyl groups could result. Vibrational bands at energies corresponding to the

C−H stretch (~0.4 eV) might be expected in this case, but none are observed. The broadening of the photoelectron lines is probably due to a combination of the above two effects, decreased Si 2*p* core hole lifetimes and additional vibrational modes, but spectra measured at much better experimental resolutions must be obtained to determine their relative importance.

3.3.2.4. SiF_4

A manifold of vibrationally and spin-orbit split bands was also fit to the Si 2*p* photoelectron spectrum of SiF_4 given in Fig. 3.3.12. Since numerous partially resolved peaks combine to give the resulting SiF_4 Si 2*p* photoelectron spectrum, it is difficult to unequivocally determine the spectral parameters with a least-squares method. The fitting procedure is simplified using the Z+1 analogous molecule PF_3, with a symmetric stretching frequency of 893cm^{-1}.[92] Since the experimental contributions to the line width are similar for both spectra, the peak widths in the SiH_4 and SiF_4 spectra are also assumed to be similar. The SiF_4 Si 2*p* spectrum was fit with eleven vibrational levels with a separation of 0.105 eV (847 cm^{-1}), each split by the Si 2*p* spin orbit coupling and the results are shown in Fig. 3.3.12. Since the bands are not completely resolved in the spectrum no anharmonicity could be included in the fitting procedure. The low intensity of the first vibrational band ($v' = 0$) causes uncertainty about other lower intensity bands preceding it in the vibrational manifold. If the first peak in the photoelectron spectrum corresponds to the vibrational ground state band ($v' = 0$) then the adiabatic ionization energy for the Si 2*p* level of SiF_4 is 111.57 ± 0.05 eV. This compares reasonably with values of 111.70 eV and 111.79 eV from previous studies,[100] in which no vibrational fine structure was resolved. The component lines in Fig. 3.3.12 are described by a linear combination of 95% Gaussian and 5% Lorentzian lineshapes with half height widths of 0.116 eV. Franck-Condon factors for the eleven vibrational levels fit to this spectrum are 1%, 2%, 6%, 13%, 18%,

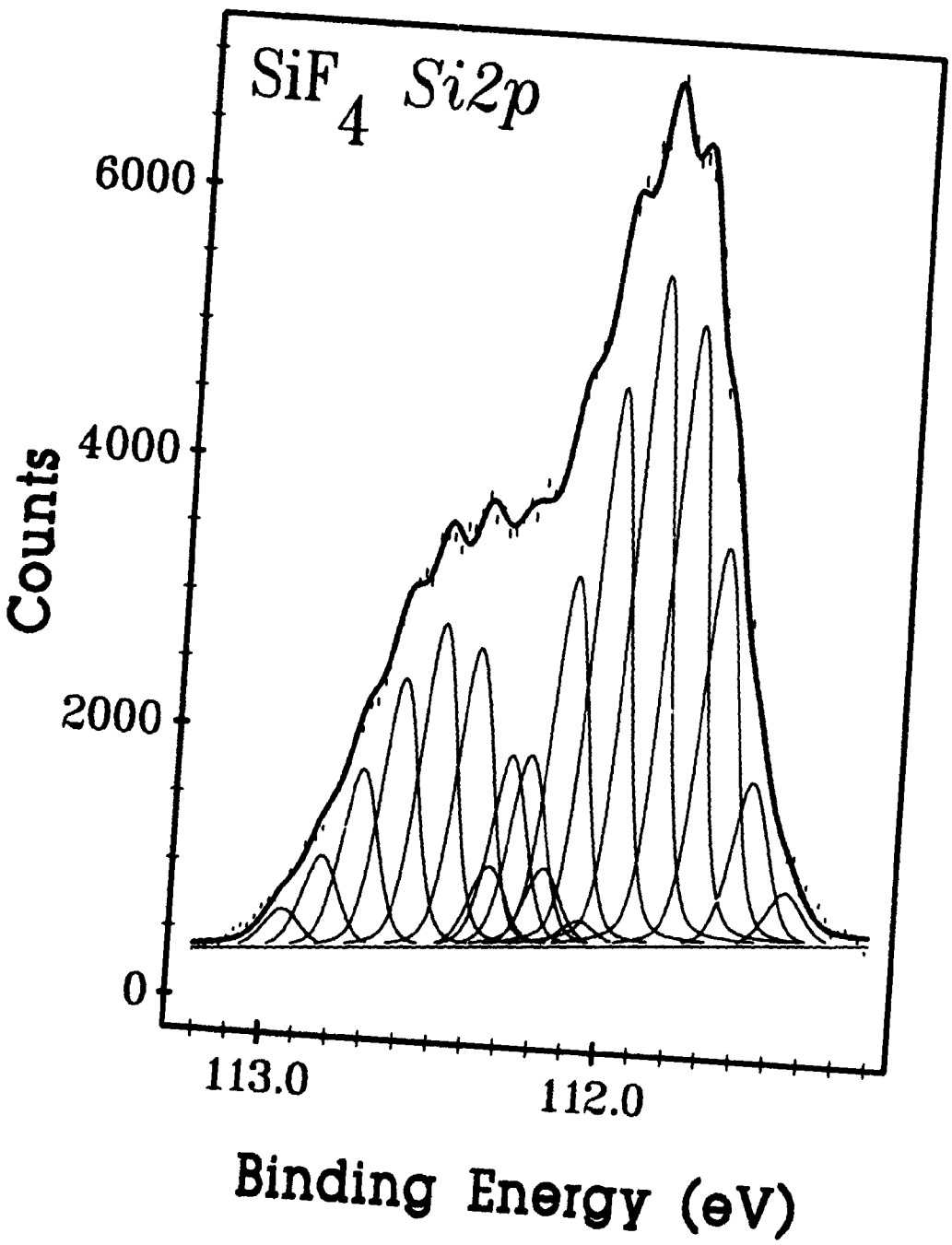

Figure 3.3.12: Experimental photoelectron spectrum of the Si *2p* levels of tetrafluorosilane, SiF_4, measured with an experimental resolution of 0.096 eV.

20%, 17%, 12%, 7%, 3%, and 1% for the $v' = 0$ to $v' = 10$ levels respectively. Better instrumental resolution is still required to estimate the chemical effect on the Si $2p$ linewidths.[24]

The implication of the large number of vibrational bands in the SiF_4 Si $2p$ photoelectron spectrum is that the equilibrium geometry of SiF_4 changes to a larger extent upon ionization than does the equilibrium geometry of SiH_4. This is represented schematically in Fig. 3.3.13 where potential energy curves for the vibrational energies of SiH_4 and SiF_4 are given. Assuming that only the *symmetric* stretching vibrational mode is excited in the ionization of a core electron, which can be argued on the grounds that the change in the equilibrium nuclear geometry upon ionization of a Si $2p$ core electron is symmetric about the central Si atom, only one dimension needs to be considered, the Si–X (X = H, F) bond length. Previous calculations for first row compounds have found that bond lengths decrease when a $1s$ electron is removed from a carbon or nitrogen atom, but increase when an oxygen or F $1s$ electron is involved.[101] The trend in bond length changes for second row atoms is not known. The ~5% increase in the energy of the Si–F stretch in the core ionized species (847 cm^{-1}) relative to the ground state (800.8 cm^{-1})[92] indicates that the removal of a Si $2p$ electron strengthens the Si–F bond. The analysis of the vibrational energies in Si $2p$ ionized SiH_4 also showed that the Si–H bond is strengthened in the core ionized species, where a ~10% increase in the vibrational energy is observed. The equilibrium bond lengths of the core ionized SiH_4 and SiF_4 are therefore assumed to be shorter than their respective bond lengths in the ground electronic state. The Frank-Condon principle, which is the approximation that the nuclear conformation readjusts after the electronic transition and not during it, implies that vibrational states in the core ionized molecules with large wavefunction amplitudes at internuclear bond distances, R′, in the range of R_{eq} for the ground vibrational level of the ground electronic state

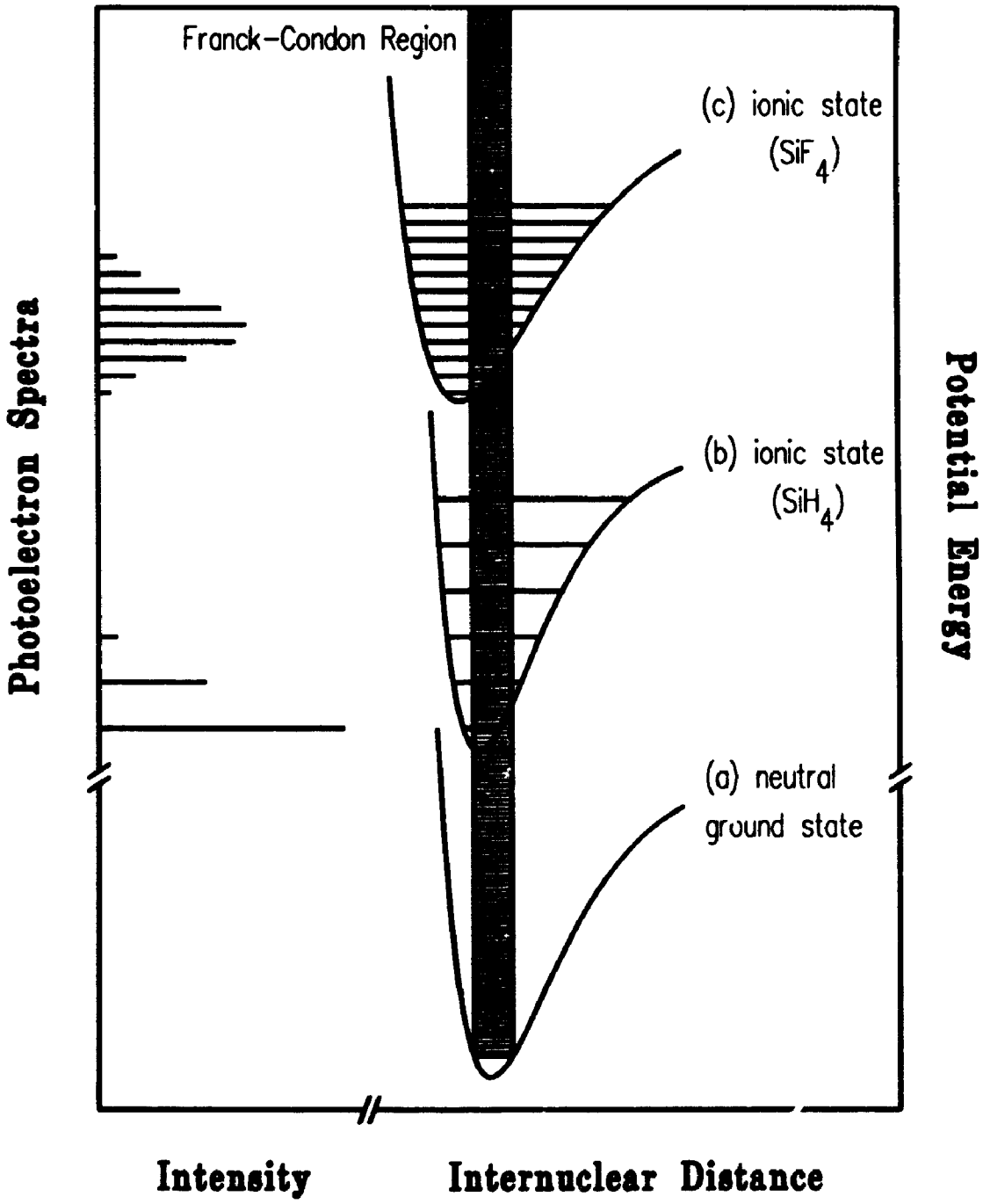

Figure 3.3.13: Schematic representation of the overlap of the Franck-Condon region of the ground vibrational state of the ground electronic state of the SiH_4 and SiH_4 molecules with the excited (ionized) electronic state vibrational levels. The electronic ground states of both molecules are represented by curve (a), the core ionized state of SiH_4 by curve (b) and the core ionized state of SiF_4 by curve (c). A detailed description is given in the text.

will be populated by in the electronic transition. As noted in section 3.1, Franck-Condon factors, which describe the relative intensities of the vibrational bands observed in the photoelectron spectra, are defined as the square of the overlap integral between the vibrational states of the initial and final electronic states of the transition. The intensity distribution of the vibrational peaks in the SiH_4 photoelectron spectrum in Fig. 3.3.6 therefore indicates that only a small change in bond length results from the removal of a Si $2p$ electron from SiH_4. This represented schematically in Fig. 3.3.13, where strong overlap between the $v = 0$ and $v' = 0$ states is shown, with weaker overlap with the $v' = 2$ and 3 states. The resulting vibrational bands in the photoelectron spectrum are shown on the left-hand side of Fig. 3.3.13, with most of the intensity in the $v' = 0$ band and less in the $v' = 2$ and 3 bands. For SiF_4, on the other hand, the large number of vibrational bands observed in Fig. 3.3.12, and the low intensity of the first vibrational band implies a greater change in the equilibrium nuclear geometries of the ground and ionized electronic states. The sixth vibrational band in the SiF_4 Si $2p$ photoelectron spectrum has the greatest intensity which shows that the overlap with the $v = 0$ state is greatest for the $v' = 5$ vibrational state. There is little overlap between the ground vibrational states ($v = 0$ and $v' = 0$) of the ground and ionized electronic states. Overall this implies a much larger change in bond length for SiF_4 than for SiH_4 following ionization of the Si $2p$ electron. This is represented in the top curve (c) in Fig. 3.3.13 where the Franck-Condon region (from the ground electronic state) overlaps very little with the $v' = 0$ vibrational state in the ionized electronic state and only a weak peak is seen for the $v' = 0$ band. The very broad distribution of vibrational bands observed in the Si $2p$ photoelectron spectrum of SiF_4, extending over 1.1 eV, is also consistent with very broad F 1s photoelectron linewidths observed previously.[73,102] It is also broader than the vibrational manifolds observed for SiH_4 and $Si(CH_3)_4$ which are $\sim$0.7 eV wide.

Photoelectron spectra of the Si 2*p* levels of SiF_4 were also measured using a variety of experimental resolutions and are presented in Fig. 3.3.14 All of the spectra are very similar to the spectrum in Fig. 3.3.12. Vibrational fine structure is partially resolved in only the high resolution ΔE=96 meV spectrum. The high resolution spectrum was measured at 135 eV while the others were measured using a photon energy of 130 eV.

Si $2p_{3/2}$ binding energy (eV)	Experimental resolution ΔE (meV)	Observed linewidth (meV)	Gauss Fraction	Vibrational splitting (meV)	Relative intensities of vibrational bands (tot=100)
111.46(5)	96	116	0.95	105	1,2,6,13,18,20,17,12,7,3,1
	180	205	0.85	105	1,2,6,13,18,20,17,12,7,3,1
	250	250	0.90	105	1,2,6,13,18,20,17,12,7,3,1
	820	425	1.0	105	1,2,6,13,18,20,17,12,7,3,1

Table 3.3.6: Summary of the experimental and fitted parameters describing the Si 2*p* photoelectron spectrum of SiF_4. Fitted values were determined by a non-linear least-squares fit of the parameters to the experimental spectra, as described in section 3.2.

The experimental spectra were deconvoluted with a manifold of eleven vibrational bands spaced 0.105 eV apart, consistent with the results for the high resolution SiF_4 Si 2*p* photoelectron spectrum and the fitted parameters are summarized in Table 3.3.6. All eleven bands are necessary to properly deconvolute the high resolution spectrum. The high vibrational level bands ($v' = 9$ and 10) are required to account for intensity observed in the spectrum above a binding energy of ~113 eV. Similarly, low vibrational level bands are required to reproduce the low intensity in the photoelectron band below ~111.6 eV. The simulated spectrum, constructed by plotting the fitted parameters, reproduces the experimental data very well, supporting the assignment of eleven vibrational bands to the Si 2*p* photoelectron spectrum of SiF_4. As the vibrational structure is not resolved in the other SiF_4 Si 2*p* photoelectron spectra, the vibrational manifold determined for the high resolution spectrum was used in the deconvolutions with only the

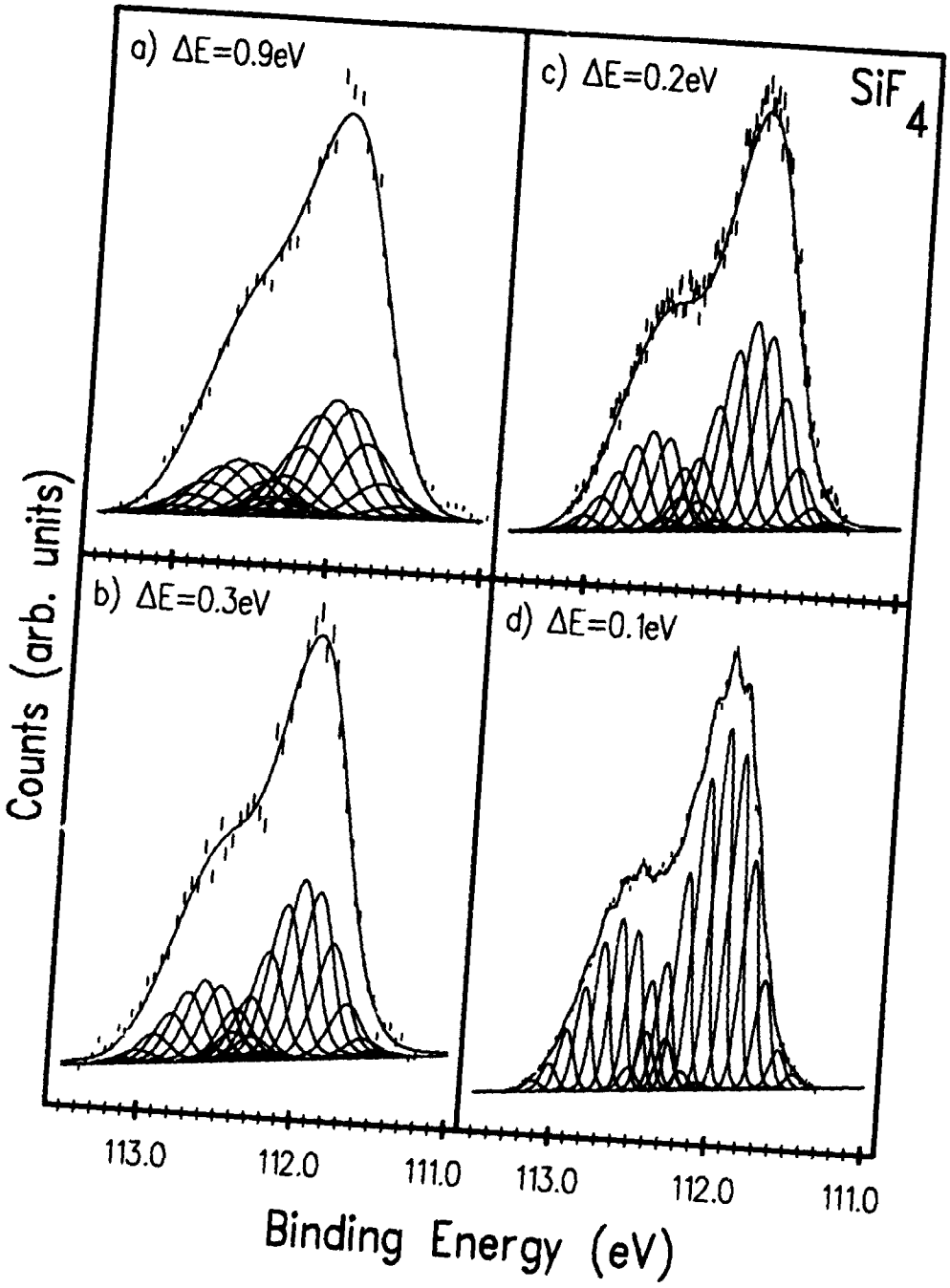

Figure 3.3.14: Experimental photoelectron spectra of the Si 2*p* levels of tetrafluorosilane, SiF_4, measured at formal experimental resolutions of (a) 820, (b) 250, (c) 180, and (d) 96 meV. The solid curves represent fitted parameters (Table 3.3.4) as in Fig. 3.3.7.

linewidths and Gauss fractions allowed vary. The different excitation energies used for the high resolution spectra is not expected to significantly affect the vibrational intensities since the Si 2*p* cross section of SiF_4 is relatively constant over this energy region.[99] Simply by increasing the linewidths of the vibrational bands and by changing the Gaussian component of the lineshape, the lower resolution spectra are fit using the vibrational manifold determined for the higher resolution spectrum.

Linewidths obtained by the least-squares fits to the SiF_4 Si 2*p* photoelectron spectra (Table 3.3.6) are consistently narrower than those obtained for the spectra of SiH_4 measured at the same formal experimental resolutions. This is consistent with the changes predicted by the valence electron density theory used to estimate chemical effects on the natural line width,[24] since the highly electronegative fluorine ligands withdraw electron density from the central Si atom resulting in longer core hole lifetimes. Better experimental resolution is still required to individually resolve the vibrational bands in SiF_4 and unequivocally determine if there is truly a chemical effect resulting in different lifetime limited linewidths for Si 2*p* photoelectron spectra of SiH_4 and SiF_4.

It should be possible to measure vibrationally resolved partial cross sections or branching ratios above the Si 2*p* core level with equivalent or slightly improved experimental resolution. Variations of $\gtrsim$5% in the Franck-Condon factors should be easily detectable at the resolution used to obtain the spectra reported here. Previous measurements of vibrationally resolved branching ratios for the $3\sigma_g$ and 5σ valence molecular orbitals of N_2[34] and CO[103] respectively, have shown that shape resonances have a noticeable effect on vibrational band intensities. Similar effects are expected for the vibrational manifolds of core level ionizations when excitation energies corresponding to the shape resonances are used.[34]

3.3.2.5. $SiCl_4$

Three experimental Si 2*p* photoelectron spectra of $SiCl_4$ are presented in Fig. 3.3.15. The spectra were measured at a photon energy of 130 eV. The overall resolution of the two Si 2*p* spin orbit peaks does not change significantly with the formal experimental resolution over the three different resolutions used, with the region between the spin orbit peaks always resolved to approximately half the height of the Si $2p_{1/2}$ peak. Vibrational broadening causes the of lack of sensitivity of the spectral resolution to the formal resolution and the same methods as those employed previously were used to fit a manifold of vibrational peaks to the spectra.

The applicability of the equivalent-cores approximation has been demonstrated in this study and it is used here to approximate the Si−Cl vibrational frequency of the Si 2*p* ionized molecule. The energy of the P−Cl symmetric stretch in PCl_3 is 0.065 eV, and this value was used in the deconvolution of the experimental $SiCl_4$ Si 2*p* photoelectron spectrum. The adiabatic ionization potential of the Si $2p_{3/2}$ level of $SiCl_4$ was found to be 110.18 eV in the least-squares procedure, a value which compares favourably with previously reported values of 110.17[97,98] and 110.25 eV.[88] The fitted peak shape resulting from the least-squares fit of the vibrational manifold reproduces the experimental line shape, as illustrated in Fig. 3.3.15 (d).

	Si $2p_{3/2}$		Si $2p_{1/2}$	
ΔE (meV)	FWHM (meV)	Gauss frac.	FWHM (meV)	Gauss frac.
440	373	0.9332	391	0.7757
220	346	0.9691	412	0.3278
180	340	1.0000	381	0.2243

Table 3.3.7: Summary of the peak widths (FWHMs) and Gauss fractions for the Si 2*p* bands of the photoelectron spectra of $SiCl_4$ in Fig. 3.3.7 (a) - (c).

The Si 2*p* photoelectron spectra of $SiCl_4$ with formal experimental resolutions of 440, 220 and 180 meV were also deconvoluted using only two bands as illustrated

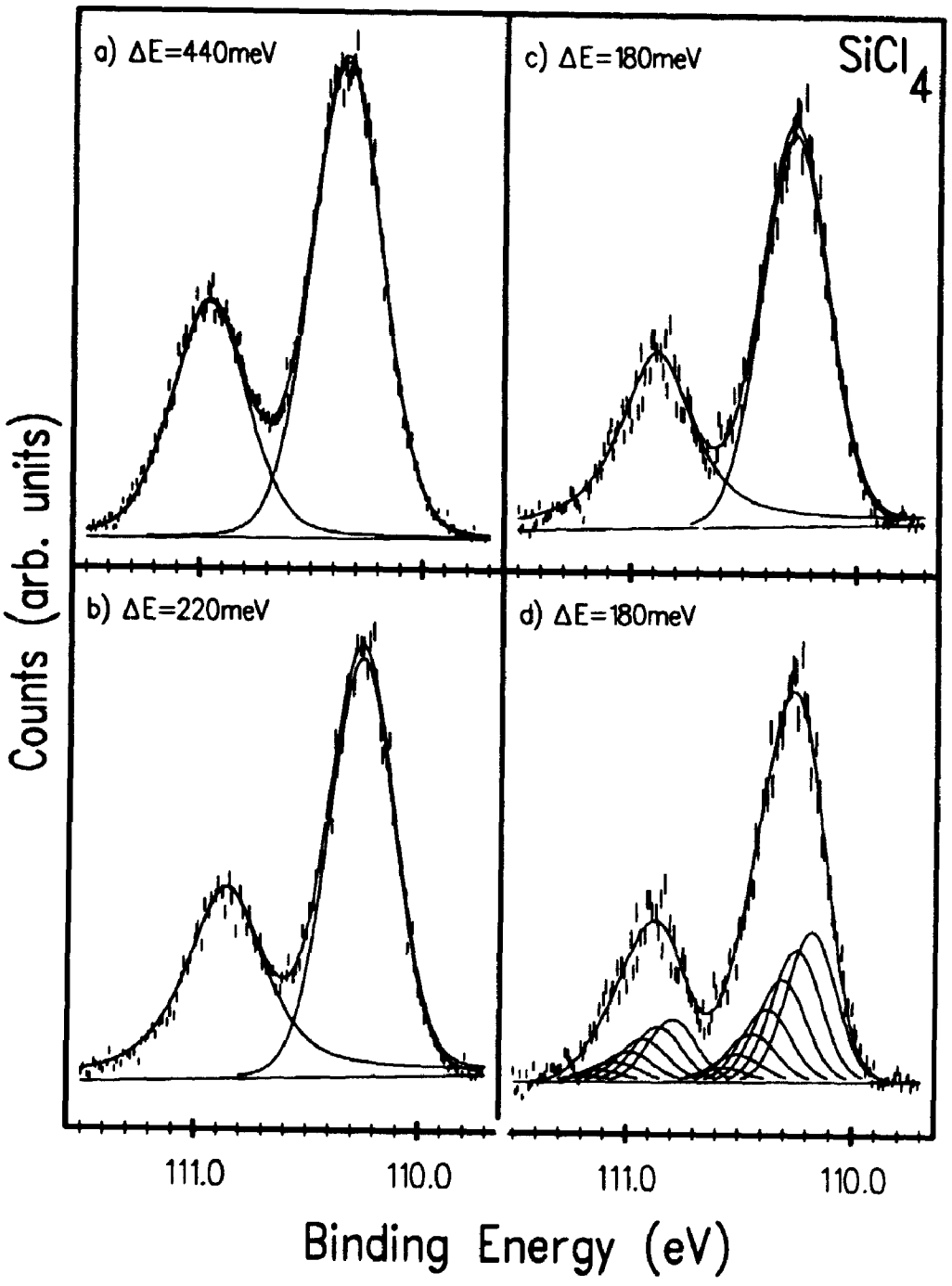

Figure 3.3.15: Experimental photoelectron spectra of the Si $2p$ levels of tetrachlorosilane, $SiCl_4$, measured at formal experimental resolutions of (a) 440, (b) 220, (c) 180, and (d) 180 meV. Solid curves in (a) - (c) represent the fit of two independently determined lines to the experimental data as described in the text. The solid curves in (d) represent the fitted parameters as in Fig. 3.3.7.

in Fig. 3.3.15 (a)-(c). Two bands, representing the Si $2p_{3/2}$ and $2p_{1/2}$ photoelectron lines, were fit to the experimental spectra to determine the effects of the unresolved vibrational structure on the lineshapes of the photoelectron lines. Parameters for the two bands (position, height, FWHM and Gauss fraction) were not constrained in the least-squares procedure. The FWHM's and Gauss fractions obtained for the two bands are listed in Table 3.3.7. Several trends are apparent from this data. For the Si $2p_{3/2}$ photoelectron line, the linewidth decreases and the Gauss fraction increases as the experimental resolution is improved. The Si $2p_{1/2}$ linewidth does not change significantly with experimental resolution, but the Gauss fraction decreases markedly as the resolution is improved. These differences are the result of the unresolved vibrational structure of the Si $2p$ photoelectron lines.

These considerations are very important for distinguishing vibrational broadening where the spin orbit doublet and vibrational splitting are not well resolved and further discussion is warranted to clarify these different widths and shapes. In the deconvolution of the photoelectron spectra, non-overlapping regions of the spectrum dominate the fit of a band to the experimental spectrum. In the two band deconvolutions of the $SiCl_4$ Si $2p$ photoelectron spectra, the high binding energy portion of the Si $2p_{3/2}$ photoelectron line overlaps with the low energy portion of the Si $2p_{1/2}$ line. The least squares procedure for the Si $2p_{3/2}$ line is therefore dominated by the $v' = 0$ vibrational band at the low binding energy side of the band. The shape of the leading edge of the ground state vibrational band is determined primarily by the lifetime of the Si $2p$ core hole and resolution of the excitation source. In this experiment, where the photon width is greater than the lifetime width, the shape of the low binding energy side of the Si $2p_{3/2}$ line is determined primarily by the photon bandwidth. When the photon resolution used to measure the spectrum is improved therefore, so should the width of the Si $2p_{3/2}$ photoelectron line decrease using a two band fit. The Gauss fraction increases with improved photon resolution because contributions from higher vibrational

bands ($v' = 1,2$) overlap with the ground vibrational band since the levels are so closely spaced. When the resolution is improved, the degree of overlap of the higher vibrational bands with the ground state band decreases and the leading edge of the photoelectron line becomes sharper. The Si $2p_{1/2}$ line is dominated by the high energy portion of the band in the deconvolution procedure which encompasses the higher levels of the vibrational manifold. When a single line is used to deconvolute the Si $2p_{1/2}$ photoelectron line therefore, the shape and breadth of the line will depend more upon the extent of the vibrational manifold. The width of the line in the deconvolution will therefore not change significantly with impr ·.d photon resolution. Improved photon resolution does decrease the degree of overlap between adjacent vibrational bands and the overall shape of the band will therefore change. A single band fit to the Si $2p_{1/2}$ line will also encompass the higher vibrational bands of the Si $2p_{3/2}$ line since ..e shape of the line for the Si $2p_{3/2}$ band is dominated by the $v' = 0$ line. As a result, when the photon resolution is improved, and the Si $2p_{3/2}$ line becomes narrower and more Gaussian, the Lorentzian component of the Si $2p_{1/2}$ line must also increase to encompass all of the higher vibrational level of the $2p_{3/2}$ line.

3.3.2.6. $(CH_3)_3SiCl$, $(CH_3)_3SiI$, Cl_2SiH_2 and CH_3SiF_3

Molecule	Si $2p_{3/2}$ E_b (eV)	Exper. resolution ΔE (meV)	Observed linewidth (meV)	Gauss Fraction	Vibr. splitting (meV)	Rel. inten. of vibr. bands (tot=100)
$(CH_3)_3SiCl$	107.12(5)	210	323	1.0	81	41,25,17,10,5,2
$(CH_3)_3SiI$	107.34(5)	250	359	1.0	81	41,25,17,10,5,2
Cl_2SiH_2	108.87(5)	200	384	1.0	287	79,17,4
CH_3SiF_3	109.69(5)	150	200	1.0	107	1,2,6,13,19,20,18,11,7,2,1

Table 3.3.8: Summary of the experimental and fitted parameters describing the Si 2p photoelectron spectra of $(CH_3)_3SiCl$, $(CH_3)_3SiI$, H_2SiCl_2 and CH_3SiF_3. Fitted values were determined by non-linear least-squares fits of the parameters to the experimental spectra, as described in section 3.2.

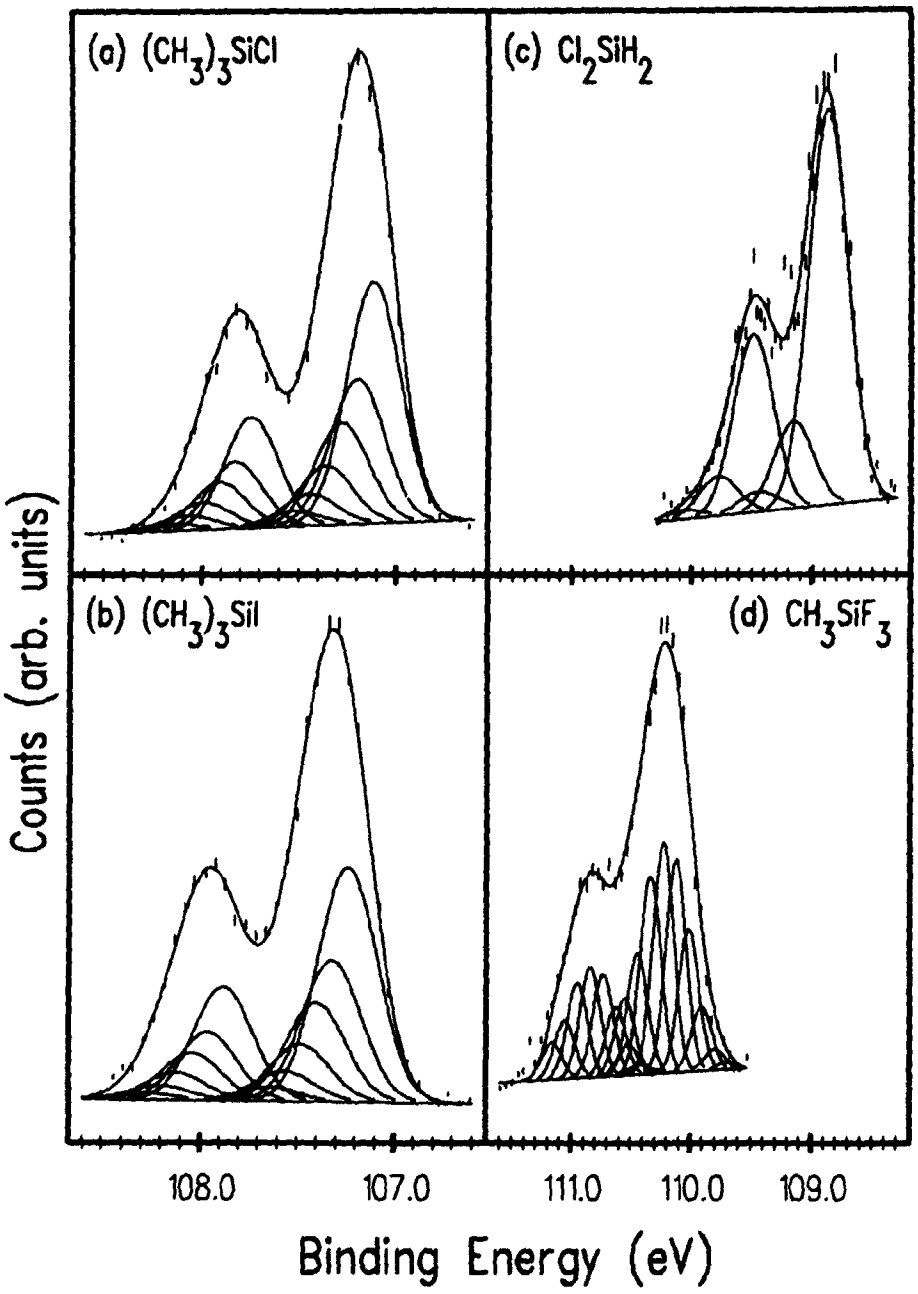

Figure 3.3.16: Experimental photoelectron spectra of the Si 2*p* levels of trimethylchlorosilane, $(CH_3)_3SiCl$, trimethyliodosilane, $(CH_3)_3SiI$, dichlorosilane, H_2SiCl_2 and methyltrifluorosilane, CH_3SiF_3 measured with experimental resolutions of ~130 meV. Solid lines represent the fit of parameters (Table 3.3.8) to the experimental spectrum as described in the text.

Photoelectron spectra of the Si 2*p* levels of $(CH_3)_3SiCl$, $(CH_3)_3SiI$, Cl_2SiH_2 and CH_3SiF_3 were measured at 130, 130, 129, and 125 eV respectively and are presented in Fig. 3.3.16. The spectra were deconvoluted with manifolds of vibrational bands and the resulting parameters are summarized in Table 3.3.8. Spectra of the trimethyl silicon halide compounds were both fit using the vibrational manifold determined for $Si(CH_3)_4$ since the energy of the Si−C stretch is greater than both the Si−Cl and Si−I stretching energies. The Si 2*p* photoelectron spectra of both trimethylhalides are very similar to the spectrum of $Si(CH_3)_4$ and the experimental spectra of the trimethylhalides are well reproduced by the fitted parameters. The vibrational structure of the Si 2*p* photoelectron spectrum of Cl_2SiH_2 was assumed to be dominated by Si−H vibrational bands, with an increased linewidth to account for the Si−Cl vibrational bands. The experimental spectrum is well described by the parameters determined by a least-squares analysis using the above approximations. Finally, the Si 2*p* photoelectron spectrum of CH_3SiF_3 was deconvoluted using a vibrational manifold very similar to the one determined for SiF_4 since the spectra appear to be very similar.

Intensities of particular vibrational bands in the Si 2*p* photoelectron spectra of mixed compounds roughly follow the number of the particular ligand. In the trimethylhalide silanes for example, the Si 2*p* photoelectron spectra are very similar to the spectrum of $Si(CH_3)_4$ since vibrational bands from the three methyl ligands dominate the manifold of vibrational bands. The Si 2*p* photoelectron spectrum of $(CH_3)_3SiH$ also has a very similar shape (Fig. 3.3.11) for similar reasons, although in this case the Si−H vibrations are spaced far enough apart to be have a noticeable effect on the spectral profile. The Si 2*p* photoelectron spectrum of CH_3SiF_3 also illustrates this point since the three fluorines dominate the one methyl ligand and the spectrum is therefore very similar to that of SiF_4.

3.4. CONCLUSIONS

High resolution Si 2*p* photoelectron spectra of eleven silicon compounds; SiH_4, $C_2H_5SiH_3$, $(CH_3)_2SiH_2$, $(CH_3)_3SiH$, $(CH_3)_4Si$, SiF_4, $SiCl_4$, $(CH_3)_3SiCl$, $(CH_3)_3SiI$, Cl_2SiH_2 and CH_3SiF_3 measured using monochromatized synchrotron radiation were reported. The spectra all exhibit vibrational structure although individual vibrational bands were resolved in the spectra of only a few of the compounds. Parameters describing the shape and position of the photoelectron lines were fit to the vibrational structure using a non-linear least-squares method. Very accurate adiabatic Si 2*p* ionization potentials were determined by this method. The equivalent-cores approximation was used to estimate the vibrational energies of the Si 2*p* core ionized molecules. The equivalent-cores model was found to yield reasonably accurate vibrational energy levels for those spectra where vibrational fine structure was resolved. The effect of unresolved vibrational structure on the overall shape of the photoelectron lines was also examined as a function of the experimental resolution. Photoelectron lines with unresolved vibrational structure were found to be asymmetric, with a sharp onset at low binding energy and a broad tail on the high binding energy side of the band.

Evidence for chemical effects on the Si 2*p* core hole lifetimes were seen in the photoelectron spectra of the alkyl silane molecules and in the spectrum of SiF_4. Linewidths of the individual vibrational bands of the Si 2*p* photoelectron lines were found to increase with the number of alkyl ligands on the central silicon atom and decrease for SiF_4. Electron density on the silicon atom increases with the number of alkyl ligands due to the electron donating properties of the alkyl groups. In SiF_4, the highly electronegative fluorine ligands withdraw electron density from the central silicon atom. A correlation between the electron density on the silicon atom and the core hole lifetime is consistent with previous theories describing the effects of valence electron density on the Auger decay rates and hence on the core

hole lifetimes. An incomplete description of the vibrational structure of the Si $2p$ spectra of the alkyl silanes could also account for some of the line broadening.

3.5. REFERENCES

1. P. Mitchell and K. Codling, Phys. Lett. A 38, 31 (1972).
2. M.J. Lynch, A.B. Gardner and K. Codling, Phys. Lett. A 40, 349 (1972).
3. M. Cornacchia, Rev. Sci. Instrum. 60, 1388 (1989).
4. A. Einstein, Ann. Phys. 17, 132 (1905).
5. T. Koopmans, Physica 1, 104 (1933).
6. D.W. Turner and M.I. Al-Joboury, J. Chem. Phys. 37, 3007 (1962).
7. K. Siegbahn, C. ordling, G. Johansson, J. Hedman, P.F. Heden, K. Hamrin, U. Gelius, T. Bergmark, L.O. Werme, R. Manne and Y. Baer, *ESCA Applied to Free Molecules*, (North Holland, Amsterdam, 1969).
8. T.A. Carlson, *Photoelectron and Auger Spectroscopy*, (Plenum Press, New York, 1975).
9. J.J. Lander, Phys. Rev. 91, 1382 (1953).
10. J.F. van der Veen, F.J. Himpsel and D.E. Eastman, Phys. Rev. B 25, 7388 (1982).
11. G.K. Wertheim and D.N.E. Buchanan, Solid State Commum. 69, 689 (1989).
12. G. Gähwiller and F.C. Brown, Phys. Rev. B 2, 1918 (1970).
13. W. Hayes and F.C. Brown, Phys. Rev. A 6, 21 (1972).
14. C.T. Chen, Y. Ma and F. Sette, Phys. Rev. A 40, 6737 (1989).
15. A.P. Hitchcock, J. Electron Spectrosc. Relat. Phenom. 25, 245 (1982), and recent updates.
16. U. Gelius, J. Electron Spectrosc. Relat. Phenom. 5, 985 (1974).
17. U. Gelius, S. Svensson, H. Siegbahn, E. Basilier, Å. Faxälv and K. Siegbahn, Chem. Phys. Lett, 28, 1 (1974).
18. U. Gelius, L. Asplund, E. Basilier, S. Hedman, K. Helenelund and K. Siegbahn, Nucl. Inst. Methods B 229, 85 (1984).

19. G.M. Bancroft, D.K. Creber and H. Basch, J. Chem. Phys. 67, 4891 (1977).

20. G.M. Bancroft ad J.S. Tse, Comments Inorg. Chem. 5, 89 (1986).

21. R.P. Gupta, J.S. Tse and G.M. Bancroft, Phil. Trans. Roy. Soc. (London) 293, 535 (1980).

22. G.M. Bancroft, J.D. Bozek, J.N. Cutler and K.H. Tan, J. Electron Spectrosc. Relat. Phenom. 47, 187 (1988).

23. J.E. Rowe, G.K. Wertheim, D.M. Riffe and N.V. Smith, contribution to *Fifteenth International Conference on X-Ray and Inner-Shell Processes*, Knoxville, Tennessee, July 1990 (unpublished)..

24. M.A. Coville and T.D. Thomas, Phys. Rev. Lett., *to be published.*

25. For overviews of this very recent work see;
C.T. Chen and F. Sette, Physica Scripta T31, 119 (1990);
P.A. Heimann, F. Sent, W. McKinney, M. Howells, R.D. van Zee, L.J. Medhurst, T. Lauritzen, J. Chin, J. Meneghetti and D.A. Shirley, Physica Scripta T31, 127 (1990);
H. Rabus, D. Arvanitis,, M. Domke, A. Puschmann, L. Wenzel, G. Comelli, G. Kaindl and K. Baberschke, Physica Script· T31, 131 (1990).

26. W.L. Jolly and D.N. Hendrickson, J. Am. Chem. Soc. 92, 1863 (1980).

27. W.L. Jolly and T.F. Schaaf, Chem. Phys. Lett. 33, 254 (1975).

28. A. Nilsson and N. Mårtensson, Phys. Rev. Lett. 63, 1493 (1989).

29. A. Nilsson and N. Mårtensson, Solid State Commun. 70, 923 (1989).

30. N. Mårtensson and A. Nilsson, Surf. Sci. 211, 303 (1989).

31. N. Mårtensson and A. Nilsson, J. Electron. Spectr. 52, 1 (1990).

32. W.H.E. Schwarz and R.J. Buenker, Chem. Phys. 13, 153 (1976).

33. H. Ågren, L. Selander, J. Nordgren, C. Nordling, K. Siegbahn and J. Muller, Chem. Phys. 37, 161 (1979).

34. J.L. Dehmer, D. Dill and S. Wallace, Phys. Rev. Lett. 43, 1005 (1979).

35. R.W. Shaw, Jr. and T.D. Thomas, Phys. Rev. Lett. 29, 689 (1972).

36. R.M. Friedman, J. Hudis and M.L. Perlman, Phys. Rev. Lett. 29, 692 (1972).

37. J.H.D. Eland, *Photoelectron Spectroscopy*, John Wiley & Sons, New York, 1974.

38. C.T. Chen and F. Sette, Phys. Scr. T31, 119 (1990).

39. A.P. Hitchcock, Physica Scripta T31, 159 (1990).

40. G.R. Wight, C.E. Brion and M.J. Van der Wiel, J. Electron Spectrosc. Relat. Phenom. 1, 457 (1973).

41. P.A. Heimann, F. Senf, W. McKinney, M. Howells, R.D. van Zee, L.J. Medhurst, T. Lauritzen, J. Chin, J. Meneghettis, W. Gath, H. Hogr[illegible] and D.A. Shirley, Physica Scripta T31, 127 (1990).

42. S.-Y. Lee and C.-H. Lai, Chem. Phys. Lett. 167, 255 (1990).

43. M. Tronc, G.C. King, R.C. Bradford and F.H. Read, J. Phys. B 9, L555 (1976).

44. M. Tronc, G.C. King and F.H. Read, J. Phys. B 12, 137 (1979).

45. A.P. Hitchcock and C.E. Brion, J. Electron Spectrosc. Relat. Phenom. 10, 317 (1977).

46. H. Rabus, D. Arvanitis, M. Domke, A Puschmann, L. Wenzel, G. Comelli, G. Kaindl and K. Baberschke, Physica Scripta. T31, 131 (1990).

47. Y. Ma, F. Sette, G. Meigs, S. Modesti and C.T. Chen, Phys. Rev. Lett. 63, 2044 (1989).

48. W.H.E. Schwarz, Chem. Phys. 11, 217 (1975).

49. H. Ågren, L. Selander, J. Nordgren, C. Nordling and K. Siegbahn, Chem. Phys. 37, 161 (1979).

50. J. Nordgren and N.Wassdahl, Physica Scripta T31, 103 (1990).

51. R. Murphy, I.-W. Lyo and W. Eberhardt, J. Chem. Phys. 88, 6078 (1988).

52. N. Correia, A. Flores-Riveros, H. Ågren, K. Helenlund, L. Asplund and U. Gelius, J. Chem. Phys. 83, 2035 (1985).

53. T.X. Carroll and T.D. Thomas, J. Chem. Phys. 92, 7171 (1990).

54. E.D. Poliakoff, L.A. Kelly, L.M. Duffy, B. Space, P. Roy, S.H. Southworth and M.G. White, J. Chem. Phys. 89, 4048 (1988).

55. N. Correia, A. Flores-Riveros, H. Ågren, L. Pettersson, M. Bäckström and J. Nordgren, J. Chem. Phys. 83, 2053 (1985).

56. T.X. Carroll, S.E. Anderson, L. Ungier and T.D. Thomas, Phys. Rev. Lett. 58, 867 (1987).

57. F. Kaspar, W. Domcke and L.S. Cederbaum, Chem. Phys. 44, 33 (1979).

58. F.K. Gel'Mukhanov, L.N. Mazalov and A.V. Kondratenko, Chem. Phys. Lett. 46, 133 (1977).

59. A. Cesar, H. Ågren and V. Carravetta,Phys. Rev. A 40, 187 (1989).

60. H. Ågren, J.Müller and J. Nordgren, J. Chem. Phys. 72, 4078 (1980).

61. A. Cesar, H. Ågren, A. Naves de Brito, S. Svensson, L. Karlsson, M.P. Keane, B. Wannberg, P.G. Fournier and J.Fournier, J. Chem. Phys. 93, 918 (1990).

62. L. Asplund, U. Gelius, S. Hedman, K. Helenelund, K. Siegbahn and P.E.M. Siegbahn, J. Phys. B 18, 1569 (1985).

63. J.D. Bozek, J.N. Cutler, G.M. Bancroft, L.L. Coatsworth, K.H. Tan, D.S. Yang and R.G. Cavell, Chem. Phys. Lett. 165, 1 (1990).

64. J.D. Bozek, G.M. Bancroft, J.N. Cutler and K.H. Tan, Phys. Rev. Lett. 67, 2757 (1990).

65. J.L. Dehmer, D. Dill and S. Wallace, Phys. Rev. Lett. 43, 1005 (1979).

66. J.B. West, A.C. Parr, B.E. Cole, D.L. Ederer, R. Stockbauer and J.L. Dehmer, J. Phys. B 13, L105 (1980).

67. T.A. Ferrett, A.C. Parr, S.H. Southworth, J.E. Hardis and J.L. Dehmer, J. Chem. Phys. 90, 1551 (1989).

68. C.T. Chen and F. Sette, Rev. Sci. Instrum. 60, 1616 (1989).

69. W.L. Jolly and D.N. Hendrickson, J. Amer. Chem. Soc. 92, 1863 (1970).

70. D.A. Shirley, Chem. Phys. Lett. 15, 325 (1972).

71. W.H.E. Schwarz and R.J. Buenker, Chem. Phys. 13, 153 (1976).

72. W.L. Jolly and T.F. Schaaf, Chem. Phys. Lett 33, 254 (1975).

73. D.J. Bristow and G.M. Bancroft, J. Amer. Chem. Soc. 10[illegible]534 (1983).

74. A. Nilsson and N. Mårtensson, Phys. Rev. Lett. 63, 1483 (1989).

75. D.T. Clark and J. Muller, Theoret. Chim. Acta(Berl.) 41, 193 (1976).

76. W.H.E. Schwarz, Chem. Phys. Lett. 40, 1 (1976).

77. D.T. Clark, I.W. Scanlan and J. Muller, Theoret. Chim. Acta(Berl.) 35, 341 (1974).

78. K.H. Tan, G.M. Bancroft, L.L. Coatsworth and B.W. Yates, Can. J. Phys. 60, 131 (1982).

79. G. Margaritondo, Rev. Sci. Instrum. 60, 1441 (1989).

80. B.W.Yates, K.H. Tan, L.L. Coatsworth and G.M. Bancroft Phys. Rev. A 31, 1529 (1985).

81. U. Gelius, E. Basilier, S. Svensson, T. Bergmark and K. Siegbahn, J. Electron Spectrosc. Relat. Phenom 2, 405 (1973).

82. M.O. Krause, " Electron Spectrometry of Atoms and Molecules", in: *Synchrotron Radiation Research*, eds. H. Winick and S. Doniach, (Plenum Press, New York, 1980).

83. J.A.R. Samson, Phil. Trans. Roy. Soc. (London) A 268, 141 (1970).

84. R.I. Jennrich and P.F. Sampson, Technometrics 10, 63 (1968).

85. L.O. Werme, T. Bergmark and K. Siegbahn, Physica Scripta 6, 141 (1972).

86. G.C. King, M. Tronc, F.H. Read and R.C. Bradford, J. Phys. B 10, 2479 (1977).

87. G.K. Wertheim, M.A. Butler, K.W. West and D.N.E. Buchanan, Rev. Sci. Instrum. 45, 1369 (1974).

88. W.B. Perry and W.L. Jolly, Inorg. Chem. 13, 1211 (1974).

89. J.E. Drake, C. Riddle, B. Glavinčevski, K. Gorzelska and H.E. Henderson, Inorg. Chem. 17, 2333 (1978).

90. M.O. Krause, J. Phys. Chem. Ref. Data, 8, 307 (1979).

91. G. Cooper, T. Ibuki and C.E. Brion, Chem. Phys. 140, 147 (1990).

92. K. Nakamoto, *Infrared and Raman Spectra of Inorganic and Coordination Compounds*, 4th Ed., (John Wiley & Sons, Toronto, 1986).

93. V. Schmidt, J. de Phys. 48, C9-401 (1987).

94. K. Helenelund, U. Gelius, P. Froelich and O. Goscinski, J. Phys. B. 19, 379 (1986).

95. W. Eberhardt, S. Bernstorff, H.W. Jochims, S.B. Whitfield and B. Crasemann, Phys. Rev. A 38, 3808 (1988).

96. M. Borst and V. Schmidt, Phys. Rev. A 33, 4456 (1986).

97. P. Kelfve, B. Blomster, H.Siegbahn, K. Siegbahn, E. Sanhueza and O. Gosinski, Physica Scripta 21, 75 (1980).

98. J.E. Drake, C. Riddle and L. Coatsworth, Can. J. Chem. 53, 3602 (1975).

99. J.D. Bozek, G.M. Bancroft and K.H. Tan, Chem. Phys. 145, 131 (1990).

100. W.L. Jolly, K.D. Bomben and C.J. Eyermann, Atom. Nucl. Data Tables 31, 433 (1984).

101. O. Goscinski, J. Müller, E. Poulain and H. Siegbahn, Chem. Phys. Lett. 55, 407 (1978).

102. R.W. Shaw, Jr. and T.D. Thomas, Chem. Phys. Lett. 22, 127 (1973).

103. R. Stockbauer, B.E. Cole, D.L. Ederer, J.B. West, A.C. Parr and J.L. Dehmer, Phys. Rev. Lett. 44, 757 (1979).

CHAPTER 4.

Core level photoionization mass spectroscopy of the fluoromethylsilane molecules around the Si 2*p* ionization edges

4.1. INTRODUCTION

Removal of inner-shell electrons from a molecule by ionization or excitation to virtual molecular orbitals often results in the dissociation of the molecule into one or more ionic fragments. Following the observation of site-specific fragmentation in core electron excited acetone[1] there has been renewed interest in establishing the connection between the initial inner-shell excited or ionized electronic state of the molecule and the resulting fragmentation pattern of the molecule.[2] Site-specific fragmentation of core excited molecules was originally proposed to account for the different ionic fragments of acetone, $(CH_3)_2CO$, obtained after C $1s \rightarrow \pi^*$ electronic excitations involving either the methyl or ketone carbons. Tunable monochromatized synchrotron radiation was essential for this study since it allowed specific core to bound electronic transitions to be selected. Prior to these measurements the fragmentation of core electron excited or ionized molecules had been studied using either X-ray line sources [3-5] or electron impact [6-8] to create the initial inner-shell electronic excitation in the molecule. Neither of these excitation methods, however, allow for *selective* excitation of specific core to bound or core to shape resonance electronic transitions without the use of coincidence measurements.

A hole in an inner-shell orbital of a molecule resulting from the excitation or ionization of a core electron will usually electronically relax before the molecule

begins to fragment. Compounds with hydrogen bonded directly to the atomic site of the core hole are the exception to this rule and they have been observed to relax via a fast dissociation involving the H atom before electronic relaxation occurs.[9–11] Electronic relaxation of the core hole therefore plays an important role in determining how the molecule will fragment. The nature of the initial electronic excitation in turn determines the electronic relaxation pathways available for the core hole. In light elements, holes in core electronic levels are filled primarily by Auger transitions.[12] When a core electron is initially excited into a virtual molecular orbital, participator Auger decay (autoionization) involving the excited electron competes with spectator resonance Auger decay, where the excited electron remains in the virtual molecular orbital, to fill the inner-shell vacancy. However, spectator Auger decay normally dominates.[13–16] Although fluorescence becomes an important decay mechanism when a "deep" inner-shell electron ($n > 2$) is removed from a "heavy" atom ($Z > 10$) in a molecule by the initial electronic excitation or ionization, a cascade of Auger processes may also occur. In this case, most of the valence electrons are removed from the molecule in an Auger cascade and the resulting highly charged molecular ion ruptures into atomic ions in a "Coulomb explosion". This was first observed for alkyl iodide compounds following ionization of the iodine *L*-shell electrons.[3,4] For "shallower" core electron holes, such as *K*-shell holes in first row atoms and *L*-shell holes in second row atoms, only a single Auger transition usually occurs and the molecule is left with two holes in the valence shell. If the core electron is promoted to a virtual orbital of the molecule by the initial electronic excitation which decays by a participator Auger decay, only a single hole in the valence shell of the molecule results. In either case the fragmentation pattern of the molecule will be determined primarily by the molecular orbitals with the valence holes[17] or by the location of the valence holes around specific atoms.[18] In polyatomic molecules there are numerous possible arrangements of the valence holes in the molecular orbitals

of the molecule and consequently many different fragmentation pathways. The presence of the excited core electron in an antibonding or Rydberg orbital further complicates the available fragmentation pathways when the core hole relaxes via a spectator resonance Auger decay,[13–16] leaving the molecule with two holes in the valence shell of the molecule in addition to the excited electron in a virtual molecular orbital.

Because the ionic fragmentation of inner-shell electron excited and ionized molecules is a multi-step process, important information about the process can be derived from a variety of different experimental measurements. Photoionization mass spectroscopy (PIMS), which can be used to associate yields of ionic fragments of a molecule with the discrete and continuum resonance structure of the inner-shell photoabsorption spectra, is by far the simplest measurement. PIMS measurements of fragment ions produced following core electron excitation or ionization were first performed using electron impact excitation sources [6–8] and excellent results continue to be obtained by this method.[19,20] With the advent of monochromatized synchrotron radiation sources, however, PIMS is more conveniently performed in a non-coincident experiment using photon excitation.[21] PIMS measurements of the ionic fragments of acetone following excitation of the C 1*s* electrons by monochromatized synchrotron radiation[1] stimulated interest in the technique. A variety of molecular systems have subsequently been studied by these methods, including simple diatomic molecules such as N_2 [22] and O_2,[23] triatomic molecules such as CS_2 [24] and the complex polyatomic organometallic compounds $M(CH_3)_4$ (M = Pb, Sn and Ge).[25]

The relationship between the electronic relaxation of a core hole and the subsequent ionic fragmentation of the molecule is best probed directly by measuring the mass spectrum of the photoions in coincidence with the Auger electrons. Auger electron-ion coincidence measurements for the relatively simple molecules N_2,[26–28] O_2,[29] CO,[28,30] N_2O,[31,32] and CS_2 [33] have been previously

reported. The Auger electron-ion spectra are very useful for correlating the electronic relaxation pathways of the core hole with the ionic fragmentation patterns of the molecules but owing to the low coincidence signal, the spectra are experimentally difficult to measure. These measurements are not readily performed for large polyatomic molecules owing to their very complex Auger and resonance Auger spectra which cannot be resolved into individual Auger bands.[13,16] Moreover, interpretation is further complicated by an incomplete understanding of the Auger spectra and resonance Auger spectra of most polyatomic molecules.[13,16]

Ionic fragments of core electron excited or ionized molecules can be associated with doubly charged parent ions resulting from the electronic relaxation of the core hole using a time-of-flight mass spectrometer to measure photoion-photoion coincidence (PIPICO) spectra.[34] Pairs of ions resulting from the dissociation of a single doubly charged ion are detected in a PIPICO measurement. Doubly charged ions can be produced by a variety of mechanisms in the core ionization region including direct double valence photoionization, autoionization accompanied by shake-off of an additional electron and Auger decay of a core ionized molecule. By measuring PIPICO spectra on and off resonances below and above a core ionization edge and associating pairs of ions to doubly charged parent ions, pathways for the relaxation of the initial core hole can be established. Relaxation processes of core electron excited molecules such as spectator resonance Auger decay and participator Auger decay which do not generate doubly charged ions cannot be detected by these methods however. PIPICO spectra measured following excitation or ionization of core level electrons have been reported for numerous diatomic molecules; N_2,[35] O_2,[36] and CO;[37] for more complex polyatomic molecules; CH_3Br,[38] $BrCF_2CF_2I$,[39] SiF_4,[40,41] and $Si(CH_3)_4$;[42] and even for several organometallic compounds; $Sn(CH_3)_4$,[43,44] $Pb(CH_3)_4$,[45] $Al(CH_3)_3$,[46] and $Ga(CH_3)_3$.[47] Kinetic energy distributions of the fragment ions can often be

extracted from PIPICO spectra, but this information can also be obtained from non-coincident time-of-flight mass spectra.[48,49] Dynamics of the dissociation of core electron excited or ionized molecules have also been probed by measuring the angular distribution of the ionic fragments. Diatomic molecules are excited into discrete molecular orbitals (and shape resonances) by linearly polarized light with specific molecular orientations. Since the electronic relaxation and ionic fragmentation of a core excited molecule usually occurs more quickly than its rotational motion, an asymmetric distribution of fragment ions results.[50] Angle resolved mass spectra of core excited N_2, O_2, and NO have been measured very recently [50–56] and the results contain information about the symmetry of the core excited states of the molecules.

Auger electron-photoion and photoion-photoion coincidence measurements and angle resolved ion yield measurements provide important evidence for a complete understanding of the dynamic processes of the molecular fragmentation following excitation of core electrons but only a small number of compounds have been studied by these techniques. Most previous studies of the molecular fragmentation following core electron excitation have concentrated on small or highly symmetric molecules but larger and more complex molecular systems (with considerably more complicated electronic structures) should also be studied as they are more likely to exhibit selective fragmentation. With the aid of the chemical series approach,[57] where changes in spectral features are studied as a function of small chemical differences in a series of related compounds, the ion yield spectra of the five fluoromethylsilane compounds, $Si(CH_3)_xF_{4-x}$; x=0-4, are reported and interpreted here. Total ion yields and total electron yields of the five fluoromethylsilane compounds have been measured in the Si 2*p* pre-edge and continuum regions and are compared with the previously reported photoabsorption spectra.[57] Photoionized mass spectra have been measured at photon energies corresponding to discrete and continuum resonances of the Si 2*p*, Si 2*s* and F

1*s* ionization edges. Partial ion yield spectra of the most abundant fragment ions were also measured across the Si 2*p* ionization edges for each of the five compounds and compared with the total ion yield curves. Determining whether preferential cleavage of the Si−C or Si−F bonds would be observed at the core edges of the mixed compounds was of particular interest. Previous experimental and theoretical results for the photoabsorption spectra of the fluoromethylsilane compounds[57] are extremely useful for interpretation of the present results as is the chemical series approach.

4.2. EXPERIMENTAL

Spectra reported here were measured using photons from the Canadian Synchrotron Radiation Facility Mark IV Grasshopper monochromator equipped with a 1200 groove/mm grating. Adjustable slit widths allowed the selection of different photon resolutions for the various spectra. The total electron and total ion yield spectra were measured at relatively high resolutions of 0.12 Å(~0.1 eV at $h\nu = 100$ eV to ~0.2 eV at $h\nu = 150$ eV) while the photoionized mass spectra and mass resolved partial photoion yield spectra were measured with the lower photon resolution of 0.4 Å(~0.3 eV at $h\nu = 100$ eV to ~0.7 eV at $h\nu = 150$ eV). High vacuum regions of the monochromator and synchrotron were isolated from the relatively high pressure in the experimental chamber with a multistage differential pumping system.[58] Total electron and ion yield spectra were measured using an electron multiplier biased to either positive or negative voltages arranged in a mutually orthogonal geometry with the incident radiation and an effusive jet of the sample gas. The sample jet was produced by introducing the gas of interest into the vacuum chamber through a 50 μm nozzle tip on an XYZ manipulator extending into the sample chamber. A 110 l/s turbopump was placed directly opposite the sample jet to maintain relatively low pressure in the sample chamber. Mass spectra and partial ion yields of the fluoromethylsilane compounds were obtained using a Balzers QMG 112 quadrupole mass filter in front of the electron multiplier. The quadrupole mass filter was situated in a mutually perpendicular geometry with the photon beam and sample jet and aligned in the direction of the polarization vector of the synchrotron radiation. The interaction region of the gas jet and incident radiation occurred inside a wire cage placed on the end of the quadrupole assembly which was used to generate the extraction field for the mass filter. The anticipated effect of the extraction field, created by applying a +100 eV potential to the wire cage, was two fold. First, it was anticipated that the extraction field would increase the acceptance angle of the quadrupole mass filter by repelling

ions in the direction of the quadrupole filter, thereby reducing the affects of any asymmetric angular distributions of the fragment ions. Second, it was expected that the positive potential of the wire cage would reduce kinetic energy effects (discrimination against high energy ions) by directing a larger proportion of the ionic fragments into the mass filter. The effectiveness of the extraction field to reduce these effects is demonstrated in the results section by a comparison with previously reported results.

The current signal from the electron multiplier was converted to a voltage using an electrometer, recorded on a chart recorder and later digitized using a 300 dpi scanner for the total ion yield and total electron yield spectra as well as for the individual mass spectra. Partial ion yield curves were obtained by stepping the monochromator and digitizing the output voltage from the electrometer with a 12 bit A/D convertor.

All of the samples used in this study were obtained commercially at high purity as in Chapter 2 and previous work.[57] The liquid samples were degassed with repeated freeze-pump-thaw cycles and used without further purification. Backing pressures of ~100 torr behind the 50 μm nozzle were used resulting in pressures of ~1-2$\times 10^{-5}$ torr in the vacuum chamber. At this pressure only an insignificant amount (<0.02%) of the incident radiation is absorbed by the sample gas over the ~20 cm separating the high vacuum region of the beamline from the interaction region. The resulting pressure in the interaction region is estimated to be ~10^{-4} torr which is low enough to avoid scattering cross section problems.

There are several factors contributing to the experimental error in this experiment. None of the spectra reported here have been corrected for the incident photon flux. Individual photoionized mass spectra were measured in less than one minute and partial photoion yields in less than five minutes however, and the decay of the photon intensity from the synchrotron is not significant over these time periods. The sensitivity of the quadrupole mass filter was not calibrated

which will affect the branching ratio values obtained. Errors in the reported branching ratios for the well resolved peaks are estimated to be <5%. Peak areas of strongly overlapping peaks (i.e. C^+, CH^+, CH_2^+ and CH_3^+) have significant errors of up to ~20% but errors for the total areas of the Me^+ bands are also estimated to be <5%. Consistency between the photoionized mass spectra of the fluoromethylsilane compounds measured at discrete photon energies and the photoion yields of individual ions as a function of photon energy indicate that there are no significant systematic errors in the methods employed.

4.3. RESULTS and DISCUSSION

4.3.1. Total electron, total ion and photoabsorption spectra

Total electron yields and total ion yields of the fluoromethylsilane compounds, $Si(CH_3)_xF_{4-x}$; x=0-4, at photon energies around the Si 2*p* core ionization edges are presented in Fig. 4.3.1 together with the corresponding photoabsorption curves from Chapter 2.[57] The total ion and electron yield curves have not been corrected for the energy dependent changes in the incident photon flux from the monochromator, but this should affect only the overall shape of the yield curves and not the positions nor intensities of the resonances. The ion and electron yields for each fluoromethylsilane compound are almost identical, as expected, since an ion and electron are produced by each ionization event. There are, however, significant differences between the total ion and electron yields and the corresponding photoabsorption spectra. Intensities of the pre-edge resonances are substantially reduced relative to the continuum features in the total electron and total ion yields versus the photoabsorption spectra. This is primarily the result of enhanced dissociative multiple ionization ($\eta > 1$) above the ionization threshold.[37] The continuum resonance just at or above the Si 2*p* ionization threshold in the methyl containing fluoromethylsilane compounds is highlighted in the electron and ion yields because of the decreased relative intensity of the pre-edge features. The intensity of the resonance at threshold varies with the number of methyl groups surrounding the central Si atom and it has previously been assigned to result from the Si–C antibonding orbitals.[57]

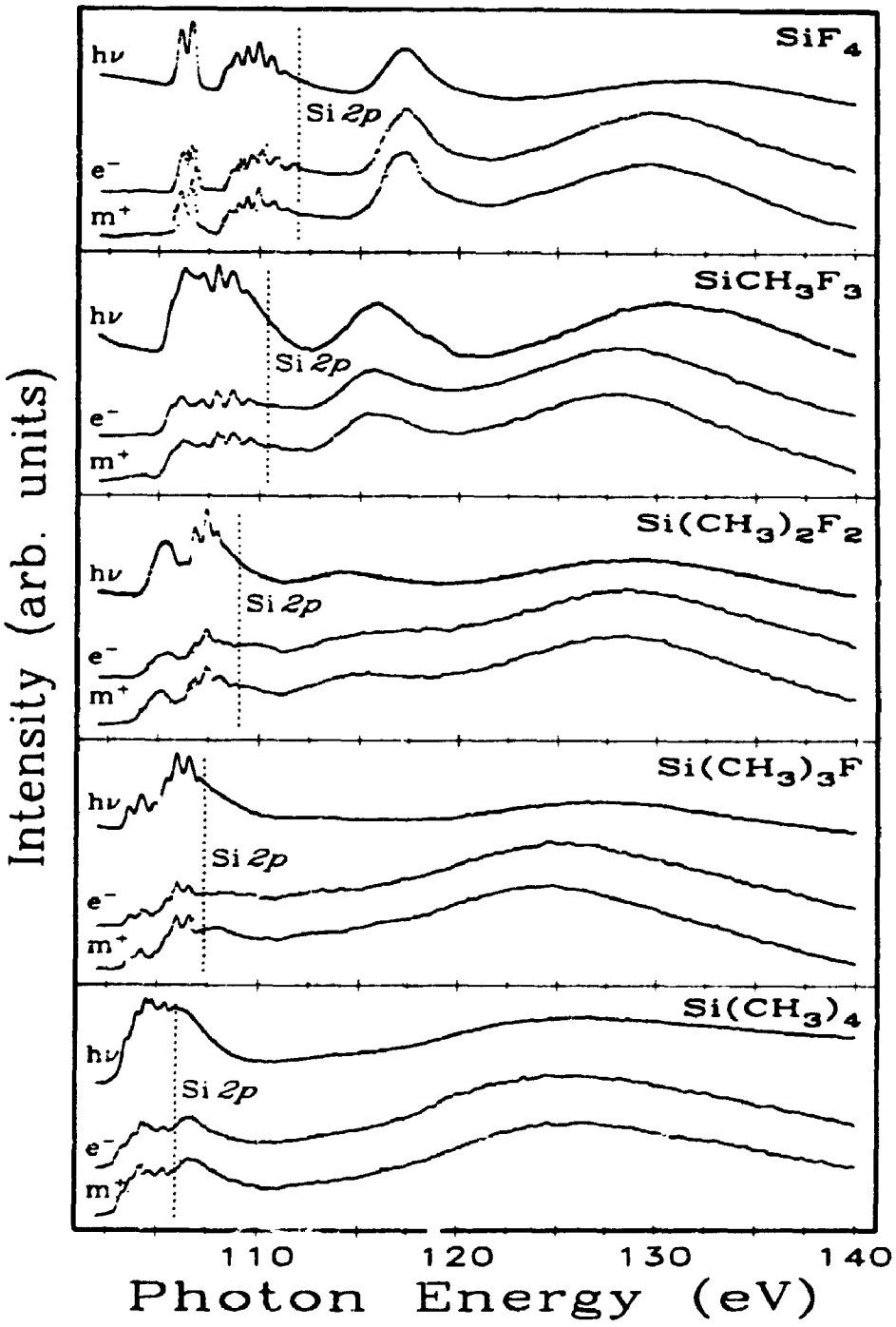

Figure 4.3.1: Photoabsorption spectra ($h\nu$) (Ref. 57), total electron yields (e^-) and total ion yields (m^+) for the fluoromethylsilane compounds around the Si 2*p* ionization edge.

4.3.2. Photoion mass spectra

Photoion mass spectra of the five fluoromethyl silane compounds, $Si(CH_3)_xF_{4-x}$; x=0-4, obtained at the photon energies indicated on the figures, corresponding to energies on and off the discrete and continuum resonances surrounding the Si 2*p*, Si 2*s* and F 1*s* ionization edges,[57] were measured using a quadrupole mass filter and representative spectra are presented in figures 4.3.2 – 4.3.6. Peaks in the photoion mass spectra have been assigned to appropriate fragment ions based on the m/z values of the peaks and, where appropriate, previous observations. The assignments of the peaks are shown on the top spectrum in each figure. The photoion mass spectra of the fluoromethylsilane compounds in Figures 4.3.2 – 4.3.6 are on arbitrary intensity scales. In the Si 2*p* region (100-145 eV), however, the spectra of SiF_4 and $SiCH_3F_3$ have been normalized so that the area of the F^+ peaks follow the F^+ partial ion yields for SiF_4 and $SiCH_3F_3$. Photoion mass spectra measured at photon energies above the Si 2*p* region (around the Si 2*s* and F 1*s* ionization edges) are normalized to the same F^+ peak area as that in the highest energy spectrum in the Si 2*p* region. Intensities of the photoion mass spectra for the three other fluoromethylsilane compounds were normalized in a similar fashion using the areas and partial ion yields of the methyl ion peaks. Areas of the photoion mass spectral peaks of the fluoromethylsilane compounds were obtained by fitting Gaussian peak shapes to the experimental spectra and used to calculate branching ratios for the peak areas. The results are summarized for excitation energies around the Si 2*p*, Si 2*s* and F 1*s* ionization edges of SiF_4 to $Si(CH_3)_4$ in Table 4.3.2 – Table 4.2.6 respectively.

Photoion mass spectra of the fluoromethylsilane compounds following excitation or ionization of the Si 2*p*, Si 2*s* and F 1*s* core electrons are all complex, exhibiting peaks for almost every one of the possible fragment ions of the parent molecules. In photoion mass spectra of SiF_4 (Fig. 4.3.2), for instance, peaks corresponding to the ions F^+, Si^+, SiF^+, SiF_2^+ and SiF_3^+ are observed as well

as for the doubly charged ions F^{2+}, Si^{2+}, SiF^{2+} and SiF_2^{2+}. With substitution of methyl groups for the fluorine atoms around the central silicon atom, progressively more complicated photoion mass spectra are observed.

In the photoion mass spectra of $SiCH_3F_3$ (Fig. 4.3.3), peaks due to the four methyl fragment ions C^+, CH^+, CH_2^+ and CH_3^+ are observed as a single unresolved band and additional peaks corresponding to the methyl containing fragments $SiMe^+$ and $SiMeF_2^+$ (Me = C+CH+CH_2+CH_3) are observed at all photon energies.

Unless they are explicitly defined, references to methyl groups (Me) in fragment ions of the fluoromethylsilane compounds refer to the sum of the peaks for C, CH, CH_2 and CH_3 in this report. Very weak peaks at m/z = 100 amu (Table 4.3.2) corresponding to the molecular ion, $SiMeF_3^+$, were also observed in the photoion mass spectra but the spectra in Fig. 4.3.3 have been truncated at 88 amu because these peaks are too weak to be seen on the scale used in the figure. The numerous sharp peaks observed above 55 amu in photoion mass spectrum of $SiCH_3F_3$ measured at 734 eV are too narrow to be ion peaks given that a mass resolution of $\sim$ 1 amu was used to obtain the spectrum. The peaks are due to electronic noise and sensitivity limitations of the equipment used in the experiment. The photoion mass spectra of $Si(CH_3)_2F_2$, $Si(CH_3)_3F$ and $Si(CH_3)_4$ are further complicated by the possible rearrangements involving the carbon and hydrogen atoms of the additional methyl groups. Upon substitution of a further methyl ligand for a fluorine atom from $SiCH_3F_3$ to $Si(CH_3)_2F_2$, additional peaks around the Si^+ peak due to $C_2H_3^+$ and SiH_2^+ [59] are seen in the photoion mass spectrum of $Si(CH_3)_2F_2$ (Fig. 4.3.4).

Rearrangements of the H atoms from the methyl group(s) onto the Si atom are responsible for many of the additional peaks which are sometimes seen with appreciable intensity in the photoion mass spectra of the methyl containing compounds, for example the peak at 49 amu in the $SiMe_3F$ spectra (Fig. 4.3.5) corresponding to $SiFH_2^+$.

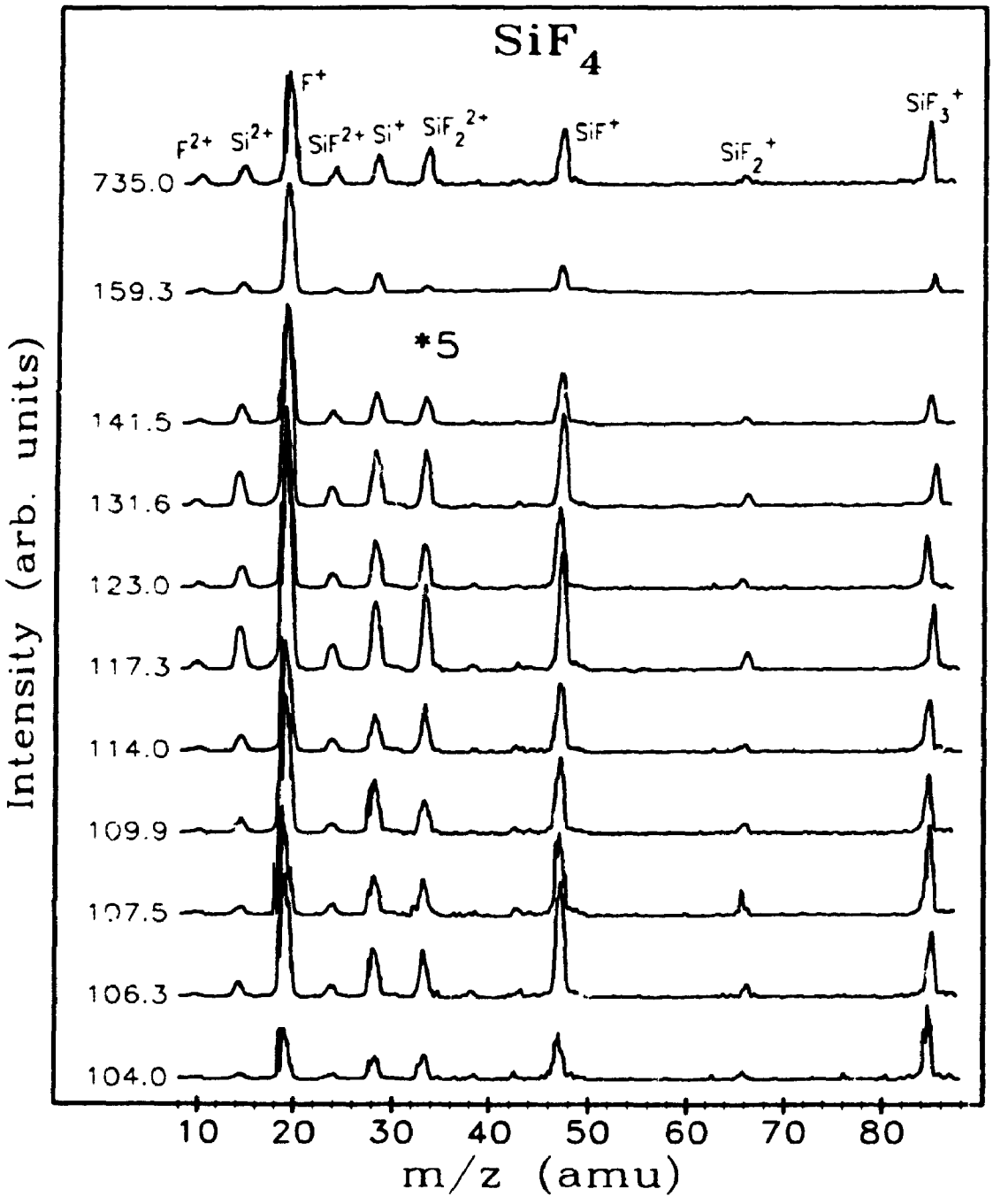

Figure 4.3.2: Photoionized mass spectra of SiF_4 measured at the photon energies indicated at the left of the spectra. The spectral intensities were normalized to the F^+ partial ion yield and are multiplied by a factor of 5 above 31 amu.

photon energy(eV)	assignment[a]	F^{2+} (9.5)	Si^{2+} (14)	F^+ (19)	SiF^{2+} (23.5)	Si^+ (28)	SiF_2^{2+} (33)	SiF^+ (47)	SiF_2^+ (66)	SiF_3^+ (85)
104.0	off resonance	0.9	4.0	49.8	3.9	21.0	3.7	6.1	1.1	9.5
106.3	Si2$p \rightarrow \sigma^*$	0.6	5.1	55.4	3.9	19.0	2.9	8.2	0.7	4.3
107.5	off resonance	1.4	4.5	49.3	4.9	20.7	2.9	7.3	1.6	7.5
109.9	Si2$p \rightarrow \sigma^*$+Rydberg	0.3	4.7	58.8	2.9	21.5	2.2	5.4	0.7	3.6
111.90	Si2p I.P.									
114.0	off resonance	1.2	7.2	55.5	5.0	16.9	3.4	6.0	0.6	4.3
117.3	Si2$p \rightarrow$ke	1.6	9.5	59.5	5.3	14.2	3.1	4.2	0.6	2.1
123.0	off resonance	1.4	8.4	55.7	5.2	17.5	3.0	5.2	0.6	3.1
131.6	Si2$p \rightarrow kt_2$	1.6	9.8	60.2	5.0	15.1	2.7	4.4	0.4	0.7
141.5	off resonance	1.3	9.0	60.2	5.6	14.4	2.2	4.3	0.5	2.4
150.0	off resonance	2.5	6.1	73.7	2.1	11.2	0.5	2.8	0.2	1.0
159.3	Si2$s \rightarrow \sigma^*$+Rydberg	2.4	6.5	73.1	2.3	11.1	0.6	2.7	0.2	1.1
163.3	Si2s I.P.									
650.0	off resonance	3.4	6.5	68.2	2.0	12.0	0.8	3.2	0.6	3.2
705.0	F1$s \rightarrow \sigma^*$+Rydberg	3.4	8.9	54.5	5.6	14.4	2.9	4.8	1.3	4.3
735.0	F1$s \rightarrow$cont. res.	4.0	8.8	56.1	6.2	12.4	2.8	4.6	0.6	4.5
800.0	off resonance	6.3	9.6	52.5	5.5	12.5	2.9	5.1	0.7	4.8

[a] Ref. 57.

Table 4.3.1: Branching ratios (%) of the peak areas from the photoionized mass spect. of SiF_4 (Fig. 4.3.2) around the Si 2p, Si 2s and F 1s ionization edge regions. Approximate m/z values are given in brackets for each fragment below the symbol.

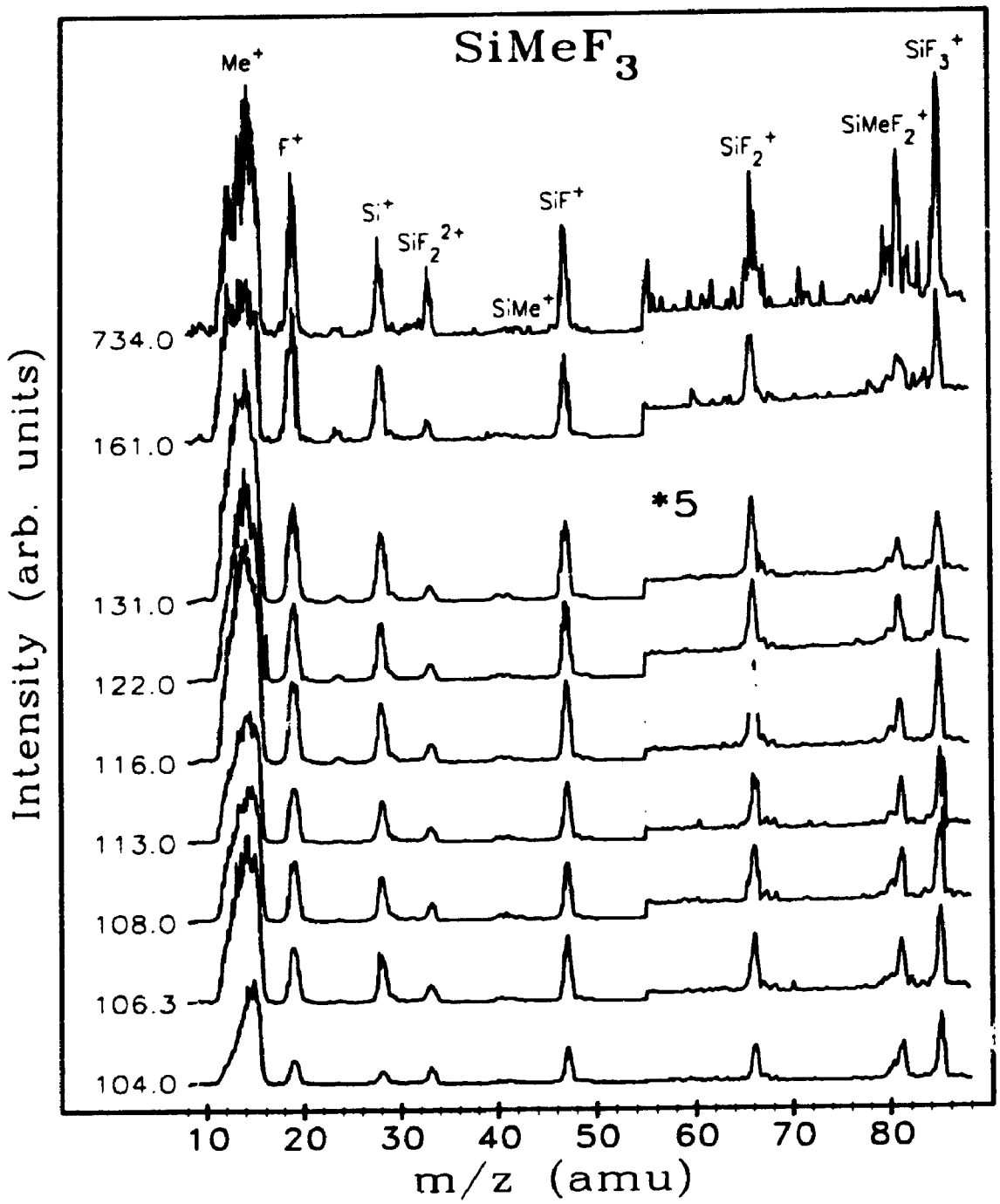

Figure 4.3.3: Photoionized mass spectra of $SiMeF_3$ measured at the photon energies indicated at the left of the spectra. The spectral intensities were normalized to the F^+ partial ion yield and are multiplied by a factor of 5 above 55 amu.

photon energy(eV)	assignment[a]	Me^+ (12-15)	F^+ (19)	Si^+ (28)	SiF_2^{2+} (33)	$SiMe^+$ (43)	SiF^+ (47)	SiF_2^+ (66)	$SiMeF_2^+$ (81)	SiF_3^+ (85)	$SiMeF_3^+$ (100)
104.0	off resonance	67.9	7.2	4.2	4.0	1.0	8.7	1.7	2.5	2.7	0.1
106.3	$Si2p \rightarrow \sigma^*$	67.7	8.6	7.1	2.5	0.9	8.2	1.3	1.6	1.9	0.2
108.0	Si2p —Rydberg	65.1	10.5	7.1	2.3	1.4	7.9	1.5	1.7	2.2	0.2
110.40	Si2p I.P.										
113.0	off resonance	66.2	10.3	6.6	2.1	1.2	8.4	1.5	1.5	2.0	0.2
116.0	$Si2p \rightarrow ke$	69.4	9.9	6.5	1.8	0.7	7.5	1.6	1.0	1.5	0.2
122.0	off resonance	68.9	9.8	6.5	1.7	0.6	8.3	1.4	1.2	1.5	0.2
131.0	$Si2p \rightarrow ka_1 + ke$	69.5	10.8	7.3	1.3	0.7	7.2	1.3	0.7	1.0	0.2
152.0	off resonance	65.0	11.9	8.3	1.6	0.7	8.1	1.6	0.9	1.6	0.2
157.0	$Si2s \rightarrow \sigma^*$	62.9	12.4	8.4	1.6	1.0	8.3	1.4	1.6	1.8	0.6
161.0	Si2s —Rydberg	64.6	13.5	8.6	1.5	0.8	7.0	1.3	1.3	1.4	0.1
161.9	Si2s I.P.										
174.0	off resonance	63.1	10.6	9.5	2.2	1.1	7.2	2.3	1.5	2.0	0.5
650.0	off resonance	62.1	10.4	6.3	3.2	1.6	6.9	1.9	3.4	3.2	1.1
705.0	$F1s \rightarrow \sigma^*$	59.6	11.9	6.9	3.6	1.2	8.4	1.5	3.0	3.4	0.6
734.0	F1s —cont. res.	62.5	11.5	7.1	3.0	0.6	7.5	1.7	2.6	2.5	0.8
800.0	off resonance	60.5	12.5	6.1	4.0	0.9	7.9	1.4	3.6	2.4	0.7

[a] Ref. 57.

Table 4.3.2: Branching ratios (%) of the peak areas from the photoionized mass spectra of $SiCH_3F_3$ (Fig. 4.3 3) around the Si 2*p*, Si 2*s* and F 1*s* ionization edge regions. Approximate m/z values are given in brackets for each fragment below the symbol.

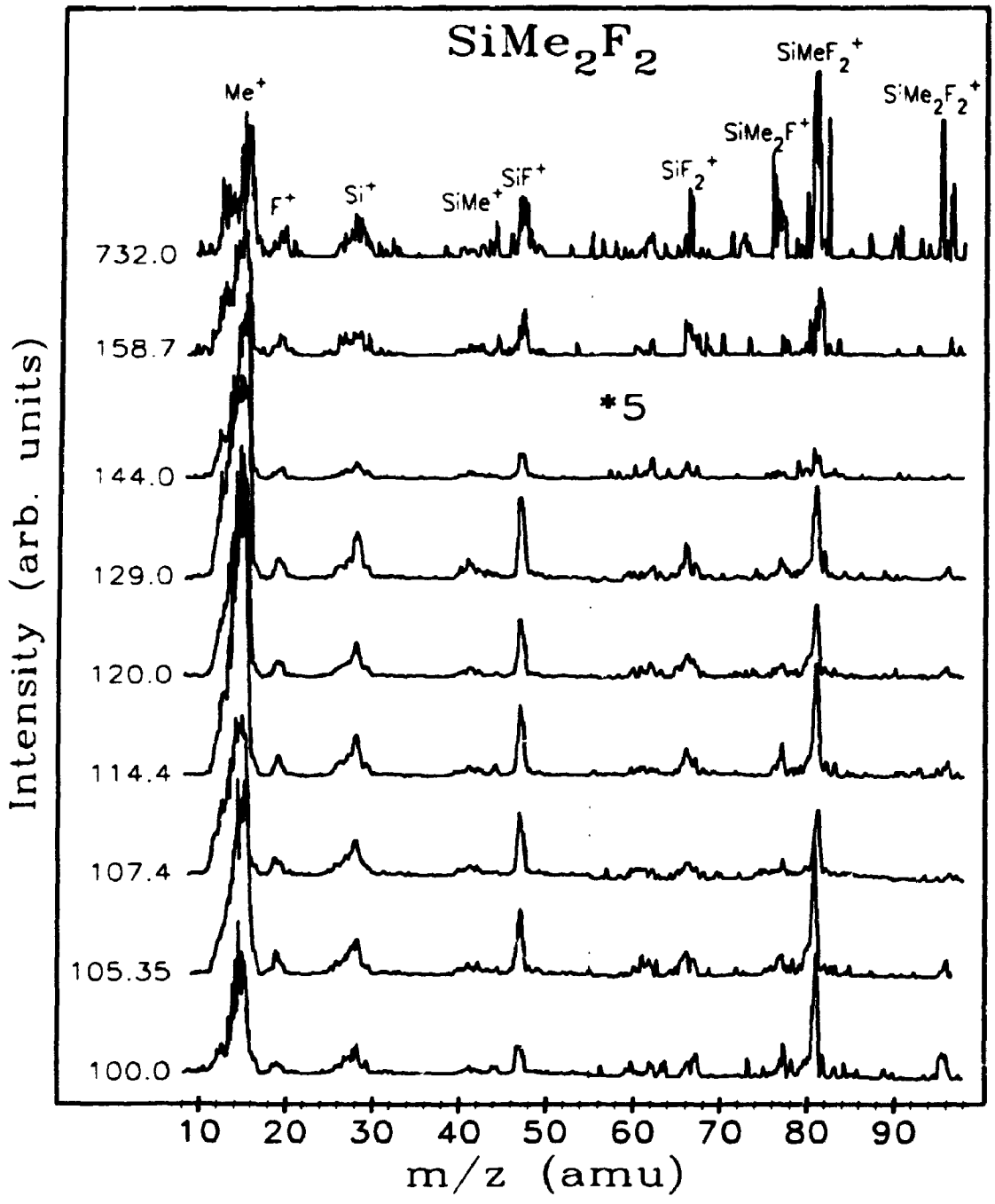

Figure 4.3.4: Photoionized mass spectra of $SiMe_2F_2$ measured at the photon energies indicated at the left of the spectra. The spectral intensities were normalized to the Me^+ partial ion yield and are multiplied by a factor of 5 above 55 amu.

photon energy(eV)	assignment[a]	Me^+ (12-15)	F^+ (19)	Si^+ (28)	$SiMe^+$ (41)	SiF^+ (47)	SiF_2^+ (66)	$SiMe_2F^+$ (77)	$SiMeF_2^+$ (81)	$SiMe_2F_2^+$ (96)
100.0	off resonance	70.9	3.3	6.7	3.1	8.6	0.9	1.1	4.4	1.0
105.35	$Si2p \rightarrow \sigma^*$	74.2	2.9	5.3	2.6	9.9	0.7	0.6	3.4	0.3
107.4	$Si2p \rightarrow$Rydberg	74.5	2.9	7.3	2.3	9.9	0.5	0.5	2.1	0.0
109.01	$Si2p$ I.P.									
114.4	$Si2p \rightarrow ka_1 + kb_1$	79.6	2.1	5.4	1.7	7.6	0.6	0.5	2.2	0.2
120.0	off resonance	78.8	2.5	5.6	1.7	8.2	0.7	0.3	1.9	0.2
129.0	$Si2p \rightarrow kb_1 + ka_1 + kb_2$	77.8	2.3	5.7	2.7	8.5	0.6	0.3	1.8	0.1
144.0	off resonance	78.7	2.9	5.5	3.0	7.8	0.6	0.2	1.3	0.1
156.0	$Si2s \rightarrow \sigma^*$	73.2	3.5	6.2	4.4	8.9	1.4	0.7	1.2	0.4
158.7	$Si2s \rightarrow$Rydberg	74.5	4.1	7.5	2.7	6.9	1.3	0.4	2.4	0.2
160.4	$Si2s$ I.P.									
172.0	off resonance	76.8	5.6	5.1	2.3	5.7	0.9	0.7	2.7	0.2
650.0	off resonance	72.0	2.5	8.6	1.9	8.4	0.6	0.7	4.6	0.8
708.0	$F1s \rightarrow \sigma^*$	70.2	4.0	6.8	3.0	9.4	0.6	1.0	4.6	0.5
732.0	$F1s \rightarrow$cont. res.	62.4	5.7	7.1	3.4	12.4	0.7	2.4	4.9	1.1
800.0	off resonance	63.9	6.9	6.5	2.7	9.5	1.1	1.0	6.8	1.6

[a] Ref. 57.

Table 4.3.3: Branching ratios (%) of the peak areas from the photoionized mass spectra of $Si(CH_3)_2F_2$ (Fig. 4.3.4) around the Si 2*p*, Si 2*s* and F 1*s* ionization edge regions. Approximate m/z values are given in brackets for each fragment below the symbol.

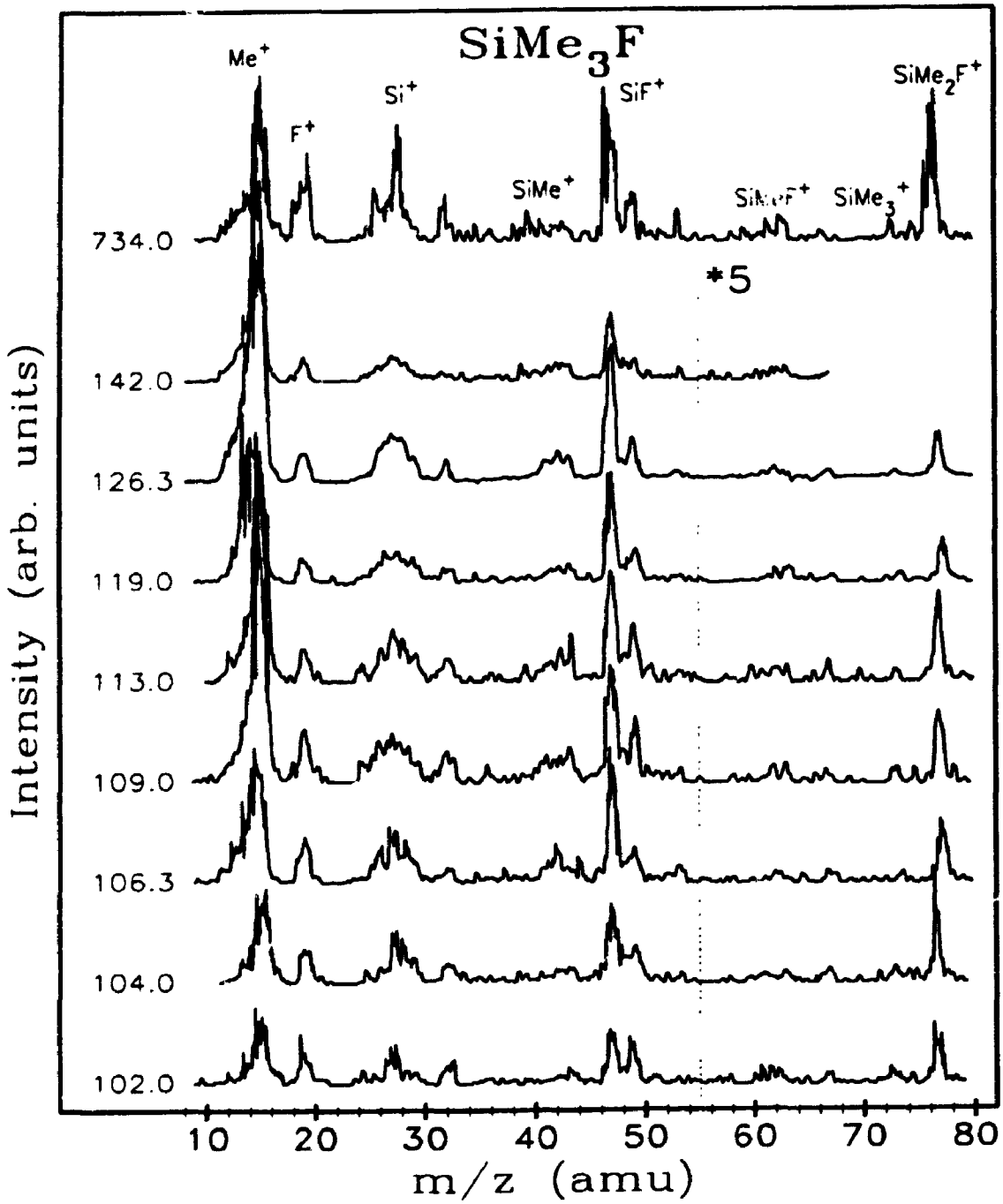

Figure 4.3.5: Photoionized mass spectra of $SiMe_3F$ measured at the photon energies indicated at the left of the spectra. The spectral intensities were normalized to the Me^+ partial ion yield and are multiplied by a factor of 5 above 55 amu.

photon energy(eV)	assignment[a)]	Me^+ (12-15)	F^+ (19)	Si^+ (28)	$SiMe^+$ (41)	SiF^+ (47)	$SiMeF^+$ (62)	$SiMe_3^+$ (73)	$SiMe_2F^+$ (77)
102.0	off resonance	49.8	7.4	7.0	4.4	18.0	2.8	2.5	8.1
104.0	Si2$p \rightarrow \sigma^*$	52.8	3.3	8.2	5.5	18.7	1.4	1.9	8.1
106.3	Si2$p \rightarrow$Rydberg	65.1	4.4	3.6	5.7	14.6	0.7	0.5	5.5
107.35	Si2p I.P.								
109.0	Si2$p \rightarrow ka_1$	71.2	3.0	3.6	4.3	11.9	0.8	0.7	4.5
113.0	Si2$p \rightarrow ka_1 + ke$	71.1	2.0	3.7	4.5	12.2	0.9	0.4	5.2
119.0	off resonance	72.3	2.1	3.7	3.1	13.5	1.1	0.5	3.6
126.3	Si2$p \rightarrow ke$	79.1	1.7	3.2	3.3	9.5	0.6	0.3	2.3
142.0	off resonance	79.4	2.4	2.3	4.6	10.0	1.3	0.0	0.0
650.0	off resonance	44.8	7.0	4.6	8.8	22.3	1.0	1.0	10.5
710.0	F1$s \rightarrow \sigma^*$	62.1	6.1	4.3	4.7	13.2	1.5	0.6	7.4
734.0	F1$s \rightarrow$cont. res.	57.5	8.2	4.3	3.6	13.9	1.9	0.9	9.7
800.0	off resonance	58.4	2.4	5.9	8.2	11.9	2.4	0.9	9.8

[a)] Ref. 57.

Table 4.3.4: Branching ratios (%) of the peak areas from the photoionized mass spectra of $Si(CH_3)_3F$ (Fig. 4.3.5) around the Si 2p, Si 2s and F 1s ionization edge regions. Approximate m/z values are given in brackets for each fragment below the symbol.

Other rearrangements are also possible and in the photoion mass spectra of $Si(CH_3)_4$ (Fig. 4.3.6), complex fragmentation patterns lead to numerous photoion peaks in the Si^+, $SiMe^+$ and $SiMe_2^+$ regions of the spectrum. Because the main concern here is the fragmentation of the Si−C and Si−F bonds, areas from peaks corresponding to loss or gain of H atoms are included with the "main line" in the branching ratio calculations of the fragment ion peak areas. When calculating branching ratios for the $SiMe^+$ peak areas for $Si(CH_3)_4$ for instance, all of the peaks in the 40 − 46 amu range (corresponding to SiC^+ to $H_3SiCH_3^+$ ions) which have appreciable intensity are included as $SiMe^+$ peaks.

Photoion mass spectra of SiF_4 [40,41] and $Si(CH_3)_4$ [34,42,60] following excitation or ionization of the Si 2*p* core electrons and of SiF_4 after excitation or ionization of the F 1*s* [18] electrons have been reported previously. Similar ionic fragments were observed in the previously reported photoion mass spectra of Si 2*p* core electron excited or ionized SiF_4.[40,41] There is a large discrepancy between the intensities of the ion peaks between the SiF_4 mass spectra reported here and those presented in Ref. 40 and Ref. 41. Intensities of the photoion mass spectra peaks corresponding to the heavier ions were greatly enhanced (relative to the spectra presented here) and a molecular ion peak, SiF_4^+, was even observed. The most intense peak in the previous photoion mass spectra of SiF_4 was the SiF_3^+ peak with a branching ratio of 50-82% across the Si 2*p* region, while in the spectra reported here the branching ratio of the SiF_3^+ peak ranges from 1-10%. The previous spectra were obtained using a time-of-flight mass spectrometer and the lower intensities of the heavier ionic fragments in the photoion mass spectra in this report result in part from the lower transmission efficiency of the quadrupole mass filter for heavier ions.[61] However, the spectra in Ref. 40 were obtained without the use of ion extraction fields to achieve uniform collection efficiency for ions regardless of their kinetic energies, and the authors of the report cautioned about the possible discrimination against energetic ions with low mass. In the more recent study of the photo-ionized

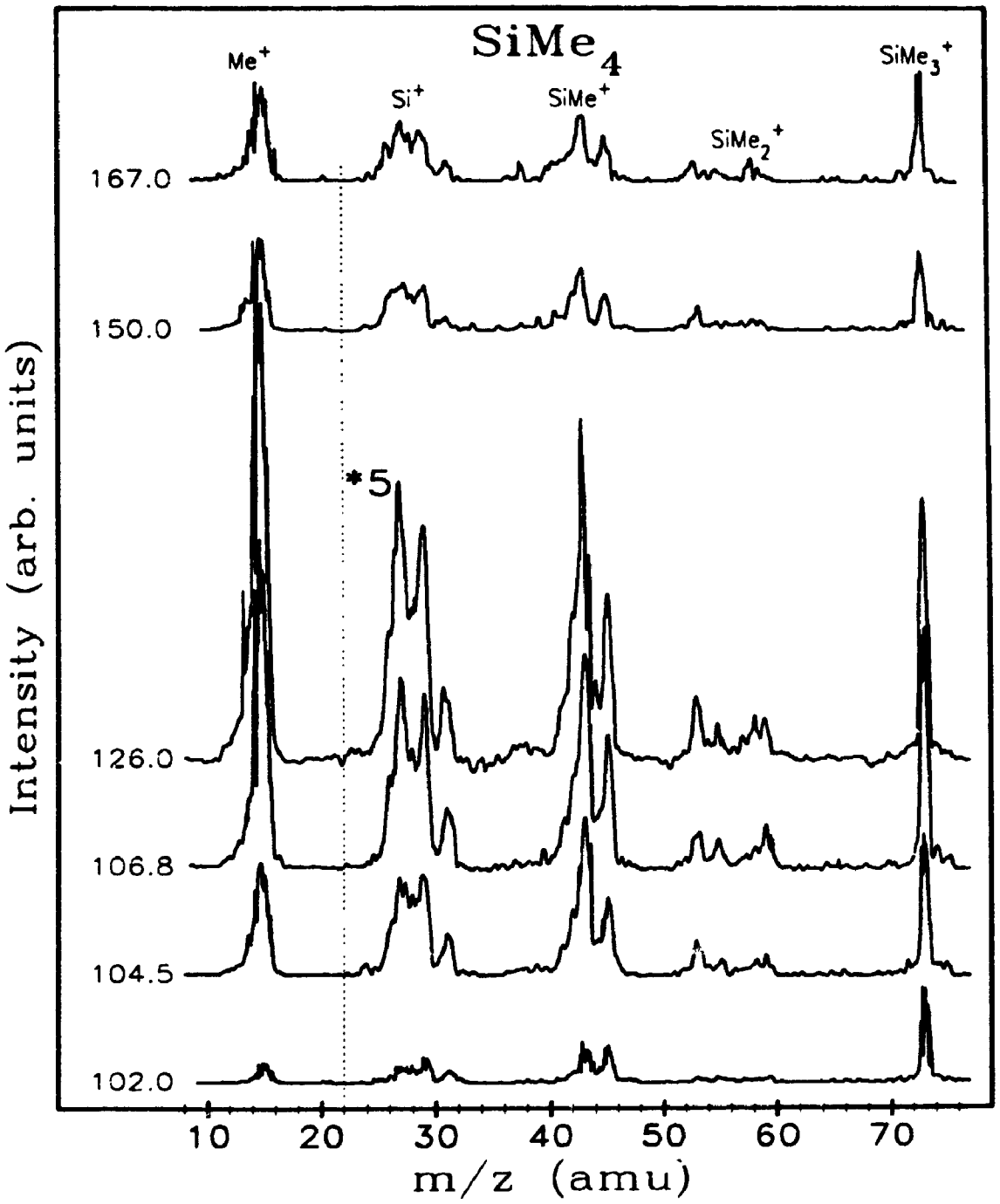

Figure 4.3.6: Photoionized mass spectra of $SiMe_4$ measured at the photon energies indicated at the left of the spectra. The spectral intensities were normalized to the Me^+ partial ion yield and are multiplied by a factor of 5 above 22 amu.

photon energy(eV)	assignment[a)]	Me^+ (12-15)	Si^+ (28)	$SiMe^+$ (43)	$SiMe_2^+$ (58)	$SiMe_3^+$ (73)
102.0	off resonance	37.1	14.6	24.3	4.4	19.6
104.5	Si2*p* →Rydberg	53.9	13.5	20.6	4.3	7.7
105.4	Si2*p* → σ^*+Rydberg	57.5	11.7	19.2	4.4	7.1
106.14	Si2*p* I.P.					
106.8	Si2*p* → ka_1	65.7	9.7	14.6	3.6	6.5
126.0	Si2*p* → $ka_1 + ke$	71.1	8.7	12.3	3.3	4.6
150.0	off resonance	68.8	7.5	13.1	4.1	6.5
154.8	Si2*s* →Rydberg	68.4	8.8	13.8	3.6	5.4
157.5	Si2*s* I.P.					
167.0	Si2*s* → cont. res.	66.0	8.7	14.1	4.1	7.1
190.0	off resonance	65.7	9.9	11.6	7.7	5.1

[a)] Ref. 57.

Table 4.3.5: Branching ratios (%) of the peak areas from the photoionized mass spectra of $Si(CH_3)_4$ (Fig. 4.3.6) around the Si 2*p* and Si 2*s* ionization edge regions. Approximate m/z values are given in brackets for each fragment below the symbol.

mass spectra of SiF_4, better agreement with the ion peak intensities given here are observed.[41] Similar branching ratios are seen for the lighter ions in Table 4.3.1 of this chapter and Table 1 of Ref. 41. For example, using the ratio of the Si^2+ to F^+ yields at a photon energy of 106.3 eV as a benchmark, a value of 1:11 is obtained from this data, a value of 1:3 from Lablanquie *et al*'s data[40] and a value of 1:10 obtained from the more recent report of Imamura.[41] The correspondence between the two data sets suggests that potential cage used around the interaction region between the synchrotron beam and the gas jet is efficiently collecting ions of all kinetic energies. Photoion mass spectra of SiF_4 following excitation and ionization of the F 1*s* electrons have also been recorded with a time-of-flight mass spectrometer.[18] These spectra are strongly biased against the heavier fragments and ions with m/z ratios of greater than 33 amu were not observed. The previously reported photoion mass spectra of $Si(CH_3)_4$ [34,42,60] were measured using a time-of-flight mass spectrometer at fairly low mass resolution and only six peaks were

observed. The intensity distribution of the peaks, while not identical with that reported here, is in reasonable agreement with these results (Fig. 4.3.6). The different sensitivities of the mass filters, while significant, are not important here since it is relative changes of the peak area branching ratios as a function of the photon energy and ligand substitution which form the basis of this report.

The relative intensities of the F^+ and Me^+ ion peaks in the photoion mass spectra of the mixed fluoromethylsilane compounds are somewhat surprising. Intensities of the Me^+ peaks exceed those of the F^+ peaks at all photon energies for all of the mixed fluoromethylsilane compounds, even $SiCH_3F_3$, which has three times the number of fluorine atoms than methyl groups around the central silicon atom. Even accounting for the possible bias of the quadrupole mass filter against the slightly heavier F^+ ions, methyl ions are significantly more abundant than fluorine ions in the core electron photoionized mass spectra of $SiCH_3F_3$. The methyl group therefore appears to be much more labile than the fluorine atom following ionization of the molecule, even at photon energies corresponding to valence ionization ($h\nu \leq 105$ eV). Ratios of the Me^+/F^+ peak areas of the mixed fluoromethylsilane compounds (Table 4.3.2 – Table 4.3.5) range from 9.4:1, 21.5:1 and 6.7:1 at photon energies below the Si 2*p* pre-edge structure (valence ionization) to 6.4:1, 33.8:1 and 46.5:1 at photon energies corresponding to the maximum in the photoabsorption cross section above the Si 2*p* edge for $SiCH_3F_3$, $Si(CH_3)_2F_2$ and $Si(CH_3)_3F$ respectively. There are two trends apparent from these ratios. Firstly, below the Si 2*p* ionization threshold, the Me^+/F^+ peak area ratio is larger for $Si(CH_3)_2F_2$ than it is for $SiCH_3F_3$, as expected, but it is also larger than for $Si(CH_3)_3F$ even though the ratio of the number of methyl groups to fluorine atoms is larger in $Si(CH_3)_3F$. There is also a corresponding increase in the relative yield of SiF^+ ions in $Si(CH_3)_3F$ versus either $Si(CH_3)_2F_2$ or $SiCH_3F_3$. Above the Si 2*p* ionization threshold, the Me^+/F^+ peak area ratio drops by ~30% for $SiCH_3F_3$ but increases by ~50% for $Si(CH_3)_2F_2$ and by ~600% for $Si(CH_3)_3F$. Removal of a Si

2*p* electron therefore results in a relative enhancement of the F^+ yield for $SiCH_3F_3$ and of the Me^+ yield for the two other mixed fluoromethylsilane compounds.

Shapes of the broad Me^+ photoion peaks which include contributions from the four ions C^+, CH^+, CH_2^+, and CH_3^+, change significantly both with photon energy for a given compound and also between the four methyl-containing fluoromethylsilane compounds. Contributions of the four ions to the Me^+ photoion peaks have been separated by fitting four peaks of equal width to the Me^+ peaks in the photoion mass spectra of the four methyl containing fluoromethylsilane compounds using a non-linear least-squares procedure. Due to the overlap of the four peaks, however, the fitted areas of the overlapping peaks are prone to fairly large errors and are therefore not included in the tables. Changes in the intensity distribution of the methyl peaks with photon energy are most pronounced in the photoion mass spectra of $SiCH_3F_3$ where the area ratio of the C^+, CH^+, CH_2^+, and CH_3^+ peaks (with respect to the total Me^+ peak area) changes from 9% : 20% : 39% : 32% in the spectrum measured below the Si 2*p* photoionization edge at 104 eV to 17% : 29% : 33% : 21% in the spectrum measured at the photoabsorption cross section maximum at 132 eV. Branching ratios of the methyl peaks in the photoion mass spectra of the other mixed fluoromethylsilane compounds also change above the Si 2*p* ionization edge, although a progressively smaller change is seen in $Si(CH_3)_2F_2$ and $Si(CH_3)_3F$. The effect is not observed in the mass spectra of $Si(CH_3)_4$ where the intensity distribution of the methyl peaks in the spectrum below the Si 2*p* edge at 102 eV, 2% : 6% : 23% : 69% is very similar to the distribution in spectra measured at photon energies above the edge at 125 eV, 3% : 10% : 16% : 71%. The increase in the degree of fragmentation of the methyl ion fragments from the photoion mass spectra measured below the Si 2*p* ionization edges to those measured above therefore follows the number of fluorine atoms in the parent molecule. While there is no evidence of $SiFH_x^+$, $SiF_2H_x^+$ or SiF_3H^+ peaks in the photoion mass spectra of $SiCH_3F_3$ (Fig. 4.3.3) which exhibits the greatest

degree of methyl ion fragmentation, a strong peak at m/z = 49 amu ($SiFH_2^+$) is present in the photoion mass spectra of $Si(CH_3)_3F$ (Fig. 4.3.5), which has the least degree of methyl ion fragmentation. Hydrogen atoms from the C^+, CH^+ and CH_2^+ fragment ions of $SiCH_3F_3$ and $Si(CH_3)_2F_2$ must therefore be present as atomic ions, atoms, molecular hydrogen or neutral molecular fragments such as SiFH, $SiFH_2$, etc. Further photoionization mass spectroscopy experiments with better mass resolution extended to $\leq$1 amu would help determine the fate of the H atoms from the methyl groups of the mixed fluoromethylsilane compounds.

Wen and Rosenberg identified a complementary trend in the relative H^+ yields from the condensed fluoromethylsilane molecules in the valence ionization region.[62] They found a marked increase in the H^+ yield when the number of fluorines in the molecule was increased, especially when the yield were normalized to the statistical number of sites available for desorption of H^+ from the fluoromethylsilane compounds. This is consistent with the increased fragmentation of the methyl ligands with increasing number of fluorine atoms in the compound observed in this report. Wen and Rosenberg also noted a strong increase in the CH_3^+ yield and a weaker increase in the F^+ yields with an increasing number of fluorine atoms in the compound.[62] The trend is reproduced in this data where the CH_3^+ yield, normalized to the number of methyl ligands in the compound, ranges from 1 for $Si(CH_3)_4$ to 1.8 for $Si(CH_3)_3F$ to 3.8 for $Si(CH_3)_2F_2$ and 7.5 for $SiCH_3F_3$ in the mass spectra measured below the Si 2*p* ionization edge (valence ionization only). The trend in the F^+ yields at the same photon energies is not as noticeable, ranging from 1 for $Si(CH_3)_3F$ to 0.2 for $Si(CH_3)_2F_2$ to 0.32 for $SiCH_3F_3$ and 1.7 for SiF_4. Wen and Rosenberg proposed a model to account for the trends in the H^+, CH_3^+ and F^+ yields that was based upon the influence of the fluorine and methyl ligands on the effective hole–hole interaction, U_{eff}, and covalent interaction, V. For effective desorption, the two electron holes in the compound must remain localized which occurs when $U_{eff} > V$. Four factors influencing U_{eff} and V were

considered in the model, the bond orbital size, bond polarity, screening of the two holes and the interaction between orbitals of homogeneous sites. Only the latter factor was found to exert a suppressing effect for the desorption of F^+ with increasing numbers of fluorine atoms.

Relative yields of other ionic fragments of the fluoromethylsilane compounds also change with photon energy in the Si 2*p* ionization edge region. In the SiF_4 photoion mass spectra (Fig. 4.3.2) for example, the relative yields of the doubly charged atomic fragments of SiF_4, F^{2+} and Si^{2+} (Table 4.3.1) increase sharply at the Si 2*p* ionization threshold while over the same photon energy range yields of the doubly charged molecular fragment SiF^{2+} does not change significantly and the yield of SiF_2^{2+} decreases slightly. The branching ratio of F^+ also increases across the Si 2*p* ionization edge, while the branching ratios of the other singly charged ions of SiF_4, Si^+, SiF^+, SiF_2^+ and SiF_3^+ decrease. Increased efficiency of F^+ fragmentation from Si 2*p* photoionized SiF_4, relative to the valence ionized molecule, explains this result quite simply. In the SiF_4 F 1*s* region, the relative yield of F^+ actually decreases above the ionization threshold (Table 4.3.1), following the trend observed previously,[18] while branching ratios of the other fragments increase. This is counterintuitive to the anticipated results where a F 1*s* core hole is expected to result in enhanced fragmentation of F^+ ions following Auger decay of the core hole.

Branching ratios of the Me^+ peaks in the photoionized mass spectra of the methyl containing fluoromethylsilane molecules have similar profiles for all four molecules. The Me^+ branching ratios are at minimum values below the Si 2*p* ionization thresholds, increase at the Si 2*p* pre-edge resonances, with the exception of $SiCH_3F_3$ where the Me^+ branching ratio drops at the Si 2*p* pre-edge features, and reach maximum values in the Si 2*p* continuum. The magnitude of the changes in the branching ratios of the Me^+ branching ratio from the minimum values below the Si 2*p* ionization threshold to the maximum values above the edge reflects the

number of methyl groups in the compound of interest. The branching ratios of the Me^+ peak at their maximum values in the Si 2*p* continuum increase from their values below threshold by 2% for $SiCH_3F_3$, 17% for $Si(CH_3)_2F_2$, 62% for $Si(CH_3)_3F$ and 78% for $Si(CH_3)_4$. As expected from these results, branching ratios for most of the methyl containing fragment ions of the fluoromethylsilane compounds, $SiMe^+$, $SiMeF_2^+$, etc., drop from maximum values below the Si 2*p* threshold to minimum values in the Si 2*p* continuum. These trends indicate that ionic fragmentation of Me^+ is enhanced by electronic transitions of the Si 2*p* electrons to discrete resonances below the edge and enhanced to a greater extent by ionization of the electrons into the Si 2*p* continuum.

The large abundance of Me^+ ions in the photoion mass spectra of the mixed fluoromethylsilane compounds and the strong enhancement of the branching ratios of the Me^+ peaks above the Si 2*p* ionization threshold indicate that electronic relaxation of the Si 2*p* core hole favours the removal of electrons from molecular orbitals associated with the methyl ligands. Since the electronic relaxation of the core hole also determines the lifetime of the core hole state, preferential fragmentation of methyl fragments must be related to the factors determining the core hole lifetime. Atomic core hole lifetimes, which are dependent upon the relaxation rate of the electron hole, have been found to vary with the electron density in the valence shell of the atom.[63] Across the first row of the periodic table for example, lifetimes of 1*s* holes decrease as reflected by the increase in photoelectron and photoabsorption linewidths. Studies of photoelectron, Auger and photoabsorption spectral linewidths of core levels in molecules have found that core hole lifetimes also vary with the chemical environment around the atomic site of the core hole,[64,65] even when contributions of vibrational splitting are considered.[66] Since core holes in light elements relax primarily via Auger decay, the lifetimes of core holes in these elements are determined by the Auger transition rates. Auger transition rates in turn, depend on the local electron

density around the atomic site of the core hole because of the highly localized nature of inner-shell electrons and the normally low rate of interatomic Auger transitions.[67] The electron density around the core hole is determined in part by the electron withdrawing and donating properties of the groups bound to the atomic site of the core hole. The electron donating or withdrawing properties of the ligands bound to an atom with a core hole therefore affect the lifetime of the hole state.[65] Chemical effects on core hole lifetimes were observed in the Si 2*p* photoelectron spectra of several alkylsilane compounds where, at a constant experimental resolution, the Si 2*p* linewidth was found to increase from 232 meV for SiH_4 to 280 meV for $(CH_3)_2SiH_2$ to 304 meV for $Si(CH_3)_4$.[66] The increase in the photoelectron linewidth with the number of methyl ligands has been assigned to be due to the increased electron density on the central Si atom from of the electron donating methyl groups.[66]

In the mixed fluoromethylsilane compounds, the electron donating properties of the methyl ligands will result in a preferential relaxation pathway for the core hole via Auger decay involving electrons from Si−Me molecular orbitals. Electrons in Si−F orbitals are more localized around the fluorine atom and will not participate in the Auger decay as often as electrons from the Si−Me bonds. In the valence bond depopulation model of ionic fragmentation [2,18] therefore, fluorine atoms will preferentially remain bound to the central Si atom and the methyl fragment ions will be most abundant. The greater yields of SiF^+ than $SiMe^+$ in the mass resolved ion spectra of the mixed fluoromethylsilane compounds (Table 4.3.2 – Table 4.3.4) along with the much greater yields of Me^+ than F^+ at all photon energies support the above explanation. This model can also explain the generally increased fragmentation of the methyl group above the Si 2*p* ionization edge in the $SiCH_3F_3^+$. The two valence hole resulting from the Auger decay of the Si 2*p* core hole will be preferentially localized in Si−Me orbital(s), fragmenting an Me^+ or Me^{2+} ion which may be stabilized by further fragmentation into the

smaller methyl fragments C^+, CH^+ and $CH_2^+ + H^+$ and neutral H atoms. In the other mixed fluoromethylsilane compounds, with more than one methyl group, localization of the two valence holes on one Si–Me bond is less likely and the degree of fragmentation of the methyl ion decreases. Fragmentation of doubly charged methyl groups into H^+ and C^+, CH^+ or CH_2^+ has been observed previously in the PIPICO spectra of the core ionized organometallic compounds $Sn(CH_3)_4$,[43,44] $Pb(CH_3)_4$,[45] $Al(CH_3)_3$,[46] and $Ga(CH_3)_3$.[47]

Lower branching ratios for the Me^+ ions at discrete resonances in the pre-edge of the photoabsorption spectrum than in the Si 2*p* continuum indicate that spectator Auger decay of the core hole may not be as predominate in the other fluoromethylsilane compounds as in SiF_4, where it is estimated to account for 60–80% of the core hole relaxations.[13,68] Partial photoionization cross sections of the valence bands of $Si(CH_3)_4$ in the Si 2*p* ionization region have been measured previously and the 21.7 eV band (assigned to the $1a_1+1t_1$ molecular orbitals[69]) was found to resonate strongly just below the Si 2*p* edge, indicating that participator Auger decay process may be more efficient than the spectator decay process for $Si(CH_3)_4$.[70] Participator Auger decay involving the 21.7 eV photoelectron band, which has a significant Si 3*s* character, will result in a singly charged molecular ion and a lesser degree of ionic fragmentation than normal Auger decay of the core hole in the ionized molecule which creates a doubly charged molecular ion. The yield of Me^+ relative to the larger fragments like $SiMe_3^+$, $SiMe_2^+$ and $SiMe^+$ is therefore expected to be lower in the pre-edge than in the ionization continuum. This is indeed what is observed for $Si(CH_3)_4$, with the molecular fragments $SiMe_3^+$, $SiMe_2^+$ and $SiMe^+$ having maxima in their branching ratios at a photon energy below the discrete resonances, smaller values at the discrete resonances and lowest values in the Si 2*p* continuum.

4.3.3. Partial ion yields

Mass selected partial ion yields of the fluoromethylsilane compounds in the Si $2p$ ionization region are presented in figures 4.3.7 – 4.3.11 for SiF_4 – $Si(CH_3)_4$ with the appropriate total ion yields for comparison. Partial ion yields of fragment ions of SiF_4 [18] and $Si(CH_3)_4$ [34,60] have been reported previously and the previous trends are in good agreement with the results presented here. Most of the partial ion yields exhibit all of the the discrete and continuum resonance features observed in the total ion yields. Resonances in the partial ion yields of the fragment ions with three ligands surrounding the central silicon atom (SiF_3^+ for SiF_4, $SiCH_3F_2^+$ and SiF_3^+ for $SiCH_3F_3$, $SiCH_3F_2^+$ for $Si(CH_3)_2F_2$, $Si(CH_3)_2F^+$ for $Si(CH_3)_3F$ and $Si(CH_3)_3^+$ for $Si(CH_3)_4$) are very weak and difficult to distinguish from the background noise. The weak discrete and continuum resonances in the partial ion yields of the fragments with three ligands bound to the Si atom indicate that excitation or ionization of the Si $2p$ electrons usually results in the fragmentation of more than one bond of the parent molecule. The majority of the the SiX_3^+; X=CH_3, F; produced in the Si $2p$ ionization region results from the underlying valence ionization continuum.[68,71] The intensities of the discrete resonances relative to the continuum resonances are much lower in the partial ion yields of the doubly charged ions of SiF_4, F^{2+}, Si^{2+} and SiF_2^{2+}, than in the total ion yield and partial ion yields of the singly charged ions. This is consistent with previous observations [40] and in agreement with the branching ratios of the doubly charged photoions. Doubly charged ions are produced with a much greater efficiency above the core ionization threshold since the predominate mode of decay of the core hole (in light atoms) is Auger decay resulting in two valence holes and the possibility of doubly charged fragment ions. Below the ionization edge doubly charged ions must be formed by double Auger processes, direct double photoionization or autoionization accompanied by shake-off,[40] processes which have have low probabilities of occurring.

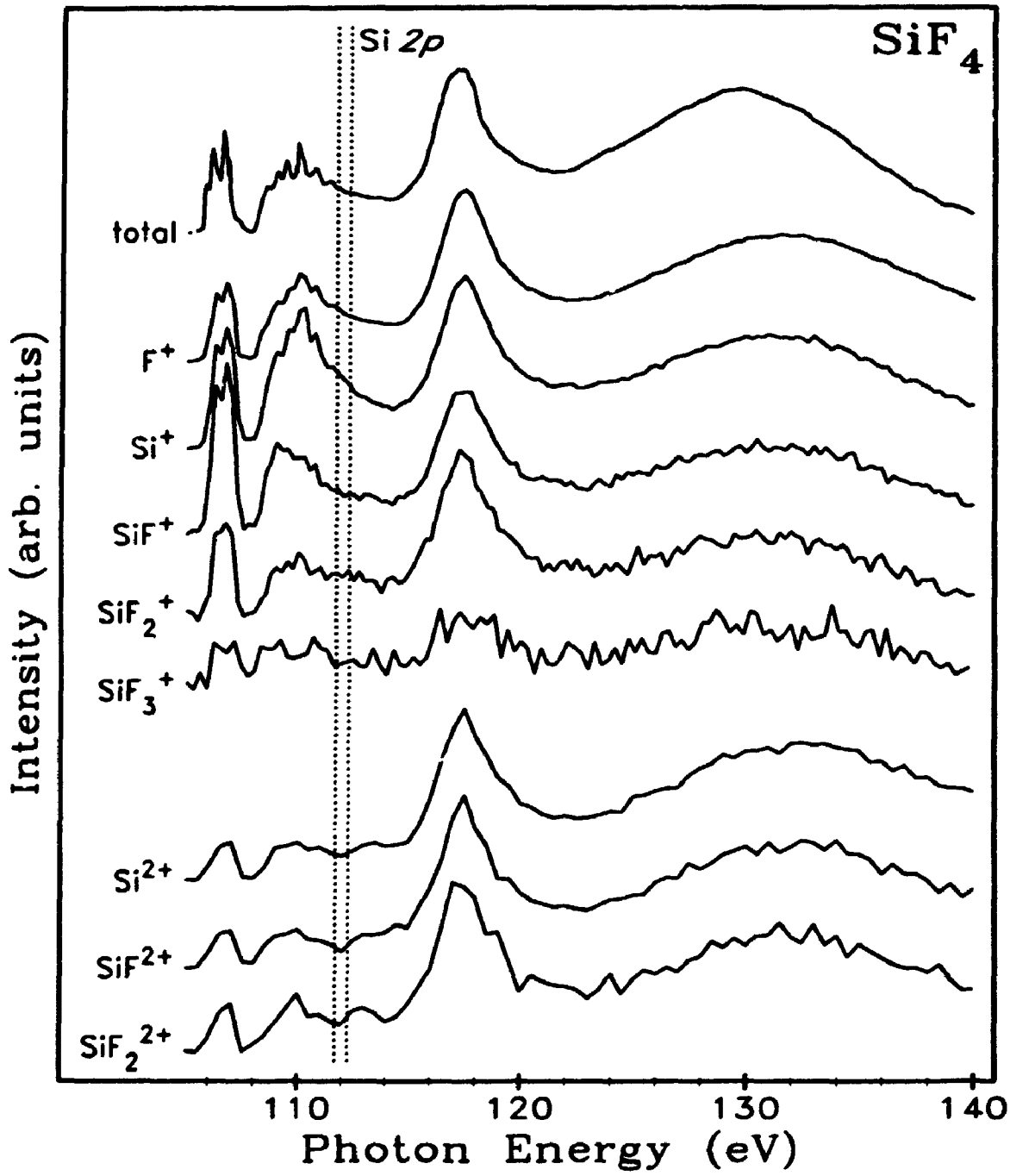

Figure 4.3.7: Partial ion yields of the fragment ions of SiF_4 and total ion yield in the Si 2*p* ionization edge region. The identity of the ion corresponding to each curve is given on the left of the figure. The $Si2p_{3/2}$ and $Si2p_{1/2}$ ionization potentials are indicated by the dashed lines.

In the Si $2p$ pre-edge region of the SiF_4 partial ion yield spectra (Fig. 4.3.7), some significant differences are observed in the spectra of different fragment ions. The partial ion yields of the atomic fragments F^+ and Si^+ are very similar to the SiF_4 total ion yield and hence to the photoabsorption spectrum in the Si $2p$ pre-edge region. For the SiF^+ and SiF_2^+ partial ion yields, however, the first discrete resonance, corresponding to the Si $2p \rightarrow \sigma^*(a_1)$ electronic transition, is greatly enhanced relative to the other discrete and continuum resonances. The effect is most pronounced in the partial ion yield of SiF^+ where the intensity of the first resonance is greater than the intensity of the continuum resonance at 117 eV. The shape of the second group of discrete resonances in the SiF^+ partial ion yield is also noticeably asymmetric with greater intensity at the peaks which have been assigned as Si $2p \rightarrow \sigma^*(t_2)$ resonances.[57] The overall shape of the pre-edge region of the SiF^+ partial ion yield of SiF_4 is similar to the Si $2p$ pre-edge photoabsorption spectrum of solid SiF_4,[72,73] where the intensities of the resonance assigned to Rydberg transitions were found to be much lower than in the gas phase photoabsorption spectrum. The mass resolved partial ion yields of the SiF^+ and SiF_2^+ fragments of SiF_4 reported previously exhibited similar enhancements which were not commented upon.[40]

The enhanced production of SiF^+ and SiF_2^+ following excitation of a Si $2p$ electron into a virtual Si–F antibonding orbital can be understood in terms of the electronic structure of the molecule after relaxation of the core hole. Below the Si $2p$ core ionization edge, resonances observed in the photoabsorption spectrum of SiF_4 are due to Si $2p \rightarrow \sigma^*$ or Rydberg electronic transitions resulting in an electronic state with a core hole and an electron in a virtual orbital. The predominate electronic decay mechanism of this state for SiF_4 is a spectator Auger decay,[13] leaving the molecule with two holes in valence orbitals and the excited electron remaining in the virtual orbital. The two valence holes can be localized in either one or two molecular orbitals and the molecule will probably fragment at

the Si−F bonds with the electron holes. When the initial excitation is a Si $2p \rightarrow \sigma^*$ electronic transition, the excited electron is in an antibonding Si−F molecular orbital and this excitation can also result in the fragmentation of a further Si−F bond. Therefore, depending on whether the valence holes resulting from the Auger decay of the core hole are localized on one or two Si−F bonds, the production of SiF_2 and SiF fragments respectively will be enhanced following the excitation of a Si $2p$ electron to an antibonding orbital. While partitioning of the positive charges among the three (SiF_2 + 2 F) or four (SiF + 3 F) fragments is not clear, the electronic relaxation scheme outlined above does explain the enhanced yields of SiF^+ and SiF_2^+ at the discrete resonances corresponding to electronic transitions to antibonding orbitals. The yield of neutral fragments of SiF_4 following Si $2p$ core excitation has been reported previously and there is a slightly larger relative yield of SiF in the pre-edge regions based on the intensities of the unresolved discrete resonances.[74]

The model of the electronic processes leading to the fragmentation of SiF_4 given above can be tested by applying it to the partial ion yields of the other fluoromethylsilane molecules. Based on the above explanation of the enhanced yields of SiF^+ and SiF_2^+ at the Si $2p \rightarrow \sigma^*$ discrete resonances in SiF_4, enhancements are expected for the SiF yields for $SiCH_3F_3$ and $Si(CH_3)_2F_2$ and for the SiMe yield for $Si(CH_3)_3F$ following electronic transitions of the Si $2p$ core electrons to the Si−F antibonding orbitals of the mixed fluoromethylsilane compounds. Yields of SiMe are also expected to be enhanced for $SiCH_3F_3$ and $Si(CH_3)_2F_2$ at the Si−F antibonding resonances, but because of the higher probability of the Si−Me valence electrons being involved in the Auger decay of the core hole, as noted in section 4.3.2, yields of $SiMe_x^+$ ions are much lower than those of SiF_x^+ ions. Resonances appearing at the lowest energy in the Si $2p$ pre-edge region of the photoabsorption spectra of the fluoromethylsilane compounds

have been previously assigned to correspond to electronic transitions to the Si–F antibonding orbitals.[57]

There appear to be small enhancements of the SiF^+ yields at these resonances for $SiCH_3F_3$ (Fig. 4.3.8) and $Si(CH_3)_2F_2$ (Fig. 4.3.9) relative to the total ion yield curves. It is difficult to discern whether the $SiMe^+$ yield is enhanced at the Si–F antibonding orbital resonance in $Si(CH_3)_3F$ (Fig. 4.3.10) because of the weak and noisy signal.

Partial ion yields of the Me^+ fragments from the fluoromethylsilane compounds all exhibit reduced intensities at the Si 2*p* pre-edge features relative to the continuum compared with the total ion yields. The continuum resonance just above threshold, which has an intensity proportional to the number of methyl ligands in the molecule, is therefore highlighted as mentioned earlier. These continuum resonances were previously assigned to Si–C antibonding orbitals in the photoabsorption spectra of the fluoromethylsilane compounds.[57] Some reduction in the relative intensity of the discrete resonances in the Me^+ ion yield was seen in previous measurements of the partial ion yields of $Si(CH_3)_4$ around the Si 2*p* ionization edge.[34,60] The reduced intensity of the discrete resonances in the Me^+ partial ion yields is most pronounced in the $Si(CH_3)_4$ spectrum (Fig. 4.3.11) and least pronounced in the spectrum of $SiCH_3F_3$ (Fig. 4.3.8). Branching ratios of the areas of the Me^+ photoion mass peaks were also observed to be lower in the Si 2*p* pre-edge regions of the fluoromethylsilane compounds than in the continuum and was explained by the enhanced autoionization of the $1a_1 + 1t_1$ valence photoelectron bands of $Si(CH_3)_4$ at the Si 2*p* pre-edge resonances resulting in less ionic fragmentation of methyl groups from the molecule. The relative importance of participator Auger decay (autoionization) versus spectator Auger decay of the core hole seems to increase with the number of methyl groups around the central silicon atom.

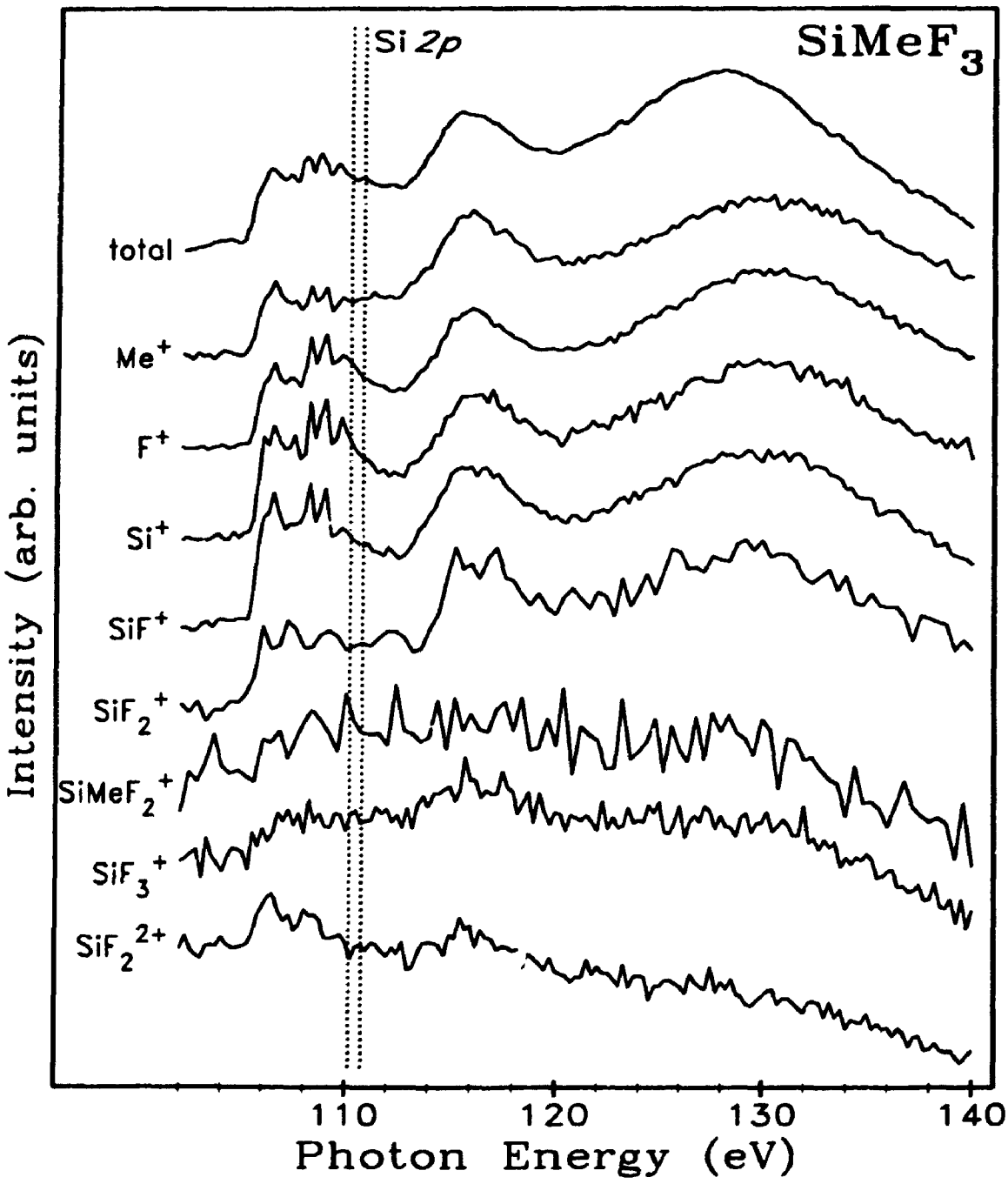

Figure 4.3.8: Partial ion yields of the fragment ions of $SiMeF_3$ and total ion yield in the Si 2*p* ionization edge region. The identity of the ion corresponding to each curve is given on the left of the figure. The $Si2p_{3/2}$ and $Si2p_{1/2}$ ionization potentials are indicated by the dashed lines.

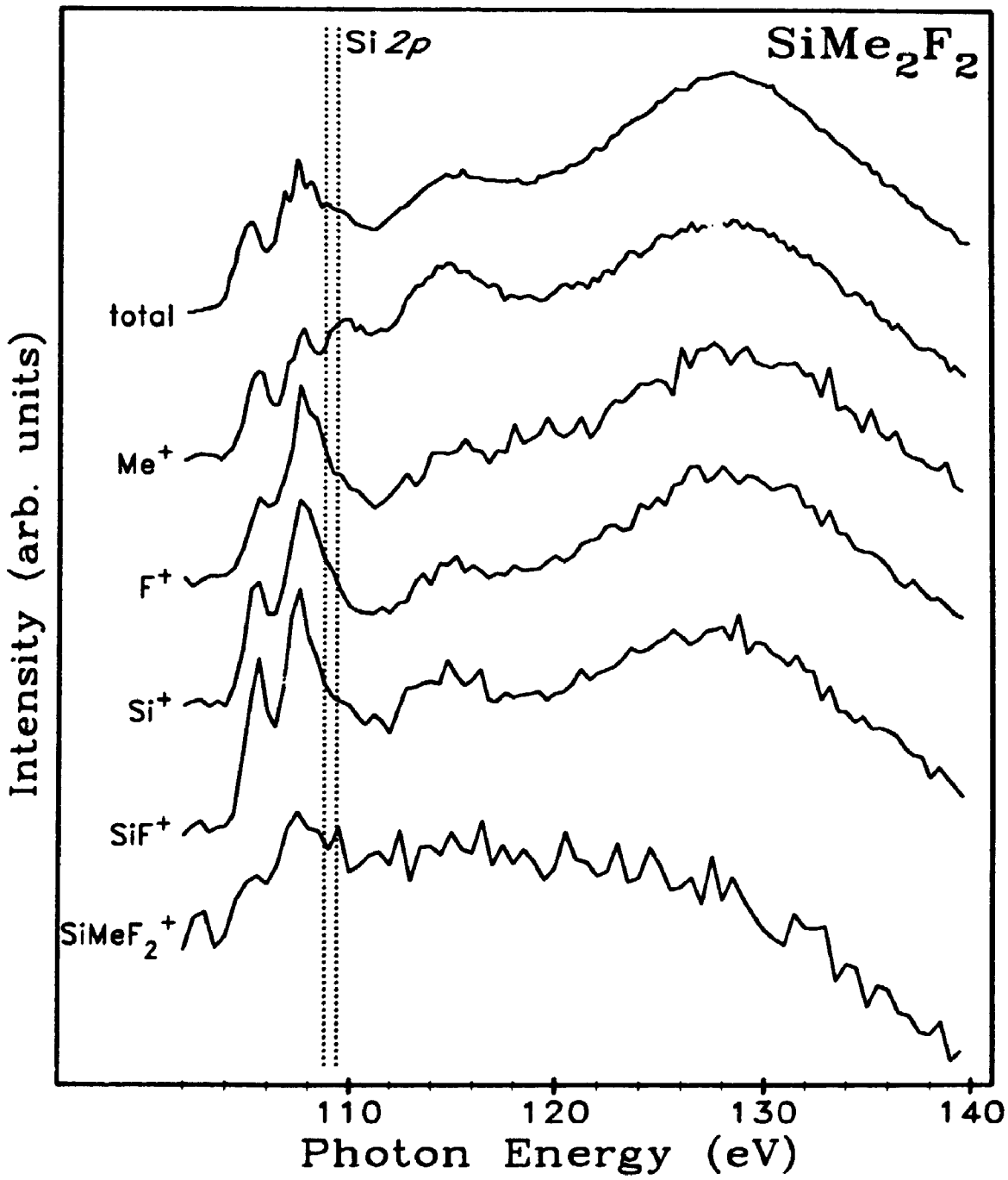

Figure 4.3.9: Partial ion yields of the fragment ions of $SiMe_2F_2$ and total ion yield in the Si 2*p* ionization edge region. The identity of the ion corresponding to each curve is given on the left of the figure. The $Si2p_{3/2}$ and $Si2p_{1/2}$ ionization potentials are indicated by the dashed lines.

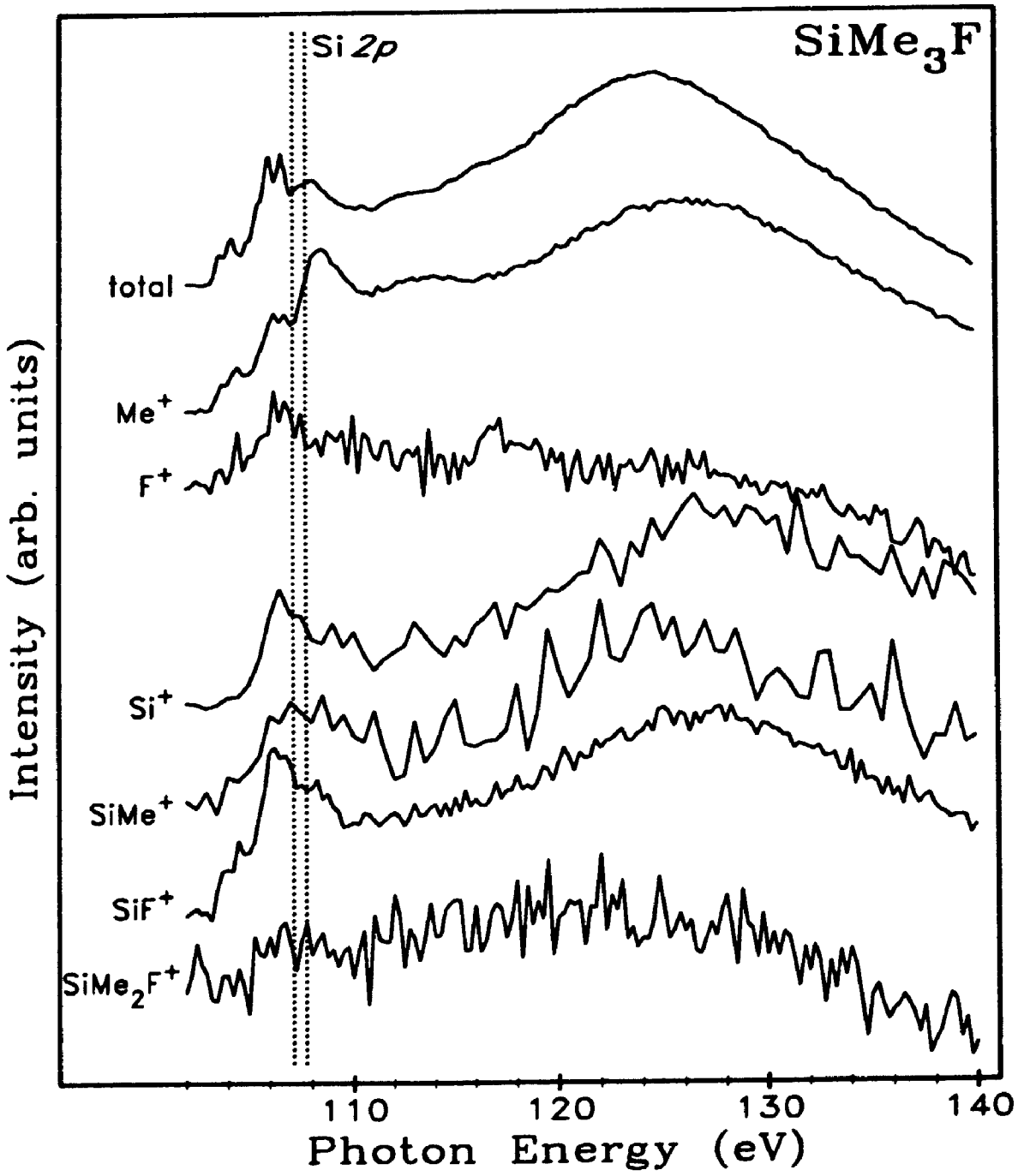

Figure 4.3.10: Partial ion yields of the fragment ions of $SiMe_3F$ and total ion yield in the Si 2*p* ionization edge region. The identity of the ion corresponding to each curve is given on the left of the figure. The $Si2p_{3/2}$ and $Si2p_{1/2}$ ionization potentials are indicated by the dashed lines.

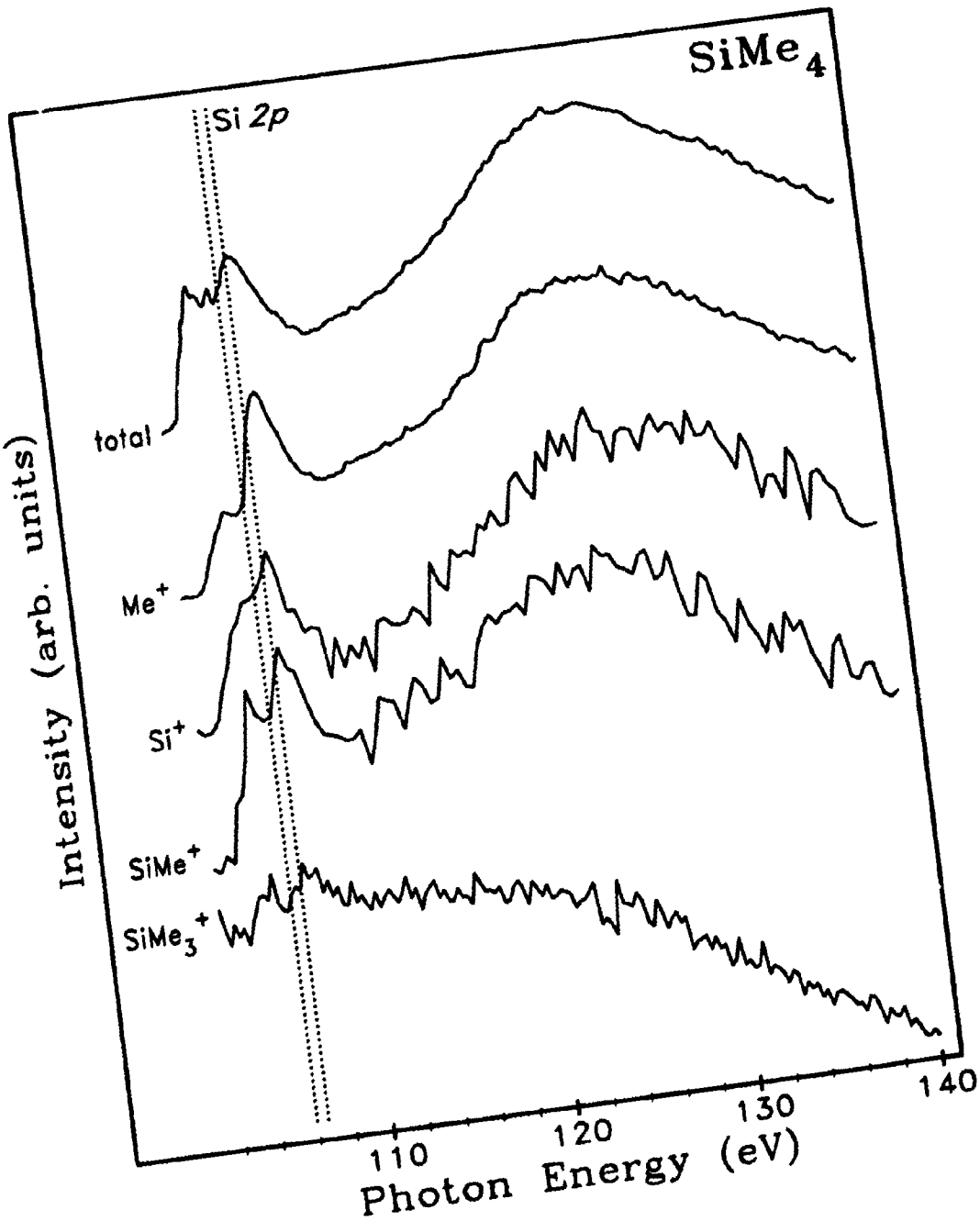

Figure 4.3.11: Partial ion yields of the fragment ions of $SiMe_4$ and total ion yield in the Si 2*p* ionization edge region. The identity of the ion corresponding to each curve is given on the left of the figure. The $Si2p_{3/2}$ and $Si2p_{1/2}$ ionization potentials are indicated by the dashed lines.

4.4. CONCLUSIONS

Total ion yields, total electron yields, photoion mass spectra and mass resolved partial ion yields of the five fluoromethylsilane compounds, $Si(CH_3)_xF_{4-x}$; x=0-4, have been measured in the discrete and continuum regions of the Si 2*p* ionization edge. Photoion mass spectra were also reported around the Si 2*s* and F 1*s* ionization edges. The total ion yields and total electron yields were found to be almost identical to each other and very similar to the corresponding photoabsorption spectra. Intensities of the discrete resonances, however, were reduced in the total ion and electron yields relative to the photoabsorption spectra.

Numerous fragment ions, both atomic and molecular, were observed after excitation or ionization of the core electrons for all five fluoromethylsilane compounds. Methyl ions were found to be the most abundant ionic fragments in the photoion mass spectra of the mixed fluoromethylsilane compounds at all photon energies. Intensities of the constituent ions in the methyl ion peak, C^+, CH^+, CH_2^+, and CH_3^+ were also found to vary between the four methyl containing fluoromethylsilane compounds and with photon energy for a given compound. The degree of fragmentation of the methyl ion was seen to increase with the number of fluorine atoms in the original molecule. Branching ratios of the methyl ion peaks were also observed to increase strongly in the Si 2*p* continuum region and less strongly at the discrete resonances. The degree of the enhancement was observed to follow the number of methyl groups around the central silicon atom, being most pronounced for $Si(CH_3)_4$ and least pronounced for $SiCH_3F_3$. The exceptional lability of the methyl groups in the mixed fluoromethylsilane compounds following excitation or ionization of a core electron was attributed to the greater participation of the Si–C valence electrons than of the Si–F valence electrons in the Auger decay processes. The assignment was based on the observed chemical effects on core level linewidths which result from the electron donating

and withdrawing properties of the groups bound to the atomic site of the core hole.

Selective fragmentation following Si 2*p* core electron excitation was observed for SiF_4 and the mixed fluoromethylsilane compounds. Yields of SiF^+ were enhanced at the first discrete resonance for SiF_4, and less noticeably for $SiCH_3F_3$ and $Si(CH_3)_2F_2$ and the yield of $SiMe^+$ was enhanced slightly at the first discrete resonance for $Si(CH_3)_3F$. The first discrete resonances in the photoabsorption spectra of the fluorine containing fluoromethylsilane compounds correspond to transitions of the Si 2*p* electrons to Si−F antibonding orbitals. Spectator decay of the core hole, resulting in a one electron, two hole state selectively removes one fluorine and two additional ligands from the central silicon atom. The shape of the SiF^+ partial ion yield for SiF_4 also provides evidence for the assignment of the discrete resonances to one antibonding orbital and multiple Rydberg orbitals in the multiply overlapping peaks below the ionization edge.

4.5. REFERENCES

1. W. Eberhardt, T.K. Sham, R. Carr, S. Krummacher, M. Strongin, S.L. Weng and D. Wesner, Phys. Rev. Lett. 50, 1083 (1983).
2. D.M. Hanson, in: *Advances in Chemical Physics*, Vol. 77, ed. I. Prigogine and S. Rice (John Wiley & Sons, Inc., New York, 1990) pp. 1 - 38.
3. T.A. Carlson and R.M. White, J. Chem. Phys. 44, 4510 (1966).
4. T.A. Carlson and R.M. White, J. Chem. Phys. 48, 5190 (1968).
5. T.A. Carlson and M.O. Krause, J. Chem. Phys. 56, 3206 (1972).
6. R.B. Kay, Ph.E. Van der Leuw and M.J. Van der Wiel, J. Phys. B 10, 2521 (1977).
7. A.P. Hitchcock, C.E. Brion and M.J. Van der Wiel, J. Phys. B 11, 3245 (1978).
8. A.P. Hitchcock, C.E. Brion and M.J. Van der Wiel, Chem. Phys. Lett. 66, 213 (1979).
9. P. Morin and I. Nenner, Phys. Rev. Lett. 56, 1913 (1986).
10. G.G.B. de Souza, P. Morin and I. Nenner, Phys. Rev. A 34, 4770 (1986).
11. H. Aksela, S. Aksela, M. Ala-Korpela, O.P. Sairanen, M. Kotokka, G.M. Bancroft, K.H. Tan and J. Tulkki, Phys. Rev. A 41, 6000 (1990).
12. T.A. Carlson, *Photoelectron and Auger Spectroscopy* (Plenum Press, New York, 1975).
13. S. Aksela, K.H. Tan, K. Aksela and G.M. Bancroft, Phys. Rev. A 33, 258 (1986).
14. S. Aksela, O.-P. Sairanen, H. Aksela, G.M. Bancroft and K.H. Tan, Phys. Rev. A 37, 2934 (1988).
15. T.X. Carroll and T.D. Thomas, J. Chem. Phys. 90, 3479 (1989).

16. G.M. Bancroft, K.H. Tan, O.-P. Sairanen, S. Aksela and H. Aksela, Phys. Rev. A 41, 3716 (1990).

17. J. Murakami, M.C. Nelson, J.L. Anderson and D M. Hanson, J. Chem. Phys. 85, 5755 (1986).

18. D.A. Lapiano-Smith, C.I. Ma, K.T. Wu and D.M. Hanson, J. Chem. Phys. 90, 2162 (1989).

19. G. Cooper, T. Ibuki and C.E. Brion, Chem. Phys. 140, 147 (1990).

20. E.B. Zarate, G. Cooper and C.E. Brion, Chem. Phys. 148, 249 (1990).

21. A.P. Hitchcock, Physica Scripta T31, 159 (1990).

22. I.H. Suzuki and N. Saito, J. Chem. Phys. 91, 5324 (1989).

23. N. Saito and I.H. Suzuki, J. Chem. Phys. 91, 5329 (1989).

24. R.G. Hayes, J. Chem. Phys. 86, 1683 (1987).

25. S. Nagaoka, S. Suzuki and I. Koyano, Nucl. Instr. Methods A266, 699 (1988).

26. W. Eberhardt, J. Stöhr, J. Feldhaus, E.W. Plummer and F. Sette, Phys. Rev. Lett. 51, 2370 (1983).

27. W. Eberhardt, E.W. Plummer, I.-W. Lyo, R. Carr and W.K. Ford, Phys. Rev. Lett. 58, 207 (1987).

28. W. Eberhardt, E.W. Plummer, C.T. Chen, R. Carr and W.K. Ford, Nucl. Instr. Methods A246, 825 (1986).

29. D.A. Lapiano-Smith, D.Y. Kim, K. Lee, C.I. Ma and D.M. Hanson, *unpublished results.*

30. W. Eberhardt, E.W. Plummer, I.W. Lyo, R. Reininger, R. Carr, W.K. Ford and D. Sondericker, Aust. J. Phys. 39, 633 (1986).

31. R. Murphy and W. Eberhardt, J. Chem. Phys. 89, 4054 (1988).

32. D.M. Hanson, C.I. Ma, K. Lee, D. Lapiano-Smith and D.Y. Kim, J. Chem. Phys. 93, 9200 (1990).

33. R.G. Hayes and W. Eberhardt, Physica Scripta 41, 449 (1990).

34. I. Nenner and J.A. Beswick, in: *Handbook on Synchrotron Radiation*, Vol. 2, ed. G.V. Marr (North-Holland, Amsterdam, 1987) p. 381.

35. N. Saito and I.H. Suzuki, J. Phys. B 20, L785 (1987).

36. N. Saito and I.H. Suzuki, J. Chem. Phys. 93, 4073 (1990).

37. A.P. Hitchcock, P. Lablanquie, P. Morin, E. Lizon, A. Lugrin, M. Simon, P. Thirg and I. Nenner, Phys. Rev. A 37, 2448 (1988).

38. I. Nenner, P. Morin, M. Simon, P. Lablanquie and G.G.B. de Souza, in: *Desorption Induced by Electronic Transitions DIET III - Proceedings of the third international workshop*, eds. R.H. Stulen and M.L. Knotec (Springer-Verlag, New York, 1988) pp. 10-31.

39. I. Nenner, P. Morin, P. Lablanquie, M. Simon, N. Levasseur and P. Millie, J. Electron Spectry. 52, 623 (1990).

40. P. Lablanquie, A.C.A. Souza, G.G.B. de Souza, P. Morin and I. Nenner, J. Chem. Phys. 90, 7078 (1989).

41. T.Imamura, C.E. Brion, I. Koyano, T. Ibuki and T. Masuoka, J. Chem. Phys. 94, 4936 (1991).

42. P. Morin, G.G.B. de Souza, I. Nenner and P. Lablanquie, Phys. Rev. Lett. 56, 131 (1986).

43. K. Ueda, E. Shigemasa, Y. Sato, S. Nagaoka, I. Koyano, A. Yagishita, T. Nagata and T. Hayaishi, Chem. Phys. Lett. 154, 357 (1989).

44. K. Ueda, E. Shigemasa, Y. Sato, S. Nagaoka, I. Koyano, A. Yagishita and T. Hayaishi, Chem. Phys. Lett. 166, 391 (1990).

45. S. Nagaoka, I. Koyano, K. Ueda, E. Shigemasa, Y. Sato, A. Yagishita, T. Nagata and T. Hayaishi, Chem. Phys. Lett. 154, 363 (1989).

46. S. Nagaoka, I. Koyano and T. Masuoka, Physica Scripta 41, 472 (1990).

47. K. Ueda, Y. Sato, S. Nagaoka, I. Koyano, A. Yagishita, and T. Hayaishi, Chem. Phys. Lett. 170, 389 (1990).

48. N. Saito and I.H. Suzuki, Chem. Phys. Lett. 129, 419 (1986).

49. N. Saito and I.H. Suzuki, Int. J. Mass Spec. 82, 61 (1988).

50. N. Saito, *Researches of the Electrotechnical Laboratory*, 910, April 1990.

51. N. Saito and I.H. Suzuki, Phys. Rev. Lett. 61, 2740 (1988).

52. N. Saito and I.H. Suzuki, J. Phys. B 22, L517 (1989).

53. N. Saito and I.H. Suzuki, J. Phys. B 22, 3973 (1989).

54. N. Saito, I.H. Suzuki, H. Onuki and M. Nishi, Rev. Sci. Instr. 60, 2190 (1989).

55. K. Lee, D.Y. Kim, C.I. Ma, D.A. Lapiano-Smith and D.M. Hanson, J. Chem. Phys. 93, 7936 (1990).

56. N. Saito and I.H. Suzuki, Phys. Rev. A 43, 3662 (1991).

57. Chapter 2, section 2, *and* J.D. Bozek, G.M. Bancroft and K.H. Tan, Chem. Phys. 145, 131 (1990).

58. K.H. Tan, G.M. Bancroft, L.L. Coatsworth and B.W. Yates, Can. J. Phys. 60, 131 (1982).

59. M.R. Litzow and T.R. Spalding, *Mass Spectrometry of Inorganic and Organometallic Compounds* (Elsevier Scientific Publishing Co , New York, 1973) pp. 229-232.

60. P.Morin, in: *Photophysics and Photochemistry above 6 eV*, ed. F. Lahmani (Elsevier, Amsterdam, 1985) p. 1.

61. J.F.J. Todd and G.Lawson, in: *Mass Spectrometry* (Butterworths, Boston, 1975) p. 298.

62. C.-R. Wen and R.A. Rosenberg, J. Vac. Sci. Technol. A 7, 1851 (1989).

63. M.O. Krause, J. Phys. Chem. Ref. Data 8, 307 (1979).

64. R.W. Shaw, Jr. and T.D. Thomas, Phys. Rev. Lett. 29, 689 (1972).

65. M. Coville and T.D. Thomas, *to be published.*

66. J.D. Bozek, G.M. Bancroft and K.H. Tan, Phys. Rev. A , *in press* (1991).

67. J.A.D. Matthew and Y. Komninos, Surf. Sci. 53, 716 (1975).

68. T.A. Ferrett, M.N. Piancastelli, D.W. Lindle, P.A. Heimann and D.A. Shirley, Phys. Rev. A 38, 701 (1988).

69. J.E. Bice, K.H. Tan, G.M. Bancroft and J.S. Tse, Inorg. Chem. 26, 4106 (1987).

70. P. Morin, G.G.B. de Souza, I. Nenner and P. Lablanquie, Phys. Rev. Lett. 56, 131 (1986).

71. G.G.B de Souza, P. Morin and I. Nenner, J. Chem. Phys. 90, 7071 (1989).

72. H. Friedrich, B. Pittel, P. Rabe, W.H.E. Schwarz and B. Sonntag, J. Phys. B 13, 25 (1980).

73. C.-R. Wen and R.A. Rosenberg, *to be published.*

74. R.A. Rosenberg, C.-R. Wen, K. Tan and J.-M. Chen, J. Chem. Phys. 92, 5196 (1990).